



João Valente Duarte

The role of long-range neural oscillatory synchrony as a mechanism underlying in perceptual coherence

Tese de Doutoramento do Programa de Doutoramento em Ciências da Saúde, ramo de Ciências Biomédicas, orientada pelo Professor Doutor Miguel Castelo-Branco e pela Doutora Maria Ribeiro e apresentada à Faculdade de Medicina da Universidade de Coimbra.

2016



UNIVERSIDADE DE COIMBRA

Universidade de Coimbra
Faculdade de Medicina



**The role of long-range neural oscillatory synchrony as a
mechanism underlying in perceptual coherence**

**O papel da sincronia de larga-escala como um
mecanismo na origem de coerência perceptual**

Doctoral Thesis of the Doctoral Programme in Health Sciences, area of Biomedical Sciences, supervised by Miguel Castelo-Branco, MD PhD, and co-supervised by Maria Ribeiro, PhD, and presented to the Faculty of Medicine of the University of Coimbra.

Tese de Doutoramento do Programa de Doutoramento em Ciências da Saúde, ramo de Ciências Biomédicas, orientada pelo Professor Doutor Miguel Castelo-Branco e pela Doutora Maria Ribeiro e apresentada à Faculdade de Medicina da Universidade de Coimbra.

João Valente Duarte

2016

The studies presented in this thesis were carried out at the Visual Neuroscience Laboratory at IBILI (Institute for Biomedical Imaging and Life Sciences), Faculty of Medicine, University of Coimbra, Portugal, and were supported by a personal fellowship from the Portuguese Foundation for Science and Technology (SFRH/BD/69735/2010) and by grants from the Portuguese Foundation for Science and Technology (UID/NEU/04539/2013; CENTRO-07-ST24-FEDER-00205) and QREN COMPETE (QREN DoIT, Nr 13853 - PPS 2).

Cover design: João Duarte and Joana Crisóstomo

Copyright © 2016 João Duarte



Agradecimentos

Começo por dirigir uma palavra de sincero agradecimento ao Professor Miguel Castelo-Branco, por me ter acolhido na sua equipa. Obrigado pela confiança que depositou em mim, por ser uma inspiração e um incentivo à curiosidade e à imaginação e pela simplicidade e amizade que sempre demonstrou.

Agradeço à Maria, que desde o primeiro dia, com amizade, simpatia e rigor, me ensinou a ser um participante (e não *subject*) activo na ciência.

Agradeço à Professora Catarina de Oliveira, minha tutora, pela sua disponibilidade e incentivo ao longo destes anos.

Deixo também um Obrigado muito especial aos colegas e amigos do Laboratório de Neurociências da Visão, IBIL e ICNAS, por serem, cada um à sua maneira, os melhores do Mundo, e por todos os momentos de partilha, não só científicos mas também de vida e de amizade. O meu dia-a-dia fez-se de muitos artigos, discussão e horas ao computador mas também de muitas gargalhadas, actividades (tudo e mais alguma coisa!) e histórias para contar. Agradeço em particular aos colegas que mais de perto contribuíram para este trabalho, Gabriel, Monika, Ricardo e Teresa, porque sozinho seria impossível. Uma palavra de agradecimento também ao Carlos, João Pedro e Sónia, pela disponibilidade e colaboração na ressonância.

Agradeço à minha família, por sempre me ter apoiado e incentivado, em particular aos meus pais, por acreditarem em mim, e ao meu irmão, por me ter mostrado o caminho.

Termino com um Obrigado muito especial à Joana, que com todo o amor, amizade e genuíno orgulho partilhou comigo este caminho.

A todos, muito obrigado!

João Duarte

Nullius in verba

The Royal Society's motto, taken to mean '*take nobody's word for it*'.
It is an expression of the determination of Fellows to withstand the domination of authority and
to verify all statements by an appeal to facts determined by experiment.

Contents

Abbreviations	XI
Abstract	XV
Resumo	XIX
Chapter 1	
General Introduction	23
Visual system	25
Neural processing and visual pathways	27
The binding problem in cognitive neuroscience	40
Top-down and bottom-up mechanisms in visual perception	44
Choice of paradigm – multistability in visual perception	46
Aims and general outline of the thesis	52
References	55
Chapter 2	
Studying brain structure and function	63
Basic physical principles of MRI	65
Structural MRI	80
Functional MRI	82
Structure of fMRI data	93
Statistical analysis of fMRI data	96
Data-driven analysis methods	102
References	108
Chapter 3	
Deconvolution approaches to fMRI data	113
Abstract	115
Introduction	117
Materials and methods	119

Results.....	128
Discussion.....	142
References.....	146
Chapter 4	
Perception of bistable motion.....	149
Introduction.....	151
Materials and methods.....	154
Results.....	168
Discussion.....	194
References.....	205
Appendix.....	211
Chapter 5	
The bistable Necker cube.....	219
Abstract.....	221
Introduction.....	221
Materials and methods.....	224
Results.....	233
Discussion.....	244
References.....	248
Chapter 6	
General discussion and conclusion.....	253
General discussion.....	255
Conclusions.....	263
References.....	264
List of publications.....	269
Curriculum Vitae.....	271

Abbreviations

1-D	One-Dimensional
2-D	Two-Dimensional
3-D	Three-Dimensional
4-D	Four-Dimensional
ANOVA	Analysis of Variance
AUC	Area Under the Curve
aPFC	Anterior Prefrontal Cortex
BA	Brodmann Area
BOLD	Blood-Oxygen-Level-Dependent contrast
CBF	Cerebral Blood Flow
CBV	Cerebral Blood Volume
CLT	Central Limit Theorem
CMRO ₂	Cerebral Metabolic Rate of Oxygen extraction
CNT	Control group
CSF	Cerebrospinal Fluid
DLPFC	Dorsolateral Prefrontal Cortex
DTI	Diffusion Tensor Imaging
df	Degrees of Freedom
dGCM	difference Granger Causality Mapping
EEG	Electroencephalography
EPI	Echo Planar Imaging
FA	Flip Angle
FDR	False Discovery Rate
FFA	Fusiform Face Area
FOV	Field of View
FWHM	Full Width Half Maximum

fMRI	Functional Magnetic Resonance Imaging
GCM	Granger Causality Mapping
GE	Gradient Echo
GLM	General Linear Model
GM	Grey Matter
Hb	Deoxyhaemoglobin
HbO ₂	Oxyhaemoglobin
MT+	Human (Middle Temporal) motion complex
HRF	Hemodynamic Response Function
IFG	Inferior Frontal Gyrus
ITS	Inferior Temporal Sulcus
IOC	Intersection Of Constraints
LCD	Liquid Crystal Display (screen)
LGN	Lateral Geniculate Nucleus
LH	Left Hemisphere
LOC	Lateral Occipital Complex
MPRAGE	Magnetization-Prepared Rapid-Acquisition Gradient Echo
MR	Magnetic Resonance
MRI	Magnetic Resonance Imaging
MST	Medial Superior-Temporal area
msec	Milliseconds
O ₂	Oxygen
PDF	Probability Density Function
PET	Positron Emission Tomography
PFC	Prefrontal Cortex
pSTS	posterior Superior Temporal Sulcus
RFX	Random Effects
RH	Right Hemisphere

ROI	Region of Interest
SEM	Standard Error of the Mean
SNR	Signal-to-Noise Ratio
SPECT	Single-Photon Emission Computed Tomography
STS	Superior Temporal Sulcus
SVM	Support Vector Machine
sec	Seconds
T2DM	Type 2 Diabetes Mellitus
TE	Echo Time
TR	Repetition Time
VBM	Voxel Based Morphometry
WM	White matter

Abstract

A stimulating area in cognitive neuroscience focuses on the investigation of neural mechanisms underlying the emergence of visual perceptual representations. Human perception of objects and scenes is exceptionally efficient, but it may be *put to test* when one is presented with figures which lead to inherently ambiguous or contradictory representations, yet possible. Multistable percepts are striking phenomena in which the visual system is presented with more than one possible interpretation of physically constant sensory information. The visual system thus has to choose among a set of potentially ambiguous alternatives and actually enters a loop of continually alternating percepts, whereby a viable visual interpretation dominates for a few seconds and is then replaced by a rival interpretation. The neural correlates of multistability remain poorly understood. It is not consensual whether disambiguation of ambiguous stimuli is achieved within the visual cortex or perceptual alternations are initiated outside the primarily sensory areas, within a network of perceptual decision involving higher level brain regions.

A particular outstanding question is how the visual system integrates global patterns of motion from its components and the role of distinct visual areas in such integration process. While this question has been commonly addressed with plaid stimuli, we used a bistable ambiguous moving stimuli that can be perceived as a coherently pattern comprehending both visual hemi-fields moving downward or as two separate objects moving inward, one in each visual hemi-field, in order to investigate the pivotal role of human MT+ in perceptual decision mechanisms. By using functional magnetic resonance imaging (fMRI) and in particular deconvolution analysis of fMRI data we could test the modulation of MT+ activity with alternative bistable percepts and also the influence of MT+ and other brain regions in the emergence of perceptual switch events. Single-subject analysis revealed higher signal changes in MT+ in response to component

percepts than to pattern percepts. This result is in agreement with the popular two stage model of motion processing, as a larger population of both component and pattern neurons in MT+ are responding during the perception of two separate objects while a smaller population of pattern neurons is responding to the integrated global image. Despite the fact bottom-up sensory adaptation in MT+ is supported as an early mechanism for perceptual decision, additional top-down mechanisms were not excluded, as specific analysis of perceptual switch-related transient signal changes revealed higher level areas that are implicated in the perceptual decision process, such as frontal areas and parietal cortex. Right superior parietal lobule (SPL) was even shown to have significant effective connectivity with MT+, as revealed by Granger causality analysis. In fact, the role of bottom-up *versus* top-down mechanisms in perceptual decision remains highly debated.

Previous neuroimaging studies have also suggested an involvement of a right fronto-parietal network regulating the balance between stable percepts and the triggering of alternative interpretations. Modulation by attention and additional top-down effects may play an important instructive role. We investigated neural activity patterns in response to perceptual changes of ambiguous Necker cube under different amounts of working memory load using a dual-task design. We hypothesized that the same regions that process working memory load are involved in perceptual switching and confirmed the prediction that perceptual reversals lead to fMRI responses that linearly depended on load. Accordingly, posterior SPL (pSPL), anterior prefrontal cortex (aPFC) and dorsolateral prefrontal cortex (DLPFC) exhibited differential fMRI signal changes in response to perceptual reversals under working memory load. Our results further support the suggestion that the pSPL may be directly involved in the emergence of perceptual reversals, given that it specifically reflects both perceptual *versus* real changes and load levels. The aPFC and DLPFC, showing a significant interaction between reversal levels and load, might subserve a modulatory role in such perceptual

reversals, in a mirror symmetric way: in the former activation is suppressed by the highest loads, and in the latter deactivation is reduced by highest loads, suggesting a more direct role of the aPFC in the triggering of perceptual switches. In sum, the work presented in this thesis, confirmed a close relation between activity changes in MT+ and perceptual switches involving differential segregation or integration of motion signals. Further investigation is needed to clarify if the dynamic reconfiguration of cell assemblies within MT+ leading to bistable percepts is mediated by local competition only or also by external sources of influence triggering perceptual transitions, such as attention. With a different ambiguous bistable paradigm we could confirm the participation of frontal and parietal brain regions in perceptual transitions, suggesting they are involved in top-down modulatory control of visual perceptual decisions.

Resumo

Uma área fascinante em neurociência cognitiva é a investigação dos mecanismos neuronais que estão na base de representações distintas na percepção visual. Em humanos a percepção de objectos e cenas é excepcionalmente eficiente, mas pode ser posta à prova quando são apresentadas figuras que são inerentemente ambíguas ou contraditórias, mas fisicamente reais. A percepção multi-estável é um fenómeno surpreendente em que o sistema visual se depara com mais que uma interpretação possível de informação sensorial constante. O sistema visual tem por isso que decidir entre um conjunto de possíveis alternativas potencialmente ambíguas e entra num ciclo de mudanças perceptuais em que uma interpretação visual viável domina por alguns segundos e é depois substituída por uma interpretação rival. Os correlatos neuronais de fenómenos de multi-estabilidade continuam pouco esclarecidos. Não é consensual se a decisão sobre estímulos ambíguos é efectuada dentro do córtex visual ou se as alternâncias perceptuais são iniciadas fora das áreas sensoriais primárias, numa rede de decisão perceptual que envolve regiões de alto nível no cérebro.

Uma questão particularmente proeminente é como o sistema visual integra padrões globais de movimento a partir dos seus componentes locais e qual o papel de diferentes áreas do cérebro nesse processo de integração. Enquanto esta questão tem sido investigada com padrões de xadrez em movimento formados por barras de diferentes orientações sobrepostas, para estudar o papel fundamental do complexo MT+ (do inglês *middle temporal*), a região de processamento de movimento, em mecanismos de decisão perceptual, aqui utilizámos um estímulo ambíguo bi-estável que pode ser percebido como um padrão de linhas que ocupam ambos os hemi-campos visuais movendo-se de forma coerente verticalmente para baixo ou como dois objectos separados, um em cada hemi-campo visual movendo-se horizontalmente para o centro. Utilizando ressonância magnética funcional (fMRI, do inglês *functional magnetic*

resonance imaging) e em particular a técnica de análise de desconvolução de dados de fMRI pudemos investigar a modulação de actividade neuronal em MT+ durante alternativas perceptuais bi-estáveis e também a influência de MT+ e outras regiões do cérebro na ocorrência de eventos de transição perceptual. A análise ao nível do indivíduo permitiu-nos observar maiores variações de sinal de fMRI em MT+ em resposta à percepção das duas componentes do estímulo em movimento do que em resposta à percepção do padrão global. Este resultado está de acordo com o modelo popular de processamento de movimento em dois níveis, já que uma maior população de neurónios tanto do tipo *component* como *pattern* em MT+ está activa durante a percepção dos dois objectos separados em hemi-campos visuais diferentes, enquanto uma menor população de neurónios *pattern* está activa durante a percepção de uma imagem global integrada em ambos os hemi-campos. Apesar de estes resultados suportarem um mecanismo de adaptação *bottom-up*, não excluimos que mecanismos *top-down* adicionais possam ter um papel na decisão perceptual na visão. A análise específica de variações de sinal transientes relacionadas com a transição perceptual revelou áreas de mais alto nível que estão implicadas no processo de decisão perceptual, como áreas frontais e no córtex parietal. Com análise de causalidade de Granger, encontramos mesmo medidas de conectividade efectiva entre o lóbulo parietal superior e a região MT+. De facto, o papel de mecanismos *bottom-up versus top-down* na decisão perceptual permanece em debate.

Estudos anteriores de neuroimagem sugeriram também o envolvimento de um circuito frontoparietal no hemisfério cerebral direito que regula o balanço entre percepções estáveis e o desencadeamento de interpretações alternativas. Neste processo, a modulação pela atenção e efeitos *top-down* adicionais podem ter um papel elucidativo importante. Investigámos padrões de actividade neuronal em resposta a alternâncias perceptuais do cubo de Necker em diferentes condições de recrutamento de memória de trabalho com uma tarefa dual. Colocámos a

hipótese de que as mesmas regiões que disponibilizam recursos para a memória de trabalho estão envolvidas nas transições perceptuais, e confirmámos a previsão de que as alternâncias da interpretação visual levam a uma variação do sinal de fMRI dependente dos níveis de memória de trabalho recrutados. De acordo, o lóbulo parietal superior posterior, o córtex anterior pré-frontal e o córtex dorso lateral pré-frontal mostraram variações de sinal fMRI em resposta às mudanças perceptuais diferentes consoante o contexto dos diferentes níveis de memória de trabalho. Os nossos resultados suportam adicionalmente a sugestão de autores anteriores de que o lóbulo parietal superior posterior está directamente envolvido na ocorrência de transições perceptuais, dado que esta área reflecte diferenças de activação neuronal tanto na comparação de transições perceptuais com mudanças reais do estímulo visual como no recrutamento de diferentes níveis de recursos de memória de trabalho. O córtex pré-frontal anterior e o córtex dorso lateral pré-frontal, que mostraram uma interacção significativa entre a quantidade de transições perceptuais e o nível de memória de trabalho recrutado, podem facilitar um processo de modulação das transições perceptuais de maneira simétrica: no primeiro a activação neuronal é suprimida pelos níveis mais elevados de memória de trabalho recrutados, e no último observámos uma deactivação neuronal menor quanto menor é a quantidade de memória de trabalho recrutada, sugerindo um papel mais directo do córtex pré-frontal anterior no surgimento de transições perceptuais.

Sumariamente, o trabalho apresentado nesta tese confirma uma relação entre a actividade neuronal na região MT+ e as transições perceptuais que envolvem integração ou segregação de informação de movimento de objectos complexos. No entanto, é necessária mais investigação para esclarecer se a reconfiguração dinâmica de sub-populações neuronais em MT+ que levam a diferentes interpretações estáveis é mediada por mecanismos de competição local apenas ou também por fontes externas ao córtex visual que influenciam o

desencadeamento de transições perceptuais, como a atenção. Com um estímulo ambíguo bi-estável diferente pudemos também confirmar a participação de regiões frontais e parietais do cérebro no processo de transição perceptual, sugerindo que estão envolvidas no controlo *top-down* da decisão perceptual na visão.

(escrito sem recurso ao novo acordo ortográfico)

Chapter 1

General Introduction

The relatively advanced state of the neuroscientific research of the visual system is relevant per se and contributes to its use as a model system for understanding general principles about how the brain processes information. In the following, basic anatomical and functional properties of the visual nervous system will be described. First, the early stages of visual processing in the eye and the pathways from the retina to the visual cortex are presented. This is followed by a brief description of central visual processing pathways. This introduction will then focus on the so-called perceptual binding problem in cognitive neuroscience and proposed solutions for the problem. An optimal paradigm of visual motion perception based on ambiguous bistable stimuli will be introduced and discussed in order to investigate how the visual system integrates information in various specialized areas so as to construct a vivid representation of the visual world. Finally this introductory chapter describes a brief overview of the processing of motion from basic sensory to perceptual levels and their neuronal correlates in the human brain. At the end of this chapter the thesis aims and outline are presented.

Visual system

Our world is largely visual and that's why the visual system is one of the most studied systems in neuroscience, because of its crucial role in human interaction with the world. It is through the eyes that humans obtain much of their information about the surrounding environment ¹. The remarkable organization of the human visual system, from the eye to distributed and specialized processing areas in the brain, allow the construction of vivid representations of the visual world.

The eye actually projects an upside down, reversed and focused picture of the external world onto the retina, which is then delivered to the brain. The light

enters the eye through the cornea (nonadjustable) and is focused by the lens (adjustable through accommodation mechanisms) into the neural portion of the retina, at the back of the eye, after passing through layers of ganglion cells, bipolar cells and photoreceptors². Then when the light arrives at the back of the retina, the photon-absorbing photopigments contained in the sensory photoreceptors, rods and cones, trigger the transduction of the information contained in light into electrical signals by the intrinsic circuitry of photoreceptors, bipolar cells, horizontal cells and amacrine cells³. The retina of each eye is divided into a temporal (lateral) hemiretina and a nasal (medial) hemiretina. The temporal visual field is projected to the nasal hemiretina and the nasal visual field is projected to the temporal hemiretina³.

Axons of ganglion cells, the output cells of the retina, leave the eye in a bundle called optic nerve and meet at the optic chiasm, where fibres from the nasal hemiretina decussate and join the fibres from the temporal hemiretina of the opposite eye, which remain uncrossed, forming the optic tract. The temporal hemiretina of one eye and the nasal hemiretina of the other eye view the same visual field so that each optic tract conveys information from the opposite hemifield of both eyes; that is, the optic tract on one side carries information related to the contralateral visual fields. The optic tracts enter the lateral geniculate nucleus (LGN) of the thalamus, which serves as a major bi-hemispheric relay station between the retina and visual cortex, as LGN receives retinal input and projects two bands of axons called optic radiations to the primary visual cortex (V1) in the brain^{2,4}. The anatomy of the human visual system is shown in Figure 1-1.

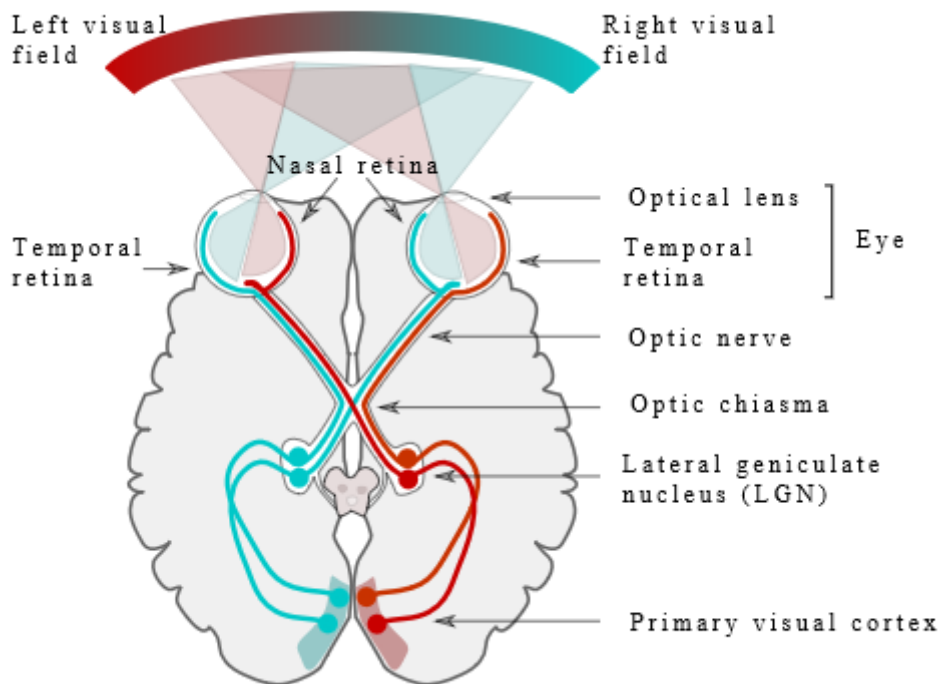


Figure 1-1. Anatomy of the visual system. Light arrives at the eye and is focused by the lens on to the retina, where photoreceptors transduce the light into electrical signals that are processed by local retinal neurons. Axons of retinal ganglion cells, the output cells of the retina, leave the retina in a bundle called the optic nerve. At the optic chiasm, some axons cross over, so that axons representing the right half of visual space travel to the left lateral geniculate nucleus (LGN) and axons representing the left half of visual space travel to the right LGN. In the LGN, the axons segregate into layers according to eye of origin and other properties. LGN relay cell axons form a band called the optic radiations and project to the primary visual cortex, where LGN axons representing each eye ramify in an alternating fashion 2. Reproduced from Miquel Perello Nieto (https://commons.wikimedia.org/wiki/File:Human_visual_pathway.svg#).

Neural processing and visual pathways

During the past few decades our understanding of the neural bases of visual perception and visually guided actions has advanced greatly. Neuronal processing of features of the visual input in the retina is highly parallel. It results from several functionally distinct ganglion cell types specialized for different

visual features, such as achromatic contrast and colors. The primary visual cortex (V1), or Brodmann area 17⁵, is the first cortical area to process visual information coming from the retina via LGN. The way whereby visual information is redistributed in V1 to other extrastriate areas has been extensively investigated in anatomical and physiological studies in primates. An important principle of cortical organization states that visual areas are organized into hierarchical, parallel processing streams¹, by which separate extrastriate cortical areas integrate different features of the visual world to achieve visual perception^{1,6-8}.

An extensively supported model of these processing streams was proposed by Ungerleider and Mishkin⁹. The model proposes the existence of two different visual pathways: the 'where' or dorsal visual pathway which processes spatial information, object location and motion cues; and the 'what' or ventral visual pathway, devoted to identification of object's features such as shape and color. The two pathways have been originally described for nonhuman primates and with brain imaging techniques, the two major processing pathways have also been convincingly demonstrated in the normal human brain¹. The dorsal and ventral visual pathways are illustrated in Figure 1-2. According to this model, in both dorsal/ventral visual streams there are cortical projections from the primary (low-level) visual cortex to extrastriate (higher-level) cortical areas, in which there is a transformation of lower level information into more abstract representations through successive processing states. At the earliest stage of visual perception V1 neurons are tuned to several features such as orientation, spatial and temporal frequency⁸, direction of motion¹⁰ or binocular depth¹¹ and color selectivity¹².

Within the dorsal visual pathway, direction-sensitive V1 cells signal direction of motion of local image features within their small receptive fields, which is subsequently sent to secondary visual cortices V3 and V5. In turn, direction-selective cells in V5, composed of two distinct regions, middle temporal - MT -

and medial superior temporal - MST, respond specially to global motion of an object or pattern as a whole ^{2,13-15}.

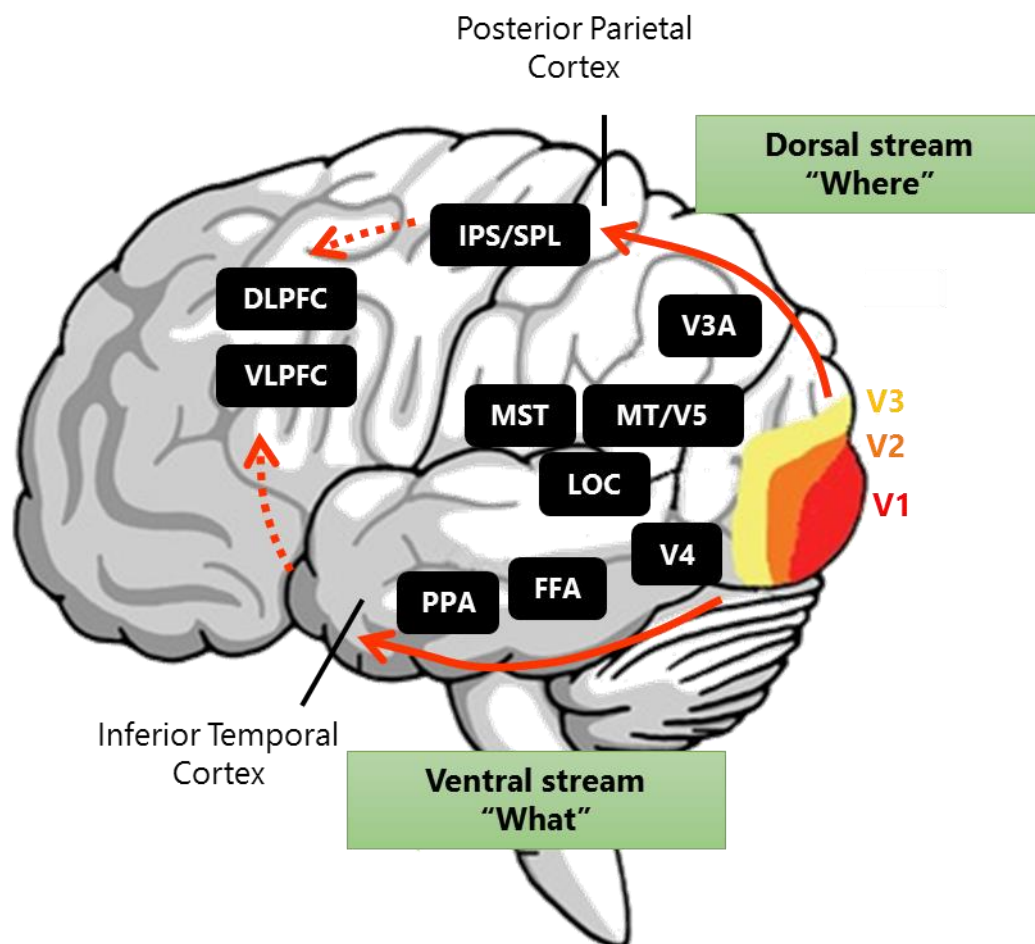


Figure 1-2. Dorsal and Ventral parallel visual pathways. Visual processing in the brain is handled, in part, by two processing streams extending from primary visual cortex: the dorsal (occipito-parietal) visual pathway ('Where') which projects from V1 to the parietal cortex and underlies processing of spatial information; and the ventral (occipito-temporal) visual pathway ('What') which spreads from V1 to the temporal lobe and is involved in object identification as well as shape and face processing. Both pathways are assumed to consist of feedforward and also feedback connections and extend into prefrontal cortex. MT, human homologue of monkey middle temporal area; MST, human homologue of monkey medial superior-temporal area; LOC, lateral occipital cortex; FFA, fusiform face area; PPA, parahippocampal place area; IPS, intra-parietal sulcus; SPL, superior parietal lobule; DLPFC, dorso-lateral prefrontal cortex; VLPFC, ventro-lateral prefrontal cortex. Adapted from ¹.

Concerning the inputs to the ventral visual pathway, V1 acts as a spatiotemporal first-order filter whereas V2 responds to illusory and second-order contours¹⁶. Cells in V4 encode curved shapes and color, being important in global form perception¹⁷. Additionally, inferior temporal regions respond selectively to global object features such as shape (e.g. faces)¹⁸. In other words, V1 might be assumed as the gateway to higher visual areas and many of these areas respond to even more specific stimuli than does V1.

Visual motion perception

One area of visual neuroscience that has witnessed greater progress is visual motion perception, possibly due to its crucial role in several important daily tasks such as detecting that something is moving to draw one's attention to it, segmentation of foreground from background, computation of 3-D shape of an object or computing the distance between several objects in a visual scene. In particular, there has been extensive research on the role of the visual system in extraction of object motion. This topic remains central within the field visual neuroscience.

This section comprises three sub-sections. We begin with a short review of the low-level motion mechanisms in the primate visual system, providing a brief explanation of low-level one-dimensional motion detection. Afterwards, we present two higher-level neural mechanisms that mediate perception of two-dimensional motion of more complex objects (which mimic the real environment). We also present a small review of the role of extrastriate visual areas in higher-level motion processing. Finally we review evidence for striate and extra-striate areas in the human brain that are implicated in the perception of visual motion, mainly drawn from experimental work from brain imaging studies.

Low-level motion processing in primary visual cortex of primates

The visual system infers motion from the changing pattern of light in the retinal image. The basis for motion processing in the primate visual system are the direction-selective (DS) cells with oriented receptive-fields in primary visual cortex⁸. At an early stage of visual processing, in primary visual cortex V1, motion signals are extracted by DS cells in V1 that essentially compute the Fourier energy of the spatiotemporal luminance patterns within their local receptive fields. As motion can be seen as continuous or sampled displays of a stimulus in different spatial locations through time, the problem of detecting motion, then, is the problem of detecting spatiotemporal orientation. Perception of motion, thus, can be mathematically modelled as spatiotemporal filters that extract spatiotemporal orientation as a simple extension of the mechanisms for extraction of pure spatial orientation in the visual system^{19,20}. This spatiotemporal energy model has become a standard theoretical framework for low-level motion analysis in early visual cortex²¹. A clear limitation in the responses of DS cells is the local nature of low-level motion extraction. The receptive fields of DS cells are spatially restricted windows within which motion is "measured". When an extended contour, such as a bar, moves through that window, the receptive field of a DS cell may be too small to "see" the ends of the bar and the cell cannot unambiguously respond to the bar's direction of motion, independent of its orientation. This can be seen as a smaller scale instantiation of the aperture problem, in which a grating moves behind a small aperture (Figure 1-3). Any motion parallel to the bar (alone or the bars of a grating) is invisible, as the luminance-defined energy features of the stimulus within the receptive field of the DS cell (or within the aperture) will not change. For example, a vertical bar moving smoothly up and to the right will traverse a series of small DS receptive fields over time. The bar will be signalled by DS cells with that specific preferred orientation – vertical. As a DS cell does not change its preferred contour

orientation, those cells can only signal the motion component perpendicular to the bar's orientation, which, in the case of a vertical bar moving up and to the right, means the rightward motion; the bar's upward component of motion produces no measurable change in luminance-defined features of the bar within the receptive fields of those cells, with a preferred vertical orientation²². In fact, there is a family of possible motions in two dimensions of a single bar that have an invisible parallel motion component and an orthogonal motion component (Figure 1-4A). All those possible motions lie along a line that is parallel to the bar and can lead to the same perception of motion of the stimulus. Therefore, DS cells in primary visual cortex can only respond to stimuli moving along an axis perpendicular to the cells' preferred orientation, which is then the cell's preferred direction of motion^{19,20,23}. These cells are characterized by strong response to a stimulus in the preferred direction and little or no response to other directions.

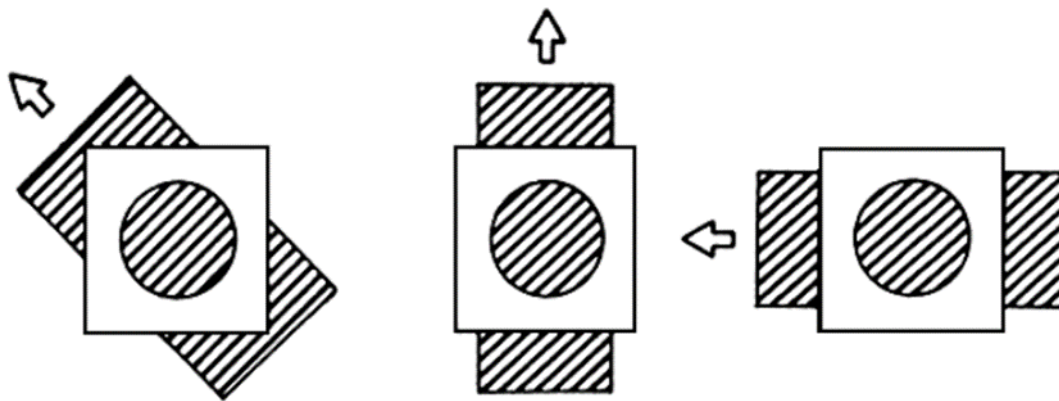


Figure 1-3. Ambiguity of motion of one-dimensional patterns. The three sections of the figure each show a surface containing an oblique grating in motion behind a circular aperture. In the left panel, the surface moves up and to the left; in the middle it moves up; in the right, it moves to the left. Note that in all three cases the appearance of the moving grating, as seen through the window, is identical: the bars appear to move up and to the left, perpendicular to their own orientation, as if produced by the arrangement shown on the left, because the motion component parallel to the grating's bars produces no changes in luminance as detected by direction-selective cells in primary visual cortex. Adapted from²⁵.

One must distinguish at this point between one-dimensional (1-D) and two-dimensional (2-D) patterns or objects. A 1-D pattern is one like a bar or grating, of which the endings are outside a DS cell receptive field or beyond the edge of a viewing aperture (Figure 1-3), that is uniform along one axis and only contains features of a single orientation. Note that when a 1-D pattern moves parallel to its orientation, its appearance does not change. A 2-D moving object changes its appearance with motion along any single axis, because it has features of more than one orientation^{21,24}. These include random dot fields, plaids (superimposed gratings with different orientations) and natural scenes, obviously.

2-D objects can be seen as composed of 1-D components. But then how can motion signalling of 1-D components in primary visual cortex DS cells, which is ambiguous (remember the family of possible motions that give rise to the same perception), be used for computation of 2-D motion? Notably, while a single moving contour cannot offer a unique solution of its motion, two moving contours (which belong to the same object) can, as long as they are not parallel²⁵. The local motion information of 1-D contours computed in DS cells of primary visual cortex is processed further and somehow combined to achieve extraction of true global direction of motion of a 2-D object by higher-level mechanisms of motion processing.

Higher-level mechanisms of visual motion

A great deal of research has focused on how the visual system processes the motion of 2-D objects. Just like the shape of a 2-D object is perceived by breaking it up into 1-D constituents, contours in that case, motion of complex objects can also be thought as arising from a combination of motion responses to local 1-D components of the object.

A popular experimental approach which has frequently been used to investigate this question involves the use of plaid stimuli, made by superimposing two gratings independently moving with different orientations (Figure 1-4B), which are designed to mimic the motion of real objects in the visual environment. These plaids can be perceived as the two independent gratings sliding one over the other or as single objects rigidly moving coherently in a single direction^{24,26}. The disambiguation of this perceptual motion problem has been explained mainly by two models of 2-D motion processing.

The first model assumes that the global motion direction and velocity is detected to be the direction and speed of “blobs” that appear in a plaid pattern, at the spatial intersections of the two component gratings. Processes based on a direction tacking not selective for orientation might detect these blob-like features and signal their motion. The motion of the plaid as a whole is obviously identical to the motion of the blobs. This low-level monocular mechanism is called the Blob Tracking (BT) model^{20,24,27}.

The second and most accepted method for combining 1-D component motion in order to explain 2-D motion is the Intersection of Constraints (IOC) model^{24,27}. Whereas each of the component 1-D gratings can only be seen to move orthogonally to its orientation, a constraint line of parallel to its orientation defines the direction and speed of all possible motions consistent with that component. The point at which two constraint lines (one for each component) intersect predicts the direction and speed of the 2-D object composed of the two 1-D components, and this is referred to as the IOC direction. In the first-stage of processing the independent component motion signals are extracted. The 1-D motion signals are then combined at a higher-order second stage of processing to extract the IOC solution for 2-D global motion (Figure 1-4B).

The two models have flaws in certain circumstances and there is controversy concerning the mechanism by which the visual system computes the direction of

2-D motion. Some authors implicate both an IOC mechanism and a blob-tracking mechanism in the perception of plaids ²⁶⁻²⁹.

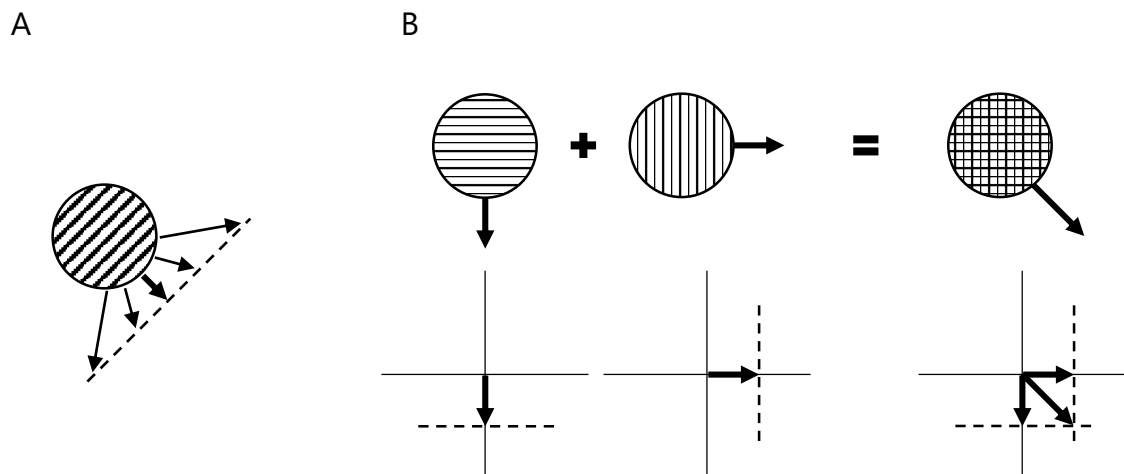


Figure 1-4. One-dimensional and two-dimensional visual motion perception. The velocity-space representation of some moving patterns. In each panel, a vector represents motion in a direction given by the vector's angle at a speed given by the vector's length. (A) A single grating moves behind an aperture. The dashed line indicates the locus of directions and speeds compatible with the perceived motion of the grating, perpendicular to the grating orientation. (B) A plaid composed of two orthogonal gratings moving at the same speed. The dashed lines give the possible motions of each grating alone. Their intersection is the only shared motion. Thus it represents the only possible motion for a single object containing both components and corresponds to what is perceived. Adapted from ²⁴.

The role of extrastriate cortex in motion processing

Electrophysiological studies in monkeys and cats revealed that neurons both in and outside the primary visual cortex are selective for the direction and speed of motion of visual stimuli ^{8,25}. Movshon and colleagues showed that while striate neurons in cats and monkeys are selective for 1-D motion only, there are neurons in monkey's extrastriate cortex responding to both 1-D and 2-D motion ^{25,30}. This

region is located in the posterior bank of the temporal sulcus and is known as middle temporal area or simply MT³¹. Cells in primary visual cortex project either directly or via V2 and V3 to MT (sometimes also termed V5). Moreover, there are also direct subcortical inputs to this area²². The fact that there are only about 25% of motion selective neurons in V1 and even less in V2^{8,32}, the major inputs to MT, supports the notion that MT is highly specialized for motion processing *per se*. A typical V1 neuron responds to a particular orientation (edge or bar) moving in a particular direction. Most MT neurons are direction-selective, each responds best to a preferred direction within its receptive field, pretty much independent of stimulus orientation or configuration^{15,25,33–36}. This sustains the belief that MT underlies the second-stage mechanism of motion processing referred above, i.e. the stage that disambiguates direction of 2-D motion. Closely related to MT is a neighbouring area, the medial superior temporal area (MST), which receives input from MT. Neurons in area MST have even larger receptive fields organized in ways that provide them with selectivity for complex optic flow such as expansion or contraction³⁷.

Physiology has identified motion-selective cells in several brain regions, but has largely focused on the best understood areas, MT and MST, and stimuli, which processing mechanisms can be computationally implemented with luminance-based motion energy models³³. The question is then if there are different types of neurons sensitive to 1-D motion, 2-D motion or both in MT. Furthermore, there has been investigation on which type of neurons are involved in the described first and second stages of motion processing.

Pattern and component neurons in MT

MT contains neurons responding to the direction of motion of single oriented contours (1-D) whether they are presented in isolation or as part of a more

complex object (2-D), which are known as *component neurons*. MT contains also neurons showing pattern selectivity, meaning that these neurons respond to the direction of 1-D contours isolated, like component neurons, but they also respond specifically to motion of more complex 2-D objects as a whole, which are known as *pattern neurons*. The receptive field of pattern neurons in MT, which is substantially larger than that of DS cells in V1, combines local (1-D) motion outputs from primary visual cortex to compute higher order (2-D) motion³⁸⁻⁴⁰. MT neurons are topographically organized in a columnar system⁴¹ and a substantial fraction of these neurons are able to extract the global direction of motion of an object independently of the orientation of its components^{34,42,43}. About 40% of MT neurons are component neurons, while about 25% are pattern neurons. There is electrophysiological evidence that neuronal computation of the IOC phase of the second-stage model described earlier is performed by pattern neurons in MT, while the properties of component neurons in V1 and MT seem to correspond to the first stage^{25,42}.

Visual motion in human brain

Psychophysical investigation has allowed to describe many aspects of human performance in motion perception. Neurophysiology permitted to characterize at the cellular and small neural network level the neural correlates of motion processing in non-human primates. Advances in neuroimaging, in particular fMRI, have brought the potential to investigate the relation neural activity and behaviour in humans, enhancing our understanding of motion processing mechanisms.

In the human brain, V1 can be relatively easily identified using well established retinotopic mapping procedures that clearly delineate the boundaries of the primary visual cortex⁴⁴. Retinotopic mapping has identified a motion sensitive

extrastriate area in the dorsal visual processing stream. This dorsal extrastriate area, called V3a ("V3 accessory", homologous with monkey visual area V3)³³, was shown to respond strongly to coherent motion in the full contralateral visual hemifield⁴⁵⁻⁴⁷. Evidence for DS neurons exhibiting direction-selectivity was found to be present also in MT in humans⁴⁸. It is well accepted that the human analogue to monkey MT is located within a relatively large expanse of tissue anterior to early, retinotopically organized visual areas, at the junction of the posterior bank of the dorsal limb of the inferior temporal sulcus with the lateral occipital gyrus or sulcus^{14,22,33,49-51}.

In most human neuroimaging studies motion responsive regions are commonly isolated based solely on a motion localizer. This makes it difficult to separate MT proper from its surrounding satellite areas, such as MST, with a strong response for ipsilateral motion stimuli, which is located in the anterior bank of the dorsal limb of the inferior temporal sulcus¹³. Thus, the entire motion responsive area in humans is usually referred to as "MT+", "MT complex" or simply "MT" for short^{22,33,35}. Nevertheless, fMRI allowed to distinguish the same sub regions within MT+ as in the macaque. Dukelow and colleagues observed a more posterior region, MT proper, which receptive fields extend only a few degrees into the ipsilateral visual field, response and a more anterior region, MST, which have receptive fields that extend well into the ipsilateral visual field, responds to both contra- and ipsilateral motion stimuli⁵².

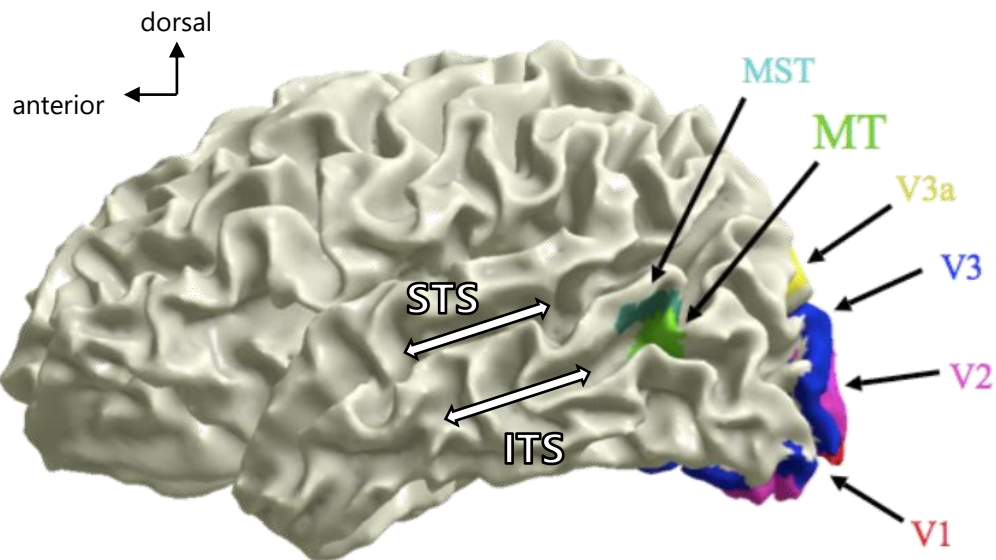


Figure 1-5. Location of human motion-responsive brain area MT+. Position of MT and MST, viewed on a 3-D cortical reconstruction of the brain (left hemisphere). MT (green) falls on the posterior bank of the occipital continuation of the inferior temporal sulcus (ITS), whereas MST (cyan) falls on the anterior bank. The superior temporal sulcus (STS) is indicated for reference. Other visual areas are shown for reference: V1, red; V2, magenta; V3, blue; V3a, yellow. Reproduced from ¹⁴.

Activity in MT+ is found to be significantly related to perception of motion of various kinds, including genuine motion, flickering ⁵³, apparent motion ⁵⁴, motion aftereffects ^{55,56}, implied motion ⁵⁷⁻⁵⁹ and bistable motion. Tootell and colleagues have shown that MT+ responds strongly to moving gratings ⁵¹, which is evidence confirming that motion processing in MT+ is driven strongly by luminance-based energy models. Just like in monkey MT, there is evidence for the existence of DS cells in human MT+ that respond to the global motion of a 2-D object within their receptive fields – pattern motion cells – as well as to a given 1-D component of motion – component motion cells ^{13,60}. Huk and Heeger observed that MT+ contains a substantial portion of pattern motion neurons, whereas V1 shows evidence for component motion cells only ¹³. This is in accordance with the second-stage model of motion processing described earlier in the macaque

monkey brain. The human brain solves ambiguity in visual motion in V1 DS cells with the addition of a further processing step in MT+, in which pattern motion cells extract the global direction of motion independent of the local components²². Notably, activation in MT+ coincident with perceptual switches during bistable motion of plaid (superimposed gratings with different orientations and motion direction) provides evidence that this region is able to respond reliably to both physical changes in the motion characteristics of the stimulus and also to perceptual changes of a physically constant stimulus^{24,28,29,61-64}.

The binding problem in cognitive neuroscience

Visual perception involves the neural integration of visual features processed in parallel⁶⁵. Neurons in different visual areas are selective for different stimulus features, as we have seen earlier⁶⁶⁻⁶⁸. The classical theories of sensory processing in the visual system assumed specialized higher visual areas to exist to solve difficult computational problems posed by the visual world and often underemphasize feedback connections that reach areas as low as V1 or the LGN^{69,70}. If we would accept a strictly hierarchical visual system with feed-forward processing, visual perception would require a master area on top to which all of the specialized high-level areas would “report”. In this top level area there would be a population of neurons responding only to a specific combination of stimulus features. This is highly unlikely, not only because of the huge amount of specific conjunctions of neurons that would be needed to represent specifically every object in the visual world as also because novel objects would not be represented. In fact, there is no anatomical evidence of such top level area¹.

The unconvincing “master area” conjecture stimulated theories of integrative processing, in which the distributed parallel processing of different visual features is integrated to form coherent percepts of the visual world. More recent

approaches emphasize the constructive nature of perception by assuming that top-down (goal-directed mechanisms such as attention) and bottom-up (stimulus-driven mechanisms) processes cooperate in everyday life to guide brain processing toward behaviourally relevant or particularly salient stimuli ^{71,72}. Physiological and functional MRI studies have indeed confirmed the key role of bottom-up and top-down neural processes in vision, which connect multiple specialized brain areas to integrate information ^{73,74}. The precise functional role of these connections is however not completely understood and remains unclear how distributed processing of different visual features is integrated to form coherent percepts of the visual world. The problem with this object representation within and across many brain areas arises when visual scenes contain multiple objects. Neuronal responses signal that a set of visual features is present but not which feature belongs to which object. Thus, neurons responding to one of the objects are indistinguishable from neurons responding to another object (see an example in Figure 1-6). This is known as the binding problem ⁶⁶. It refers to the process used by the brain to combine (or "bind") the results of many sensory operations into a single percept. By solving the binding problem the brain somehow segregates elements in complex global patterns, a process that allows us to distinguish them as discrete objects.

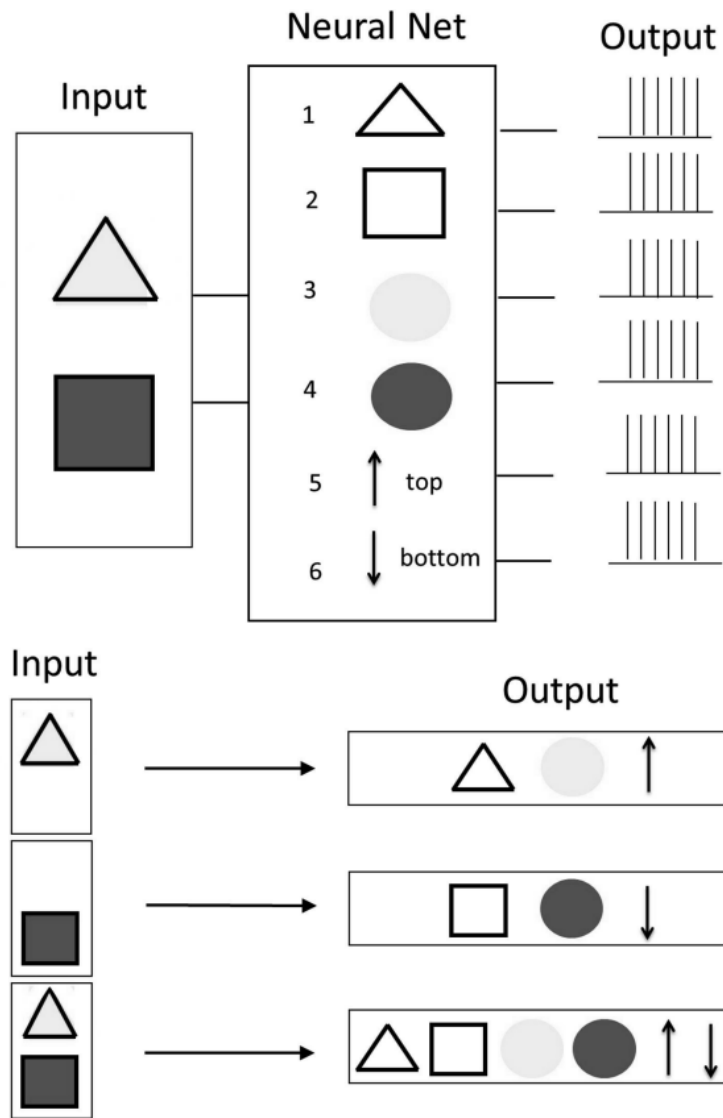


Figure 1-6. Classical illustration of the binding problem. At the input of a hypothetical neural network consisting of six neurons, different visual images are presented that can either be yellow or blue triangles or rectangles in an upper or lower position. If for example either a yellow triangle in the top position or a blue square in the bottom position is presented, always the three corresponding “feature neurons” are activated. However, a problem occurs in the case that not only one but two objects are presented to the network simultaneously. In this case, all six feature neurons are activated concurrently and without further measures, it cannot be concluded which feature belongs to what object. Reproduced from ¹¹⁹.

There are three main approaches to the solution of the binding problem, all considering basic low-level feature detectors. One of the proposed solutions is constructed in the basis of convergent hierarchical coding units, which are assumed to be neurons (or neuronal populations) selective for conjunctions of low level features, such as “yellow triangle on top”. This strategy would be highly redundant and limited by combinatorial explosion of possible conjunction of features ⁷⁵. Another solution considers that attention binds the information of basic features and delimitates each object for further processing ⁷⁶. However, the successful segmentation of the image into the constituent objects is actually a prerequisite for the appropriate positioning of the attentional focus. Thus, somehow the binding problem would have to be solved beforehand, in order to identify neurons to inhibit or enhance their responses further. A more flexible solution, especially when multiple visual objects have to be represented simultaneously across potentially overlapping neuronal populations in early visual areas, uses a temporal binding mechanism: neurons excited by features of the same object fire synchronously, while neurons excited by features of different objects do not. A crucial advantage of this coding strategy is that it allows multiple assemblies to become active at the same time without becoming confounded.

Controversy of the temporal coding in visual perception

The temporal binding hypothesis was first supported by reports of synchrony between distant neuronal assemblies correlating with holistic perception in monkeys ⁷⁷. Nonetheless, despite compelling evidence in nonhuman studies suggesting that dynamic neural assemblies can arise from the synchronized firing of neurons, the question of whether integration of visual features, i.e. visual binding, relies on this synchronous activity triggered early on controversy and heated debate ⁷⁸. Conflicting results under similar experimental conditions and

paradigms contribute to this impasse. For instance, there are reports of synchronous activity that correlates with single object perception and anti-correlates with surface segregation^{62,79} but also reports of absent temporal binding^{80,81}. In humans long-range synchronization in the gamma frequency band has been claimed to underlie coherent and unified percepts as well⁸²⁻⁸⁴. However, in most paradigms visual input changes, and attention/eye movements and cognitive arousal remain a problem. Thus, in effect the binding-by-synchrony theory is still controversial^{81,85,86}.

Top-down and bottom-up mechanisms in visual perception

There is still a debate in the scientific literature about the contribution of low- and high-level visual areas in the origin of visual perception⁸⁷. Despite being still controversial, the temporal binding hypothesis is fully compatible with the integrative mechanisms described earlier for visual perception. Visual scenes containing multiple objects are processed by means of competitive interactions that occur automatically. These interactions can be modulated by bottom-up processes based on stimulus driven properties and also top-down processes determined by the individual's goals⁷². Both top-down and bottom-up mechanisms may play an important role in visual processing. There is evidence that bottom-up mechanisms induce temporal relationships among visual cortical areas but also that these are influenced by top-down modulation from higher order areas^{66,88}. Furthermore, the idea of top-down can, depending on the context, be used with different meanings (see Figure 1-7). The most used variant is anatomical, meaning that in visual processing there are both feedforward connections (bottom-up mechanism) and feedback connections (top-down mechanism) between visual areas at different levels of processing (Figure 1-7A). Alternatively, there is the so-called dynamicist idea of top-down (Figure 1-7B), in

which the activity of local populations of neurons can influence another neuronal assembly at the same level of processing ⁷¹. Thus, the enhancement of synchronization between visual areas may be based on a combination of both bottom-up and top-down influence from higher order areas, between areas at the same processing level or even within one area ^{71,89}. Because these two processes cooperate in everyday life to bias processing toward behaviourally relevant stimuli, it has proven difficult to study interactions between top-down and bottom-up mechanisms.

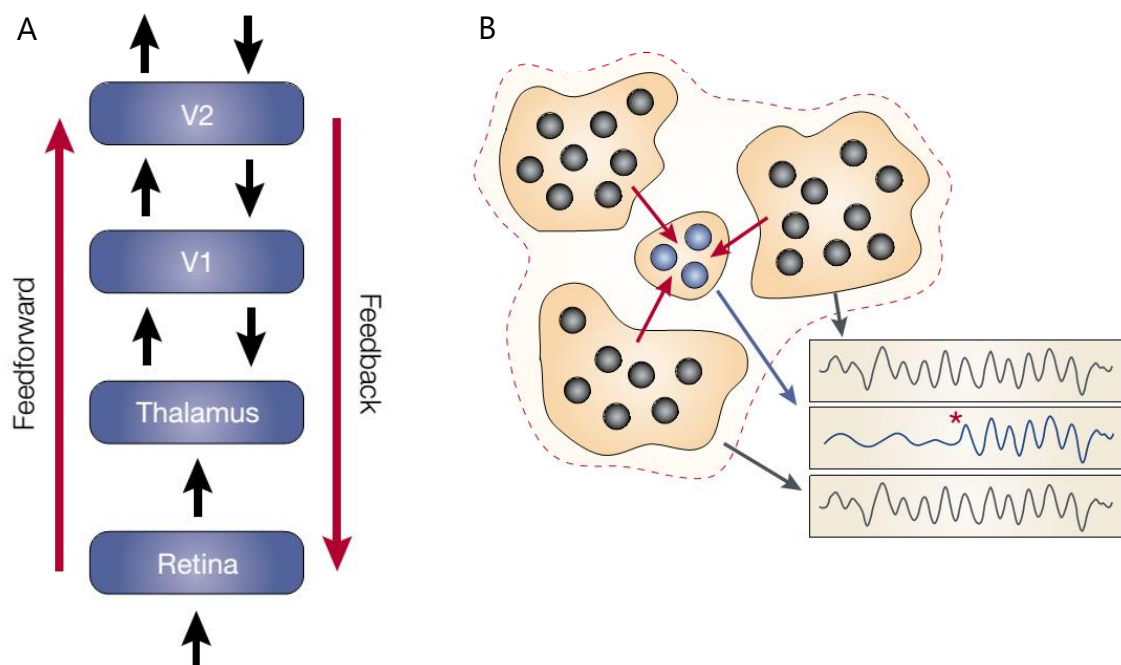


Figure 1-7. Variants of top-down mechanisms. The idea of top-down and bottom-up mechanisms may be ambiguous. (A) The most used variant is anatomical, meaning that in visual processing there are both feedforward connections (bottom-up mechanism) and feedback connections (top-down mechanism) between visual areas at different levels of processing. (B) Alternatively, there is the so-called dynamicist idea of top-down, in which the activity of already synchronized local populations of neurons can influence another neuronal assembly at the same level of processing after some point in time. The functional meaning is that new or different stimulus features (processed by blue neurons) may be incorporated into a broader context or perception, leading to a reinterpretation of the stimulus. This might occur between areas at the same level of processing or within one brain area. Adapted from ⁷¹.

Choice of paradigm – multistability in visual perception

Vision is designed to guide behaviour and a behaving organism cannot afford to be halted by indecision. An exciting area in cognitive neuroscience concerns the investigation of neural mechanisms underlying the emergence of visual perceptual representations. Multistable interpretations of the visual world are striking phenomena which may occur when the retinal image is compatible with multiple perceptual solutions. This occurs even when the physical pattern of retinal stimulation remains constant. Perceptual decision-making is thus defined by the choice of an interpretation among a set of two (or more) valid alternatives based on peripheral sensory evidence and may crucially affect subsequent action selection⁹⁰. A particular challenge is posed to perceptual decision-making in a context when multiple interpretations are available in the scene leading to rivalrous/conflicting percepts⁶¹⁻⁶⁴. This context is instantiated under multistable conditions, whereby the pattern of sensory stimulation in the retina remains constant and still its perceptual appearance can change dramatically over time and switch back and forth. A simple example is bistability, such as binocular rivalry, in which two different images are presented to each eye, which compete for perception. In this paradigm observers are often requested to press a given button any time the interpretation changes, as a result of perceptual decision mechanisms⁹¹.

Multistable stimuli are thus well suited to investigate perceptual integration of visual information and understand the role of top-down or bottom-up mechanisms in feature integration. Visual bistability is indeed an important phenomenon because it can be used as a tool with the aim to understand the neural mechanisms underlying perceptual decision making⁹².

There are theories of bottom-up mechanisms as the most important for the perception of ambiguous figures⁹³ while others suggest that perceptual decisions might be induced by feedback from higher to lower levels of processing⁹⁴. The

role of bottom-up *versus* top-down mechanisms in perceptual decision remains highly debated, as a growing number of studies indicate that both perceptual processes play definable roles in the perception of ambiguity^{69,87,95–99}. On the one hand, bottom-up sensory adaptation represent a strong mechanism in perceptual decision models^{46,63}. On the other hand, modulation by attention and additional top-down effects may also play an important instructive role.

Neural correlates of perceptual decision

We do not exactly know where and how visual information is processed in the brain to arrive at a difficult perceptual decision. There is evidence from neuroimaging and behavioural studies that binocular rivalry is addressed by competitive interactions at different brain regions^{91,100,101}. Although it is accepted that rivalry depends on low-level interactions, there is debate about high-level modulatory mechanisms in dominance of a stimulus¹⁰⁰. Furthermore, its generalizability to multistable perceptual phenomena remains debatable¹⁰¹.

Experiments on primates and humans have demonstrated that perceptual decision-making relies on gathering and interpreting information in lower order sensory regions^{90,102–104}. However, relatively recent studies have shown that the representation of visual information in lower order sensory regions is not sufficient to achieve perception^{105,106}, and further processing of visual information in higher order cortical areas is crucial to discriminate visual objects^{90,107}. The role of frontal regions in perceptual decision-making is an ongoing discussion^{90,108,109}. There is evidence that neuronal activity in dorsolateral prefrontal cortex is modulated as a function of the amount of perceptual evidence, and shows greater task-positive fMRI signal and connectivity modulation during perceptual decision^{108,110}.

Indeed sensory systems representing external information and cognitive systems addressing task difficulty and interpretation of conflict may co-exist during perceptual decision making. Thus, the need to separate distinct cognitive components and elucidate their roles in perceptual interpretation has been emphasized ^{111,112}. A recent study demonstrated that when observers passively experienced rivalry without explicitly reporting perceptual switches, differential neural activity in frontal areas was absent, while occipital and parietal regions showed consistent activation patterns, suggesting that frontal areas are not involved in perceptual alternations, at least in which concerns binocular rivalry ¹¹³. These results are consistent with a recent study demonstrating that retinotopic representations in early visual areas play a role in the dynamics of perceptual alternations ¹¹⁴.

Perception of ambiguous figures

The visual system integrates one percept at a time. If an ambiguous stimulus is viewed for an extended period of time, one perceives it as switching back and forth between the possible interpretations. Sometimes the perceptual system fails to produce a stable unambiguous percept, especially if the visual information is equally compatible with different perceptual interpretations as in the case of ambiguous figures. A prominent example is the Necker cube (Figure 1-8) whose perceived front-back orientation reverses spontaneously. Perceptual reversals occur without any physical change of the stimulus and hence provide a distinct possibility to study how perceptual interpretations are constructed irrespectively of low level stimulus properties ⁹⁹.

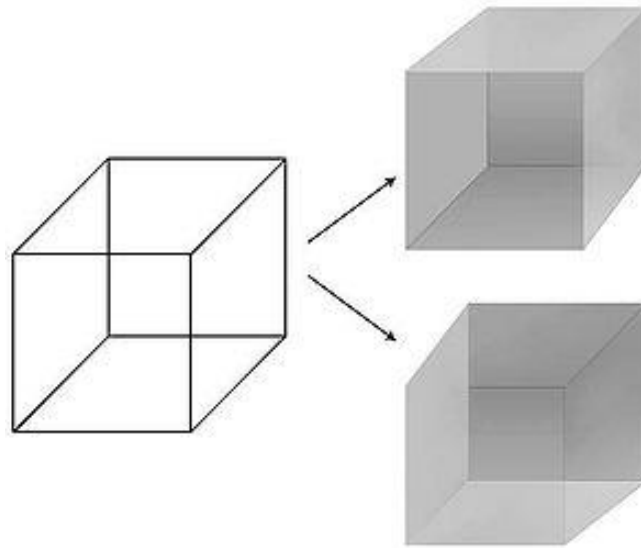


Figure 1-8. The Necker cube. The Necker Cube: The left “transparent” line drawing version can be perceived in one of two distinct possible interpretations shown on the right. Without any other cue, the visual system flips back and forth between these two interpretations. If you stare at the Necker cube long enough, you will alternate between these two versions ¹²⁰.

The origin of perceptual reversals is still highly under debate regarding whether low or high level visual mechanisms play a major role in determining perceptual decisions ⁸⁷. There are studies suggesting that bottom-up mechanisms such as adaptation are the most important for the perception of ambiguous figures: the neural channels determining one of the available percepts satiate and thus perceptual interpretation changes to the alternative one ⁹³. The cognitive theories suggest that perceptual decisions might be induced by feedback from higher to lower levels of processing, for example, by activation of a high-level “exploratory” mechanism that directs selective attention in a way that causes a recurrent “renewal” of the image in low-level perceptual systems ⁹⁴.

Bistable component and pattern motion perception

Other striking examples of multistability are moving plaid patterns. These are formed by superimposed moving gratings which can be perceived either as two independently transparent surfaces moving in different directions - component motion - or as a single surface moving in an intermediate direction - pattern motion - that results from the perceptual fusion of the former. Component motion or pattern motion representations are the two alternative perceptual solutions.

How the visual system integrates global patterns of motion from its components and the role of distinct visual areas within the visual processing stream in such integration process remains an outstanding question. These stimuli have been used to investigate with functional MRI whether the motion sensitive area MT+ is involved in perceptual segmentation and integration of motion signals related to such perceptual surfaces. It is known that cortical area MT+ contains cells responding to 1-D components of a moving pattern (component neurons), as well as cells responding to the global 2-D motion of a pattern (pattern neurons)¹¹⁵. Furthermore, there is evidence that motion sensitive area MT+ itself is involved in mediating the switches between the two percepts^{61,64}. It remains however unclear how full integration of multiple globally moving surfaces is achieved within the whole visual hierarchy, namely within higher level regions MST and dorsal stream regions within intraparietal sulcus.

Evidence for top-down influence in perception of motion in MT+

While neurophysiology has focused on bottom-up processing of motion, once more neuroimaging is of great help in the investigation of higher-order motion phenomena with human observers who can report their perceptual experiences unambiguously.

There is evidence that MT+ receives input from other sources besides earlier visual areas. Implied motion⁵⁷, voluntary attentional shift to moving dots¹¹⁶ or imagination of moving dots⁷³ all produce increased activity in MT+. Considered together, these findings imply that MT+ activity is modulated not only by the physical characteristics of visual stimuli but also by feedback connections from higher order brain areas.

Aims and general outline of the thesis

The neuronal mechanism underlying perceptual decision processes and the putative role of high order frontal regions in perception have been widely studied but many aspects remain either unknown or controversial. In this thesis we aimed to understand the role of top-down mechanisms in feature integration and determine the brain regions underlying perceptual transitions. We also investigated how brain regions at the same processing level might interact in the context of perceptual decision making.

In Chapter 2 we provide an overview of the methodological approaches used in this thesis, namely the origin, analysis and interpretation of the fMRI signal.

In Chapter 3 we present a particular application of deconvolution analysis of fMRI data. This experiment design and statistical analysis in fMRI studies allow to empirically extract important features of neuronal response to visual stimuli from hemodynamic variable responses in human brain, as measured with fMRI.

In Chapter 4 we aimed to extend the simplistic view of single site dominating triggering of perceptual decision, by combining a novel paradigm requiring large scale interhemispheric integration of information to assess the role of multiple visual regions involved in motion surface reconstruction and their top-down or bottom-up modulation. We chose a visual paradigm that forcibly requires interhemispheric integration of information for emergence of perceptual binding. We used an ambiguous visual stimulus that can be perceived as one coherent moving object or two objects moving independently and separated by the vertical meridian. We took advantage of a previously described bistable stimulus that critically engages both visual hemifields and, consequently, requires integration across both visual hemispheres to form a coherent percept^{117,118}, as represented in Figure 1-9, which closely resemble the pattern and transparent motion of drifting plaids differing in that the gratings are presented in a non-overlapping configuration.

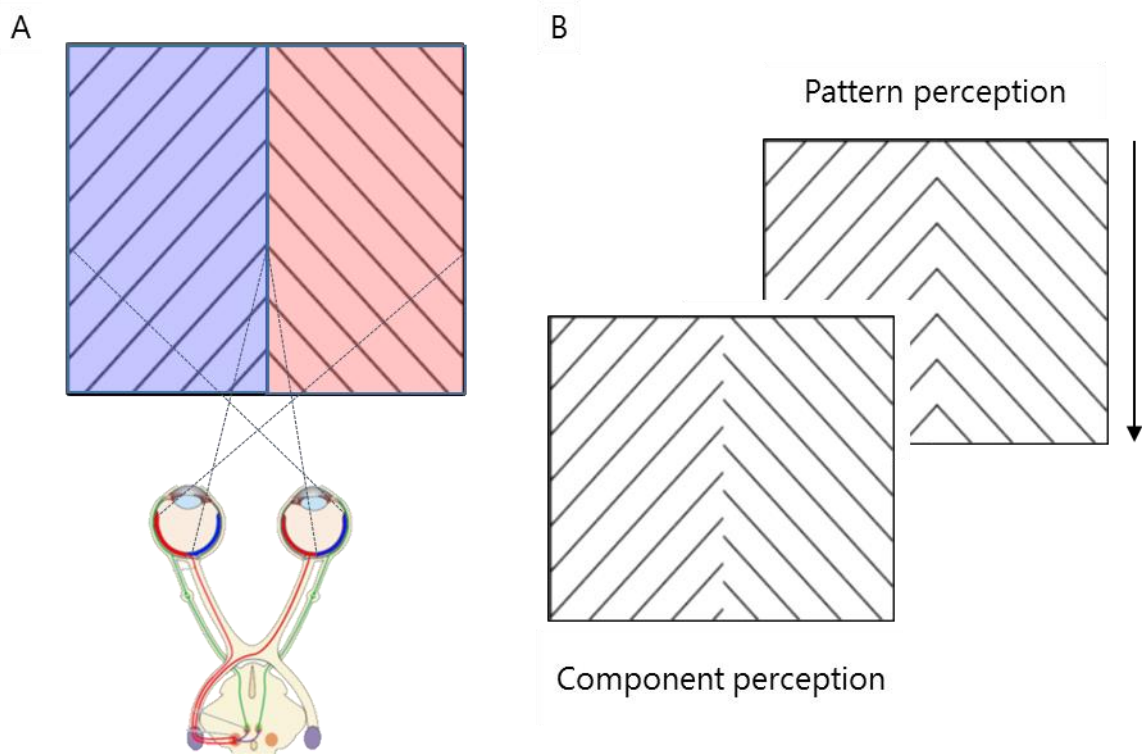


Figure 1-9. Ambiguous moving roof-shaped lines. The stimulus was first described by Wallach ^{117,118}. (A) The angled constantly moving lines form a bistable stimulus that critically engages both visual hemifields with minimal contamination of the opposite hemifield. The percepts elicited by this ambiguous bistable stimulus closely resemble the pattern and transparent motion of drifting plaids (formed by superimposed gratings), differing in that the gratings are presented in a non-overlapping configuration. (B) The “roof-shaped” stimulus can thus be perceived as a single unified pattern/object moving downward or as two surfaces/objects describing a horizontal movement inwards, accompanied by the striking perceptions of being segregated across hemispheres.

The investigation of the neural correlates of perceptual transitions provides new insights into complex cortical networks of motion-sensitive areas driven by bottom-up and top-down neural processes. Furthermore, necessary interhemispheric integration of visual input will determine perceptual transitions (between perceiving one coherent object and two separate objects). This will hopefully contribute to understand how the visual system reconstructs such representations from its components. In other words we aimed to provide high

temporal and spatial resolution mapping of perceptual motion integration mechanisms, to unravel bottom-up and top-down decision mechanisms. Importantly, the use of an ambiguous stimulus allows us to separate the neuronal activity due to stimulus input from activity related to stimulus perception.

In the discussion of Chapter 4 we also briefly present the results and main conclusions of an EEG study of the role of neuronal synchronization in perceptual integration of motion across hemispheres.

Another ambiguous figure, the Necker cube, was used to investigate brain mechanisms that induce perceptual bistability, by exploring how neural activity in response to perceptual decisions is affected by concurrent recruitment of attentional resources.

In Chapter 5 we present a study of the effect of working memory load (WML) in perceptual decision. If working memory resources are actively involved in the construction of the available percepts of the ambiguous stimulus, a concurrent WML will decrease the reversal rates and modulate the efficiency of the neural processes involved in reversals, since it depletes the available attentional resources.

In Chapter 6 we provide a general discussion regarding low level and high level influences in integration of sensory information and their effect in visual perception. We further present strategies for future deeper investigation of open issues in the current body of knowledge on this area.

References

1. Goebel, R., Muckli, L. & Kim, D. in *The Human Nervous System* (eds. Paxinos, G. & Mai, J. K.) (Elsevier Academic Press, 2004).
2. Van Hooser, S. D. & Nelson, S. B. Visual System. *Encycl. Life Sci.* 1–8 (2005).
3. Noback, C. R., Strominger, N. L., Demarest, R. J. & Ruggiero, D. A. *The Human Nervous System, Structure and Function.* (Humana Press, 2005).
4. Hofer, S., Karaus, A. & Frahm, J. Reconstruction and dissection of the entire human visual pathway using diffusion tensor MRI. *Front. Neuroanat.* **4-15**, 1–77 (2010).
5. Garey, L. J. *Brodmann's Localisation in the Cerebral Cortex.* (Springer, 2006).
6. Ungerleider, L. G. & Haxby, J. V. 'What' and 'where' in the human brain. *Curr. Opin. Neurobiol.* **4**, 157–165 (1994).
7. Desimone, R. & Ungerleider, L. G. Multiple visual areas in the caudal superior temporal sulcus of the macaque. *J. Comp. Neurol.* **248**, 164–189 (1986).
8. Hubel, D. & Wiesel, T. Receptive fields and functional architecture of monkey striate cortex. *J. Physiol.* **195**, 215–243 (1968).
9. Ungerleider, L. G. & Mishkin, M. in *Analysis of Visual Behavior* (eds. Ingle, D. J., Goodale, M. A. & Mansfield, R. J.) 549–586 (The MIT Press, 1982).
10. Carandini, M., Anthony Movshon, J. & Ferster, D. Pattern adaptation and cross-orientation interactions in the primary visual cortex. *Neuropharmacology* **37**, 501–511 (1998).
11. Cumming, B. & DeAngelis, G. C. The physiology of stereopsis. *Annu. Rev. Neurosci.* **24**, 203–238 (2001).
12. Horwitz, G. D. & Hass, C. A. Nonlinear analysis of macaque V1 color tuning reveals cardinal directions for cortical color processing. *Nat. Neurosci.* **15**, 913–919 (2012).
13. Huk, A. C. & Heeger, D. J. Pattern-motion responses in human visual cortex. *Nat. Neurosci.* **5**, 72–75 (2002).
14. Huk, A. C., Dougherty, R. F. & Heeger, D. J. Retinotopy and Functional Subdivision of Human Areas MT and MST. *J. Neurosci.* **22**, 7195–7205 (2002).
15. Van Essen, D., Maunsell, J. & Bixby, J. The middle temporal visual area in the macaque: myeloarchitecture, connections, functional properties and topographic organization. *J. Comp. Neurol.* **199**, 293–326 (1981).
16. Von Der Heydt, R., Peterhans, E. & Baumgartner, G. Illusory contours and cortical neuron responses. *Science* **224**, 1260–1262 (1984).
17. Desimone, R. & Schein, S. J. Visual properties of neurons in area V4 of the macaque:

- sensitivity to stimulus form. *J. Neurophysiol.* **57**, 835–868 (1987).
18. Kanwisher, N., McDermott, J. & Chun, M. M. The fusiform face area: a module in human extrastriate cortex specialized for face perception. *J. Neurosci.* **17**, 4302–4311 (1997).
 19. van Santen, J. P. & Sperling, G. Temporal covariance model of human motion perception. *J. Opt. Soc. Am. A* **1**, 451–473 (1984).
 20. Adelson, E. H. & Bergen, J. R. Spatiotemporal energy models for the perception of motion. *J. Opt. Soc. Am. A* **2**, 284–299 (1985).
 21. Sun, P., Chubb, C. & Sperling, G. Two mechanisms that determine the Barber-Pole Illusion. *Vision Res.* **111**, 43–54 (2015).
 22. Blake, R., Sekuler, R. & Grossman, E. in *The Primate Visual System* (eds. Kaas, J. & Collins, C.) 311–344 (CRC Press, 2004).
 23. Fennema, C. L. & Thompson, W. B. Velocity determination in scenes containing several moving objects. *Comput. Graph. image Process.* **9**, 301–315 (1979).
 24. Adelson, E. H. & Movshon, J. A. Phenomenal coherence of moving visual patterns. *Nature* **300**, 523–525 (1982).
 25. Movshon, J. A., Adelson, E. H., Gizzi, M. S. & Newsome, W. T. The analysis of moving visual patterns. *Pattern Recognit. Mech.* 117–151 (1985).
 26. Alais, D., Wenderoth, P. & Burke, D. The size and number of plaid blobs mediate the misperception of Type-II plaid direction. *Vision Res.* **37**, 143–150 (1997).
 27. Alais, D., Wenderoth, P. & Burke, D. The contribution of one-dimensional motion mechanisms to the perceived direction of drifting plaids and their aftereffects. *Vision Res.* **34**, 1823–1834 (1994).
 28. Burke, D., Alais, D. & Wenderoth, P. A Role for a low level mechanism in determining plaid coherence. *Vision Res.* **34**, 3189–3196 (1994).
 29. Wenderoth, P., Alais, D., Burke, D. & van der Zwan, R. The role of the blobs in determining the perception of drifting plaids and their motion aftereffects. *Perception* **23**, 1163–1169 (1994).
 30. Gizzi, M. S., Katz, E., Schumer, R. A. & Movshon, J. A. Selectivity for orientation and direction of motion of single neurons in cat striate and extrastriate visual cortex. *J. Neurophysiol.* **63**, 1529–1543 (1990).
 31. Zeki, S. Functional organization of a visual area in the posterior bank of the superior temporal sulcus of the rhesus monkey. *J. Physiol.* **236**, 549–573 (1974).
 32. De Valois, R. L., Yund, E. W. & Hepler, N. The orientation and direction selectivity of cells in macaque visual cortex. *Vision Res.* **22**, 531–544 (1982).

33. Culham, J., He, S., Dukelow, S. & Verstraten, F. A. Visual motion and the human brain: what has neuroimaging told us? *Acta Psychol. (Amst)*. **107**, 69–94 (2001).
34. Movshon, J. A. & Newsome, W. T. Visual response properties of striate cortical neurons projecting to area MT in macaque monkeys. *J. Neurosci.* **16**, 7733–7741 (1996).
35. Kolster, H., Peeters, R. & Orban, G. A. The retinotopic organization of the human middle temporal area MT/V5 and its cortical neighbors. *J. Neurosci.* **30**, 9801–9820 (2010).
36. Maunsell, J. H. & Van Essen, D. C. Functional properties of neurons in middle temporal visual area of the macaque monkey. I. Selectivity for stimulus direction, speed, and orientation. *J. Neurophysiol.* **49**, 1127–1147 (1983).
37. Saito, H. *et al.* Integration of direction signals of image motion in the superior temporal sulcus of the macaque monkey. *J. Neurosci.* **6**, 145–157 (1986).
38. Wilson, H. R., Ferrera, V. P. & Yo, C. A psychophysically motivated model for two-dimensional motion perception. *Vis. Neurosci.* **9**, 79 (1992).
39. Simoncelli, E. P. & Heeger, D. J. A model of neuronal responses in visual area MT. *Vision Res.* **38**, 743–761 (1998).
40. Simoncelli, E. P. & Heeger, D. J. Representing retinal image speed in visual cortex. *Nat. Neurosci.* **4**, 461–462 (2001).
41. Albright, T. D., Desimone, R. & Gross, C. G. Columnar organization of directionally selective cells in visual area MT of the macaque. *J. Neurophysiol.* **51**, 16–31 (1984).
42. O’Keefe, L. P. & Movshon, J. A. Processing of first- and second-order motion signals by neurons in area MT of the macaque monkey. *Vis. Neurosci.* **15**, 305–317 (1998).
43. Albright, T. D. Direction and orientation selectivity of neurons in visual area MT of the macaque. *J. Neurophysiol.* **52**, 1106–1130 (1984).
44. Sereno, M. *et al.* Borders of multiple visual areas in humans revealed by functional magnetic resonance imaging. *Science* **268**, 889–893 (1995).
45. Braddick, O. J. *et al.* Brain areas sensitive to coherent visual motion. *Perception* **30**, 61–72 (2001).
46. Huk, A. C., Ress, D. & Heeger, D. J. Neuronal basis of the motion aftereffect reconsidered. *Neuron* **32**, 161–172 (2001).
47. Tootell, R. B. *et al.* Functional analysis of V3A and related areas in human visual cortex. *J. Neurosci.* **17**, 7060–7078 (1997).
48. Levinson, E. & Sekuler, R. Inhibition and disinhibition of direction-specific mechanisms in human vision. *Nature* **256**, 144–146 (1975).
49. Zeki, S. *et al.* A direct demonstration of functional specialization in human visual cortex. *J.*

- Neurosci.* **11**, 641–649 (1991).
50. Watson, J. *et al.* Area V5 of the human brain: evidence from a combined study using positron emission tomography and magnetic resonance imaging. *Cereb. Cortex* **3**, 79–94 (1993).
 51. Tootell, R. B. *et al.* Functional Analysis of Human MT and Related Visual Cortical Areas Using Magnetic Resonance Imaging. *J. Neurosci.* **15**, 3215–3230 (1995).
 52. Dukelow, S. P. *et al.* Distinguishing Subregions of the Human MT+ Complex Using Visual Fields and Pursuit Eye Movements. *J. Neurophysiol.* **86**, 1991–2000 (2001).
 53. Muckli, L. *et al.* Apparent motion: event-related functional magnetic resonance imaging of perceptual switches and states. *J. Neurosci.* **22**, RC219 (2002).
 54. Sterzer, P., Russ, M. O., Preibisch, C. & Kleinschmidt, A. Neural correlates of spontaneous direction reversals in ambiguous apparent visual motion. *Neuroimage* **15**, 908–916 (2002).
 55. He, S., Cohen, E. R. & Hu, X. Close correlation between activity in brain area MT/V5 and the perception of a visual motion aftereffect. *Curr. Biol.* **8**, 1215–1218 (1998).
 56. Taylor, J. G. *et al.* The network of brain areas involved in the motion aftereffect. *Neuroimage* **11**, 257–70 (2000).
 57. Kourtzi, Z. & Kanwisher, N. Activation in human MT/MST by static images with implied motion. *J. Cogn. Neurosci.* **12**, 48–55 (2000).
 58. Pavan, A., Cuturi, L. F., Maniglia, M., Casco, C. & Campana, G. Implied motion from static photographs influences the perceived position of stationary objects. *Vision Res.* **51**, 187–194 (2011).
 59. Senior, C. *et al.* The functional neuroanatomy of implicit motion perception or ‘representational momentum’. *Curr. Biol.* **10**, 16–22 (2000).
 60. Culham, J. C., Cavanagh, P. & Kanwisher, N. G. Attention response functions: characterizing brain areas using fMRI activation during parametric variations of attentional load. *Neuron* **32**, 737–745 (2001).
 61. Castelo-Branco, M. *et al.* Activity patterns in human motion-sensitive areas depend on the interpretation of global motion. *Proc. Natl. Acad. Sci.* **99**, 13914–13919 (2002).
 62. Castelo-Branco, M., Goebel, R., Neuenschwander, S. & Singer, W. Neural synchrony correlates with surface segregation rules. *Nature* **405**, 685–689 (2000).
 63. Kozak, L. R. & Castelo-Branco, M. Peripheral influences on motion integration in foveal vision are modulated by central local ambiguity and center-surround congruence. *Investig. Ophthalmol. Vis. Sci.* **50**, 980–988 (2009).
 64. Castelo-Branco, M. *et al.* Type of featural attention differentially modulates hMT+

- responses to illusory motion aftereffects. *J. Neurophysiol.* **102**, 3016–3025 (2009).
65. Kandel, E. R., Schwartz, J. H., Jessel, T. M., Siegelbaum, S. A. & Hudspeth, A. *Principles of Neural Science*. (McGraw Hill, 2013).
 66. Engel, A. K., Roelfsema, P. R., Fries, P., Brecht, M. & Singer, W. Role of the temporal domain for response selection and perceptual binding. *Cereb. cortex* **7**, 571–582 (1997).
 67. Gregory, R. L. Knowledge in perception and illusion. *Philos. Trans. R. Soc. Lond. B. Biol. Sci.* **352**, 1121–1127 (1997).
 68. Wandell, B. A. Computational Neuroimaging: Color Representations and Processing. *Psychology* 1–26 (1999).
 69. Hochstein, S. & Ahissar, M. View from the top: Hierarchies and reverse hierarchies in the visual system. *Neuron* **36**, 791–804 (2002).
 70. Singer, W. Neuronal Synchrony: A Versatile Code Review for the Definition of Relations? *Neuron* **24**, 49–65 (1999).
 71. Engel, A. K., Fries, P. & Singer, W. Dynamic predictions: oscillations and synchrony in top-down processing. *Nat. Rev. Neurosci.* **2**, 704–716 (2001).
 72. McMains, S. & Kastner, S. Interactions of top-down and bottom-up mechanisms in human visual cortex. *J. Neurosci.* **31**, 587–597 (2011).
 73. Goebel, R., Khorram-Sefat, D., Muckli, L., Hacker, H. & Singer, W. The constructive nature of vision: direct evidence from functional magnetic resonance imaging studies of apparent motion and motion imagery. *Eur. J. Neurosci.* **10**, 1563–1573 (1998).
 74. Yokoi, I. & Komatsu, H. Relationship between neural responses and visual grouping in the monkey parietal cortex. *J. Neurosci.* **29**, 13210–21 (2009).
 75. Buzsáki, G. *Rhythms of the Brain*. (Oxford University Press, 2006).
 76. Herzog, M. in *Encyclopedia of Neuroscience* (eds. Binder, M. D., Hirokawa, N. & Windhorst, U.) 388–391 (Springer Berlin Heidelberg, 2009).
 77. Gray, C. M. The temporal correlation hypothesis of visual feature integration: still alive and well. *Neuron* **24**, 31–47 (1999).
 78. Shadlen, M. N. & Movshon, J. A. Synchrony unbound: A critical evaluation of the temporal binding hypothesis. *Neuron* **24**, 67–77 (1999).
 79. Kreiter, A. K. & Singer, W. Stimulus-Dependent Synchronization of Neuronal Responses in the Visual Cortex of the Awake Macaque Monkey. *J. Neurosci.* **16**, 2381–2396 (1996).
 80. Thiele, A. & Stoner, G. Neuronal synchrony does not correlate with motion coherence in cortical area MT. *Nature* **421**, 366–370 (2003).
 81. Palanca, B. J. & DeAngelis, G. C. Does neuronal synchrony underlie visual feature grouping?

- Neuron* **46**, 333–346 (2005).
82. Mima, T., Oluwatimilehin, T., Hiraoka, T. & Hallett, M. Transient interhemispheric neuronal synchrony correlates with object recognition. *J. Neurosci.* **21**, 3942–3948 (2001).
 83. Tallon-Baudry, C. Oscillatory synchrony and human visual cognition. *J. Physiol.* **97**, 355–363 (2003).
 84. Innocenti, G. M. Dynamic interactions between the cerebral hemispheres. *Exp. Brain Res.* **192**, 417–423 (2009).
 85. Roelfsema, P. R. Cortical algorithms for perceptual grouping. *Annu. Rev. Neurosci.* **29**, 203–227 (2006).
 86. Uhlhaas, P. J. *et al.* Neural synchrony in cortical networks: history, concept and current status. *Front. Integr. Neurosci.* **3**, 1–19 (2009).
 87. Long, G. M. & Toppino, T. C. Enduring Interest in Perceptual Ambiguity: Alternating Views of Reversible Figures. *Psychol. Bull.* **130**, 748–768 (2004).
 88. Engel, A. K., Fries, P., Konig, P., Brecht, M. & Singer, W. Temporal binding, binocular rivalry, and consciousness. *Conscious. Cogn.* **8**, 128–151 (1999).
 89. Engel, A. K. & Singer, W. Temporal binding and the neural correlates of sensory awareness. *Trends Cogn. Sci.* **5**, 16–25 (2001).
 90. Heekeren, H. R., Marrett, S. & Ungerleider, L. G. The neural systems that mediate human perceptual decision making. *Nat. Rev. Neurosci.* **9**, 467–479 (2008).
 91. Fries, P., Castelo-Branco, M., Engel, A. K. & Singer, W. in *Binocular rivalry and perceptual ambiguity* (eds. Maass, W. & Bishop, C. M.) (MIT Press, 2005).
 92. Kornmeier, J. & Bach, M. Ambiguous figures - what happens in the brain when perception changes but not the stimulus. *Front. Hum. Neurosci.* **6**, 1–23 (2012).
 93. Toppino, T. C. & Long, G. M. Selective adaptation with reversible figures: don't change that channel. *Percept. Psychophys.* **42**, 37–48 (1987).
 94. Leopold, D. A. & Logothetis, N. K. Multistable phenomena: Changing views in perception. *Trends Cogn. Sci.* **3**, 254–264 (1999).
 95. Long, G. M., Toppino, T. C. & Kostenbauder, J. F. As the cube turns: evidence for two processes in the perception of a dynamic reversible figure. *Percept. Psychophys.* **34**, 29–38 (1983).
 96. Hochberg, J. & Peterson, M. A. Piecemeal organization and cognitive components in object perception: perceptually coupled responses to moving objects. *J. Exp. Psychol. Gen.* **116**, 370–380 (1987).
 97. Kornmeier, J., Hein, C. M. & Bach, M. Multistable perception: When bottom-up and top-

- down coincide. *Brain Cogn.* **69**, 138–147 (2009).
98. Intaitė, M., Noreika, V., Šoliūnas, A. & Falter, C. M. Interaction of bottom-up and top-down processes in the perception of ambiguous figures. *Vision Res.* **89**, 24–31 (2013).
 99. Intaitė, M., Koivisto, M. & Castelo-Branco, M. Event-related potential responses to perceptual reversals are modulated by working memory load. *Neuropsychologia* **56**, 428–438 (2014).
 100. Tong, F., Meng, M. & Blake, R. Neural bases of binocular rivalry. *Trends Cogn. Sci.* **10**, 502–511 (2006).
 101. Blake, R., Brascamp, J. & Heeger, D. J. Can binocular rivalry reveal neural correlates of consciousness? *Philos. Trans. R. Soc. London. Ser. B Biol. Sci.* **369**, 20130211 (2014).
 102. Newsome, W. T. & Paré, E. B. A Selective Impairment of Motion Perception Following Lesions of the Middle Temporal Visual Area (MT). *J. Neurosci.* **8**, 2201–2211 (1988).
 103. Salzman, D. C., Murasugi, C. M., Britten, K. H. & Newsome, W. T. Microstimulation in visual area MT: effects on direction discrimination performance. *J. Neurosci.* **12**, 2331–2355 (1992).
 104. Rorie, A. E. & Newsome, W. T. A general mechanism for decision-making in the human brain? *Trends Cogn. Sci.* **9**, 41–43 (2005).
 105. Marotta, J., Genovese, C. & Behrmann, M. A functional MRI study of face recognition in patients with prosopagnosia. *Neuroreport* **12**, 1581–1588 (2001).
 106. Avidan, G., Hasson, U., Malach, R. & Behrmann, M. Detailed exploration of face-related processing in congenital prosopagnosia: 2. Functional neuroimaging findings. *J. Cogn. Neurosci.* **17**, 1150–1167 (2005).
 107. Avidan, G. & Behrmann, M. Functional MRI reveals compromised neural integrity of the face processing network in congenital prosopagnosia. *Curr. Biol.* **19**, 1146–1150 (2009).
 108. Heekeren, H. R., Marrett, S., Bandettini, P. A. & Ungerleider, L. G. A general mechanism for perceptual decision-making in the human brain. *Nature* **431**, 859–862 (2004).
 109. Rebola, J., Castelhana, J., Ferreira, C. & Castelo-Branco, M. Functional parcellation of the operculo-insular cortex in perceptual decision making: an fMRI study. *Neuropsychologia* **50**, 3693–3701 (2012).
 110. Lamichhane, B. & Dhamala, M. Perceptual decision-making difficulty modulates feedforward effective connectivity to the dorsolateral prefrontal cortex. *Front. Hum. Neurosci.* **9**, 1–9 (2015).
 111. Filimon, F., Philastides, M. G., Nelson, J. D., Kloosterman, N. A. & Heekeren, H. R. How Embodied Is Perceptual Decision Making? Evidence for Separate Processing of Perceptual

- and Motor Decisions. *J. Neurosci.* **33**, 2121–2136 (2013).
112. Ruff, D. A., Marrett, S., Heekeren, H. R., Bandettini, P. A. & Ungerleider, L. G. Complementary roles of systems representing sensory evidence and systems detecting task difficulty during perceptual decision making. *Front. Neurosci.* **4**, 1–10 (2010).
113. Frässle, S., Sommer, J., Jansen, A., Naber, M. & Einhauser, W. Binocular Rivalry: Frontal Activity Relates to Introspection and Action But Not to Perception. *J. Neurosci.* **34**, 1738–1747 (2014).
114. Yamashiro, H. *et al.* Activity in early visual areas predicts interindividual differences in binocular rivalry dynamics. *J. Neurophysiol.* **111**, 1190–1202 (2014).
115. McDonald, J. S., Clifford, C. W., Solomon, S. S., Chen, S. C. & Solomon, S. G. Integration and segregation of multiple motion signals by neurons in area MT of primate. *J. Neurophysiol.* **111**, 369–378 (2014).
116. O’Craven, K. M., Rosen, B. R., Kwong, K. K., Treisman, A. & Savoy, R. L. Voluntary attention modulates fMRI activity in human MT-MST. *Neuron* **18**, 591–598 (1997).
117. Wallach, H. Über visuell wahrgenommene Bewegungsrichtung. *Psychol. Forsch.* **20**, 325–380 (1935).
118. Wuerger, S., Shapley, R. & Rubin, N. ‘On the visually perceived direction of motion’ by Hans Wallach: 60 years later. *Perception* **25**, 1317–1367 (1996).
119. Velik, R. From simple receptors to complex multimodal percepts: a first global picture on the mechanisms involved in perceptual binding. *Front. Psychol.* **3**, 259 (2012).
120. Koch, C. in *The quest for consciousness: a neurobiological approach* 270 (Roberts & Company Publishers, 2004).

Chapter 2

Studying brain structure and function:

A magnetic resonance imaging
approach

Magnetic resonance imaging (MRI), which led to the Nobel Prize in Physiology or Medicine *winner* in 2003, awarded to Paul C Lauterbur and Peter Mansfield ¹, has become the most important imaging modality in human neuroscience. Its non-invasive nature and versatility make MRI a powerful method for obtaining detailed anatomical and functional information about living tissue without the use of damaging radiation such as X-rays. MRI uses signals originating from the body's own molecules after a radiofrequency perturbation, while PET and SPECT require introduction of a radioactive label into the body with a drawback of exposure to low levels of ionizing radiation.

This chapter provides an overview of the MRI methods employed throughout this thesis to assess brain structure and function, from physical to physiological principles and data analysis.

Basic physical principles of MRI

The majority of MRI techniques rely on water, which constitutes about two-thirds of human body tissue, to develop information on brain structure and function. MRI signals arise from the interaction of the strong magnetic field that exists inside the MRI scanner with unpaired protons of hydrogen nuclei in the water content of the brain ². In fact, all nuclei with an odd number of protons are magnetically excitable. The reason that MRI mainly depends on hydrogen is because hydrogen protons are abundant in human tissue and possess particularly favourable magnetic properties. MRI is based on sophisticated technology that excites and receives the signal re-emitted by hydrogen protons in the tissue.

More specifically, protons in the nuclei of hydrogen atoms in water possess a spin, they rotate about its axis at a constant velocity. Protons possess a positive electrical charge, which also spins around with the proton. A moving electrical charge is in fact an electrical current. Consequently, spinning protons create their

own small magnetic fields. In a normal environment all protons spin randomly about many rotational axes and, thus, cancel each other out (Figure 2-1A). This is the reason why our body has no net magnetization. However, when a strong magnetic field is introduced (actually our body is introduced in the strong magnetic field existent within the MR scanner) the protons align with that static homogeneous magnetic field (B_0), either parallel or antiparallel to it (Figure 2-1B). These orientations that a spinning proton can take against the external magnetic field are not of equal energy. Spin states which are oriented parallel to B_0 are lower in energy than in the absence of the external magnetic field. In contrast, spin states whose orientations are antiparallel to B_0 are higher in energy than in the absence of the external magnetic field ³. The protons will be distributed throughout the two spin states available. In equilibrium, a slightly larger proportion of spinning protons align parallel to B_0 , at the lower energy level (Figure 2-1C).

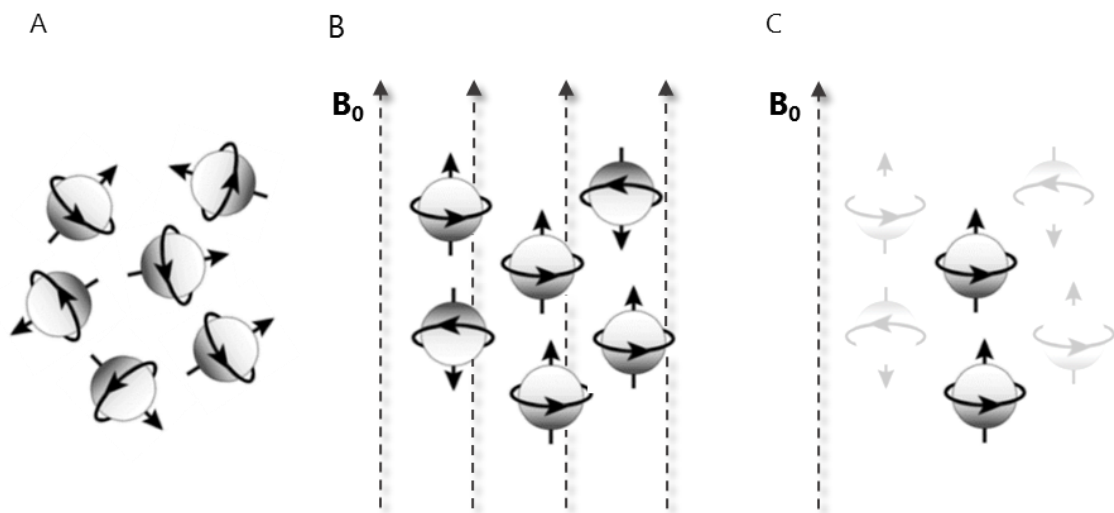


Figure 2-1. Spinning protons are little magnets because of the spin property. (A) Without an external magnetic field, the directions of the spins are randomly distributed. (B) When placed within a large magnetic field, the spins align either with the field (parallel) or against the field (antiparallel). (C) A slight excess of spins align with the external magnetic field resulting in a very small net magnetic field parallel to the external magnetic field that is difficult to detect. Adapted from ³.

This difference depends on the strength of the applied magnetic field. The excess of spinning protons aligned with the external magnetic field results in a net microscopic magnetization, aligned parallel to the magnetic field B_0 . In other words, the tissue gets magnetized. Moreover, the aligned spinning protons no longer rotate about their axes only, they start wobbling around the lines of the external magnetic field, much as a spinning top wobbles around the axis of the Earth when the force of gravity competes with its spin. This wobbling is called precession: while spinning, protons now rotate very fast about the axis of B_0 . Precession of protons (Figure 2-2) occurs at the precession frequency ω_0 , or Larmor frequency:

$$\omega_0 = \gamma B_0 \quad (\text{Equation 1})$$

The precession frequency is dependent on the gyromagnetic ratio (γ), a constant unique of each nucleus, and the external magnetic field B_0 . For hydrogen protons, $\gamma = 42.56$ MHz per Tesla. Therefore, at the magnetic field strength of a 3-Tesla scanner, the precession frequency of hydrogen protons is 128 MHz.

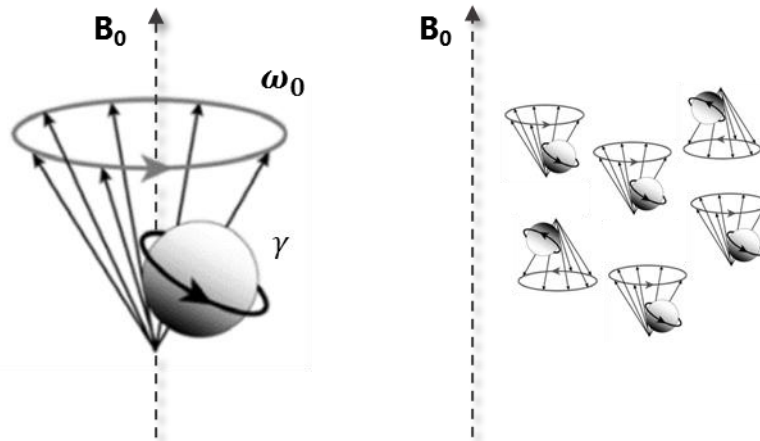


Figure 2-2. Nuclear spin precession. The spins rotate around the direction of the external magnetic field. This motion is called precession. The precession frequency, or Larmor frequency (ω_0) is dependent on the gyromagnetic ratio (γ) and the external magnetic field (B_0). Adapted from ^{3,4}.

Origin of MR signal

For sake of clarity, if we consider a coordinate system XYZ like the one used in school, we can represent the magnetic field lines as the z-axis. The x-y plane is perpendicular to the external magnetic field B_0 and is also referred to as the transverse plane. We can also represent one spin, at a particular moment in time, as a vector (Figure 2-3A). But there are millions and millions of protons in the brain (and other tissues). And because there are so many protons, there is one proton precessing parallel to the magnetic field for each proton precessing antiparallel to the magnetic field, pointing in the exact opposite direction, thus cancelling each other. However, as said before, there are slightly more protons

precessing parallel to the magnetic field than those precessing antiparallel to it, and these protons are not cancelled by others (Figure 2-3B). At least such cancellation is not complete. As there are many protons precessing this fast, spin vectors parallel to z-axis are pointing in different directions of the x-y plane at different specific points in time. Consequently, they still cancel each other out in the horizontal plane because protons precess randomly (not in phase). In contrast, the vertical component of the vectors parallel to the z-axis add up along the external magnetic field. Thus, the magnetization of the tissue is represented by M_0 in the z-axis, which corresponds to the excess of protons in the lower energy state, aligned parallel to the magnetic field (Figure 2-3C). As this is a longitudinal sum up vector, it is called longitudinal magnetization. However, this vector (which represents a magnetic force) is not measurable because it is in the same direction, parallel to the external magnetic field.

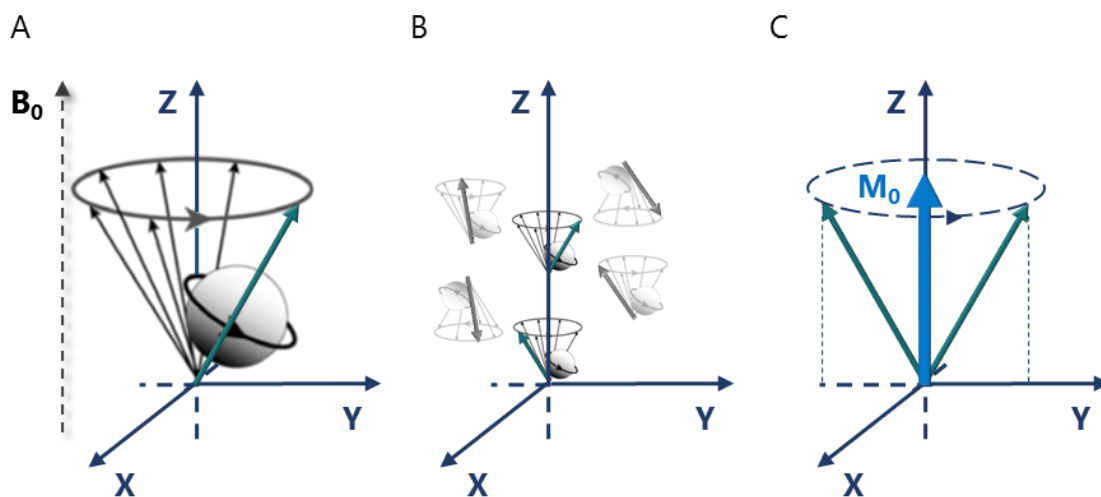


Figure 2-3. Longitudinal magnetization. (A) We can represent the magnetic field and the spins in a XYZ coordinate system, in which the z-axis corresponds to B_0 , the x-y plane is perpendicular to B_0 and each precessing spin is represented by a vector. (B) The spins (each represented by one vector) align either parallel or antiparallel to the external magnetic field. Most of them cancel each other out, but there are more of them aligned parallel to B_0 . Thus, we are left with some spins (two in this case) pointing in the direction of B_0 . (C) These spins still cancel each other out in the x-y plane. In contrast, the vertical component of the vectors parallel to the z-axis add up along the external magnetic field. Thus, the magnetization of the tissue is represented by M_0 in the z-axis, which corresponds to the excess of protons in the lower energy state, aligned parallel to the magnetic field. This is called longitudinal magnetization. Adapted from ^{5,77}.

So how can we measure tissue magnetization? We send a radio wave.

We actually send a short burst, not an electromagnetic wave with long duration. This electromagnetic pulse is in the range of radio frequency waves, so that it is called a radio frequency or RF pulse. When protons are irradiated with an RF pulse with their precession frequency they are able to exchange energy with it. Some get "excited" and absorb energy from the RF pulse. This important principle is called resonance and gives the method *magnetic resonance imaging* its name. The RF pulse disrupts the protons natural alignment (Figure 2-4A) and forces them into a non-natural realignment with the static magnetic field of the MR

scanner. By absorbing energy in the resonance frequency, some protons are induced to a transition from the parallel orientation, a lower energy state, to the antiparallel orientation, a higher energy state. This has an effect in tissue magnetization. There are now more cancelling protons (pairs of protons pointing in opposite directions). Consequently, the longitudinal magnetization of the tissue decreases (Figure 2-4B).

Furthermore, the RF pulse has another important effect in tissue magnetization. As we can see in Figure 2-4B, before the application of the RF pulse the protons randomly point in all directions in the x-y plane, cancelling their magnetic forces in the transverse plane. Due to the RF pulse, the excited protons precess in phase. They now point in the same direction perpendicular to the external magnetic field, and their vectors add up also in this direction. As a result, the RF pulse creates a magnetic vector pointing to the side to which the precessing protons are pointing at any moment, in the transverse plane. This is called transversal magnetization (Figure 2-4C). In other words, the tissue magnetization vector M_0 moves down towards the x-y plane and thus can be divided into a vertical or longitudinal component M_z , along the axis of B_0 (the z-axis) and a horizontal or transverse component M_{xy} , along the x-y plane. With the RF pulse, in practice, the longitudinal component of M_0 decreases (Figure 2-4B) and a transverse component M_{xy} is established (Figure 2-4C). The strength and duration of the RF pulse can be adjusted to modulate the extension and the angle α of the rotation of the vector M_0 towards the transverse plane (Figure 2-4D). The transversal magnetization vector M_{xy} then precesses around the direction of B_0 with angular velocity ω_0 given by Equation 1, the Larmor equation (Figure 2-4E). The magnetic field created by precession thus changes in time, which according to Faraday's law generates radio frequency waves. Ultimately it is this signal that is measured (received) in the receiver coil (antenna) in MRI.

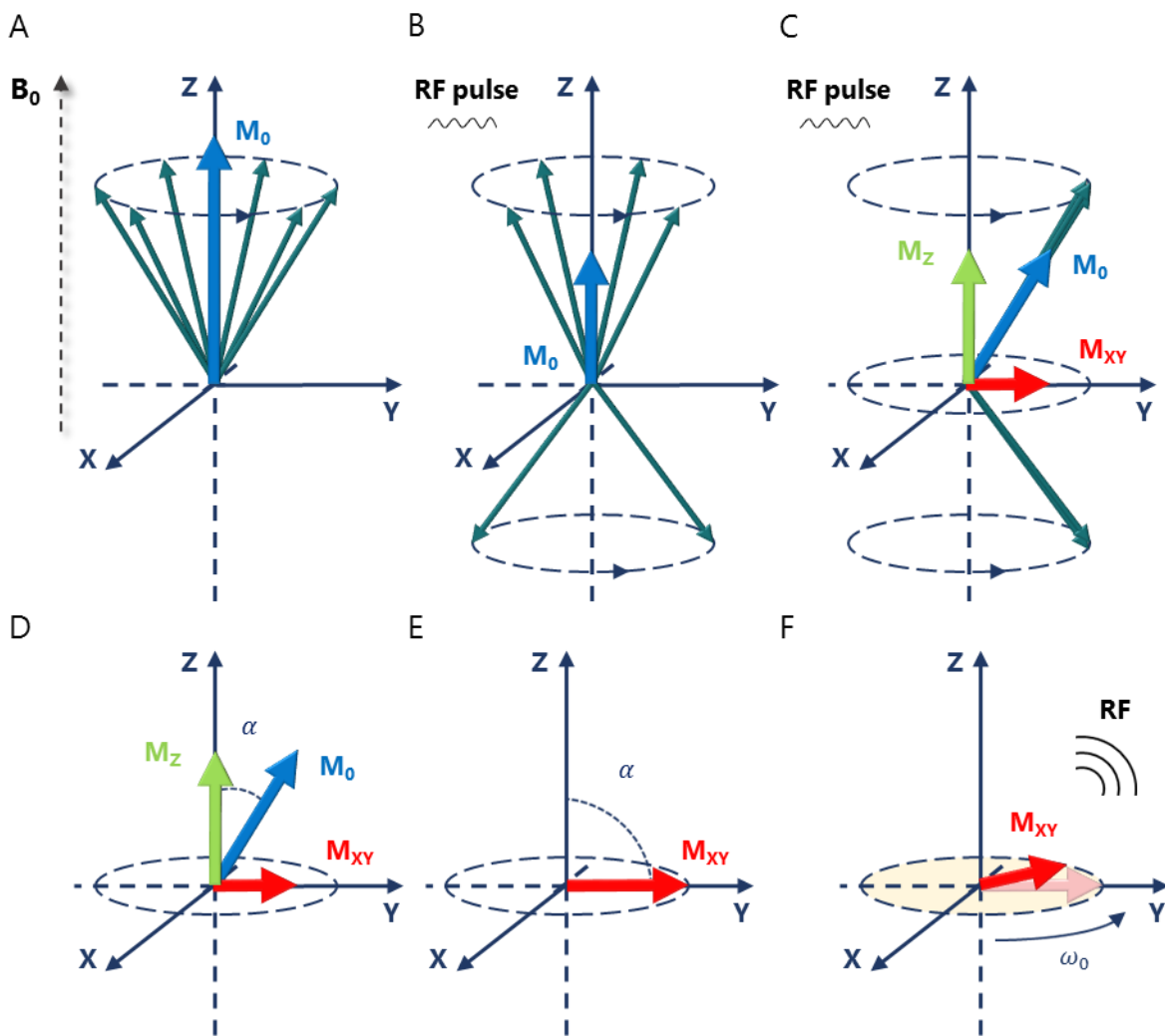


Figure 2-4. Excitation and transversal magnetization. (A) By placing the body in an external magnetic field we can establish a new magnetic vector, longitudinal magnetization (M_0), along the external field. Sending a radio frequency pulse has two effects on the protons. (B) After the RF pulse is sent in, we assume that some protons (in this case 2 out of 6) switch to a higher level of energy (antiparallel orientation). These protons cancel the same number of protons aligned parallel. As a consequence, the longitudinal magnetization M_0 decreases. (C) The RF pulse also causes the protons to precess in step, in phase. This phenomenon establishes a new magnetization in the x-y plane, a new transversal magnetization. (D) The strength and duration of the RF pulse can be adjusted to modulate the extension and the angle α of the rotation of the vector M_0 towards the transverse plane. (E) Depending on the RF pulse, longitudinal magnetization may even totally disappear. (F) The transversal magnetization vector M_{xy} then moves around the direction of B_0 with the precessing protons, generating radio frequency waves that can be measured. Adapted from ^{3,5}.

And what happens when the RF pulse is turned off? Simply, protons relax.

When the RF pulse is turned off, the excited protons relax back to their lower energy state and the MR signal decays due to interactions between proton magnetic fields, which is known as relaxation⁴. MR signal decay occurs because of two simultaneous types of relaxation effects: the longitudinal relaxation and the transversal relaxation (Figure 2-5), characterized by time constants T_1 and T_2 , respectively⁵.

On the one hand transversal relaxation is caused by spin dephasing. Therefore, in a T_2 weighted image the falling out of synchrony or the dephasing of rotating protons is emphasized. Dephasing occurs relatively quickly (transversal relaxation progresses faster than longitudinal relaxation) and results largely from the loss of energy to spinning protons nearby (it is also influenced by such factors as the quality of the magnets used). Spin-spin interactions lead to different local magnetic field strengths and, thus, different precession frequencies leading to phase shifts. The amplitude of the signal at any moment in time is determined by the sum of the spin vectors. When the spins are all in phase (Figure 2-5A), the maximum signal is obtained. When the spins are completely out of phase (Figure 2-5B), the signal is completely lost. Over time, M_{XY} decays to zero with a time constant T_2 with values in the range of 30-50 msec. Due to magnetic field inhomogeneities in the static magnetic field and in physiological tissue, the spins get out of phase actually faster than T_2 and therefore the measured MR signal in the receiver coil, the free induction decay (FID), decays with the shorter time constant T_2^* :

$$M_{XY} = M_0 e^{-\frac{t}{T_2^*}} \quad (\text{Equation 2})$$

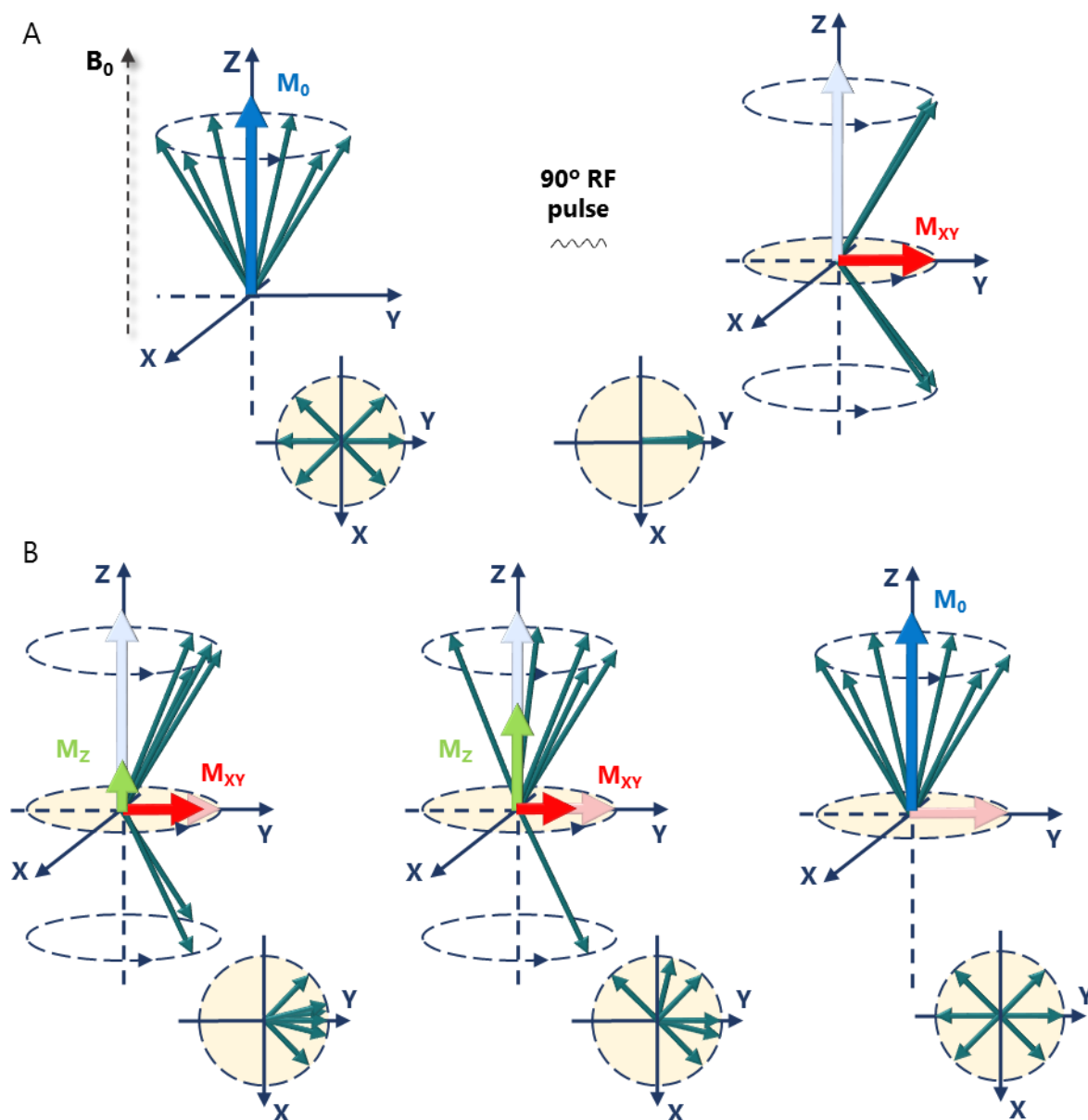


Figure 2-5. Representation of T1 and T2 relaxation processes in MRI. (A) When the protons are aligned with B_0 , a horizontal radio frequency pulse is applied to tip them so that they precess in the horizontal x-y plane in phase. (B) The horizontal pulse is then turned off and the rotating protons begin to move out of phase with one another - dephasing (easily observed in the representation of spins in the x-y plane, bottom right plots). This is the transverse relaxation, causing loss of the transverse component of magnetization (M_{XY}) and a weakened dephasing signal in the horizontal field at an exponential rate with time-constant T_2 . Dephasing occurs relatively quickly. After withdrawal of the horizontal pulse the protons also realign with the vertical magnetic field, with restoration of longitudinal magnetization. This "righting" of the protons occurs more slowly than the dephasing and is measured indirectly. This is the longitudinal relaxation, which causes recovery of the longitudinal magnetization (M_Z) towards M_0 at an exponential rate with time-constant T_1 . Adapted from ^{3,4}.

On the other hand, the longitudinal relaxation component emphasized in T_1 weighted images is the “righting” of tipped protons as they go back into the low energy state and realign parallel with the original magnetic field B_0 (Figure 2-5, first and last plots). The rate of this relaxation is influenced by non-excited molecules in the surrounding tissue, called the lattice, to which part of the energy re-emitted as RF waves is transmitted. The spin–lattice interactions thus determine the speed of T_1 recovery, which is unique to every tissue. The increase (recovery) of the longitudinal component M_z to M_0 follows an exponential function with time constant T_1 with values in the range of 300–2000 msec:

$$M_z = M_0(1 - e^{-\frac{t}{T_1}}) \quad (\text{Equation 3})$$

Tissue-specific T_1 and T_2 values enable MRI to differentiate between different types of tissue when using properly designed MRI pulse sequences. Variations that occur in the molecular environment in different brain structures and compartments provide contrast and the ability to see the spatial orientation of various brain structures. Other types of radiological imaging depend on one local property of the tissue. For example, in computed tomography (CT) the image is a map of the X-ray absorption coefficient and in nuclear medicine studies the image is a map of the radioactive tracer concentration or a related measure. But with MRI, contrast between one tissue and another in an image can be varied simply by varying the way the image is derived based on a given measure as the MR signal depends on a number of tissue properties. Moreover, the fact that local field inhomogeneities lead to different precession frequencies, increasing the speed of dephasing, is an important observation for functional MRI because local field inhomogeneities also depend on the local physiological state, especially the state of local blood oxygenation, which itself depends on the state of local neuronal activity. Measurements of changing local magnetic field

inhomogeneities (T_2^* parameter), thus, provide indirect measurements of local neuronal activity³. In T_2^* -weighted sequences, contrast is maximized because spins have enough time to dephase and relax when acquisition starts thus increasing the signal-to-noise ratio (SNR)⁶. These concepts of contrast optimization are of major importance for functional imaging studies providing the possibility to image the metabolic consequences of neuronal activity patterns in the brain.

Spatial localization of MR signal

We know how the MR signal is generated, but how does the machine determine where the signal is coming from (spatial localization)?

The spatial information comes from magnetic resonance imaging ability to localize the signal in the three-dimensional volume of the brain. This is accomplished by using magnetic gradient coils, in which the strength of the magnetic field changes gradually along an axis. There are three gradient coils in the scanner (called x, y and z), each oriented along a different plane of the body, all of them far less powerful than the main magnet (Figure 2-6).

The magnetic field strength is manipulated to be different in several position within the scanner, which in turn makes the amount of energy released by relaxing protons in the brain to be dependent on their original position in a predictable manner. The spatial distribution of water protons can be mathematically recovered from the resulting signal. When rapidly turned on and off, the gradient magnets allow the scanner to image the body in "slices". Using medical terminology, the transverse (or axial, or x-y) planes slice the brain from top to bottom; the coronal (x-z) plane slice the brain lengthwise from front to back; and the sagittal (y-z) planes slice you lengthwise from side to side (Figure 2-7).

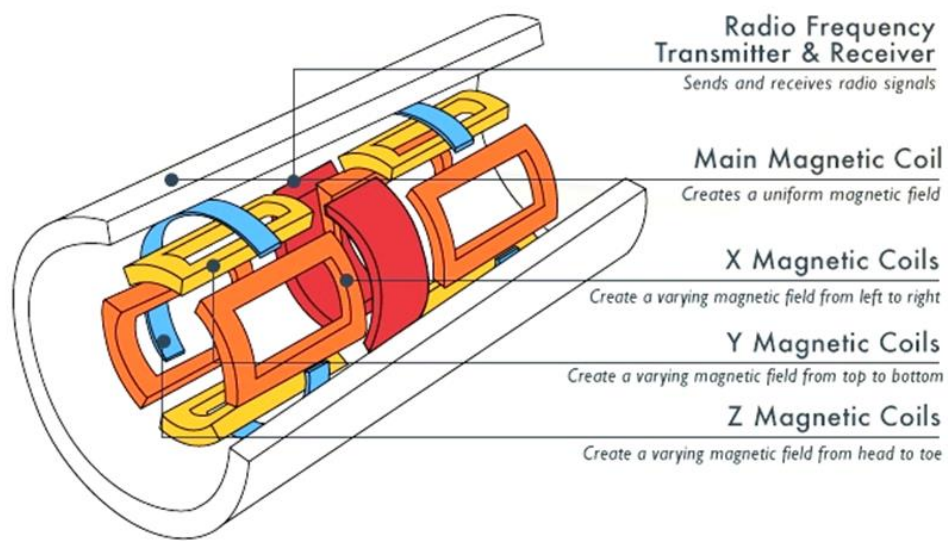


Figure 2-6. MRI scanner gradient magnet coils. Reproduced from <http://eu.mouser.com>.

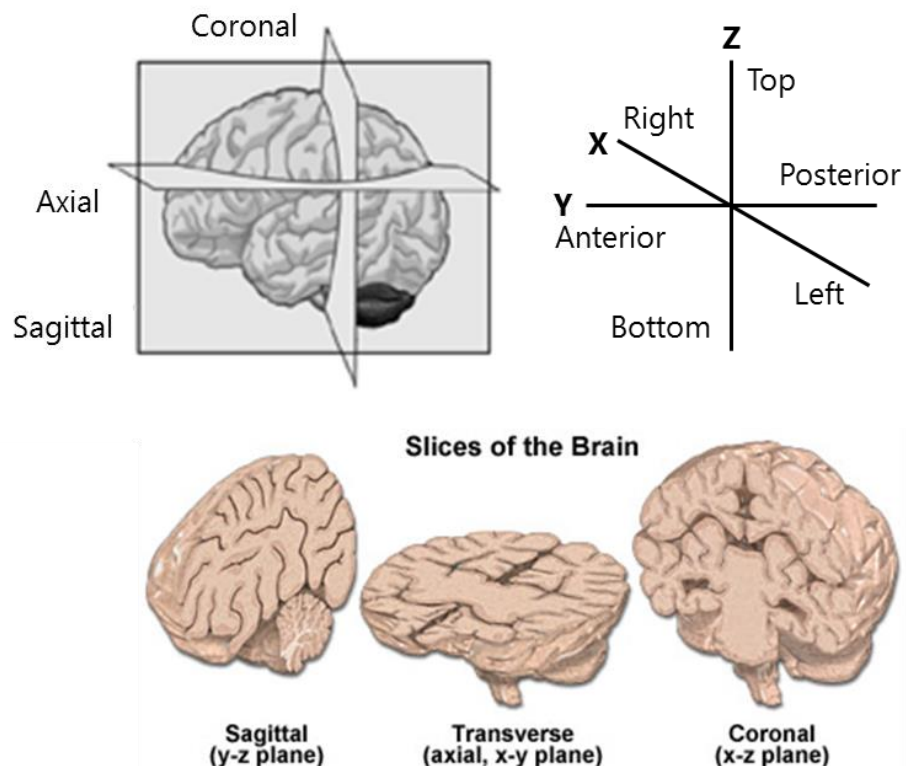


Figure 2-7. Section arrangements on different planes (coronal, sagittal and axial) of the brain. Adapted ⁷⁸.

One magnetic gradient is used to excite a single slice of the subject's brain. Then, when one slice of the brain is selected, the other two gradients subdivide that slice into rows and columns of pixels. Thus, the x, y and z gradients can be used in combination to generate image slices, one pixel at a time, based on location and signal strength information that it receives from the corresponding voxel (voxel = volume element, analogous to pixel = picture element) in the subject's brain (Figure 2-8). Each voxel represents a group of hydrogen protons with a unique sum of frequencies and phases. The intensity, or brightness, of each pixel is proportional to the strength of the RF energy received from the corresponding voxel after RF excitation and relaxation.

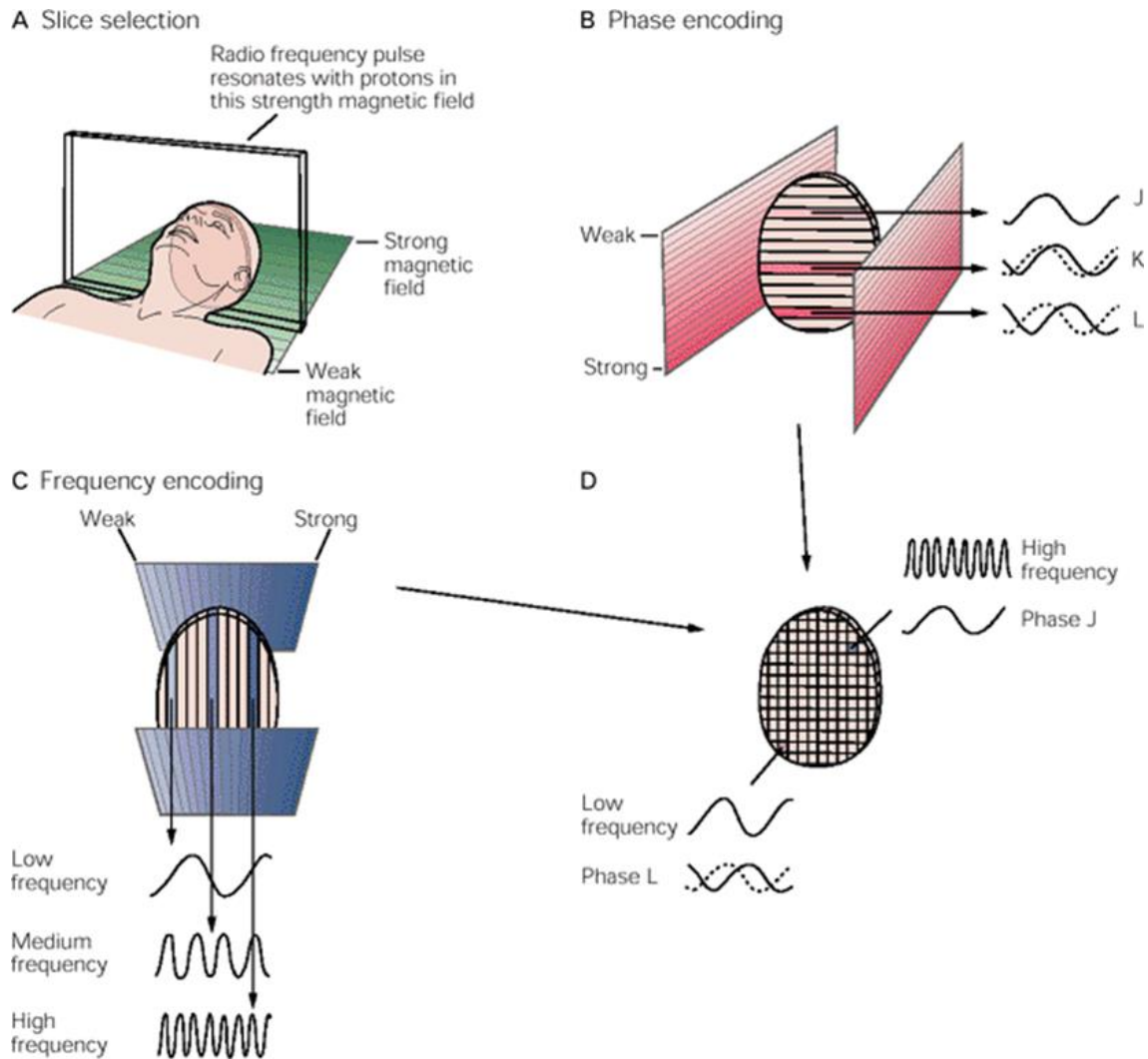


Figure 2-8. Three-dimensional encoding of the MR signal. The signals emitted from a three-dimensional volume are encoded by first exciting a single slice of tissue, then applying two different gradients to divide it into rows and columns of pixels. A patient is placed in a magnetic field whose strength is graded along an axis (for simplicity the magnets are shown here as planes). A) This gradient effectively divides the tissue into slices. A slice is selected for imaging by using a specific radio frequency pulse. B) The slice is then subdivided into rows by grading the strength of the magnetic field along a second axis. Protons in each row will be precessing at different phase. When the second magnetic gradient is turned off each row maintains this unique phase C) The slice is further divided into columns by grading the vertical magnetic fields so that protons in each column precess at a different frequency. D) With this encoding, each pixel in a slice will have a unique signal. The use of the Fourier transform allows to identify the signal coming from each pixel. Reproduced from ⁴.

Structural MRI

Anatomical MRI images have contrast, the areas with high signal are bright on the image and the areas with low signal are dark on the image. As described above, the contrast can be achieved with the adjustment of RF pulse sequences and imaging parameters. But what makes it achievable is that different local tissues in the brain have different physical properties, i.e. T_1 recovery, T_2 decay and proton density. Thus, structural imaging relies on these differences to measure MR signals that can be translated into detailed maps of brain anatomy. The proton density (PD) is the number of excitable spins per unit volume. Proton density determines the maximum signal that can be obtained from a given tissue. The image contrast in PD images is not dependent on T_1 or T_2 relaxation. The signal is completely dependent on the amount of protons in the tissue. Less protons means low signal and appear as dark areas on the image whereas more protons produce a lot of signal and will be bright on the image. The T_1 time of a tissue is the time it takes for the excited spins to recover and be available for the next excitation. The T_2 time determines how quickly an MR signal fades after excitation. Protons have different relaxation rates and corresponding T_1 and T_2 time constants depending on whether they are embedded in fat, cerebrospinal fluid, white matter or grey matter ⁴. The relaxation rates of cerebrospinal fluid (CSF) are slower than those of grey matter (GM), and those of GM are slower than the relaxation rates of white matter (WM) for both T_1 and T_2 time constants (Figure 2-9). In T_1 -weighted images, tissues with a faster longitudinal relaxation rate appear bright and those with a slower relaxation rate appear dark. As an example, for any given point in time, in T_1 -weighted images WM is brighter (stronger MR signal) than GM. Grey matter signal is on the other hand is stronger than that of CSF. Therefore GM is brighter than CSF. These differences in signal intensity are exactly opposite for a T_2 -weighted image (Figure 2-10).

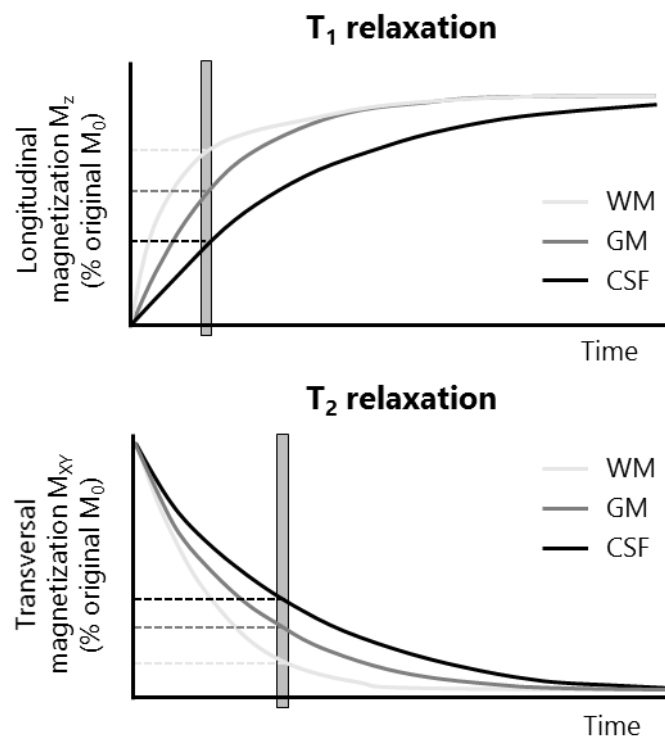


Figure 2-9. T_1 and T_2 constants in brain tissues. Relaxation curves for white matter (WM), grey matter (GM) and cerebrospinal fluid (CSF). The horizontal axis on the top graph represents repetition time (TR, a sequence parameter) in seconds, while in the bottom graph it represents echo time (TE, a sequence parameter) in milliseconds. For a given relaxation time (grey bar), the WM signal is stronger than GM and GM signal is stronger than that of CSF in T_1 -weighted images. In T_2 -weighted images, for any given transversal relaxation time (grey bar) the CSF signal is stronger than GM and GM signal is stronger than that of WM Adapted from ².

For quantitative structural brain analysis normally only T_1 -weighted and T_2 -weighted images are used. T_1 -weighted imaging offers the greatest segmentation clarity between GM, WM and CSF, and is therefore most frequently used for quantitative MRI studies of brain morphology. On the other hand, T_2 -weighted imaging may be preferably used for quantification of intracranial volume, given that these images have increased signal intensity of CSF that allows easier quantification of CSF and brain parenchyma together.

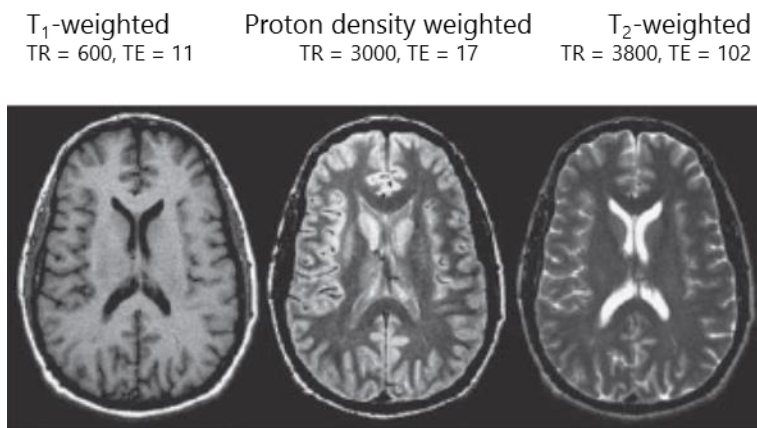


Figure 2-10. Magnetic resonance images of the same anatomical section showing a range of tissue contrasts. In the first image, cerebrospinal fluid is black, whereas in the last image it is bright. Contrast is manipulated during image acquisition by adjusting several parameters, such as the TR and the TE (times given in milliseconds), which control the sensitivity of the signal to the local tissue relaxation times T₁ and T₂ and the local proton density. In the proton density weighted image GM is brighter than CSF, despite CSF has the highest proton density. The reason is that the T₁ of CSF is too long, and for TR = 3 seconds the CSF signal is still substantially T₁-weighted. Adapted from ².

Functional MRI

Physiological principles

Functional MRI (fMRI) shows the brain in action. It is a non-invasive, modern imaging technique that allows to measure brain activity and to elucidate processes involved in specific functions of the human brain ^{7,8}. Neuronal activity consumes energy. The energy requirements of the brain are amazingly high, although the brain represents only about 2% of the body mass. Its glucose and oxygen demands account for approximately 20% of those of the whole organism. These substances are supplied to the brain by the vascular system. A similar disparity is observed for cerebral blood flow, which represents over 10% of total cardiac output ⁹. In order to overcome the energy requirements of the neurons,

the oxygen levels in activated brain areas have to be re-established. As the brain possesses anatomically distinct processing regions, with different functions, blood “rushes” to each region according as it is most active. As a consequence, cerebral blood volume and blood flow surrounding active areas increase with neuronal activity, thus increasing the delivery of oxygen and glucose – a mechanism known as neurovascular coupling^{3,9,10} (Figure 2-11). And blood is a unique, endogenous, source of physiological contrast in MRI due to its oxygenation-sensitive paramagnetic characteristics⁷. Thus, the idea behind fMRI is that changes in regional neuronal activity involved in brain functioning, such as memorizing a phrase or remembering a name, are coupled to changes in regional cerebral blood flow, oxygenation and energy metabolism in surrounding areas to supply the required glucose and oxygen^{6,8-10}. The change in cerebral blood flow with a change in neural activity during task activation is the primary signal used for mapping brain activity with fMRI⁷.

Neurovascular coupling

The vascular response to the increased energy demand is called the hemodynamic response – increased local cerebral blood flow (CBF) as well as increased cerebral blood volume (CBV). Because CBF and metabolism are coupled, the cerebral metabolic rate of oxygen extraction (CMRO₂) is also coupled with CBF. At rest, the imbalance between CBF and CMRO₂ is remarkably uniform across the brain. The arterial part of the vascular system transports oxygenated blood to the capillary bed where the chemically stored energy (oxygen) is transferred to the neurons³. The venous system transports the less oxygenated blood away from the capillary bed. When the brain is stimulated, both CBF and CMRO₂ increase. However, PET studies have shown that neuronal activity causes a smaller increase in CMRO₂ than the increase in CBF^{11,12}. That is, with neuronal

activation CBF increases much more than $CMRO_2$, causing less O_2 to be removed from each unit volume of blood - the total delivery of oxygen exceeds consumption demands. Thus, the hemodynamic response not only compensates quickly for the slightly increased oxygen extraction rate but it is so strong that the mismatch between CBF and $CMRO_2$ changes results in a substantial local increase in the capillary and venous oxygenation level ⁶.

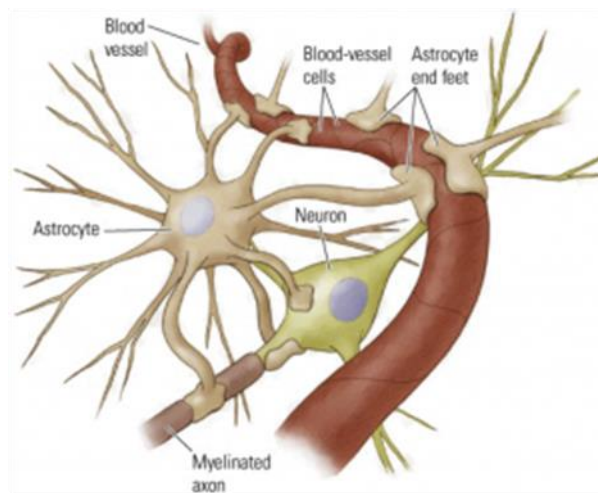


Figure 2-11. Neurovascular coupling refers to the relationship between local neuronal activity and subsequent changes in cerebral blood flow. The magnitude and spatial location of blood flow changes are tightly linked to changes in neural activity through a complex sequence of coordinated events involving neurons, glia, and vascular cells. Astrocytes seem to play an especially important role. Essentially the astrocyte detects the firing of neurons around it which causes it to signal the blood vessels around it to dilate. Reproduced from <http://jonlieffmd.com>.

Oxygen is transported in the blood via the haemoglobin molecule. If haemoglobin carries oxygen, it is called oxyhaemoglobin (HbO_2), while it is called deoxyhemoglobin (Hb) when it is devoid of oxygen. While the arterial network contains almost only oxygenated blood, the capillary bed and the venous part of the vascular system contain a mixture of oxygenated and deoxygenated blood. Given that oxygenated and deoxygenated blood have different magnetic

properties, they have different effects in the magnetic resonance signal. On the one hand, deoxyhemoglobin contains paramagnetic (strong susceptibility to magnetic field) iron and leads to magnetic field distortions and MR signal loss. On the other hand, oxyhaemoglobin contains diamagnetic (weak susceptibility to magnetic fields) oxygen-bound iron ⁷ and therefore does not distort the surrounding magnetic field.

The BOLD effect

The different magnetic properties of oxy- and deoxyhemoglobin are in the basis of the venous blood-oxygenation level dependent (BOLD) contrast, the most common method of fMRI ^{13,14}. The BOLD signal is predominantly believed to be a relative imbalance between increases in local cerebral blood flow and concurrent (albeit smaller) increases in oxygen metabolism with neuronal activity, which causes a transient drop in the deoxyhemoglobin to oxyhaemoglobin ratio (Figure 2-12).

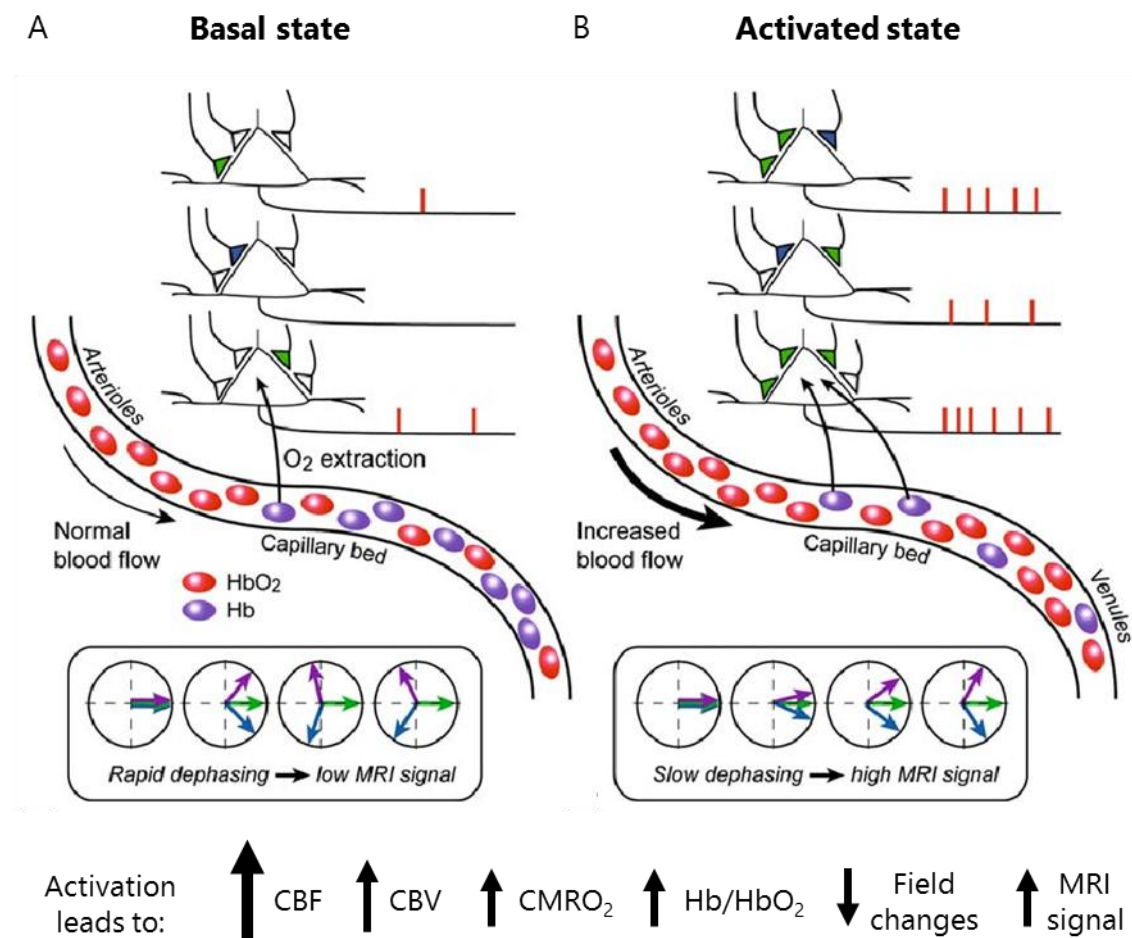


Figure 2-12. Illustration of the physiological changes leading to fMRI data. (A) If a cortical region is in baseline mode, neural activity – including synaptic signal integration and spike generation – is low (upper part). Cerebral blood flow (CBF) is at a basal level. A constant oxygen extraction rate fuelling neural activity leads to a fixed deoxyhemoglobin (Hb) to oxyhaemoglobin (HbO₂) ratio in the capillary bed and venules. Since Hb is paramagnetic, it distorts the magnetic field. The Hb-related magnetic field inhomogeneities lead to rapid dephasing of excited spins resulting in a low MRI signal level (lower part). (B) If the cortical region is activated, synaptic signal integration and spiking activity increases, leading to an increased oxygen extraction rate (upper part). CBF strongly increases delivering oxygen beyond local need, which essentially flushes Hb away from the capillary bed (middle part). Since HbO₂ does not substantially distort the homogeneity of the local magnetic field, excited spins dephase slower than in the baseline state (lower part) resulting in an enhanced MRI signal (BOLD effect). Adapted from ³.

More specifically, during the hemodynamic response (oversupply of oxygenated blood), the oxy- to deoxyhemoglobin ratio increases locally, resulting in a more homogeneous local magnetic field. As follows from the basic physical principles of MRI, excited spins dephase slower in a more homogeneous magnetic field leading to a stronger measured MRI signal in the activated state of the brain when compared to a resting state ^{3,6} (Figure 2-12). The BOLD effect, thus, measures increased neuronal activity indirectly because the time it takes for dynamic changes to occur in blood flow is much longer than that for neurons to fire off their electrochemical messages.

The BOLD imaging technique is used widely because of its high sensitivity and easy implementation. Because the BOLD signal is dependent on various anatomical, physiological, and imaging parameters ¹⁵ its interpretation with respect to physiological parameters and neuronal origin is fairly complicated and still not fully understood ¹⁶⁻¹⁹. However, BOLD constitutes the most common functional imaging method applied in human neuroscience. Thus, inference of alterations of neuronal activities by mapping local changes in cerebral blood flow (BOLD signal) requires the understanding of the relationship between neuronal activity and the hemodynamic response, the so called neurovascular coupling (Figure 2-13A).

The BOLD hemodynamic response

The evoked fMRI signal, is delayed with respect to the fast occurring neuronal activity. The time course of the slow and delayed coupling between neuronal and vascular activity follows a typical hemodynamic response (Figure 2-13B).

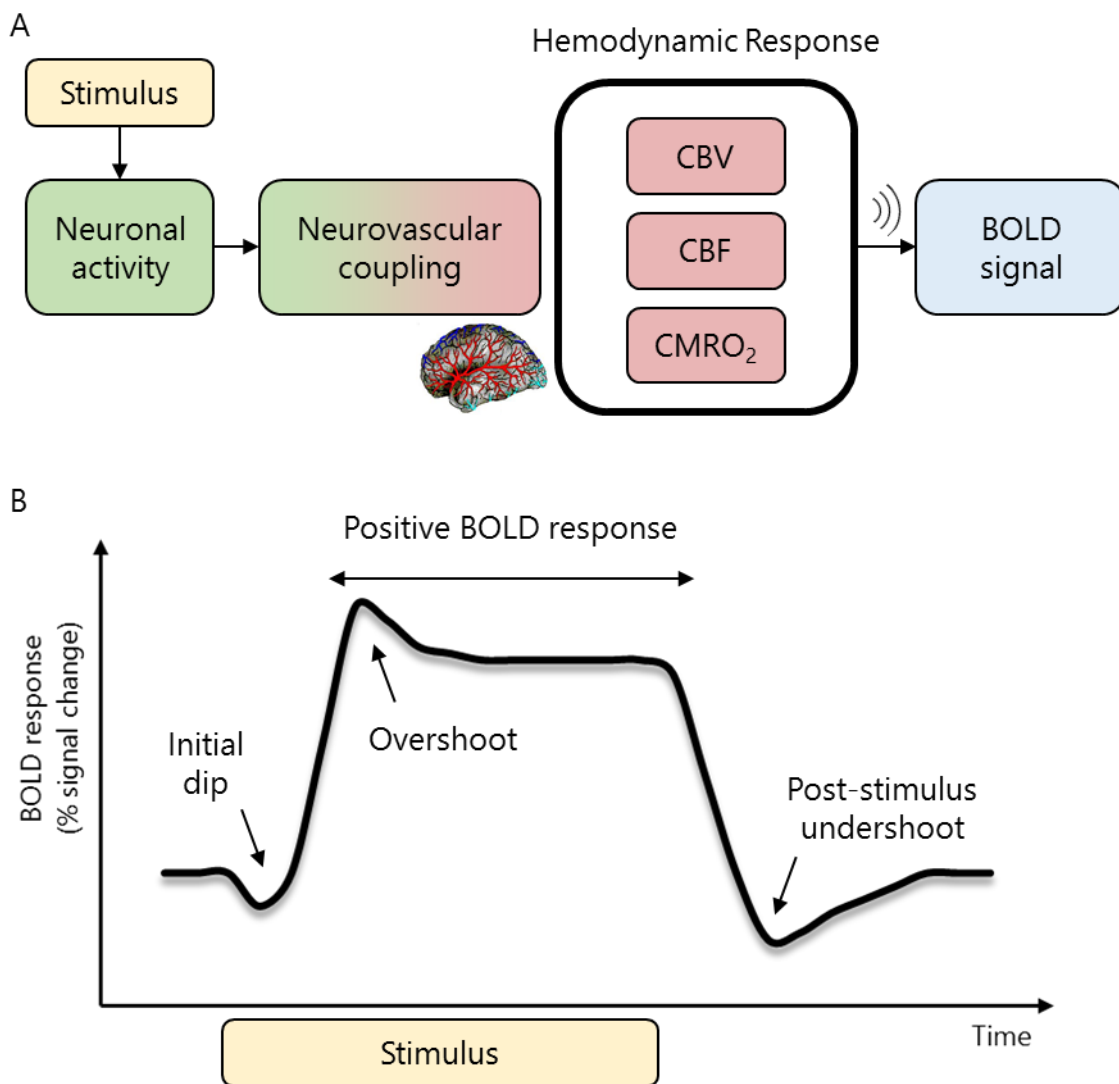


Figure 2-13. (A) From neuronal activity to BOLD MRI signal. The BOLD signal reflects the ratio of diamagnetic oxyhemoglobin to paramagnetic deoxyhemoglobin. Neuronal activity alters this ratio by influencing several factors including cerebral blood flow (CBF), cerebral blood volume (CBV) and cerebral blood oxygen consumption (CMRO₂). (B) Idealized time course of the BOLD hemodynamic response to a long stimulus. After a long stimulation event (there is an initial dip, not reliably measured in human fMRI studies though) the signal often rises initially to a higher value (overshoot) than the subsequently reached plateau. When the stimulus is turned off, the signal often falls below the baseline signal level (undershoot), which is then approached slowly. Adapted from ^{3,79}

A local increase of neuronal activity immediately leads to an increased oxygen extraction rate in the capillary bed and, thus, in an increase in the relative

concentration of deoxyhemoglobin³. This fast response to increased neuronal activity is described as the initial dip^{20,21}. After a short time the increased local neuronal activity also leads to a strong increase in local blood flow, overcompensating for the amount of oxygen being extracted^{2,22}. We thus observe a positive BOLD response that starts to rise after 2–3 sec (oversupply phase). The maximal amplitude of the hemodynamic response typically occur about 5–6 sec following the stimuli presentation onset and returns to baseline 10 sec later. If the neuronal activity is extended in time, the peak may be similarly extended into a plateau, typically with slightly lower amplitude than the peak (overshoot). After cessation of the stimulus and before the BOLD signal returns to the pre-stimulus baseline level occurs an undershoot, most probably due to an accumulation of deoxyhemoglobin in the vessels. At this time, the cerebral blood flow and the oxygen extraction rate have already returned to baseline. However the elastic properties of the dilated venules will require many seconds until baseline size is reached. Thus the cerebral blood volume takes more time to return to baseline. In this time more deoxyhemoglobin will accumulate reducing BOLD signal below pre-stimulus baseline level. If the stimulus is short in duration (less than one second), the complete return of the hemodynamic response profile to baseline happens about 20 s after stimulation. These changes in fMRI BOLD signal are delayed with respect to the fast occurring neuronal activity. Despite this sluggish response, the latency of response onsets appear to reflect quite precisely neuronal onset times²³. It is important to note that in practice this profile of the BOLD hemodynamic response may have different shapes depending on the design of the fMRI experiment, the stimulus conditions and/or the subjects' variability²⁴ including the presence of co-morbidities such as diabetes²⁵.

Neuronal activity as a function of the BOLD hemodynamic response

Functional magnetic resonance imaging is widely used to investigate human brain function non-invasively. As described before, the BOLD fMRI signal is a consequence of the hemodynamic response of the vascular system to neuronal activity. In fact, the fMRI signal can only measure hemodynamic changes in the cerebral vasculature, such as blood flow, blood volume or intravascular magnetic susceptibility. It is thus an indirect measurement of brain function as the exact relationship between this kind of signal and the neural activity is still under study^{17,18,22,26,27}. For the sake of simplicity, the neurovascular coupling is ubiquitously approximated by a linear transform model in BOLD fMRI experiments. The linear characterization of this transformation of neuronal activity to BOLD signal implies, e.g. that a doubling in the amplitude of neuronal activity results in a doubling of the amplitude of the BOLD signal, and so on⁶. Only in this way, it is possible to make an inverse inference from BOLD signal measured into neuronal activity.

The response to a very short stimulus (less than one second) is called the impulse response function or, in the context of fMRI, the BOLD hemodynamic response function (HRF). The HRF is very consistent within a subject and can be measured empirically by investigating the BOLD signal in response to brief periods of neuronal activity in known cortical areas (e.g. neuronal activity in primary motor cortex in response to button press). However, it varies significantly across subjects^{24,28}.

The function that is most commonly used by neuroscience community is a sum of two gamma functions, with parameters defining the onset and dispersion of the response peak²⁹ (Figure 2-14). This approach makes it possible to model both the peak of the response and the undershoot. The expected initial dip (Figure 2-13) has not been reliably detected in standard human fMRI measurements thus is not included in the standard convolution kernels. Given the shape of the HRF

one can then predict the expected time course of BOLD signal in response to any arbitrary long neuronal activity pattern.

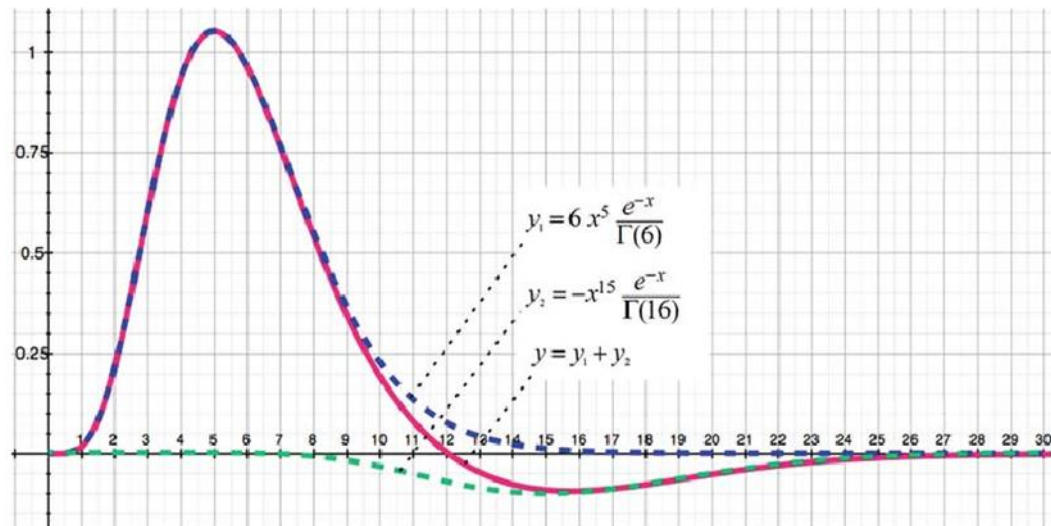


Figure 2-14. A two-gamma function enables modelling of typical hemodynamic impulse responses. One gamma function models the peak ($\tau = 6$) and dispersion ($\sigma = 5$) of the positive BOLD response while the second gamma function models the peak and dispersion ($\tau = 16$ and $\sigma = 15$, respectively) of the undershoot response. Parameter A scales the amplitudes of the individual gamma functions ($A = 6$ for the positive response and $A = -1$ for the undershoot).

There are several methods of analyzing BOLD fMRI data to infer neuronal activity related to stimulation protocols from an *a priori* defined HRF. The more commonly used by neuroscientists is a univariate technique in which a statistical model is applied to each voxel independently within a BOLD fMRI dataset. The creation of the model is of particular importance for the analysis and subsequent interpretation of the results. First, the stimulation conditions (manipulated in the experimental protocol) are transformed into predicted neuronal input time courses, i.e. according to the timing of each experimental stimulation trial one can assume that the neurons in cortical areas responsible for processing that stimulus

will be active as long as the stimulus is being presented – the neuronal response to a single trial is represented as a box-car function. For example, a simple blocked experimental design might be predicted to produce a uniformly greater amount of bulk neuronal activity during an experimental condition as compared to a control condition. The expected BOLD fMRI response is then obtained by convolving the input time course (the stimulation box-car time course) with the BOLD HRF^{30,31}. As was mentioned previously, knowledge of the HRF is sufficient to predict the BOLD fMRI signal that will result from any arbitrary pattern of neural activity through the mathematical process of convolution⁶.

In practice, actually these models do not fit a particular stimulation trial rather the combination of all the trials of each condition experimental condition within the time of the experiment, which is called a predictor. This way one gains greater consistency to slightly different patterns of response across trials of the same stimulation condition. The resulting statistical model, composed of predictors for all conditions of interest in the experimental protocol, is then used to evaluate the fMRI data from each voxel within the brain. The resulting weights upon the predictors (termed beta values) can be evaluated alone or in combinations using t and F statistics. These weights represent an indirect measurement of neuronal activity.

Note that the linear model is reasonably valid only for stimuli with sufficient temporal separation, otherwise there can be non-linear interactions^{29,32}. Furthermore, the convolution approach requires the valid specification of the time course of assumed neuronal response profiles. However, in high level cortical areas, e.g. frontal areas involved in working memory, the neuronal response profile might differ substantially with respect to stimulus timing. In case it is difficult to specify proper “neuronal” input response profiles, a more general approach should be used, e.g. deconvolution analysis (described later, see²⁵). Nonetheless, assuming that neuronal responses are correctly specified, it appears

reasonable to use the same HRF for all brain regions to predict expected BOLD signal time courses since neurovascular coupling should be similar in different brain areas.

Structure of fMRI data

A major goal of fMRI measurements is the localization of the neural correlates of sensory, motor and cognitive processes. Another major goal of fMRI measurements is the characterization of the response profile in various regions-of-interest (ROIs) by retrieving plots of averaged signal time courses for different experimental conditions.

In order to better understand different fMRI preprocessing and analysis steps, we must understand key concepts of fMRI data.

Designs of fMRI experiments

During fMRI data acquisition, subjects are enrolled in a task (e.g. sensory, motor, or cognitive) to study a specific brain function. Paradigm choices relate to the problem of isolating the task or process for which a meaningful brain map is intended. Importantly fMRI data does not provide an absolute signal of brain activity rather proton density and T_2 tissue contrast varying across brain regions. BOLD related signal fluctuations, thus, have neither a defined origin nor a unit³. Signal strengths thus cannot be interpreted absolutely but have to be assessed relative to the signal strength in other conditions. This generally involves a comparison between the activity patterns elicited by at least two different experimental conditions: a condition of interest, and a control condition. The comparison between conditions of interest or between a condition of interest and the control condition is called a contrast and constitutes the basis of most fMRI

studies. As BOLD fMRI experiments by necessity include multiple task conditions, several ways of ordering the presentation of these conditions exist. Two main formats can be used in the design of fMRI experiments: *block* design and *event-related* design³³.

In the block design several trials are clustered in blocks (one block lasts on average 16 to 60 seconds), each of which contains only trials of the same condition. Blocked designs are suited for investigation of whether activity of a given voxel (or region) changes in response to the experimental manipulation. Blocked designs thus exhibit superior detection power and are less sensitive to differences in the shape and timing of the hemodynamic models because the statistical analysis of such block designs compares the mean activity obtained in the different experimental blocks³⁴. On the other hand, blocked designs have the obvious difficulty that the subject can anticipate trial types.

In turn, in event-related designs the individual trials of different conditions are presented in a random sequence instead of being sequentially presented in a block^{35,36}. Event-related designs offer an important advantage, the possibility to present stimuli in a randomized order, which avoids adaptation or anticipation and may be critical in cognitive tasks. In this type of design, each event is separated from the subsequent event by a period named intertrial interval (ITI). If the ITI is long enough to allow the complete rise and fall of the hemodynamic response to return to baseline, then the BOLD responses to each of the events do not overlap. This is called a slow event-related design. In contrast, designs with short temporal intervals between trials are called rapid event-related designs. While the measured response of rapid event-related designs will contain a combination of overlapping responses from closely spaced trials, condition specific event-related time courses can be isolated using deconvolution analysis^{37,38}. Event-related designs are generally better suited for estimation of the time course of the hemodynamic response in response to the experimental

stimulation, as it presents short condition events, and thus does not require an *a priori* model of the HRF. Such information is especially used when making inferences about the relative timing of neuronal activity, about processes occurring in different parts of the trial and about functional connectivity³⁹, although classic event related designs are not well suited for functional connectivity analyses in fMRI. In general, block and event-related designs can be statistically analyzed using the same mathematical principles.

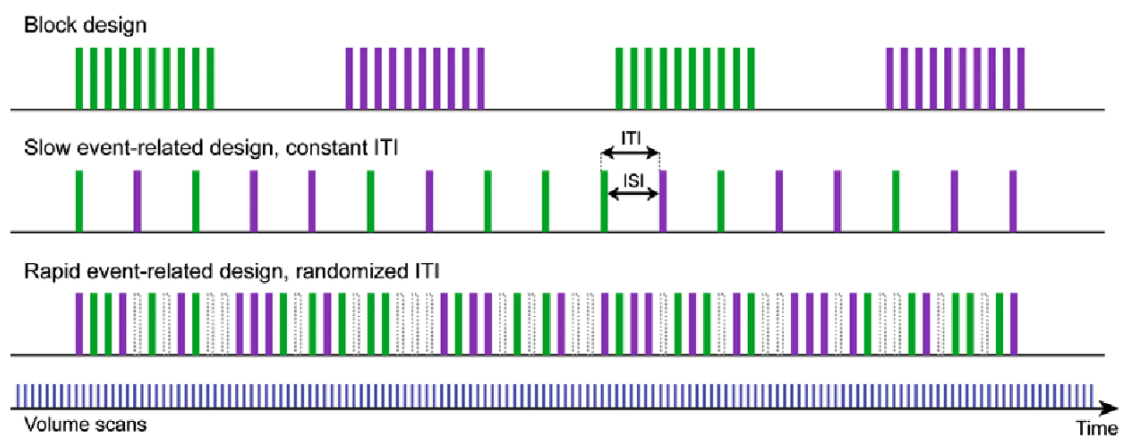


Figure 2-15. Schematic representation of block and event-related designs. In a block design (upper row), trials (events) belonging to the same condition are grouped together and are separated by a baseline block. In slow event-related designs, trials of different conditions appear in randomized order and are spaced sufficiently far apart to avoid largely overlapping BOLD responses. In rapid event-related designs, stimuli are closely spaced leading to substantial overlap of evoked fMRI responses. If ITIs are randomized, the evoked responses can be decomposed into condition-specific response profiles by deconvolution analysis. Reproduced from³.

Preprocessing of functional data

In a perfect world, BOLD fMRI images would be acquired instantaneously from a stationary brain of uniform shape. Unfortunately, this is not the case, and a

number of processing steps must be performed prior to the statistical analysis of fMRI data. During an fMRI experiment usually each subject undergoes a single experimental session. Each session includes collection of anatomical images and one or more functional runs, which consist of time series of three-dimensional (3-D) functional volumes of data. One run is thus a four-dimensional (4-D) volume spanning space and time information. The sequential 3-D volumes are acquired in different points in time and the MR sequence parameter time of repetition (TR – time interval between successive excitation pulses) is the time it takes to acquire an entire brain volume. The volume in turn is made up of multiple slices, as described earlier. Slices are acquired at different points in time within the TR and contain thousands of voxels that together form an image of the brain. During data acquisition subjects may move their heads. Thus, an important preprocessing step is to perform head motion correction, by adjusting translation and rotation parameters to realign the image of the brain obtained at each point in time back to the first image acquired at the start of the scanning session. In order to reduce other artifact and noise-related components in fMRI signal, due to magnetic field inhomogeneities or subject's movement, a series of preprocessing steps is typically performed in time courses of individual voxels prior to statistical data analysis. The most essential steps of these preprocessing operations include: slice scan timing correction, linear and non-linear detrending and spatial and temporal filtering of the data.

Statistical analysis of fMRI data

Statistical data analysis aims at identifying those brain regions exhibiting increased or decreased responses in specific experimental conditions as compared to other (e.g. rest) conditions. The obtained statistical values, one for

each voxel, form a three-dimensional statistical map representing an indirect measure of neuronal activation during each stimulation condition.

The General Linear Model

In standard fMRI analyses the assessment of brain responses is performed independently for the time course of each voxel. This is the case of the core tool for fMRI data analysis - the General Linear Model (GLM). A schematic representation of a GLM is presented in Figure 2-16. The GLM aims to explain or predict the variation of a dependent variable in terms of a linear combination (weighted sum) of several reference functions, the predictors. The dependent variable corresponds to the observed fMRI time course of a voxel and the reference functions correspond to time courses of expected (idealized) fMRI responses for different conditions of the experimental paradigm, determined by convolution of the HRF with box-car functions. By applying the least squares method each predictor time course gets an associated weight (beta value), quantifying its potential contribution in explaining the voxel time course⁴⁰⁻⁴². The GLM procedure estimates the beta values by minimizing the sum of squared error values. While the exact interpretation of beta values depends on the details of the design matrix, a large positive (negative) beta weight typically indicates that the voxel exhibits strong activation (deactivation) during the modelled experimental condition relative to baseline³.

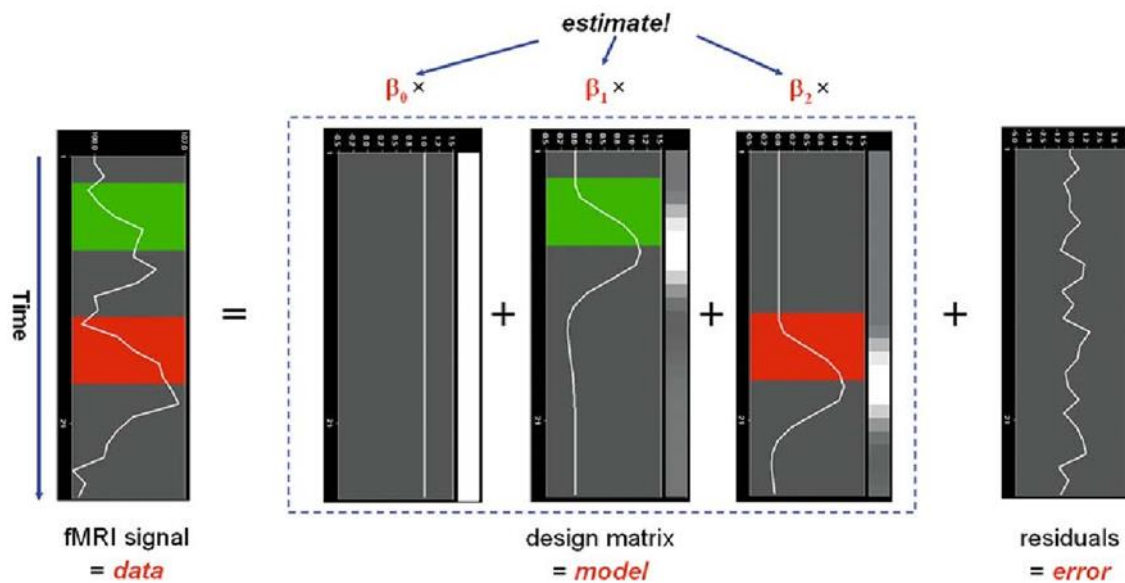


Figure 2-16. Graphical display of a GLM. Time is running from top to bottom. Left side shows observed voxel time course (data). In this example the model (design matrix) consists of three predictors, the constant and two main predictors (middle part). Filled green and red rectangles depict stimulation time while the white curves depict expected BOLD responses. Beta values have to be estimated (top) to scale the expected responses (predictors) in such a way that their weighted sum predicts the data values as good as possible (by the least squares method). Unexplained fluctuations (residuals, error) are shown on the right side. Reproduced from ³.

Comparisons between conditions can be formulated as contrasts, which are linear combinations of beta values corresponding to null hypotheses. To test, for example, whether activation in a single condition deviates significantly from baseline, the null hypothesis would be $H_0: b_1 = 0$. To test whether activation in condition 1 is significantly different from activation in condition 2, the null hypothesis would state that the beta values of the two conditions would not differ, i.e. $H_0: b_1 = b_2$ or $H_0: (+1) b_1 + (-1) b_2 = 0$. The values used to multiply the respective beta values are often written as a contrast vector. The result is a three-dimensional statistical map in which every voxel in the brain contains a corresponding statistical value for the contrast of the weights of conditions of

interest. The final step of analysis involves assigning a level of statistical significance to those values, after correcting for the multiple comparisons problem because of testing the statistical hypotheses massively in many voxels in the brain. This allows visualizing anatomical information in large parts of the brain while statistical information is shown only in those regions exhibiting significant signal modulations³.

Both blocked and event-related designs can be analyzed with standard GLM after convolution of box-car neuronal inputs with the HRF. On the other hand, the shape of the HRF (subject to variability in different brain areas within and across subjects) can be estimated in a condition-related fashion by modelling each trial with a set of impulse functions. This approach is called a deconvolution analysis and allows estimating any response shape after a short stimulus. Even in rapid event-related designs, despite overlapping responses, fitting such a deconvolution GLM recovers the underlying condition-specific response profiles^{3,43,44}. A concrete implementation of this procedure is presented in Chapter 3 and Chapter 4.

Deconvolution analysis

Both blocked and event-related designs can be analyzed with standard GLM after convolution of box-car neuronal inputs with the hemodynamic response function (HRF). In experiments with relatively long blocks of stimulation the amplitude (beta value) of response to each condition can be well estimated. However, in event-related experiments, because of the intrinsic hemodynamic properties of neurovascular response (which is the origin of the fMRI BOLD signal) the results can be distorted. It is mathematically feasible to estimate condition amplitudes with standard convolution GLM in rapid event-related designs, but the procedure might lead to non-optimal fit of the model due to overlapping responses to

different conditions, in case conditions are presented within shorter times than the span time of the complete HRF (which is not necessarily critical, provided linearity holds). Furthermore, distorted results might also be obtained if the assumed standard BOLD response shape - HRF - is not verified to be true. Because a single estimate of the hemodynamic response is used to analyze the data from different subjects, this approach assumes that any variability that exists between subjects in hemodynamic response is minor. If this assumption is not true, then the general approach of using a standard HRF to analyze BOLD fMRI data from different subjects will result in suboptimal power and perhaps invalid inference²⁴. There is the possibility to estimate the true hemodynamic response function for each stimulation condition from the data. Deconvolution analysis is a general approach to estimate condition-related response profiles using a flexible and interpretable set of functions³. It can be easily implemented as a GLM by defining an appropriate design matrix modelling each time point after stimulus onset by its own predictor (delta or "stick" functions). In order to capture the BOLD response for short events, 20 seconds are typically modelled after stimulus onset. Despite overlapping responses, fitting such a GLM "recovers" the underlying condition-specific response profiles in a time series of beta values, as shown in Figure 2-17.

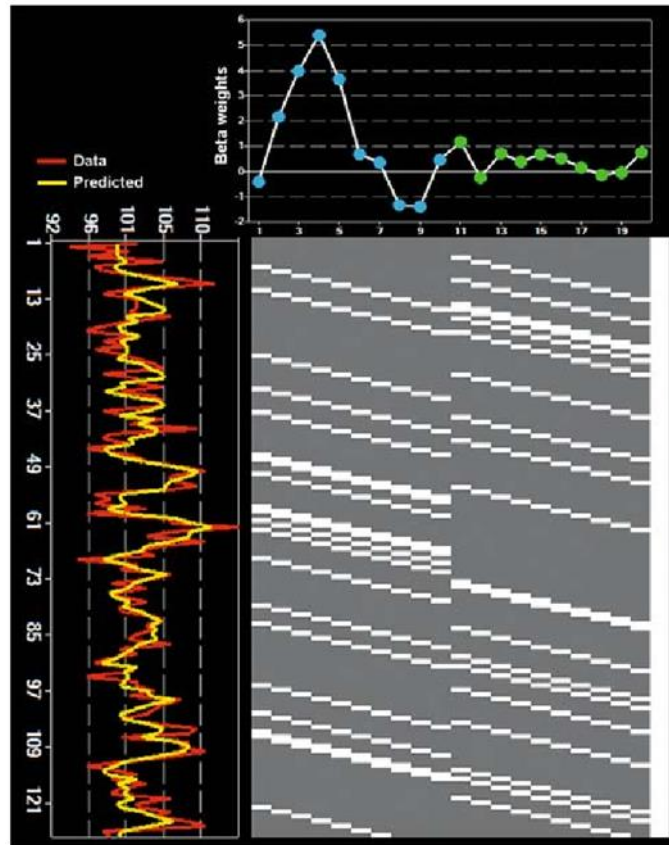


Figure 2-17. Deconvolution analysis of a rapid event-related design. Time runs from top to bottom, design matrix depicted in graphical view. Beta values are plotted horizontally at positions corresponding to the respective predictor. Each condition is modeled with 10 “stick” predictors making it possible to estimate the time course of condition-related responses as if stimuli were presented in a slow event-related design. Beta values may be compared within and across conditions.

The deconvolution model is very flexible allowing any response shape to be captured. This implies, however, that nonsense event-related time courses will also be detected spuriously. It thus is more appropriate to apply the deconvolution approach to a set of regions-of-interest (ROIs) identified previously on statistical maps obtained with a standard GLM or in a separate localizer experiment. In Chapter 3 we provide an important practical implementation of this approach to fMRI analysis. We employed ROI-based deconvolution analysis of fMRI data in healthy subjects and diabetic patients, a

population prone to cerebrovascular disease, in order to probe neurovascular coupling as empirically extracted from fMRI data²⁵. Experimental procedures and implementation details are potentially useful for subsequent studies.

Data-driven analysis methods

MRI data, either functional or structural, is intrinsically very rich. It might happen that unnoticed interesting spatio-temporal relationships exist in the data, when analyzed only with standard hypothesis-driven methods. Data-driven methods on the other hand are exploratory in nature, allowing to extract interesting information automatically from the data without the need to explicitly specify statistical models in advance. One popular data-driven method, independent component analysis – ICA, has been successfully applied to perceptual decision tasks in cognitive neuroscience⁴⁵ and clinical investigation in schizophrenia⁴⁶. Another approach with great potential is the application of multivariate pattern analyses to MRI data, both structural and functional, which offers the possibility of localizing spatially distributed effects. These might be too weak to be discovered by single voxel analysis, but its joint effect might be significant^{47–49}.

Multivariate pattern analysis – Support Vector Machines

In contrast to the standard statistical analysis analyzing data voxel-wise, data-driven multivariate methods enable the identification of distributed discriminative patterns of activation (in the case of functional MRI) or brain tissue (in the case of structural MRI) in the absence of *a priori* hypotheses. One very useful approach that has been subject of growing interest in the last years is the use of machine learning classifiers. A growing number of studies has shown that machine learning classifiers can be successfully used to extract exciting new information from

neuroimaging data⁴⁸. A classifier is built based on a set of rules to determine the class, either a binary or multiclass problem, of different unknown (instances of) categories based on their discriminative characteristics, which are called features^{42,48}. Furthermore, much of these methods are able to provide a measure of the importance (or weight) of each feature for the decision function and consequently for the classification task. If the decision function is linear, this means we are working with a linear classifier. One very popular instance of linear classifiers is a Support Vector Machine – SVM⁵⁰⁻⁵².

The idea of the SVM algorithm is to define a decision boundary that separates the objects from different classes based on their descriptive features, as generally as possible. In other words, the algorithm determines the maximal separation margin, which is the distance between the decision boundary and the closest objects (actually data points) of each class. These are called the support vectors and that's why the classifier is called Support Vector Machine⁵³. The generalization goal is to allow for the best possible prediction of new unseen instances of the same kind of data. A graphical representation of a binary SVM is shown in Figure 2-18.

Let us consider a classification task of a dataset of objects, in which an object can be seen as an array of features that describes it. Each object belongs to a certain class. Part of the dataset is given to the SVM, along with the labels' (classes to which every object belongs to) assignment. This is called the training set, in which the SVM will learn the decision boundary between (two or more) classes. Then, after the learning phase the remaining objects are given to the SVM without the labels' assignment. This is called the test set and the objective of the trained SVM is now to predict the label of each new object and classify it, by applying the decision function^{54,55}.

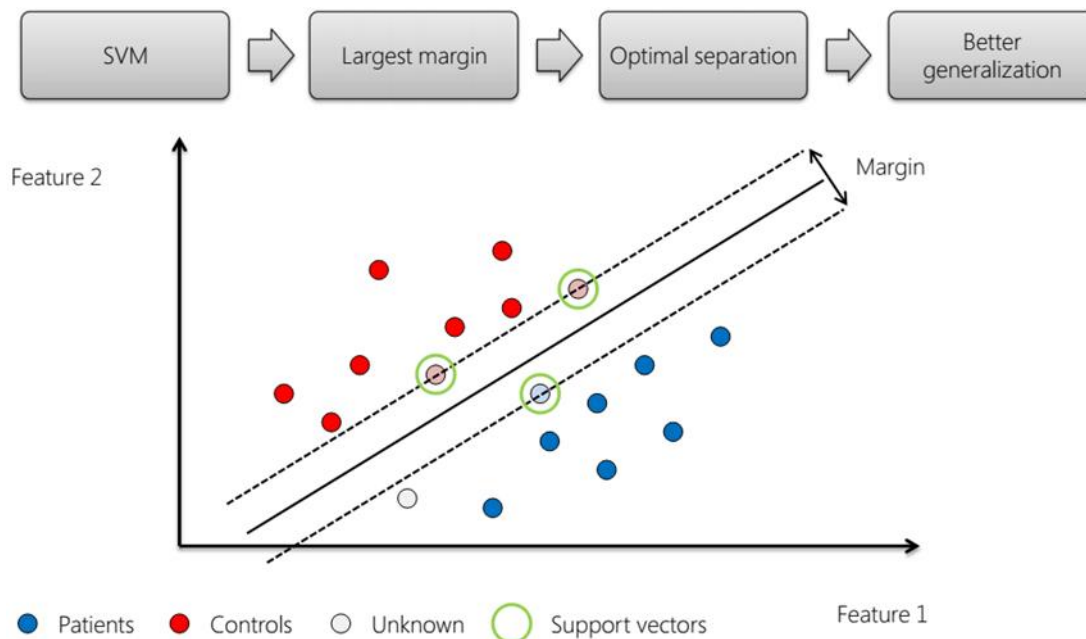


Figure 2-18. Schematic representation of a binary SVM classifier. In this example two groups of subjects (two classes, patients and controls) can be separated based in two distinct features of each group (feature 1 and feature 2). The support vectors mark the largest margin with the optimal separation between groups. The largest margin ensures the maximal generalization capacity of the classifier regarding new data (unknown subject). If more features are available a higher dimensional space is used.

Real life problems are usually highly non-linear and therefore the definition of a decision boundary in the original input space is not an easy task. To overcome this issue, decision hyperplanes are determined in a high-dimensional feature space and a unique global optimal separation solution can be found either for linear or non-linear boundaries without much computational costs, using the so called "kernel trick", as represented in Figure 2-19 ⁴⁸.

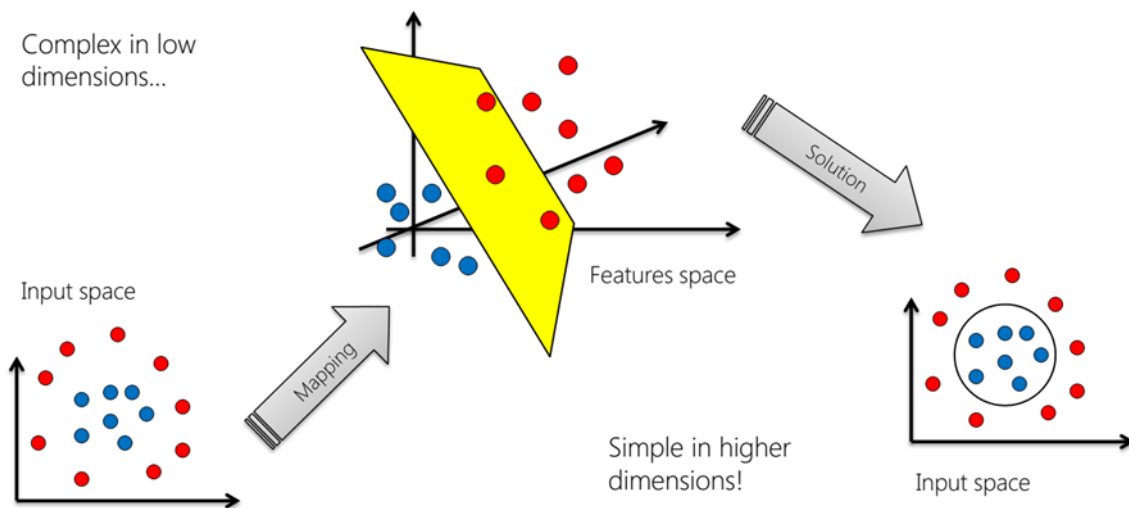


Figure 2-19. The kernel trick. A great advantage of the SVM is that it allows to find a linear boundary even when the classification problem is too complex to be solved in the original input space. By using the so called “kernel trick” the SVM algorithm maps the input feature space into a higher-dimensional space, in which the decision boundary is linear – it is called hyperplane in case of more than 3 dimensions. Then, it returns to the original input space and draws the solution of the classification problem that was learned.

Currently in brain imaging, SVM is the most frequently implemented classifier⁴⁸. The SVMs have been early on used in computational learning theory⁵⁰ and are now used with many applications in biomedical statistical pattern classification in cognitive neuroscience^{56–59} or in the context of clinical diagnosis/treatment predictions^{55,60–63}. The size of the available data is typically limited. To optimize the data exploration, to increase the size of the test set and to avoid overfitting (loss of generalization ability of the model), cross-validation is used, in particular the leave-one-out cross validation scheme⁴⁸. The idea is to divide the original dataset containing N data points of each class into N subsets containing one single data point of each class and then train the classifier in $N-1$ subsets and test it in the remaining unseen set. This is repeated N times and the classification results are averaged to obtain performance measures as accuracy, sensitivity and

specificity. To evaluate the statistical significance of the classification procedure a common used method is permutation testing^{64–66}.

Permutation testing consists in determining the probability of obtaining the observed classification results if the null hypothesis, that there is no information about the label in the data, was true. The null distribution is achieved by repeating many times the same classification scheme with a random shuffling of the labels each time. Over many repetitions, this yields a sample of classification results under the null hypothesis that there is no class information in the data^{67,68}. A fundamental question that arises is the normality of the null distribution. Although the permutation distribution should behave in accord with the central limit theorem (CLT), this might not be true in all circumstances. A parallel collaboration work on this topic evaluated the accordance level of permutation distributions of classification accuracies to normality expected under the CLT. A simulation study has been carried out using fMRI data that were collected while human subjects responded to visual stimulation paradigms⁶⁹.

In a recent paper we describe a contribution for the understanding and practical implementation of a data-driven (non-hypothesis constrained) approach to MRI data. We used SVMs to directly distinguish the structural MR images of healthy controls from brain scans of patients with Neurofibromatosis Type 1⁴⁹. Furthermore we compared the method with a standard model-driven approach – Voxel Based Morphometry. This SVM approach is a proof of concept, useful for subsequent studies with fMRI data.

Connectivity analysis

The multivariate approach to data analysis, by its nature, allows these methods to detect functionally connected networks of brain areas. There is an increasing interest and development of mathematical tools for the analysis of brain

connectivity in recent years. We assist to a shift in emphasis from voxel-wise functional segregation (activation) of brain regions to distributed functional integration of brain areas ⁷⁰. Many approaches have been used to model the interaction between spatially remote brain regions more explicitly. From simple correlation of signal time courses from two regions (e.g. linear correlation coefficient) describing statistical dependencies between data – functional connectivity – to mechanistic models of directed interactions that generated those dependencies – effective connectivity ⁷¹.

Functional connectivity can be calculated condition-wise, i.e. separately for different experimental conditions, in a way that it allows to investigate the modulation of activity correlation of two brain regions in different cognitive contexts ^{3,72}.

The directed effective connections are often symbolized by arrows connecting boxes each representing a different brain area. Thus effective connectivity describes the causal influences that a brain area exerts over another ⁷¹. An interesting data-driven approach to effective connectivity modelling is provided by methods based on the concept of Granger causality ⁷³. The great advantage of this method is that it is flexible enough to automatically estimate measures of effective connectivity in the whole-brain for reference voxel or region of interest without the specification of explicit connectivity models ⁷⁴⁻⁷⁶.

References

1. Nobelprize.org. The Nobel Prize in Physiology or Medicine 2003. at <http://www.nobelprize.org/nobel_prizes/medicine/laureates/2003/>
2. Buxton, R. B. *An Introduction to Functional Magnetic Resonance Imaging: Principles and Techniques*. (Cambridge University Press, 2002).
3. Goebel, R. in *Clinical Functional MRI* 9–51 (2007).
4. Kandel, E. R., Schwartz, J. H., Jessel, T. M., Siegelbaum, S. A. & Hudspeth, A. *Principles of Neural Science*. (McGraw Hill, 2013).
5. Schild, H. H. *MRI made easy*. (Schering AG, 1990).
6. Faro, S. H. & Mohamed, F. B. *BOLD fMRI: A Guide to Functional Imaging for Neuroscientists*. (Springer, 2010).
7. Bandettini, P. A., Wong, E. C., Hinks, R. S., Tikofsky, R. S. & Hyde, J. S. Time course EPI of human brain function during task activation. *Magn. Reson. Med.* **25**, (1992).
8. Kwong, K. K. *et al.* Dynamic magnetic resonance imaging of human brain activity during primary sensory stimulation. *Proc. Natl. Acad. Sci. U. S. A.* **89**, (1992).
9. Magistretti, P. J. Neuron-glia metabolic coupling and plasticity. *Exp. Physiol.* **96**, (2011).
10. Haydon, P. G. & Carmignoto, G. Astrocyte control of synaptic transmission and neurovascular coupling. *Physiol. Rev.* **86**, (2006).
11. Fox, P. T., Raichle, M. E., Mintun, M. A. & Dence, C. Nonoxidative glucose consumption during focal physiologic neural activity. *Science* **241**, (1988).
12. Fox, P. T. & Raichle, M. E. Focal physiological uncoupling of cerebral blood flow and oxidative metabolism during somatosensory stimulation in human subjects. *Proc. Natl. Acad. Sci. U. S. A.* **83**, (1986).
13. Ogawa, S., Lee, T., Kay, A. & Tank, D. Brain magnetic resonance imaging with contrast dependent on blood oxygenation. *Proc. Natl. Acad. Sci. U. S. A.* **87**, 9868–9872 (1990).
14. Ogawa, S., Lee, T.-M., Nayak, A. S. & Glynn, P. Oxygenation-sensitive contrast in magnetic resonance image of rodent brain at high magnetic fields. *Magn. Reson. Med.* **14**, 68–78 (1990).
15. Ogawa, S., Menon, R. S., Kim, S.-G. & Ugurbil, K. On the characteristics of functional magnetic resonance imaging of the brain. *Annu. Rev. Biophys. Biomol. Struct.* **27**, (1998).
16. Arthurs, O. J. & Boniface, S. How well do we understand the neural origin of the fMRI BOLD signal? *Trends Neurosci.* **2336**, (2002).
17. Logothetis, N. K. The neural basis of the blood-oxygen-level-dependent functional

- magnetic resonance imaging signal. *Philos. Trans. R. Soc. Lond. B. Biol. Sci.* **357**, 1003–1037 (2002).
18. Logothetis, N. K. & Wandell, B. A. Interpreting the BOLD signal. *Annu. Rev. Physiol.* **66**, 735–769 (2004).
 19. Logothetis, N. K. What we can do and what we cannot do with fMRI. *Nature* **453**, (2008).
 20. Buxton, R. B., Uludağ, K., Dubowitz, D. J. & Liu, T. T. Modeling the hemodynamic response to brain activation. *Neuroimage* **23**, (2004).
 21. Hu, X. & Yacoub, E. The story of the initial dip in fMRI. *Neuroimage* **62**, 1103–1108 (2012).
 22. Logothetis, N. K., Pauls, J., Augath, M., Trinath, T. & Oeltermann, A. Neurophysiological investigation of the basis of the fMRI signal. *Nature* **412**, 150–7 (2001).
 23. Menon, R. S. & Kim, S. G. Spatial and temporal limits in cognitive neuroimaging with fMRI. *Trends Cogn. Sci.* **3**, (1999).
 24. Aguirre, G., Zarahn, E. & D'Esposito, M. The variability of human, BOLD hemodynamic responses. *Neuroimage* **8**, 360–369 (1998).
 25. Duarte, J. V *et al.* Early disrupted neurovascular coupling and changed event level hemodynamic response function in type 2 diabetes: an fMRI study. *J. Cereb. Blood Flow Metab.* **35**, 1671–1680 (2015).
 26. Lippert, M. T., Steudel, T., Ohl, F., Logothetis, N. K. & Kayser, C. Coupling of neural activity and fMRI-BOLD in the motion area MT. *Magn. Reson. Imaging* **28**, 1087–94 (2010).
 27. Watanabe, M., Bartels, A., Macke, J. H., Murayama, Y. & Logothetis, N. K. Temporal jitter of the BOLD signal reveals a reliable initial dip and improved spatial resolution. *Curr. Biol.* **23**, 2146–2150 (2013).
 28. Handwerker, D. A., Ollinger, J. M. & D'Esposito, M. Variation of BOLD hemodynamic responses across subjects and brain regions and their effects on statistical analyses. *Neuroimage* **21**, 1639–1651 (2004).
 29. Friston, K. J., Josephs, O., Rees, G. & Turner, R. Nonlinear event-related responses in fMRI. *Magn. Reson. Med.* **39**, 41–52 (1998).
 30. Stephan, K. E., Harrison, L. M., Penny, W. D. & Friston, K. J. Biophysical models of fMRI responses. *Curr. Opin. Neurobiol.* **14**, 629–635 (2004).
 31. Henson, R. N. & Friston, K. J. in *Statistical Parametric Mapping* 178–192 (2007).
 32. Robson, M. D., Dorosz, J. L. & Gore, J. C. Measurements of the temporal fMRI response of the human auditory cortex to trains of tones. *Neuroimage* **7**, (1998).
 33. Jezzard, P., Matthews, P. M. & Smith, S. M. *Functional MRI: An Introduction to Methods.* (2001).

34. Amaro Jr., E. & Barker, G. J. Study design in fMRI: basic principles. *Brain Cogn.* **60**, 220–232 (2006).
35. Josephs, O., Turner, R. & Friston, K. J. Event-related fMRI. *Hum. Brain Mapp.* **5**, 243–248 (1997).
36. Buckner, R. L. *et al.* Detection of cortical activation during averaged single trials of a cognitive task using functional magnetic resonance imaging. *Proc. Natl. Acad. Sci. U. S. A.* **93**, 14878–14883 (1996).
37. Dale, A. M. & Buckner, R. L. Selective averaging of rapidly presented individual trials using fMRI. *Hum. Brain Mapp.* **5**, 329–340 (1997).
38. Rosen, B. R., Buckner, R. L. & Dale, A. M. Event-related functional MRI: past, present, and future. *Proc. Natl. Acad. Sci. U. S. A.* **95**, 773–780 (1998).
39. Huettel, S. A. Event-related fMRI in cognition. *Neuroimage* **62**, 1152–1156 (2012).
40. Friston, K. J., Jezzard, P. & Turner, R. Analysis of functional MRI time-series. *Hum. Brain Mapp.* **1**, (1994).
41. Friston, K. J. *et al.* Statistical parametric maps in functional imaging: A general linear approach. *Hum. Brain Mapp.* **2**, (1995).
42. Mahmoudi, A., Takerkart, S., Regragui, F., Boussaoud, D. & Brovelli, A. Multivoxel pattern analysis for fMRI data: A review. *Comput. Math. Methods Med.* **2012**, (2012).
43. Dale, A. M. Optimal experimental design for event-related fMRI. *Hum. Brain Mapp.* **8**, 109–114 (1999).
44. Glover, G. H. Deconvolution of Impulse Response in Event-Related BOLD fMRI. *Neuroimage* **9**, 416–429 (1999).
45. Castelo-Branco, M. *et al.* Activity patterns in human motion-sensitive areas depend on the interpretation of global motion. *Proc. Natl. Acad. Sci.* **99**, 13914–13919 (2002).
46. Van De Ven, V. G. *et al.* The spatiotemporal pattern of auditory cortical responses during verbal hallucinations. *Neuroimage* **27**, 644–655 (2005).
47. Norman, K. A., Polyn, S. M., Detre, G. J. & Haxby, J. V. Beyond mind-reading: multi-voxel pattern analysis of fMRI data. *Trends Cogn. Sci.* **10**, 424–430 (2006).
48. Pereira, F., Mitchell, T. & Botvinick, M. Machine learning classifiers and fMRI: a tutorial overview. *Neuroimage* **45**, (2009).
49. Duarte, J. V *et al.* Multivariate pattern analysis reveals subtle brain anomalies relevant to the cognitive phenotype in neurofibromatosis type 1. *Hum. Brain Mapp.* **35**, 89–106 (2014).
50. Vapnik, V. N. *The nature of statistical learning theory.* (Springer, 1995).
51. Burges, C. J. C. A Tutorial on Support Vector Machines for Pattern Recognition. *Data Min.*

- Knowl. Discov.* **2**, 121–167 (1998).
52. Cristianini, N. & Shawe-Taylor, J. *An introduction to Support Vector Machines and other kernel-based learning methods.* (2000).
 53. Hsu, C., Chang, C. & Lin, C. A Practical Guide to Support Vector Classification. *Bioinformatics* **1**, 1–16 (2010).
 54. Mourão-Miranda, J., Bokde, A. L. W., Born, C., Hampel, H. & Stetter, M. Classifying brain states and determining the discriminating activation patterns: Support Vector Machine on functional MRI data. *Neuroimage* **28**, 980–95 (2005).
 55. Ecker, C. *et al.* Investigating the predictive value of whole-brain structural MR scans in autism: a pattern classification approach. *Neuroimage* **49**, 44–56 (2010).
 56. LaConte, S., Strother, S., Cherkassky, V., Anderson, J. & Hu, X. Support vector machines for temporal classification of block design fMRI data. *Neuroimage* **26**, 317–329 (2005).
 57. Cox, D. D. & Savoy, R. L. Functional magnetic resonance imaging (fMRI) ‘brain reading’: detecting and classifying distributed patterns of fMRI activity in human visual cortex. *Neuroimage* **19**, 261–270 (2003).
 58. Haynes, J.-D. & Rees, G. Decoding mental states from brain activity in humans. *Nat. Rev. Neurosci.* **7**, 523–534 (2006).
 59. Mitchell, T. M., Hutchinson, R., Niculescu, R. S., Pereira, F. & Wang, X. Learning to Decode Cognitive States from Brain Images. *Mach. Learn.* 145–175 (2004).
 60. Klöppel, S. *et al.* Automatic classification of MR scans in Alzheimer’s disease. *Brain* **131**, 681–9 (2008).
 61. Ecker, C. *et al.* Describing the Brain in Autism in Five Dimensions - Magnetic Resonance Imaging-Assisted Diagnosis of Autism Spectrum Disorder Using a Multiparameter Classification Approach. *J. Neurosci.* **30**, 10612–10623 (2010).
 62. Marzelli, M. J., Hoeft, F., Hong, D. S. & Reiss, A. L. Neuroanatomical spatial patterns in Turner syndrome. *Neuroimage* **55**, 439–447 (2011).
 63. Magnin, B. *et al.* Support vector machine-based classification of Alzheimer’s disease from whole-brain anatomical MRI. *Neuroradiology* **51**, 73–83 (2009).
 64. Mukherjee, S., Golland, P. & Panchenko, D. Permutation Tests for Classification. *J. Mach. Learn. Res.* **1**, 1–48 (2000).
 65. Golland, P. & Fischl, B. Permutation tests for classification: towards statistical significance in image-based studies. *Lect. Notes Comput. Sci.* **2732**, 330–41 (2003).
 66. Ojala, M. & Garriga, G. C. Permutation Tests for Studying Classifier Performance. in *IEEE International Conference on Data Mining* 908–913 (2009).

67. Pereira, F. & Botvinick, M. Information mapping with pattern classifiers: a comparative study. *Neuroimage* **56**, 476–496 (2011).
68. Gaonkar, B. & Davatzikos, C. Analytic estimation of statistical significance maps for support vector machine based multi-variate image analysis and classification. *Neuroimage* **78**, 270–283 (2013).
69. Al-Rawi, M. S., Freitas, A., Duarte, J. V., Cunha, J. P. & Castelo-Branco, M. Permutations of fMRI classification may not be normally distributed. *Stat. Methods Med. Res.* **In press**, (2015).
70. Friston, K. J. Functional and effective connectivity: a review. *Brain Connect.* **1**, 13–36 (2011).
71. Stephan, K. E. & Friston, K. J. Analyzing effective connectivity with fMRI. *Wiley Interdiscip. Rev. Cogn. Sci.* **1**, 446–459 (2010).
72. Cisler, J. M., Bush, K. & Steele, J. S. A comparison of statistical methods for detecting context-modulated functional connectivity in fMRI. *Neuroimage* **84**, (2014).
73. Deshpande, G. & Hu, X. Investigating Effective Brain Connectivity from fMRI Data: Past Findings and Current Issues with Reference to Granger Causality Analysis. *Brain Connect.* **2**, 235–245 (2012).
74. Goebel, R., Roebroeck, A., Kim, D. & Formisano, E. Investigating directed cortical interactions in time-resolved fMRI data using vector autoregressive modeling and Granger causality mapping. *Magn. Reson. Imaging* **21**, 1251–1261 (2003).
75. Roebroeck, A., Formisano, E. & Goebel, R. Mapping directed influence over the brain using Granger causality and fMRI. *Neuroimage* **25**, 230–242 (2005).
76. Abler, B. *et al.* Investigating directed influences between activated brain areas in a motor-response task using fMRI. *Magn. Reson. Imaging* **24**, 181–185 (2006).
77. Stippich, C. *Clinical functional MRI: presurgical functional neuroimaging.* (Springer, 2007).
78. Rosenbloom, M., Sullivan, E. V & Pfefferbaum, A. Using magnetic resonance imaging and diffusion tensor imaging to assess brain damage in alcoholics. *Alcohol Res. Heal.* **27**, (2003).
79. D’Esposito, M., Deouell, L. Y. & Gazzaley, A. Alterations in the BOLD fMRI signal with ageing and disease: a challenge for neuroimaging. *Nat. Rev. Neurosci.* **4**, 1–11 (2003).

Chapter 3

Deconvolution approaches to fMRI

data:

Probing hemodynamic response functions and neurovascular coupling in healthy subjects and Type 2 Diabetes Mellitus

This chapter was based on: **Duarte JV**, Pereira JMS, Quendera B, Raimundo M, Moreno C, Gomes L, Carrilho F & Castelo-Branco M (2015). Early disrupted neurovascular coupling and changed event level hemodynamic response function in type 2 diabetes: an fMRI study. *Journal of Cerebral Blood Flow & Metabolism* 35(10): 1671-1680.

This chapter provides an important practical contribution of this thesis in the methodological aspects of fMRI analysis. We implemented a deconvolution approach to fMRI data in healthy subjects and diabetic patients, a population prone to cerebrovascular disease, in order to probe neurovascular coupling and neuronal response as empirically extracted from fMRI data. This work was important, because it set the ground to test the robustness of deconvolution approaches in fMRI studies of motion perception. These approaches were also used in chapter 4.

Abstract

Type 2 diabetes mellitus (T2DM) patients develop vascular complications and have increased risk for neurophysiological impairment. Vascular pathophysiology may alter the blood flow regulation in cerebral microvasculature, affecting neurovascular coupling. Reduced fMRI signal can result from decreased neuronal activation or disrupted neurovascular coupling. The uncertainty about pathophysiological mechanisms (neurodegenerative, vascular or both) underlying brain function impairments remains.

In this cross-sectional study we investigated if the hemodynamic response function (HRF) in lesion-free brains of patients is altered by measuring BOLD response to visual motion stimuli. We used a standard block design to examine the BOLD response and an event-related deconvolution approach. Importantly, the latter allowed for the first time to directly extract the true shape of HRF without any assumption and probe neurovascular coupling, using performance-matched stimuli. We discovered a change in HRF in early stages of diabetes.

T2DM patients show significantly different fMRI response profiles. Our visual paradigm therefore demonstrated impaired neurovascular coupling in intact

brain tissue. This implies that functional studies in T2DM require the definition of HRF, only achievable with deconvolution in event-related experiments.

Further investigation of the mechanisms underlying impaired neurovascular coupling is needed to understand and potentially prevent the progression of brain function decrements in diabetes.

Introduction

Type 2 diabetes mellitus (T2DM) seems to be associated with increased risk for brain function loss and long-term cognitive impairment, which are well documented in verbal and visual memory domains, information processing speed and executive functioning¹⁻³. It is crucial to understand the neurobiological correlates of early brain dysfunction in T2DM to develop and follow-up preventive interventions^{1,3}.

The majority of the studies investigated structural differences in the brain of T2DM patients and revealed a consistent finding of atrophy^{1,3}, particularly in cortical and subcortical grey matter⁴⁻⁶ but the association between sensory, cognitive deficits and brain structure is still poorly understood, in particular at early stages of the disease, when there are no evident structural lesions^{1,4,6}.

Concerning functional studies, results are not as consistent³. There are reports of changed cerebral blood flow in T2DM patients³, although a study with a larger sample found no significant differences when accounting for brain volume⁷. Recent studies examined the relation of cognition, brain volume or white matter alterations with both cerebral blood flow and cerebrovascular reactivity and found no significant relationships^{8,9}. Notably, a number of functional MRI (fMRI) studies relied on BOLD (Blood Oxygenation Level-Dependent) signal¹⁰ to indirectly measure neuronal activity and investigate neurophysiological impairment. Studies addressing resting-state fMRI found reduced functional connectivity between several regions of the "default mode network" in T2DM patients, which has been related to impaired episodic memory processing in older participants¹¹. In previous studies the relation between brain activity and performance impairment was either not tested¹² or reductions in connectivity between default mode regions were not performance related¹³. A recent study reported distributed activity changes in T2DM patients, including the temporal gyrus, in which activity was negatively correlated with executive functioning,

suggesting a joint effect of structural and functional alterations¹⁴. A later study however reported abnormal resting-state brain activity in the absence of structural differences in T2DM patients, which was associated with cognitive impairment¹⁵. The uncertainty about pathophysiological mechanisms underlying behavioural impairments and brain dysfunction remains. It could be neurodegenerative, vascular or a combination of both. It should be noted that the measure of neuronal activity relies on neurovascular coupling, which can be altered in the presence of cerebrovascular disease. Attenuated BOLD responses may be caused by impaired vascular reactivity and not by impaired neuronal activity.

The vascular response triggered by neuronal activation – the so-called hemodynamic response function or HRF – elicits variations in the BOLD signal as measured in fMRI¹⁶. An important pathophysiological mechanism in T2DM might be the early alteration of the blood flow auto regulation (the intrinsic ability of the brain vascular bed to functionally maintain its needed supply) in cerebral microvasculature, reflecting impaired neurovascular coupling and altered HRF. In patients with stroke it has been shown that the HRF can be altered, which may result in misinterpretation or underestimation of fMRI signal^{17,18}. The only way to disentangle vascular from neural impairment driven changes in the BOLD response is to also use stimuli that are performance matched, thereby using similar neural and cognitive resources.

To elucidate the disruption of neurovascular coupling the use of event-related designs is crucial, as it allows to extract by deconvolution the real hemodynamic response to a single stimulus event, without any assumption [see e.g.¹⁹ for a detailed explanation]. We therefore queried whether T2DM patients present an HRF that is different from the canonical one. Unlike previous studies, which emphasized the experimental block design, here we used for the first time an event-related approach, which is the only one that can directly tackle this

question. If the hemodynamic regulation is affected in the brain of T2DM patients as directly measured at the event level it could be the basis for findings of no activation or underactivation at the more macroscopic block level. This could provide support for the interpretation of neurovascular coupling changes expressed in the fMRI signal changes and their relation to behavioural measurements. We examined the HRF in the human brain by using both a block and an event-related experimental design to investigate the BOLD response to a visual speed discrimination task in the whole brain and specifically in three regions-of-interest (ROIs). One of the regions, MT+/V5, was selected independently of the task as it is one of the visual brain regions that can be most reliably localized due to its well established motion selectivity^{20–22}. Furthermore we investigated two other regions that were significantly activated during this type of task: the insula, known for its role in perceptual decision mechanisms, and the inferior frontal gyrus, which plays a role in executive functioning. We discovered a significant difference in the HRF of T2DM patients, reflecting impaired neurovascular coupling and altered fMRI response amplitudes in all investigated brain areas. An important implication of these results is the requirement of event-related deconvolution approaches in fMRI studies in T2DM (and other vascular diseases). Standard block designs cannot extract the true HRF and may mask the findings and interpretation of true differences in brain responses.

Materials and methods

Participants

We recruited 121 participants (70 controls and 51 T2DM). An expert neuroradiologist had access to both standard clinical 2-D-FLAIR and 3-D-SPACE

T2-weighted images to perform the neuroradiological assessment of all participants and examine for the presence of white matter hyper intensities. We excluded participants with vascular or structural lesions or any changes that could confound our results. After applying exclusion criteria we could select 51 type 2 diabetes participants (30M, 21F) and 29 age-matched controls (14M, 15F). Table 3-1 details the participants' demographic and clinical data. In this cross-sectional study participants had normal or corrected to normal vision (as further confirmed by fundus photography and optical coherence tomography) and no history of neurological or psychiatric disease.

T2DM patients were diagnosed in the Endocrinology Department of the University of Coimbra Hospital using standard WHO criteria ^{23,24}, including the recent recommendation of a cut-off point of 6.5% for HbA1c (in addition to the criteria based on fasting plasma or tolerance test glucose levels), and were recruited among the T2DM clinical population of this Department. Inclusion criteria for patient group: 1-Age between 40 and 75 years-old; 2-Diabetes mellitus type 2 for at least one year prior to the commencement of this study; 3-Informed written consent. Matched controls were recruited from the general population of the Hospital or University staff as follows. Inclusion criteria for control group: 1- Age between 40 and 75 years-old; 2 & 3-Diabetes mellitus type 2 diagnosis excluded based on levels of glycated haemoglobin (HbA1c) and fasting glucose; 4-Informed written consent. The diagnosis and the severity of diabetic retinopathy was carried by expert hospital professionals, based on a technical report following the guidelines of the Early Treatment Diabetic Retinopathy Study (ETDRS). For each participant, ocular dominance was determined using the hole-in-the-card test (Dolman method). Hand dominance was ascertained using the Edinburgh inventory. All participants indicated informed written consent. The Helsinki Declaration of 1975 (and as revised in 1983) guidelines were followed

throughout the study. The Ethics Committee of the Faculty of Medicine of the University of Coimbra approved all experimental procedures.

Table 3-1. Characteristics of study participants

	Controls	T2DM	^a <i>P-value</i>
<i>n</i>	29	51	
Age (years)	56.67 (6.43)	59.73 (7.90)	0.069
Gender (M/F)	14/15	30/21	0.558
Discrimination threshold (deg/sec)	1.39 (1.34)	2.44 (1.88)	0.004
Duration of the disease (years)		12.37 (8.76)	
HbA _{1c} (NGSP, %)	5.51 (0.39)	9.24 (2.28)	< 0.001
HbA _{1c} (IFCC, mmol/mol)	36.82 (4.38)	77.49 (24.96)	< 0.001
Visual acuity	0.95 (0.15)	0.84 (0.25)	0.018
	No DR	93	37
	Questionable DR	7	14
	Mild NPDR		32
Diabetic retinopathy (%)	Moderate NPDR		11
	Moderately severe NPDR		6
	Severe NPDR		
Body Mass Index (BMI, Kg/m ²)	25.34 (3.23)	29.83 (4.97)	< 0.001
Blood pressure controlled by medication (e.g. beta-blockers) (%)	25	78	< 0.001
Blood pressure – systolic (mmHg)	125.31 (17.39)	135.20 (19.80)	0.106
Blood pressure – diastolic (mmHg)	73.23 (9.32)	75.68 (12.65)	0.517

Blood total cholesterol (mg/dL)		209.27 (34.05)	167.82 (51.72)	< 0.001
Blood cholesterol HDL (mg/dL)		58.50 (13.01)	41.35 (11.46)	< 0.001
Blood cholesterol LDL (mg/dL)		142.00 (27.35)	110.25 (31.96)	< 0.001
Atherogenic index		3.70 (0.81)	4.22 (1.28)	0.112
Triglycerides (mg/dL)		119.58 (75.57)	157.68 (76.77)	0.005
Apolipoprotein A 1 (mg/dL)		167.30 (23.18)	136.59 (28.17)	< 0.001
Apolipoprotein B 100 (mg/dL)		99.19 (17.68)	87.92 (24.28)	0.003
	Yes (%)	8	4	
Smoking habits	No (%)	76	76	0.725
	Quit (%)	16	20	
	Yes (%)	39	22	
Alcoholic habits	No (%)	61	76	0.259
	Quit (%)	0	2	
Exercise habits	Yes (%)	54	34	0.095
	No (%)	46	66	
Anti-diabetic medication	Oral (%)		9.1	
	Insulin (%)		36.4	
	Oral + insulin (%)		54.5	

Data are means (\pm SD). ^a *P*-value by t-test or Wilcoxon rank sum test for continuous variables and χ^2 test for categorical variables. Diabetic retinopathy (DR) severity grades were attributed based on the ETDRS (Early Treatment Diabetic Retinopathy) scale. At all categories DR is non-proliferative (NPDR).

Abbreviations: BMI, body mass index; F, female; HDL, high-density lipoprotein; IFCC, International Federation of Clinical Chemistry; LDL, low-density lipoprotein; M, male; NGSP, National Glycohaemoglobin Standardization Program; NPDR, non-proliferative diabetic retinopathy.

Stimulus presentation and apparatus

We wrote our experiments in MATLAB, using the Psychophysics Toolbox extensions^{25,26}. Stimuli were projected by means of an LCD projector (Avotec Real Eye Silent Vision 6011, resolution 1024 x 768, 60Hz refresh rate) onto a screen pad positioned in the bore at a distance of 163 cm from the projector (image size in the screen pad was 22.62° x 17.06° visual degrees; mirror distance from screen was 50 cm). Stimuli were viewed monocularly with the dominant eye while the other eye was covered with an opaque eye patch.

Psychophysics

The psychophysical task (performed inside the scanner to select stimulus levels) consisted on a two-alternative forced choice test aimed to determine a speed discrimination threshold by comparing the speed of two white dots, a reference dot and a target dot with mean luminance 22.9 cd/m², moving on a grey background with mean luminance 9.39 cd/m². The dots composing each trial were randomly presented one in each visual hemifield simultaneously for 400 msec at an eccentricity of 7.5° along the horizontal meridian, with each dot moving back and forth along a path of 2° visual degrees with a pseudo-random linear trajectory (between 0 and 180 degrees). Dot size was 0.22° x 0.22° and fixation cross size was 0.33° x 0.33°. The subject reported which dot moved faster by means of a button press with a Cedrus Lumina LP-400, LU400 PAIR MR-compatible response box. The speed of the target dot of the successive trials was determined using a descending logarithmic staircase which determined the number of trials and allowed the estimation of the discrimination threshold. The staircase had 6 reversals (2 practice/4 experimental). It allowed to compute speeds from 24 degrees/second (initial target speed) to 5 degrees/second

(reference speed) using a step value that ranged from 1 dB to 0.05 dB. The speed discrimination threshold was then estimated using the mean of the last 4 reversals.

Stimuli and functional MRI tasks

Each participant performed three experimental runs: two presenting the stimuli in blocks and one in an event-related design. All participants were presented with the same randomized sequences. Both block and event-related designs are represented in Figure 3-1. The stimuli characteristics were the same as in the psychophysical task, except the duration. In the block design runs the reference dot always moved at 5 degrees/second and the target dot moved with one of four different values: the reference speed (reference condition), the reference speed incremented of the individual threshold of discrimination (threshold condition), the reference speed incremented of 3 times the previous threshold (sub-maximum condition) and an arbitrarily defined high speed value of 20 degrees/second (maximum condition). The reference condition was presented 2 times (both visual hemifields with the dot moving with the reference speed). Each of the three remaining conditions was repeated four times with the faster dot appearing two times in each visual hemifield. This yields 29 blocks of alternated visual stimulation (14 blocks of 12.5 seconds each) and baseline fixation (15 blocks of 12.5 seconds each). In the event design stimulation paradigm the alternation between stimulation and baseline fixation is maintained but only the threshold and the sub-maximum conditions were presented. Because of efficiency reasons (as event-related designs have much lower statistical power than block designs we need much more trials per event) each of the two conditions (representing representative and intermediate difficulty levels) was presented 20 times (10 times per hemifield). Each visual stimulation period lasted 400 msec and the

baseline fixation period lasted 4600, 7100 or 9600 msec, which occurred randomly. Variable inter stimulus intervals must be used in the experimental design in order to uniquely estimate the large amount of beta values from overlapping responses. Participants were instructed to maintain fixation on a white cross during the whole experiment and report the faster dot during the baseline fixation periods succeeding the stimulation blocks/events. The computation of the speed values was individually tuned to ensure that we would analyze fMRI signal changes in identical performance conditions across participants.

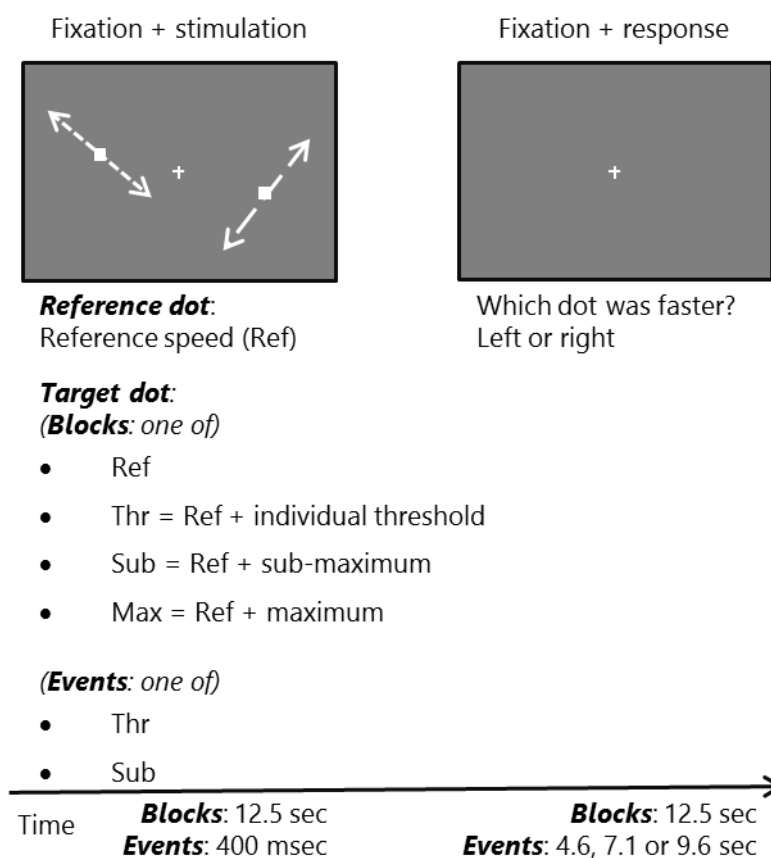


Figure 3-1. Visual speed discrimination task. Graphical representation of the experimental protocols of block and event-related experiments of visual motion discrimination (see Methods section for a detailed explanation).

Image acquisition

The MR scans (2012-2014) were acquired at the Portuguese Brain Imaging Network facilities, on a 3T research scanner (Magnetom TIM Trio, Siemens, phased array 12-channel birdcage head coil).

We acquired a 3-D anatomical MPRAGE (magnetization-prepared rapid gradient echo) scan using a standard T₁w gradient echo pulse sequence (TR = 2530 msec; TE = 3.42 msec; TI = 1100 msec; flip angle 7°; 176 slices with voxel size 1 x 1 x 1 mm; FOV 256 mm). A functional imaging series consisted of 2 runs of 145 gradient-echo (GE) echo planar imaging (EPI) brain scans (TR 2500 msec; TE = 30 msec; flip angle 90°; 36 interleaved slices with voxel size 3 x 3 x 3 mm; FOV 256 mm) in a block design stimulation paradigm with measurement of BOLD signal and 1 run of 116 gradient-echo (GE) echo planar imaging (EPI) scans (TR 2500 msec; TE = 30 msec; flip angle 90°; 36 interleaved slices with voxel size 3 x 3 x 3 mm; FOV 256 mm) in an event-related design stimulation paradigm with measurement of BOLD signal.

MT+/V5 functional localizer

To analyse the BOLD signal in the motion responsive ROI we used a functional MT+/V5 localizer based on dot motion^{22,27}. We presented an independent group of participants (data not shown) a moving-dot task, which has been used in imaging and neurophysiological studies based on both single and multiple dots^{22,28}. The random effects (RFX) general linear model (GLM) analysis of BOLD responses in Talairach space confirmed that MT+/V5 was successfully activated in the expected coordinate locations (peak voxel Talairach coordinates X = -45, Y = -66, Z = 2 in the left and X = 42, Y = -66, Z = -2 in the right) and this ROI was

selected by choosing the whole cluster that survived an FDR (false discovery rate) corrected P -value = 0.001 with cluster extent threshold correction.

fMRI data processing and statistical analysis

Image processing and analysis were carried out using BrainVoyager QX 2.6 (Brain Innovation, Maastricht, The Netherlands). We applied slice scan time correction, linear trend removal, temporal high-pass filtering (2 cycles per run), slight spatial smoothing (FWHM 4 mm) and interscan head motion correction. Functional scans were coregistered with each individual anatomical scan in Talairach space.

In order to ensure that we were investigating differences in BOLD signal related to the HRF and not the task difficulty levels we included in our GLM confound predictors accounting for the incorrect trials. In other words, we only investigated BOLD signal variation explained by correct responses to the task, ensuring the differences at the vascular and not cognitive level.

Statistical analysis was performed using an RFX GLM which allows modelling explicitly both within-subjects and between-subjects variance components in order to generalize findings to the population level ²⁹. The data for each subject is concatenated resulting in mean effect estimates per condition (first level). Then the estimated first-level mean effects enter the second level as the new dependent variable (instead of the raw data) and are analyzed across subjects (group analysis). Since the analysis at the second level explicitly models the variability of the estimated effects across subjects, the obtained results can be generalized to the population [see e.g. ³⁰ for a detailed explanation].

Predictors for the four stimulation conditions were used to estimate condition effects (beta values) separately for each subject. The subsequent resulting group statistical maps were corrected for multiple comparisons using the FDR correction at P -value < 0.001 with cluster extent threshold. We defined two additional regions of interest based on the thresholded RFX-GLM statistical maps: one at the

insula because of its known role in decision making processes and one in the inferior frontal gyrus (IFG) because of its role in executive functioning. We extracted the mean BOLD activity within the three ROIs and compared between groups. We further examined the average BOLD fMRI response time-courses for each stimulation condition in the three ROIs.

For the event-related design, we applied both the standard RFX-GLM analysis and deconvolution analysis within the previously defined ROIs in order to separate the contributions of different events. A deconvolution analysis consists of an alternative to the standard GLM analysis as the entire shape of the HRF is not fixed in advance. It allows to estimate the HRF for each event type. In this approach of linear deconvolution each condition is coded in a user-specified number of "stick" predictors each modelling separately the BOLD response at one data point with respect to the onset of that condition. This allows a more flexible fitting of the model and allows the user to compare conditions on the single data point basis [see e.g. ³¹ for a detailed explanation]. Furthermore, this is done at the individual level in a way that each participant has its own HRF estimated by deconvolution.

Results

Behavioural performance

We observed a statistically significant difference in the mean (standard deviation) psychophysical threshold of speed discrimination between T2DM patients and controls: $\text{thr}_{\text{CNT}} = 1.39$ (1.34) deg/sec and $\text{thr}_{\text{T2DM}} = 2.44$ (1.88) deg/sec (Mann-Whitney test $P\text{-value} = 0.0043$, see Table 3-1).

In this study it was critical to study BOLD responses and neurovascular coupling under performance matched conditions (in threshold units), in addition to

physically matched stimuli. For this reason and given that stimuli were chosen (tailored) for subsequent fMRI scanning taking also into account levels above and below individually determined thresholds, overall response accuracy while scanning did not show a significant difference between control and diabetic participants. Controls and patients could therefore be performance matched in both blocked and event-related experiments, reaching leveraged average and matched accuracy values for easier discrimination trials (data not shown). Furthermore, to ensure we would be analyzing hemodynamic effects rather than differences in cognitive processes we included only trials with correct task response in the fMRI analysis procedures.

fMRI findings

In the blocked experiment we can observe similar statistical maps for controls and T2DM patients, although the map of T2DM patients show an interesting bilateral activation in all three previously described ROIs while the control group shows a right lateralization in activation of higher level areas.

In Figure 3-2 we can observe the overlap between the RFX GLM statistical maps with the independent MT+/V5 localizer used for investigation of the HRF in the visual motion responsive area. The independent localizer (data not shown) is consistent with prior reports of its localization^{21,27}. We defined two additional ROIs based on the thresholded RFX GLM statistical maps for further analysis of the HRF: one at the insula (Figure 3-3) because of its known role in decision making processes and one in the inferior frontal gyrus (Figure 3-4) because of its role in executive function.

For the standard GLM analysis of the event-related experiment, analyzed using a canonical HRF, we found a striking effect of the visual speed discrimination task. In the control group we observe a similar pattern of response across the brain as

in the block experiment. Notably, in T2DM patients we observed very little or no significant activations at the same statistical threshold, for the event-related design experiment. We rather observe large deactivation regions, although one can see that most of the regions present a statistic value on the lower extreme of the thresholded scale.

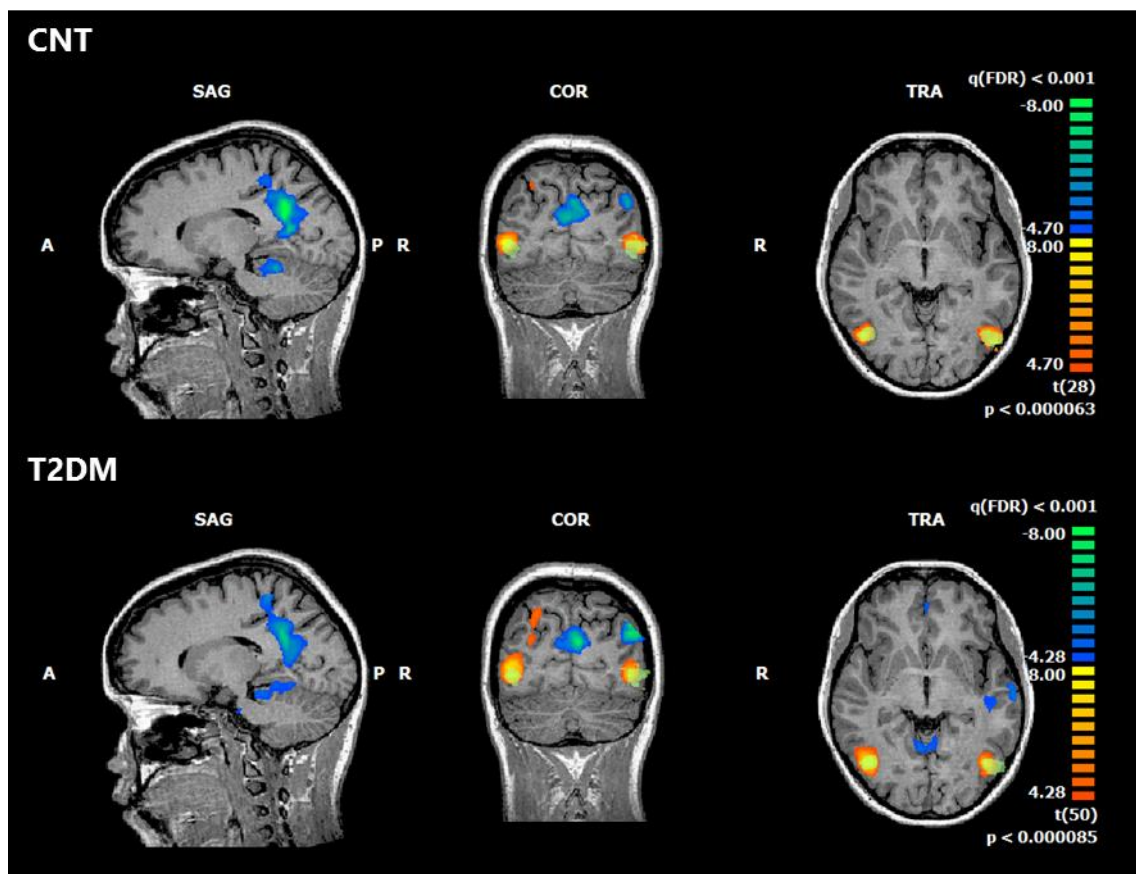


Figure 3-2. BOLD fMRI response in MT+/V5 during the block design experiment for controls (CNT) and diabetic patients (T2DM). Both maps are corrected for false discovery rate (FDR) at P -value < 0.001. One can see significant activations within the middle temporal area (MT+/V5), being well overlapped with the independent localizer shown in green. The peak voxel has Talairach coordinates [X = -45; Y = -66; Z = 2] in the left and [X = 42; Y = -66; Z = -2] in the right. We used this ROI to extract the fMRI BOLD signal for further analysis of the response profile in both groups.

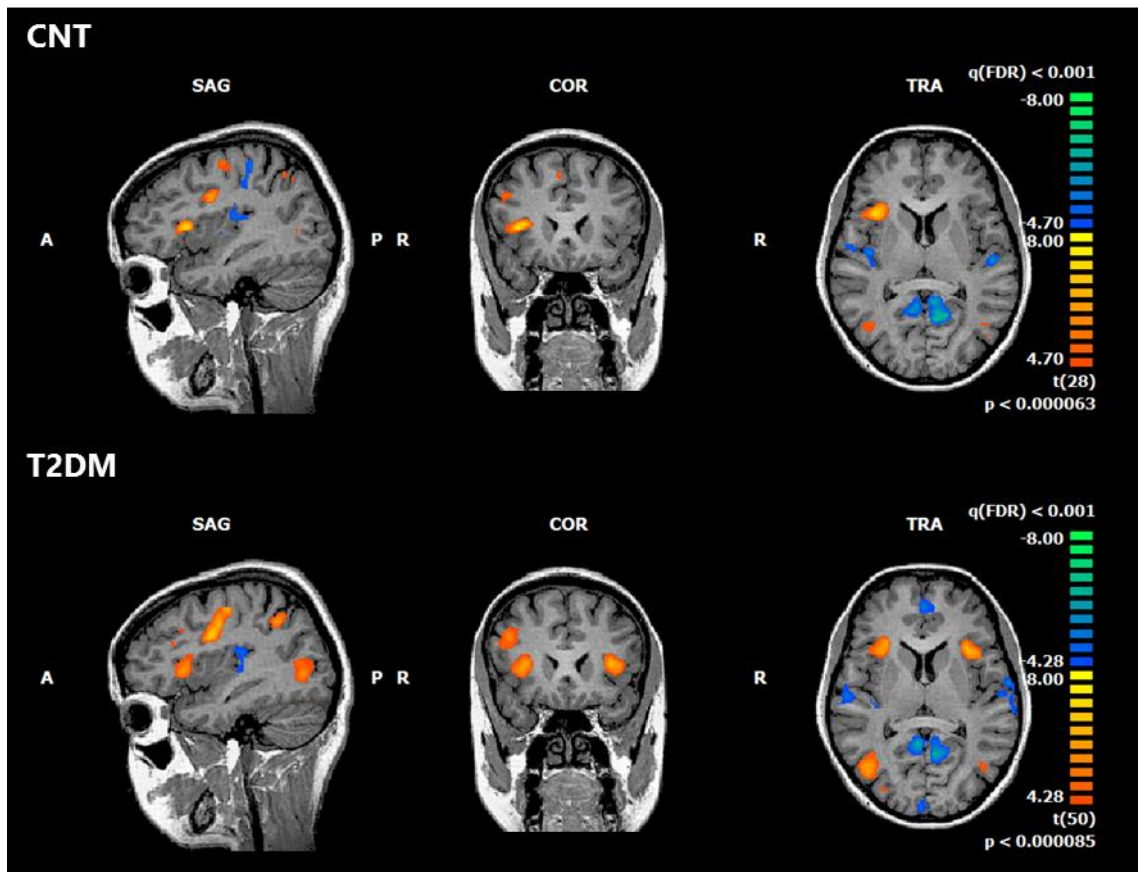


Figure 3-3. BOLD fMRI response in the insula during the block design experiment for controls (CNT) and diabetic patients (T2DM). Both maps are corrected for false discovery rate (FDR) at P -value < 0.001 . One can see significant activations within part of the insula, corresponding to Brodmann area 13. The peak voxel has Talairach coordinates $[X = 36; Y = 17; Z = 7]$ and $t = 7.873521$. We used this ROI to extract the fMRI BOLD signal for further analysis of the response profile in both groups.

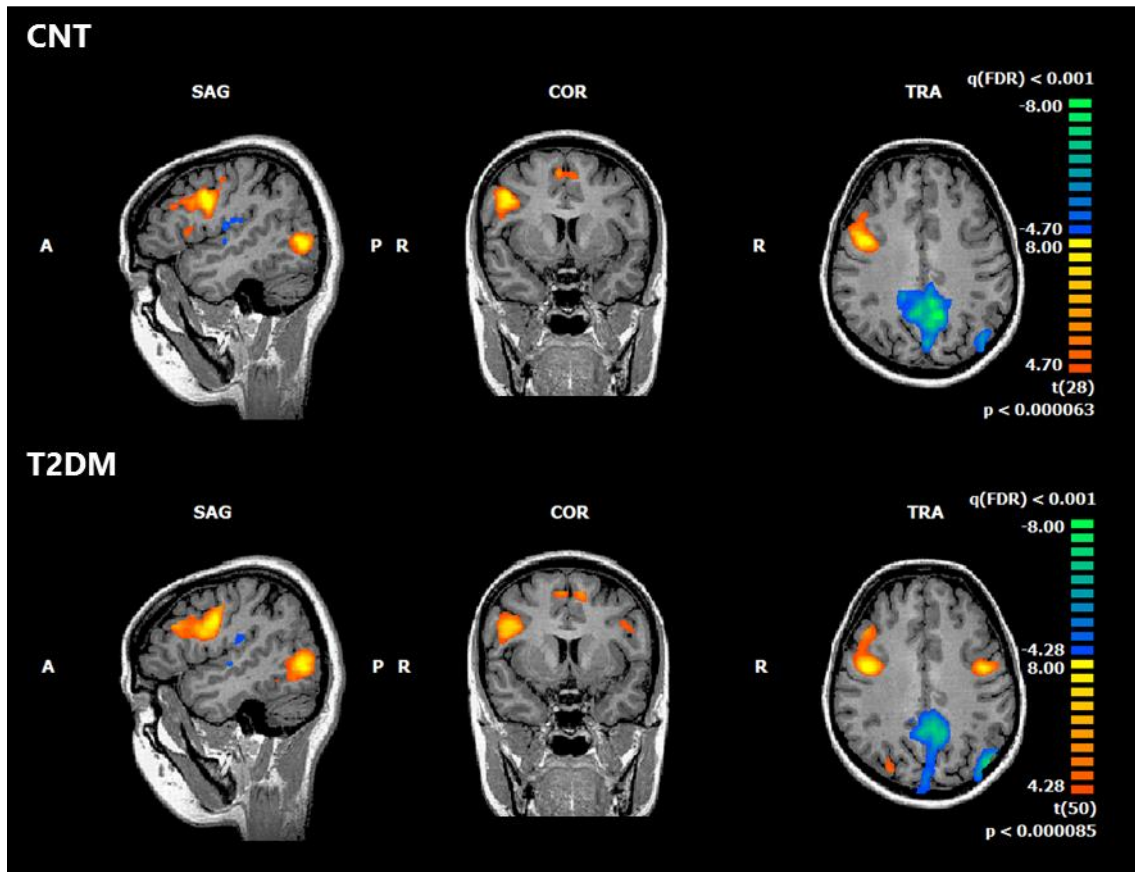


Figure 3-4. BOLD fMRI response in inferior frontal gyrus during the block design experiment for controls (CNT) and diabetic patients (T2DM). Both maps are corrected for false discovery rate (FDR) at P -value < 0.001 . One can see significant activations within part of the inferior frontal gyrus (IFG), corresponding to Brodmann area 9. The peak voxel has Talairach coordinates $[X = 42; Y = 2; Z = 31]$ and $t = 9.717579$. We used this ROI to extract the fMRI BOLD signal for further analysis of the response profile in both groups.

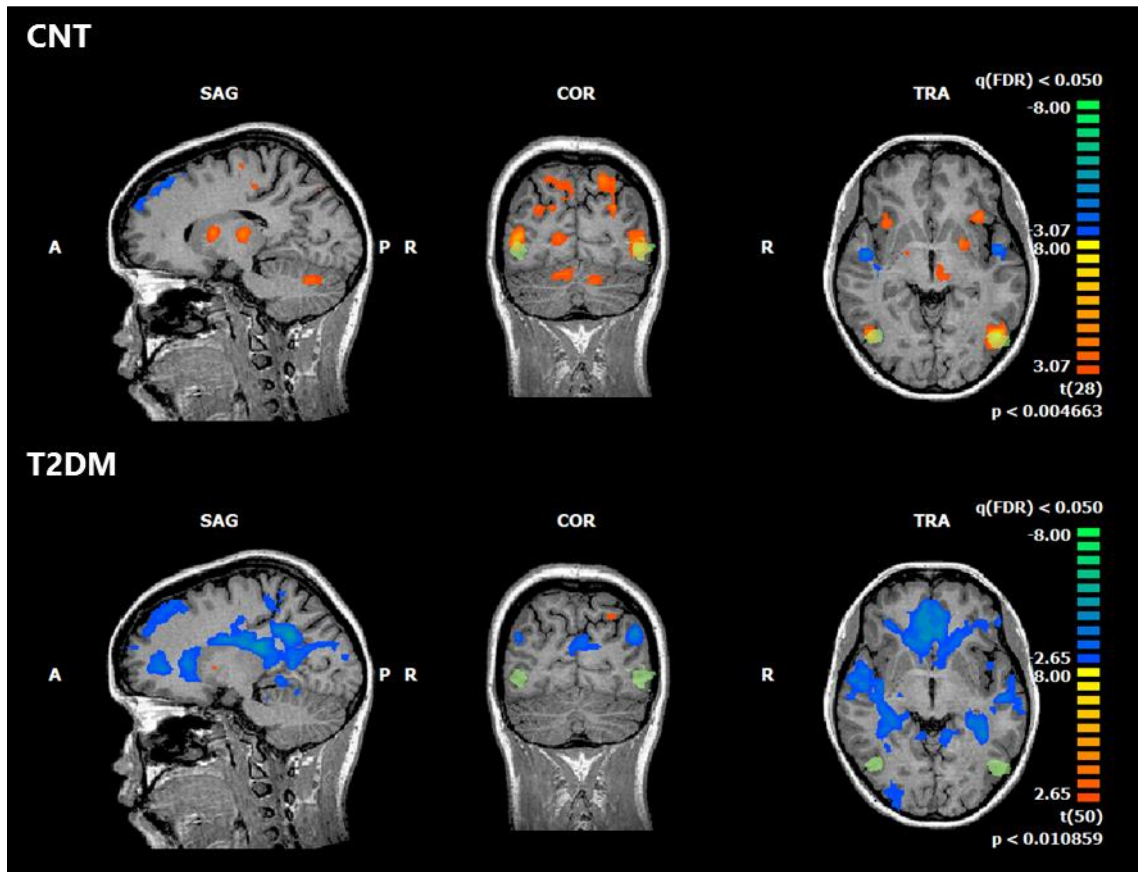


Figure 3-5. BOLD fMRI response in MT+/V5 during the event-related experiment for controls (CNT) and diabetic patients (T2DM), using a canonical hemodynamic response function (HRF). Both maps are corrected for false discovery rate (FDR) at P -value < 0.05 . One can see significant activations within the middle temporal area (MT+/V5) of control participants, being well overlapped with the independent localizer shown in green. Note the absence of significant activation in the statistical map of T2DM patients, which shows mainly deactivations relative to baseline. The peak voxel of MT+/V5 has Talairach coordinates $[X = -45; Y = -66; Z = 2]$ in the left and $[X = 42; Y = -66; Z = -2]$ in the right. We used this ROI to extract the true HRF from fMRI BOLD signal in both groups.

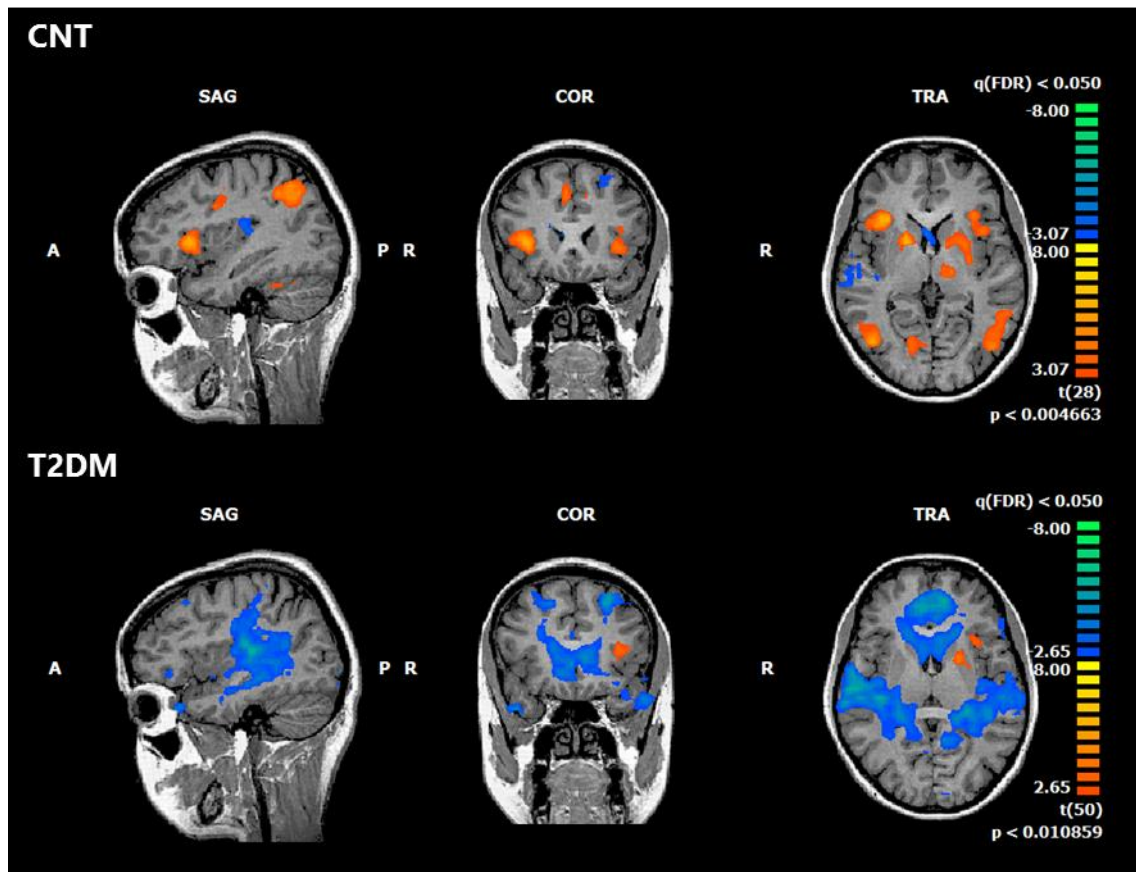


Figure 3-6. BOLD fMRI response in the insula during the event-related experiment for controls (CNT) and diabetic patients (T2DM), using a canonical hemodynamic response function (HRF). Both maps are corrected for false discovery rate (FDR) at P-value < 0.05. One can see significant activations within part of the insula, corresponding to Brodmann area 13, in control participants. Note the absence or reduced significant activation in the statistical map of T2DM patients, which shows mainly deactivations relative to baseline. The peak voxel of the insula has Talairach coordinates [X = 36; Y = 17; Z = 7] and $t = 7.873521$. We used this ROI to extract the true HRF from fMRI BOLD signal in both groups.

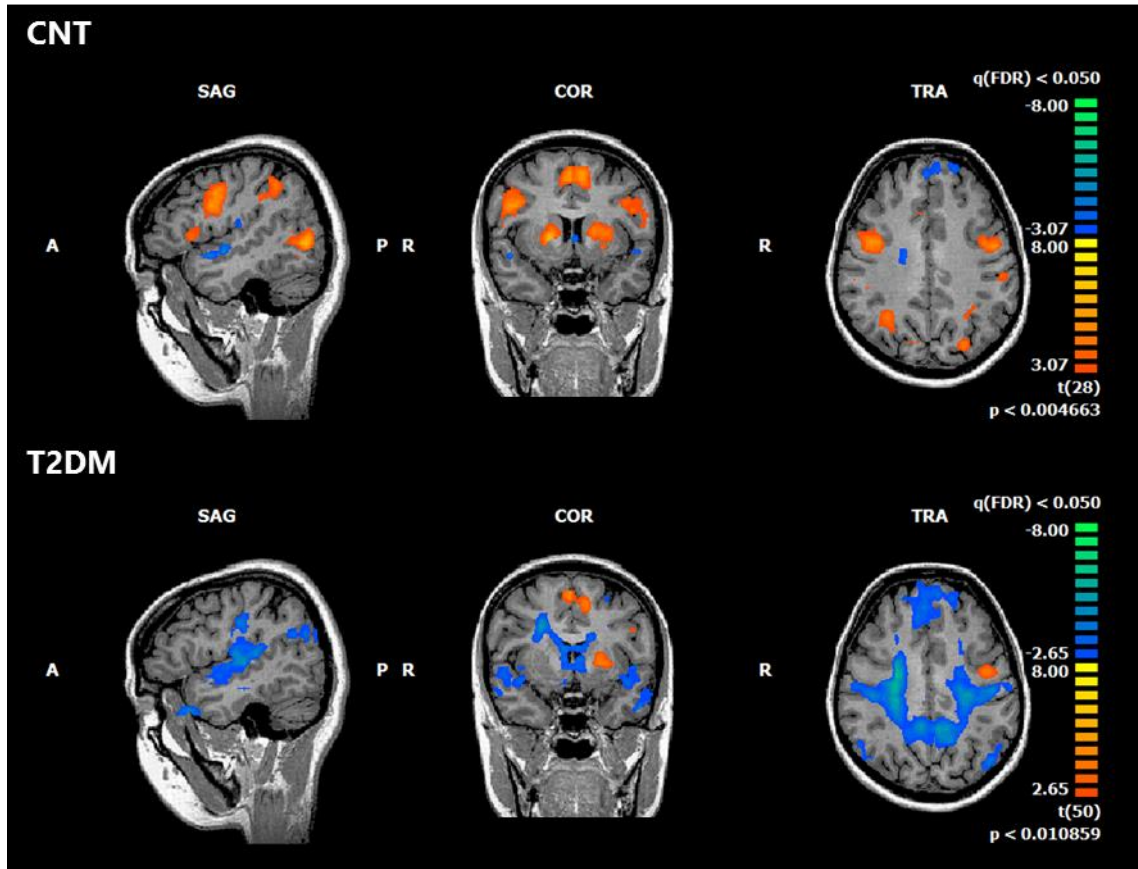


Figure 3-7. BOLD fMRI response in inferior frontal gyrus during the event-related experiment for controls (CNT) and diabetic patients (T2DM), using a canonical hemodynamic response function (HRF). Both maps are corrected for false discovery rate (FDR) at P -value < 0.05. One can see significant activations within part of the inferior frontal gyrus (IFG), corresponding to Brodmann area 9, in control participants. Note the absence or reduced significant activation in the statistical map of T2DM patients, which shows mainly deactivations relative to baseline. The peak voxel of IFG has Talairach coordinates $[X = 42; Y = 2; Z = 31]$ and $t = 9.717579$. We used this ROI to extract the true HRF from fMRI BOLD signal in both groups.

ROI based activation differences

We used the independently defined MT+/V5 and the functionally defined insula and IFG ROIs to further investigate the BOLD response during the visual speed discrimination separately in controls and diabetic participants.

In Figure 3-8 we show the average group beta values for all ROIs, extracted from the standard RFX GLM analysis of the BOLD response during the block and event-related designed experiments. We found significantly lower beta values in T2DM patients compared to controls in the block experiment ($P_{insula} = 0.011$; $P_{IFG} < 0.001$; $P_{MT+} < 0.001$) as well as in the event-related experiment ($P_{insula} = 0.024$; $P_{IFG} = 0.043$; $P_{MT+} = 0.002$). These values represent the average BOLD signal change in these areas during all periods of stimulation, which are suggested to be systematically lower in the T2DM group.

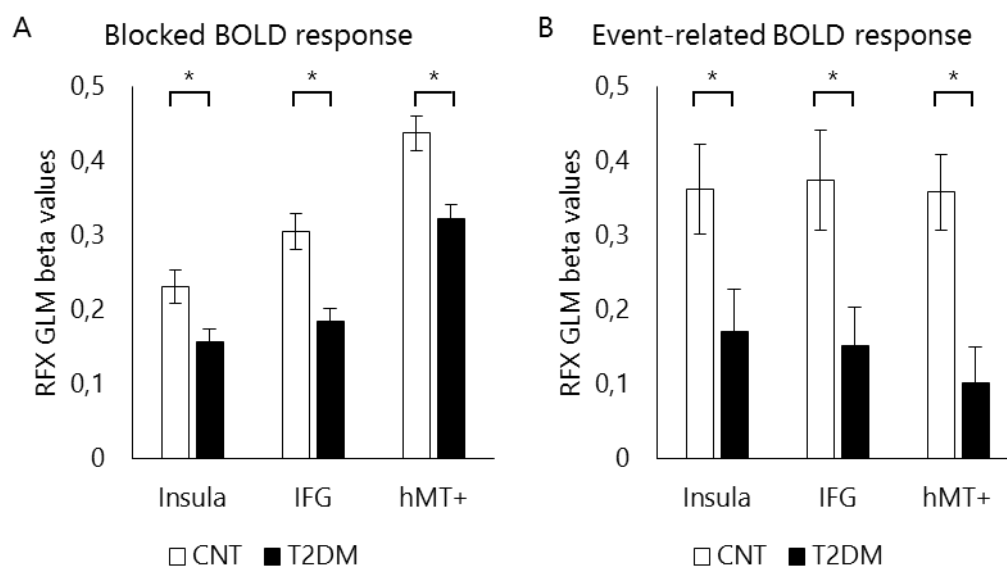


Figure 3-8. Mean BOLD activity within the three selected regions-of-interest (ROIs) during (A) block design runs and (B) event-related experiment. Significant differences between groups are indicated by $*P\text{-value} < 0.05$. Values are presented as mean \pm SEM and were extracted using a standard RFX-GLM procedure with a fixed canonical HRF.

General BOLD response profiles – block design

The average time courses of the BOLD fMRI response to each condition within the three ROIs during the blocked experiment are shown in Figure 3-9. We found globally higher amplitude in controls compared with T2DM patients except for the trials presenting a discrimination task between the reference speed and the maximum speed, which is the easiest condition. The difference in the response amplitude can be distinguished as a function of the timing and difficulty of the stimulation block. Interestingly, these differences are more pronounced in the beginning of the blocks during the sub-maximum and maximum conditions (easy conditions, panels C and D in Figure 3-9) while it appears later in the period during the reference and threshold conditions (difficult conditions, panels A and B in Figure 3-9). This suggests that participants hold higher responses during more difficult discrimination blocks while in easier ones they decide faster and return to baseline sooner. T2DM patients tend to present this decision mechanism somehow diminished.

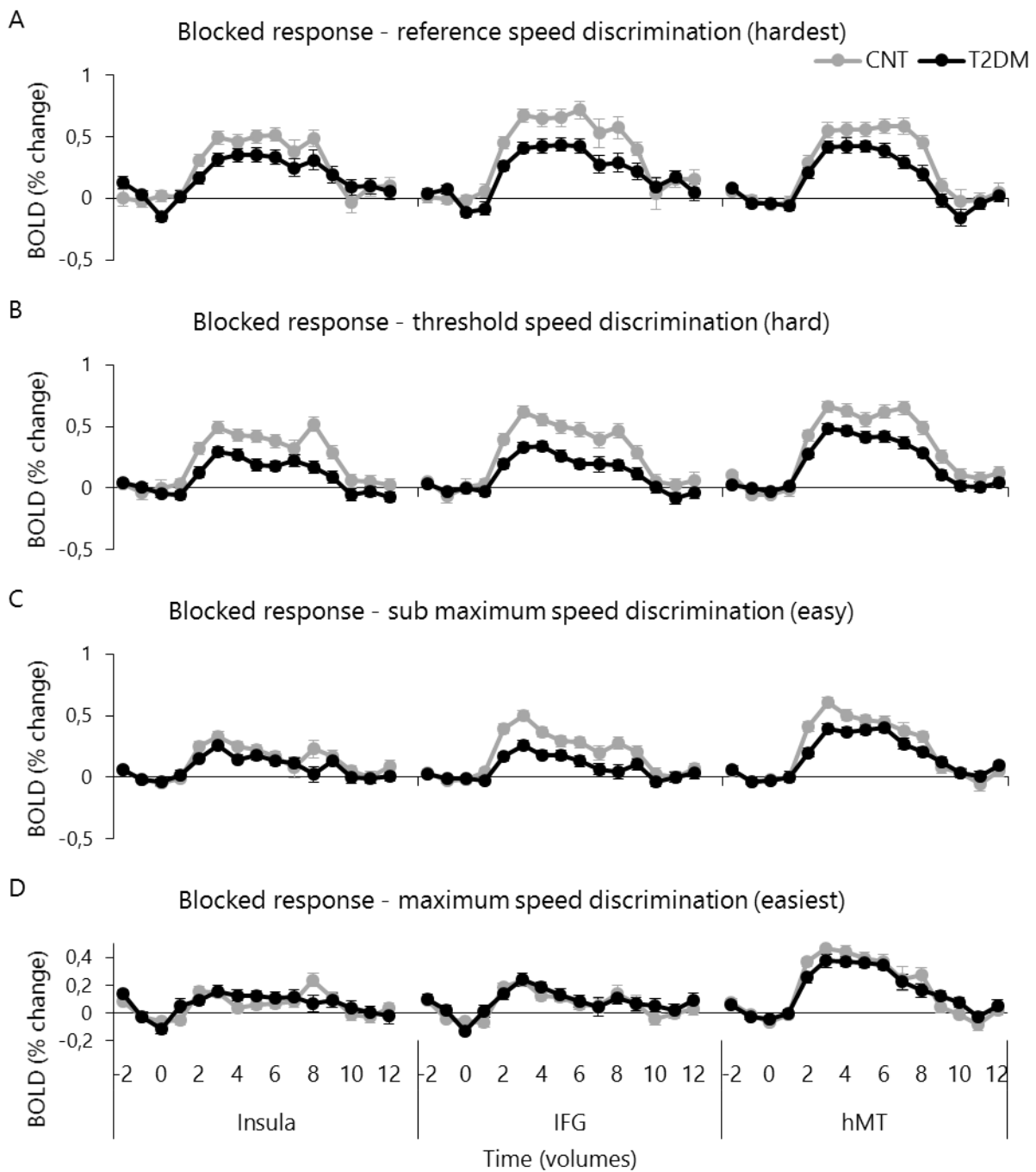


Figure 3-9. Averaged time course of the BOLD fMRI response within the three ROIs for the (A) reference, (B) threshold, (C) sub-maximum, and (D) maximum speed differences during the block design experiment. Values are presented as mean % signal change \pm SEM and were extracted using a standard RFX-GLM procedure with a fixed canonical HRF.

True estimation of hemodynamic response function

In the event-related experiment, we employed for the first time in T2DM a deconvolution based GLM analysis, which is used explicitly to remove the effect of the impulse response from the measurements in order to attempt more accurately to depict the time course of the neuronal activity from the measured BOLD response. In Figure 3-10 we show the global average of the estimated HRF for each group from both threshold and sub-maximum events and over the three regions of interest (panel A), and also the ROI-specific HRF for each event type (panels B to D). In the specific case of the deconvolution GLM the beta weights of the GLM allow to reconstruct the entire BOLD response to each condition from the data. The height of the peak response was significantly lower in T2DM ($P = 0.02$) as well as the “pre-peak dip”. In T2DM patients the characteristic undershoot of the HRF does not seem to occur before returning to baseline (see significant data points in the global HRF - Figure 3-10A). In addition, we performed a sensitivity and specificity analysis of the HRF of T2DM patients *versus* healthy controls. We computed the ROC (receiver operating characteristic) curve for the peak amplitude of the HRF. The area under the curve (AUC) was found to be significantly different from the null hypothesis of no discrimination between groups (AUC = 0.65; SEM = 0.06; P -value = 0.03).

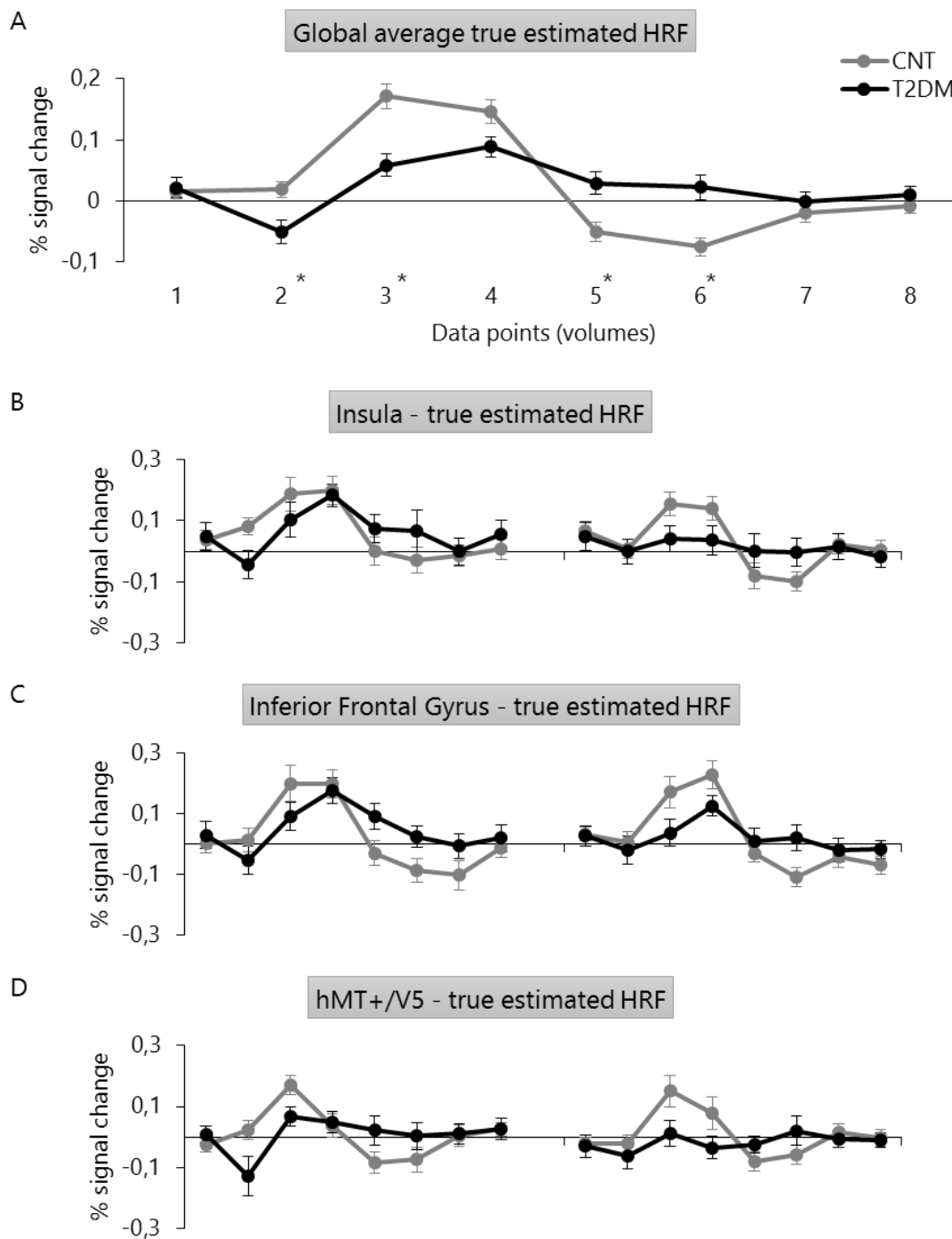


Figure 3-10. True estimated hemodynamic response function (HRF) in the brain. The global average true estimated HRF is presented in (A) for each group from both threshold and sub-maximum events and over the three regions of interest. The * represents a significant difference between groups at P -value < 0.05 (with Bonferroni correction for multiple comparisons). ROI-specific estimated true HRF of the BOLD fMRI response within (B) Insula, (C) Inferior Frontal Gyrus and (D) MT+/V5 during the event-related experiment are also shown. Values were extracted by deconvolution of the BOLD signal and are presented as mean \pm SEM.

Discussion

This study aimed at assessing the stimulus driven BOLD hemodynamic response in neurologically intact patients with type 2 diabetes mellitus, without any neuroradiological signature of brain damage. We investigated fMRI signal changes in response to a visual speed discrimination task, using both block and, most importantly, event-related designs, which allowed for the extraction (by deconvolution) of the real hemodynamic response function.

Our results revealed differences in the amplitude of BOLD signal changes as in the time course of the HRF of diabetic patients (Figure 3-8 to Figure 3-10). The event-related design and the possibility to implement response deconvolution allowed to determine that T2DM participants had dissimilar physiological response curves (lower global amplitude, peak height, "dip" and undershoot). This shows that the HRF is changed and thereby that neurovascular coupling is disturbed even in apparently normal intact brains. These differences cannot be attributed to the documented processing impairment since task performance was tailored across groups and, importantly, fMRI signal analysis accounted for the correct trial responses only. Intermediate stimulus levels were adjusted to near and above individual threshold levels to ensure performance matching. Note that it is impossible to completely match the task at the stimuli parameters and performance levels at the same time (although all participants had performance or physically matched stimuli, and only correct responses were used). In this type of studies the literature recommendation is to normalize the stimuli to individual threshold units ^{32,33}. Notably we also tested the association between global activation measures and diabetic retinopathy grades in this subgroup of patients and we did not find a significant correlation. We assume that abnormalities in the HRF in this subgroup could not have driven the main findings of this study. The differences in the hemodynamic response are an effect of T2DM rather than

retinopathy (which was expected given that the inclusion criteria were anyway mild).

In sum, microvascular pathophysiology is the likely explanation for our results, in line with previously suggested pervasive injuries to the vascular bed^{16,34}. The BOLD fMRI signal change is due to variations of deoxyhemoglobin concentration in the cerebral vasculature and can be affected by local changes in blood flow, blood volume and oxygen consumption. As a consequence, the temporal and spatial characteristics of the BOLD time course can be influenced by differences in the vascular bed³⁵. It is also plausible that increased levels of baseline blood flow might reduce the BOLD signal amplitude. This should be measured in future studies using arterial spin labelling or contrast agents MRI techniques.

The use of both blocked and in particular event-related paradigms was unique in our study. The latter allowed to investigate and directly estimate the transient hemodynamic response to a short stimulus and to extract it without making assumptions as to its shape^{36,37}. This is particularly useful in the case of an event-related design because standard averaging, as in the case of standard GLM analysis of block designs, is not effective in directly estimating the event-related HRF responses. This enables the study of this hemodynamic response function as a measure of auto regulatory processes. Neuronal activation imposes an increase in oxygen demand in functionally relevant brain areas, which is managed by regulatory increases in blood supply to optimize oxygen supply³⁸. In the presence of cerebrovascular disease, the oxygen reserve may not be sufficient to respond to the stimulus, resulting in a loss of auto regulation^{39,40}. In this situation, the standard HRF is changed and induces subsequent alterations in the BOLD signal time course.

We speculate that the differences in the temporal dynamics and magnitude of BOLD responses may reflect the degree of collateralization required in patients compared with controls^{16,41}. Future studies are needed to find the local

determinants of changed HRF shape and whether they are predictive of clinical progression.

The identified BOLD signal changes in diabetic patients may therefore partially be explained by changes in the cerebral vasculature that modifies its capacity to adapt to local demands. In fact, assessment of fMRI activation in a damaged brain might depend on the constraints due to decreased oxygen delivery during activation. Consequently, these results yield an increased concern about the limits of functional MR imaging in evaluating patients with T2DM, at least using a canonical HRF. Using a standard canonical HRF to model the BOLD response may result in misestimating the response parameters. Previous event-related studies have identified significant variability in the shape of the hemodynamic response across healthy young adult⁴² and elderly subjects. Some studies have reported that hemodynamic impairment can affect fMRI signal detection³⁴. The present study confirms these findings and reports for the first time the dynamic variations of BOLD signal in individuals with type 2 diabetes in several brain regions, and at the event level. We suggest that in fMRI studies with diabetic patients, each participant's HRF should be measured using a long trial event-related study, conducted during each experimental fMRI session. Information about the hemodynamic parameters can then be used to optimize data analysis. The use of standard fixed GLM analysis of block designs might camouflage true differences in BOLD signal and consequently bias the interpretation about brain function in T2DM and other vascular diseases.

Future longitudinal studies are needed to assess the predictive value of BOLD fMRI in the assessment of auto regulatory capacity in diabetic patients. BOLD fMRI has the advantage of being a non-invasive method and may compare favourably with other approaches. Our results suggest that a simple visual activation paradigm is sensitive in detecting alterations in the hemodynamic response of individuals with type 2 diabetes.

Functional MR imaging remains a useful tool in the indirect assessment of neuronal function, but its results should be approached with caution when evaluating patients with altered hemodynamic function as in the case of type 2 diabetes. Event-related designs, as used in this study, will become very important to help extract the true shape of the hemodynamic response function, which is a promising new measure. Participants with type 2 diabetes show a different fMRI response profile: lower peak amplitude, lower dip and no undershoot before returning to baseline. Future studies will allow a more complete understanding of hemodynamic model parameters and the underlying physiology of the BOLD signal to improve the utility of functional brain mapping in the context of diabetes.

References

1. Biessels, G. J. & Reijmer, Y. D. Brain changes underlying cognitive dysfunction in diabetes: what can we learn from MRI? *Diabetes* **63**, 2244–52 (2014).
2. Biessels, G. J., Strachan, M. W., Visseren, F. L., Kappelle, L. J. & Whitmer, R. A. Dementia and cognitive decline in type 2 diabetes and prediabetic stages: towards targeted interventions. *lancet. Diabetes Endocrinol.* **2**, 246–255 (2014).
3. Ryan, J. P., Fine, D. F. & Rosano, C. Type 2 Diabetes and cognitive impairment: contributions from neuroimaging. *J. Geriatr. Psychiatry Neurol.* **27**, 47–55 (2014).
4. Espeland, M. A. *et al.* Influence of type 2 diabetes on brain volumes and changes in brain volumes: results from the Women’s Health Initiative Magnetic Resonance Imaging studies. *Diabetes Care* **36**, 90–97 (2013).
5. Brundel, M., van den Heuvel, M., de Bresser, J., Kappelle, L. J. & Biessels, G. J. Cerebral cortical thickness in patients with type 2 diabetes. *J. Neurol. Sci.* **299**, 126–130 (2010).
6. Moran, C. *et al.* Brain atrophy in type 2 diabetes: regional distribution and influence on cognition. *Diabetes Care* **36**, 4036–4042 (2013).
7. Tiehuis, A. *et al.* Cerebral perfusion in relation to cognitive function and type 2 diabetes. *Diabetologia* **51**, 1321–1326 (2008).
8. Brundel, M. *et al.* Cerebral haemodynamics, cognition and brain volumes in patients with type 2 diabetes. *J. Diabetes Complications* **26**, 205–209 (2012).
9. van den Berg, E. *et al.* A 4 year follow-up study of cognitive functioning in patients with type 2 diabetes mellitus. *Diabetologia* **53**, 58–65 (2010).
10. Ogawa, S., Lee, T.-M., Nayak, A. S. & Glynn, P. Oxygenation-sensitive contrast in magnetic resonance image of rodent brain at high magnetic fields. *Magn. Reson. Med.* **14**, 68–78 (1990).
11. Chhatwal, J. & Sperling, R. Functional MRI of Mnemonic Networks across the spectrum of Normal Aging, Mild Cognitive Impairment and Alzheimer’s Disease. *J. Alzheimer’s Dis.* **31**, S155–S167 (2012).
12. Zhou, H. *et al.* Impairments in cognition and resting-state connectivity of the hippocampus in elderly subjects with type 2 diabetes. *Neurosci. Lett.* **473**, 5–10 (2010).
13. Musen, G. *et al.* Resting-state brain functional connectivity is altered in type 2 diabetes. *Diabetes* **61**, 2375–2359 (2012).
14. Xia, W. *et al.* Altered baseline brain activity in type 2 diabetes: A resting-state fMRI study. *Psychoneuroendocrinology* **38**, 2493–2501 (2013).

15. Cui, Y. *et al.* Altered spontaneous brain activity in type 2 diabetes: a resting-state functional MRI study. *Diabetes* **63**, 749–760 (2014).
16. Carusone, L. M., Srinivasan, J., Gitelman, D. R., Mesulam, M. M. & Parrish, T. B. Hemodynamic response changes in cerebrovascular disease: implications for functional MR imaging. *AJNR Am. J. Neuroradiol.* **23**, 1222–1228 (2002).
17. Bonakdarpour, B., Parrish, T. & Thompson, C. Hemodynamic response function in patients with stroke-induced aphasia: implications for fMRI data analysis. *Neuroimage* **36**, 322–331 (2007).
18. Altamura, C. *et al.* The longitudinal changes of BOLD response and cerebral hemodynamics from acute to subacute stroke. A fMRI and TCD study. *BMC Neurosci.* **10**, (2009).
19. Dale, A. M. & Buckner, R. L. Selective averaging of rapidly presented individual trials using fMRI. *Hum. Brain Mapp.* **5**, 329–340 (1997).
20. Castelo-Branco, M. *et al.* Activity patterns in human motion-sensitive areas depend on the interpretation of global motion. *Proc. Natl. Acad. Sci.* **99**, 13914–13919 (2002).
21. Castelo-Branco, M. *et al.* Type of featural attention differentially modulates hMT+ responses to illusory motion aftereffects. *J. Neurophysiol.* **102**, 3016–3025 (2009).
22. Goebel, R., Khorrám-Sefat, D., Muckli, L., Hacker, H. & Singer, W. The constructive nature of vision: direct evidence from functional magnetic resonance imaging studies of apparent motion and motion imagery. *Eur. J. Neurosci.* **10**, 1563–1573 (1998).
23. World Health Organization. *Definition, Diagnosis and Classification of Diabetes Mellitus and its Complications - Part 1: Diagnosis and Classification of Diabetes Mellitus.* (Geneva, 1999).
24. World Health Organization. *Use of Glycated Haemoglobin (HbA1c) in the Diagnosis of Diabetes Mellitus.* (2011).
25. Brainard, D. H. The Psychophysics Toolbox. *Spat. Vis.* **10**, 433–436 (1997).
26. Pelli, D. G. The VideoToolbox software for visual psychophysics: transforming numbers into movies. *Spat. Vis.* **10**, 437–442 (1997).
27. Graewe, B. *et al.* Impaired Processing of 3D Motion-Defined Faces in Mild Cognitive Impairment and Healthy Aging: An fMRI Study. *Cereb. Cortex* **23**, 2489–2499 (2013).
28. Newsome, W. T. & Paré, E. B. A Selective Impairment of Motion Perception Following Lesions of the Middle Temporal Visual Area (MT). *J. Neurosci.* **8**, 2201–2211 (1988).
29. Penny, W., Holmes, A. & Friston, K. J. *Random effects analysis in Human Brain Function.* (Academic Press, 2003).
30. Beckmann, C. F., Jenkinson, M. & Smith, S. M. General multilevel linear modeling for group analysis in FMRI. *Neuroimage* **20**, 1052–1063 (2003).

31. Glover, G. H. Deconvolution of Impulse Response in Event-Related BOLD fMRI. *Neuroimage* **9**, 416–429 (1999).
32. Bosten, J. M. *et al.* Individual differences provide psychophysical evidence for separate on- and off-pathways deriving from short-wave cones. *J. Opt. Soc. Am. A. Opt. Image Sci. Vis.* **31**, A47–A54 (2014).
33. To, M., Regan, B., Wood, D. & Mollon, J. Vision out of the corner of the eye. *Vision Res.* **51**, 203–214 (2011).
34. Rossini, P. *et al.* Does cerebrovascular disease affect the coupling between neuronal activity and local haemodynamics? *Brain* **127**, 99–110 (2004).
35. Menon, R. S. *et al.* BOLD based functional MRI at 4 Tesla includes a capillary bed contribution: echo-planar imaging correlates with previous optical imaging using intrinsic signals. *Magn. Reson. Med.* **33**, 453–9 (1995).
36. Buckner, R. L. *et al.* Detection of cortical activation during averaged single trials of a cognitive task using functional magnetic resonance imaging. *Proc. Natl. Acad. Sci. U. S. A.* **93**, 14878–14883 (1996).
37. Josephs, O., Turner, R. & Friston, K. J. Event-related fMRI. *Hum. Brain Mapp.* **5**, 243–248 (1997).
38. Baron, J. C. *et al.* Reversal of focal 'misery-perfusion syndrome' by extra-intracranial arterial bypass in hemodynamic cerebral ischemia. A case study with 15O positron emission tomography. *Stroke* **12**, 454–459 (1981).
39. Reinhard, M. *et al.* Cerebral autoregulation dynamics in acute ischemic stroke after rtPA thrombolysis. *Cerebrovasc. Dis.* **26**, 147–155 (2008).
40. Dohmen, C. *et al.* Identification and clinical impact of impaired cerebrovascular autoregulation in patients with malignant middle cerebral artery infarction. *Stroke* **38**, 56–61 (2007).
41. Roc, A. C. *et al.* Altered hemodynamics and regional cerebral blood flow in patients with hemodynamically significant stenoses. *Stroke* **37**, 382–387 (2006).
42. Handwerker, D. A., Gonzalez-Castillo, J., D'Esposito, M. & Bandettini, P. A. The continuing challenge of understanding and modeling hemodynamic variation in fMRI. *Neuroimage* **62**, 1017–1023 (2012).

Chapter 4

Perception of bistable motion:

The role of interhemispheric integration
mechanisms

Introduction

Visual perception of motion is crucial for human survival. The information provided by moving objects and self-motion allows for an effective adaptation to the environment, especially in the interaction with other moving agents. However, the visual input of the surrounding environment is not always solvable in a unique way by computation from sensory input. The human visual brain thus needs to solve disambiguation problems, and bistable motion provide a tool to study these mechanisms. This is well instantiated by the question whether motion signals coming from co-existing contours arise from single or multiple objects. Separating a two-dimensional image into its one-dimensional components (1-D simple oriented patterns) is not completely straightforward. A 1-D pattern is one like an extended grating, edge or bar: it is uniform along one single axis and motion is perceived in general orthogonally to this axis, behind the edge of a viewing aperture or behind the borders of the receptive field of a neuron ¹.

Several primate physiology studies and human functional neuroimaging have identified numerous visual motion-sensitive areas, which are involved in the processing of motion information ²⁻⁹. The extrastriate area MT+, composed of MT/V5 proper plus a number of neighbouring regions such as the medial superior temporal area MST, is very well known to be involved in the perception of global motion ⁹⁻¹¹. It remains however not completely understood how full integration of multiple globally moving surfaces - 2-D motion - is achieved within the whole visual hierarchy, namely within higher level regions MST and dorsal stream regions within the intraparietal sulcus.

A popular laboratory technique which has frequently been used to investigate this question has involves the use of plaid stimuli, made by superimposing two gratings of different orientations ¹²⁻¹⁸. Despite being physically constant, this type of stimulus produces perceptual bistability, in which observer's spontaneously switch perception between two independent moving objects (component

motion) or one single object moving coherently (pattern motion). There is already evidence that during exposure to ambiguous bistable moving stimuli MT+ underlies the integration or segregation of motion components in the visual field and that the spontaneous switches between different perceptual interpretations are directly reflected in brain activity in this region¹⁵. There is also evidence from electrophysiological and fMRI data that cortical activity that integrates visual information across hemifields takes place at extrastriate areas involved in late visual processing and that MT+ and V1 may contribute to bilateral visual integration during early visual processing¹⁹. Furthermore, callosal connections between MT+ of both hemispheres were shown to be correlated with bistable perception in the context of binocular rivalry and interhemispheric spread of traveling waves of stimulus dominance²⁰. It is important to investigate how one can generalize to the context of interhemispheric integration of ambiguous stimuli that relate to bistable perception of objects that are either perceptually separated in both visual hemifields or perceived as a single unitary object. These regions are optimal candidates for the investigation of how non-overlapping moving surfaces comprising a bistable stimulus, restricted to individual visual hemifields, are parsed into different objects or interhemispherically integrated into a single moving pattern.

We take advantage of a paradigm leading to perceptual emergence of distinct stimulus interpretations using physically constant bistable stimuli, controlling for stability of visual input. In this way we could investigate the neural correlates of competition between bistable alternative neural representations which lead to the generation of antagonistic perceptual interpretations. Our proposed paradigm requires motion integration across interhemispheric regions that allows testing models that were proposed to account for the perceived coherent motion of a moving plaids¹². The most accepted model assumes that the true direction of motion of a plaid pattern is given by the intersection of constraints, a 2-D velocity

space where direction and velocity of the plaid's components intersect. The intersection of constraints mechanism is thought to require two successive stages of processing. The first evaluates the directions of movements of the 1-D local contours and the second computes the true direction of motion of the 2-D composite object by integrating over the output of the local analysers²¹⁻²³. It is known that the second-stage of motion processing occurs at the primate region MT (corresponding to the cortical complex MT+ in humans), which contains both component and pattern neurons responding to 1-D components of a moving pattern and to the global 2-D motion of an object, respectively. In this fMRI study we will test for the neural correlates of such stages, and whether they can be identified at single or multiregional levels.

Research on bistable perception has been strongly influenced by the debate about whether decision involves bottom-up or top-down mechanisms²⁴. The top-down view-point assumes active cognitive processes as being pivotal for stimulus reversals, while in bottom-up theories automatic and local mechanisms sensitive to adaptation during early visual processing cause the reversals²⁵. Bottom-up theories are mainly supported by evidence for adaptation of low-level localised processes²⁴. Top-down theories, on the other hand, highlight influences of higher order brain areas and cognitive processes²⁶. As there is ample evidence for both bottom-up and top-down effects in bistable perception, it has become clear that both types of effects have to be implemented in theoretical models of bistable perception.

The human visual MT+ complex seems to be pivotal for perceptual decision and the role of distinct visual regions in interhemispheric bistability and their top-down modulation needs to be elucidated.

Limitation in the temporal resolution of fMRI signals has led most researchers to focus on where information is processed in the brain - functional segregation, although functional/effective connectivity approaches have also been used. To

improve our understanding of how the brain processes information we investigated interactions between activated brain areas during perceptual decision- functional integration²⁷. We employed a model-free approach to investigate both functional connectivity, which is the simple correlation between measured time courses, and effective connectivity, which measures the directed influence one brain region exerts over another^{28–30}. The directed influences between brain regions was investigated using the concept of Granger causality^{27,31}. Causality is framed in terms of predictability. Specifically, given two discrete time courses x and y , we say that y Granger causes x if we can predict the current value of x using the past values of both x and y better than we can when using the past values of x itself alone. This method and several variants have been applied to neurophysiological data to gain insight in the direction of influences between neural systems³². We thus ask what are the brain regions subserving motion integration and surface reconstruction? We also asked what the role of parietal and frontal regions is, in particular in which concerns top-down effects.

Materials and methods

Participants

We recruited 30 healthy participants (18 male; mean age \pm standard deviation = 28.37 ± 5.48 years) to take part in the study. All participants had normal or corrected-to-normal vision and no history of neurological or psychiatric disease. Participants were naive as to the specific experimental question, except two co-authors of this study. All participants were right-handed, as confirmed by Edinburgh Handedness Inventory³³. All participants performed both the ambiguous (main task) and unambiguous (control) perceptual task.

All participants indicated informed written consent in accordance to the declaration of Helsinki. The experiments were conducted in compliance with the safety guidelines for MR research on humans. The ethical committee of the Faculty of Medicine of the University of Coimbra formally approved the study, including MRI procedures.

Stimulus presentation and apparatus

We wrote our experiments in MATLAB (The Mathworks, Inc.), using the Psychophysics Toolbox extensions^{34,35}. The stimuli were shown inside the MR scanner by means of an LCD screen (Avotec Real Eye Silent Vision 6011 - resolution 1024 x 768, refresh rate 60 Hz) located ~156 cm away from the participant (image size in the screen was 22.62° x 17.06° visual angle degrees). Participants viewed the screen through a mirror mounted above their eyes. Participants responded to visual stimuli using a fibre-optical MRI-compatible response box (Cedrus Lumina LP-400, LU400 PAIR - Cedrus Corporation, San Pedro, CA 90734, USA). To determine whether participants were able to maintain central fixation during the experimental task, eye tracking data (sample frequency 1000 Hz) were recorded inside the scanner using eye tracker software Eyelink 1000 (SR Research, Ottawa, Ontario, Canada). The eye tracker was individually calibrated with a 9-point calibration routine in the beginning of each experiment.

Ambiguous and unambiguous stimuli description

To achieve clear-cut long-range visual integration we used a bistable (i.e. ambiguous) stimulus first described by Wallach^{36,37} that elicits perception of one coherent object or two separate objects, separated by the vertical meridian. This visual paradigm forcibly requires interhemispheric integration when perceptual

coherence occurs. We also constructed a control unambiguous stimulus by adding a background texture.

The ambiguous stimulus, a descending roof-shaped pattern, consisted of angled black lines on a white background, mirrored at the vertical meridian of the visual field and moving continuously downward. A schematic representation of the stimulus is presented in Figure 4-1. After prolonged viewing under continuous motion the physically unchanged pattern produces two possible interpretations which alternate spontaneously: a single pattern moving downward - coherent motion (Figure 4-1A) - or two independent surfaces moving horizontally inward - incoherent motion (Figure 4-1B). The latter perceptual state was commonly associated with reports of an illusory structural change of the pattern, the two halves of the pattern seem to be divided by a phase offset defining a very thin line in the middle (virtual). Observers were asked to fixate the centre of the stimulus aperture, so the path of the vertices and the field halves produced during inward motion fall onto the vertical meridian of the retina. Stimulus' properties were as follows: contrast 100%; duty cycle 6%; spatial frequency 0.6 cycle/°; orientation 45° relative to x-axis (left-side image); motion speed 5 °/sec; stimulus size 10° x 11° (vertical x horizontal) visual angle in degrees; viewing distance 70 cm, reproducing the stimulus first described by Hans Wallach (1935). A central blue cross (visual angle 0.1°) was present as a fixation target at the visual midline to avoid gaze drift.

To create a fully unambiguous control stimulus, we used the same exactly bistable patterns on top of which we added grey dots (600 dots; contrast 10%; visual angle 0.2°) randomly distributed throughout the image on top of the lines (Figure 4-1C). By adding dot textures to the lines one can force perception to be fully unambiguous (100% inward moving dots on each half of the image imply incoherent perception - incoherent percept, 100% downward moving dots in the whole image imply downward perception – coherent percept). The dots moved

at the same speed as the grating pattern either coherently downward or incoherently inward. The two possible interpretations of the stimulus were thus unambiguous.

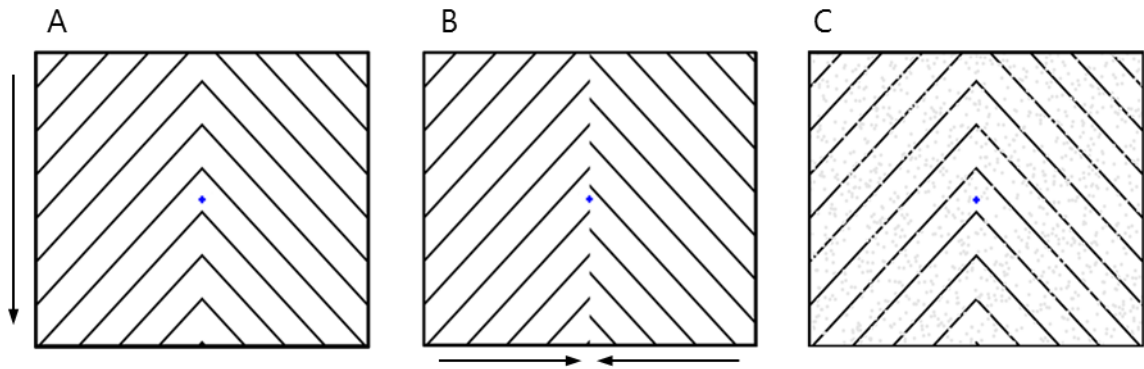


Figure 4-1. Roof-shaped moving stimulus. Bistability resulting from continuous viewing of the ambiguous moving stimulus was characterized by alternating periods of interpreting the figure in its coherent conformation (A), i.e. both sides of the image meet at the centre with no lag and are perceived as a single object moving downward, and its incoherent configuration (B), characterized by horizontal motion of both halves of the image as two independent objects moving towards the centre, an illusory border separating both sides and lines and appearing, illusorily, to be out of phase. Arrows indicate the perceived direction of motion, coherent (A) or incoherent (B). The control stimulus was an unambiguous stimulus (C) in which we added a background texture of grey dots. By adding the texture we strongly induced perception of motion of the two sides of the image in the same direction as the moving dots, either coherent or incoherent.

Experimental design and procedure

Before entering the MR scanner, participants were presented the ambiguous stimulus and instructed to look for a while, to ensure they were able to spontaneously switch perception. If a participant was initially unable to perceive the ambiguity of the image, the experimenter prompted him/her until the participant was able to perceive the figure in both interpretations. Then each

participant performed a short practice block of 2 minutes outside the scanner in order to get used to the task, in which he/she was asked to report perceptual switches by a button press. In the scanner each participant was presented ambiguous and unambiguous conditions in separate runs.

The main perceptual task consisted of presentations of blocks of the ambiguous moving stimulus for 1 minute, during which participants were asked to report the perceived direction of motion by pressing and holding one of two buttons corresponding to either a coherent motion percept or an incoherent motion percept. One experimental run with the ambiguous stimulus consisted of 6 minutes in which the following periods were sequentially presented: the static image for 10 seconds, followed by 5 blocks of 60 seconds with the ambiguous moving stimulus interleaved with 4 blocks of 15 seconds with the static image of the stimulus. During the whole experimental run participants were asked to maintain fixation at the central cross. Participants were instructed to report the perceived direction of motion during motion periods only and could abstain from reporting either of the two directions in case of doubt (which happened in less than 2% of the total duration of the experiment). A schematic representation of the experimental runs with the ambiguous stimulus is presented in Figure 4-2. Each participant performed at least 2 of these experimental runs with the ambiguous stimulus (some performed 3 or 4 runs) and were given time to rest between runs.

For the unambiguous perceptual task, at least 1 run was performed (some participants performed 2 unambiguous runs), lasting 6 minutes as well. The duration of each unambiguous motion block was randomly set to 4 to 6 seconds, and participants reported the perceived direction of motion as in the ambiguous task. Each motion period contained only one of the unambiguous percepts, either coherent or incoherent motion, and was followed by a period of 8 to 10 seconds with the static image of the stimulus. A schematic representation of the

experimental runs with the unambiguous stimulus is presented in Figure 4-3. During the whole experimental run participants were asked to maintain fixation at the central cross. Participants were instructed to report the perceived direction of motion during motion periods only. The reason why motion unambiguous periods were kept short was due to the fact that prolonged observation of the unambiguous stimulus could still result in spontaneous perceptual switches (which was reported by a few participants during pilot experimentation). Data of each participant were acquired in one single scanning session, both ambiguous and unambiguous experimental runs.

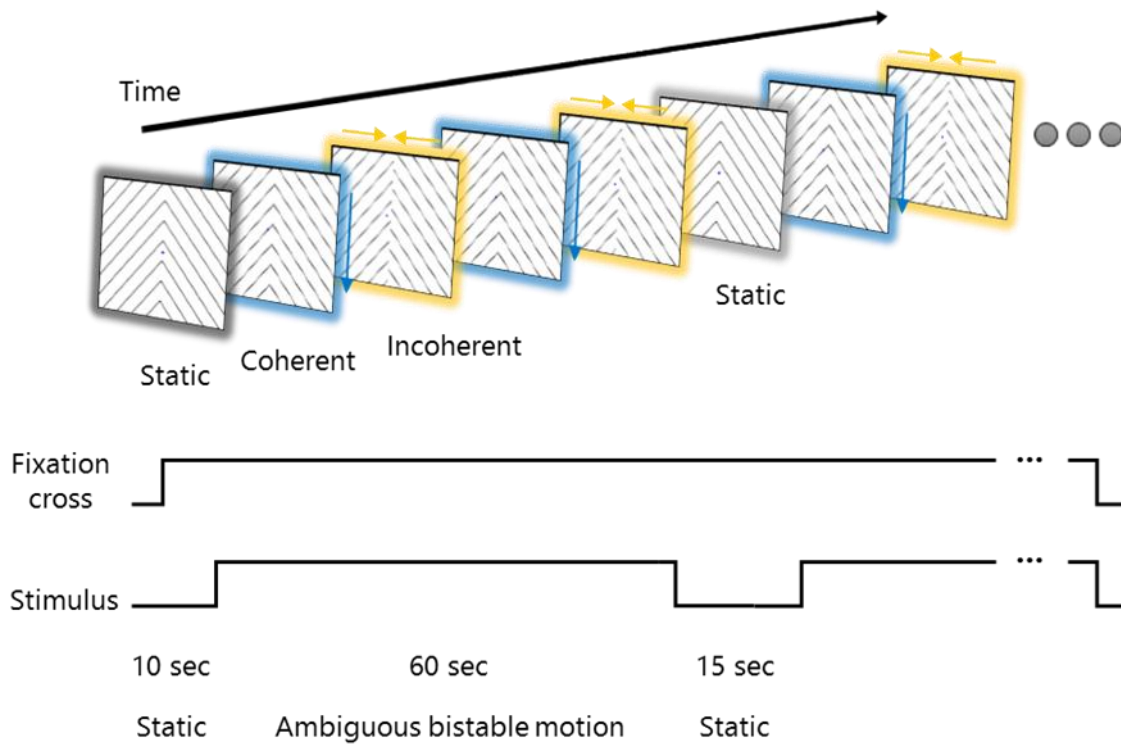


Figure 4-2. Ambiguous bistable motion task. Bistability resulting from continuous viewing of the ambiguous moving stimulus was characterized by alternating periods of interpreting the figure in its coherent conformation and its incoherent configuration. Arrows indicate the perceived direction of motion, coherent or inward. Participants were instructed to maintain fixation the whole time. Each of the five long ambiguous bistable motion periods (60 seconds each) was preceded and followed by static images of the stimulus. During motion periods participants were instructed to report each and every switch on their own perception of the stimulus.

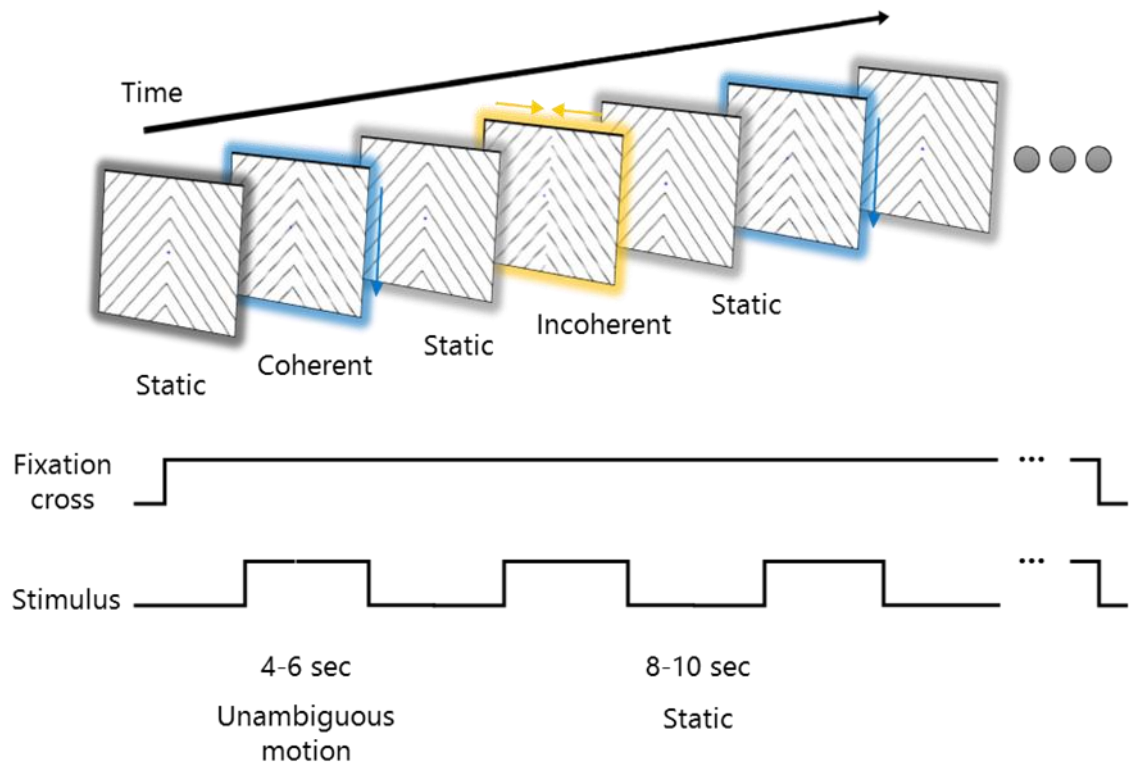


Figure 4-3. Unambiguous roof-shaped moving stimulus. In the unambiguous control stimulus we added a background texture of grey dots to the same roof-shaped pattern. By adding the texture we strongly induced perception of motion of the two sides of the image in the same direction as the moving dots, either coherent or incoherent. Arrows indicate the direction of motion. Participants were instructed to maintain fixation the whole time. Each motion period (4 to 6 seconds each) was preceded and followed by static images of the stimulus (8 to 10 seconds each). During motion periods participants were instructed to report the perceived direction of motion.

Behavioural analysis and perceptual dynamics

A bistable stimulus is characterised by the fact that there are at two different interpretations or percepts of this stimulus. None of these is absolutely stable, but rather will perception change spontaneously between the different percepts. These perceptual changes are subjective experiences and the timing of their occurrence cannot be exactly predicted. Usually there are considerable inter-

individual differences in the temporal dynamics of the perceptual changes, thus we conducted individual behavioural analysis of bistable perception data. We computed mean duration times for each percept and corresponding percentage of total bistable viewing time. Results are presented in Figure 4-4 and Figure 4-5. Bistable perception is characterised by the stochastic nature of perceptual switches. That means that the timing of a perceptual switch cannot be exactly predicted. One can only estimate the probability of a perceptual switch to occur after a particular time - the probability density function (PDF) of percept duration. For each percept the probability density function gives an estimate of how likely the occurrence of a particular duration time will be. For each participant the durations of each percept were separately binned to an adequate time-window (20 bins covering the maximum percept duration). In order to describe the statistical distribution of percept duration and study the temporal dynamics of perceptual reversals both the gamma and the lognormal distributions were fitted to the data using the maximum likelihood method to estimate the parameters, as these are two popular candidates for fitting perceptual duration data of ambiguous stimuli³⁸⁻⁴⁰. Both distributions were fitted over the same interval of the time axis, namely from zero to the longest percept duration that occurred. Results of gamma and lognormal fitting are plotted in Figure 4-6. The maximum likelihood estimates of α and β (gamma distribution) or σ and μ (lognormal distribution) parameters were calculated for each participant and the goodness of fit assessed using the Kolmogorov-Smirnov test (P -value > 0.05). The results were plotted as boxplots and are shown in Figure 4-6.

Functional image acquisition

Data were collected with a Siemens Magnetom TIM Trio 3T research scanner with a phased array 12-channel birdcage head coil (Siemens, Munich, Germany). The

MR scanning session began by acquiring a 3-D anatomical T1-weighted MPRAGE (magnetization-prepared rapid gradient echo) pulse sequence (TR = 2530 msec; TE = 3.42 msec; TI = 1100 msec; flip angle 7°; 176 single shot interleaved slices (no gap) with voxel size 1 x 1 x 1 mm; FOV 256 mm). Functional images (2 ambiguous and 1 unambiguous runs, at least) were acquired axially using a T2*-weighted gradient echo (GE) echoplanar imaging (EPI) sequence covering the whole brain. Each functional series consisted of 180 volumes (TR = 2000 msec, TE = 40 msec, flip angle = 90°, 35 interleaved slices (no gap) with voxel size 3 × 3 × 3 mm; FOV 256 mm) of BOLD signal measurements. During the whole scanning session the head of the participant was stabilized by means of foam pillows placed on both sides of the head.

fMRI data preprocessing

In the beginning of each acquisition sequence, the first 2 volumes of functional data were automatically discarded in the scanner to allow the magnetization to reach a steady state. The data were analyzed using BrainVoyager QX 2.8 (Brain Innovation, Maastricht, The Netherlands). Functional volumes were realigned, corrected for interleaved slice-scanning time and linear trends were removed from the signal. The time-series of each voxel was divided by its mean intensity to convert the data units from image intensity to fractional signal change, and to compensate for distance from the surface coil. Inter-scan head motion correction was performed by adjusting all the functional runs with the first functional run presented right after the anatomical scan. Although the motion that occurred during scanning is corrected in the data preprocessing, it is possible that residual signal changes due to motion might be present. Especially fast movements may induce fast fluctuations in the data. Therefore, we included the motion parameters estimates in the statistical analysis. We improved the motion predictors by

removing linear trends and de-meaning, ensuring that the predictors could be fitted more closely to the data (from which linear trends were also removed). To standardize the scaling of the predictors we applied a z-transformation, which scales the data according to its own variation. The motion estimates contain both low and high frequency components. However we used a high pass filter to include this high frequency noise only in the analysis. We employed a high pass filter to model only the fast movements, rather than slow motion that may correlate more closely with the actual BOLD signal. We also applied temporal high-pass filtering (2 cycles per run) to functional images in order to compensate for a slow fMRI signal drift. We then coregistered functional scans with the participants' corresponding anatomical (T1-weighted) scan and applied slight spatial smoothing (FWHM 3 mm) for individual data analysis. For group analysis we spatially normalized both anatomical and functional data into Talairach stereotactic space and moderately spatially smoothed fMRI data with a 6 mm full-width at half-maximum gaussian kernel (FWHM 6mm). The cortical sheets of the individual subjects and a template brain were reconstructed as polygon meshes based on the high-resolution T1-weighted structural three-dimensional recordings. The white-grey matter boundary was segmented, reconstructed, smoothed, morphed, and inflated as described elsewhere^{41,42}. A morphed surface always possesses a link to the folded reference mesh so that functional data can be correctly projected onto partially inflated representations.

Statistical data analysis

The subjectively defined perceptual phases between two successive switches were used for multiple linear regression analysis of the BOLD signal time course. Using the standard hemodynamic response function (HRF) modelled with a two-gamma function⁴³, hemodynamic predictors were computed from the subjects'

indications of perceptual phases, coherent and incoherent, and a general linear model (GLM) was computed for every voxel in group analysis and single-subject analysis of thirty participants. In the first approach we defined the coherent and incoherent motion periods during the ambiguous bistable motion experiment from the participants' button presses to indicate their own perception. We subtracted each individual's reaction time, computed from the unambiguous experiment, to every time of button press to reliably identify the beginning of each perceptual state. We excluded the first volume after motion periods end to avoid motion aftereffects. In the second approach we built specific separate predictors to comprise only transient switch-related activity (*switch* predictors) or activity during stable perceptual states (*phase* predictors). Switch predictors had a duration of one volume (2 seconds), also corrected for reaction time. Phase predictors included the remaining perceptual phases between switches. We excluded the first perceptual phase of each motion block to exclude unspecific stimulus onset effects. Predictors for the periods of each percept were determined from the stimulation protocol for the unambiguous experiment. Contrast analysis of the predictors comprising the two perceptual phases was used to find regions in which average activity was higher during phases of coherent motion perception than during phases of incoherent motion perception at the individual level.

Group analysis was performed with RFX-GLM (random effects), which allows modelling explicitly both within-subjects and between-subjects variance components in order to generalize findings to the population level⁴⁴. In the first level, a whole-brain RFX-GLM is computed individually to estimate condition effects (beta values) separately for each subject (first level). Then the estimated first-level mean effects enter the second level as the new dependent variable (instead of the raw data) and are analyzed across subjects (group analysis). Since the analysis at the second level explicitly models the variability of the estimated

effects across subjects, the obtained results can be generalized to the population [see e.g. ⁴⁵ for a detailed explanation].

Statistical maps were corrected for multiple comparisons using the False Discovery Rate (FDR) method for correction of multiple comparisons at P -value < 0.05 at single-subject level and P -value < 0.001 at group level. In order to present the statistical results of the group analyses we used a standard Talairach brain (both for volume slices and 3-D cortical representations of brain hemispheres). We extracted regions of interest (ROIs) from the functional statistical map to further examine the BOLD time courses in these regions and study connectivity in the functional networks comprising these regions. Functional response profiles were extracted after the subtraction of the average BOLD signal during the fixation condition. Event-related average time courses were computed for each subject. Segments representing the same perceptual state were averaged over successive runs.

We also applied a GLM deconvolution analysis within ROIs in order to separate the contributions of different events – perceptual switches. A deconvolution analysis consists of an alternative to the standard GLM analysis as the entire shape of the HRF is not fixed in advance. It allows to estimate the HRF for each event type. In this approach of linear deconvolution each condition is coded in a user-specified number of "stick" predictors each modelling separately the BOLD response at one data point with respect to the onset of that condition. This allows a more flexible fitting of the model and allows the user to compare conditions on the single data point basis [see e.g. ⁴⁶ for a detailed explanation]. Furthermore, this is done at the individual level in a way that each participant has its own HRF estimated by deconvolution.

Individual MT+ localization

We investigated the responses to bistable perceptual states within MT+ and higher order areas. The left and right MT+ was functionally located in every participant with an individual GLM analysis of the unambiguous motion experiment. The MT+ was defined as the voxels in the middle temporal region responding significantly to the balanced contrast of motion Coherent + Incoherent > Static. The individual statistical maps were thresholded at *P-value* corrected for FDR at 0.05 level.

Granger causality mapping

The directed influence between MT+ and other regions of the brain was investigated using Granger Causality Mapping (GCM) in BrainVoyagerQX, which is a technique that allows to compute measures of effective connectivity in fMRI data using the theory of Granger causality^{27,31}. In short, GCM is computed for a given ROI, which is considered the reference region. The GCM is a statistical map containing both sources of influence to the reference region and targets of influence from the reference region to any other voxel in the brain. It is argued that the most unbiased view on directed interactions is given by the difference between interactions of the reference region as source and interactions of the reference region as target, which is called the *difference* GCM (dGCM) map. We used each MT+ in the left and right hemisphere of the brain, individually localized in each participant, to compute outgoing and incoming influence to MT+. Conceptually, regions that present a positive value in the dGCM map are regions whose activation is consistently predicted by the past activation (i.e. previous time-points) of MT+. Sources of influence have a negative value in the dGCM map and are regions whose activations help to consistently predict the future (i.e. next time-points) of MT+. Individual GCMs were computed as detailed in²⁷. We then

computed RFX-GCM maps at the group level by performing one sample t-tests of connectivity measures > 0 and thresholded the maps at $P\text{-value} < 0.05$ with Bonferroni correction for multiple comparisons.

To be able to compute GCM maps we could not use the split protocols according to reported perceptual switches, as individual conditions (coherent/pattern motion and incoherent/component motion) had variable and often too short durations. We computed GCMs using the whole ambiguous bistable motion periods as a single condition, in order to get an estimate of connectivity between brain regions during the perceptual decision task.

Results

Behavioural analysis

The dynamics of bistability was studied based on the duration of the reported percepts. The perceptual changes are subjective experiences and the timing of their occurrence cannot be exactly predicted. Usually there are considerable inter-individual differences in the temporal dynamics of the perceptual changes. Thus, we individually calculated the average duration of each percept, as well as the percentage of total time reporting coherent or incoherent perception, according to the reported reversals. The results are plotted in Figure 4-4.

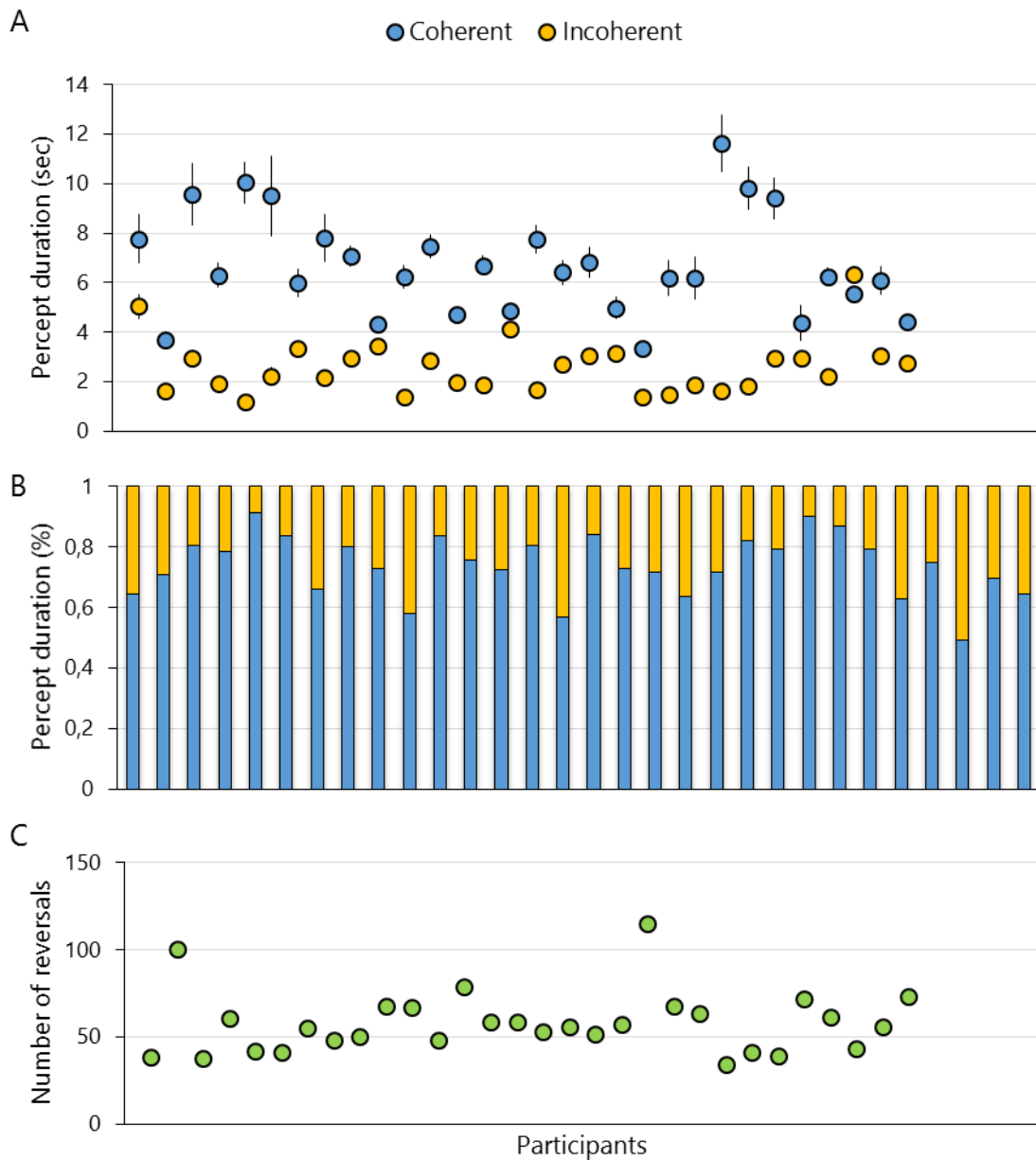


Figure 4-4. Inter-individual variability of average percept durations during ambiguous bistable stimulation. (A) Each dot represents the average duration of each percept. Whiskers represent \pm SEM. (B) Average percentage of total time viewing each percept. (C) Number of reversals reported by each participant.

During bistable ambiguous stimulation participants perceived on average the coherent condition for 6.71 ± 0.38 sec (mean \pm standard error of the mean) while the mean duration of the incoherent condition was 2.6003 ± 0.21 sec (Figure

4-5A). Moreover, the mean duration of the coherent percept was significantly longer than that of incoherent (P -value < 0.0001, Wilcoxon signed rank test). In the present study, bistability is not equiprobable, as in the Necker cube. We observed that rivalry was asymmetrical and biased towards coherent motion. Similar to what is perceived with plaids the present stimulus was always first seen moving coherent, describing a descending global motion⁴⁷. We estimated an average $74\pm 2\%$ probability of perceiving coherent motion - in other words, incoherent motion was seen an average of $9\pm 2\%$ of the total viewing time (see Figure 4-5B). The inter-individual variability of number of reversals reported is presented in Figure 4-5C.

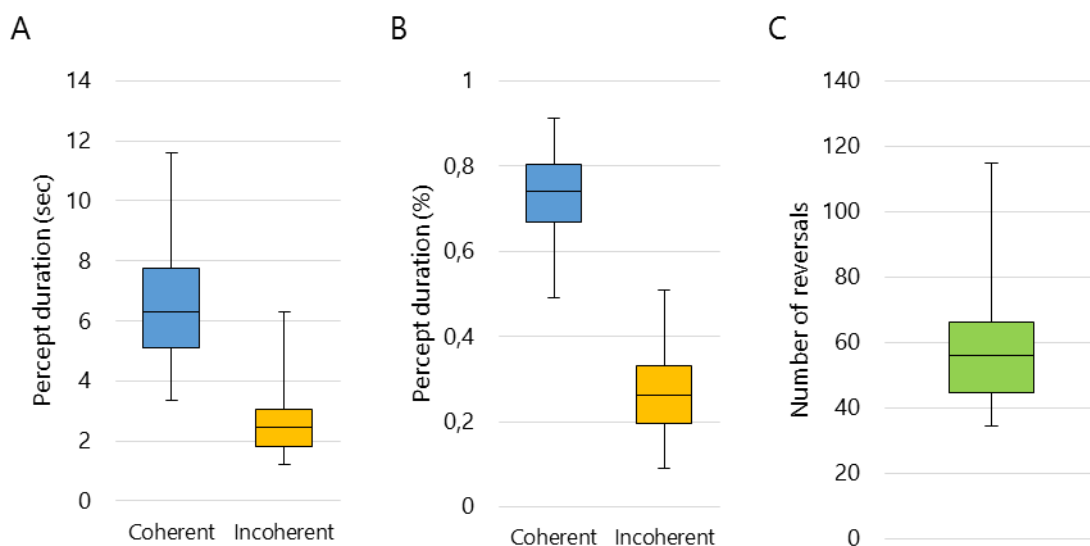


Figure 4-5. Group average percept durations and number of reversals during ambiguous bistable stimulation. Each box with whiskers presents the average duration of each percept (A) or the average perceptual dominance measured as percentage of total time viewing each percept (B) in 30 participants, displaying median, 25% and 75% quartile, and extreme values. The mean duration of the coherent percept was significantly longer than that of incoherent (P -value < 0.0001, Wilcoxon signed rank test). Durations were calculated as the difference between consecutive reported reversals. (C) Inter-individual variability of number of reversals.

Although other alternative percepts were compatible with the ambiguous stimulus (e.g. oblique orthogonal motion of both halves towards the centre) these were found in pilot studies to be rare events and were seldom reported by participants. At any rate, for the purposes of the present study, the alternative configurations could be safely categorized as incoherent motion since a separation of both halves of the image was a common feature to all.

Similarly to other bistable stimuli, the durations of each percept followed a gamma or lognormal distribution (Figure 4-6A), which are typical of perceptual rivalry and denote the presence of competing neural representations^{39,48}. We individually assessed the gamma and lognormal fit to the histogram of each percept durations with Kolmogorov-Smirnov test and considered a good fit for a *P-value* > 0.05, showing no significant deviation. The results are plotted as boxplots and are shown in Figure 4-6B. The lognormal distribution somehow produces a better fit to durations of the coherent percept, judged by taking into account the median *P-value* (0.46 for lognormal fit and 0.45 for gamma fit) and the 25%-to-75% boxes (Figure 4-6B on top). The *P-value* of lognormal fit was higher (representing a better fit) than the *P-value* of gamma fit to coherent duration in 16 participants against better gamma fit in 14 participants. On the other hand durations of incoherent percept are better described by a gamma distribution (median *P-value* of 0.56 for gamma fit and 0.28 for lognormal fit). We observed a better gamma fit to incoherent duration in 17 participants against better lognormal fit in 11 participants. Overall, for both coherent and incoherent percepts, only 2 out of 30 participants failed to achieve a significant gamma or lognormal fit (*P-value* < 0.05) for both coherent and incoherent duration. The rejection of both gamma and lognormal fits (as well as *P-values* not significantly larger than 0.05) might be due to low number of data points, i.e. durations, in individual data sets (mean number of reversals per participant were about 58).

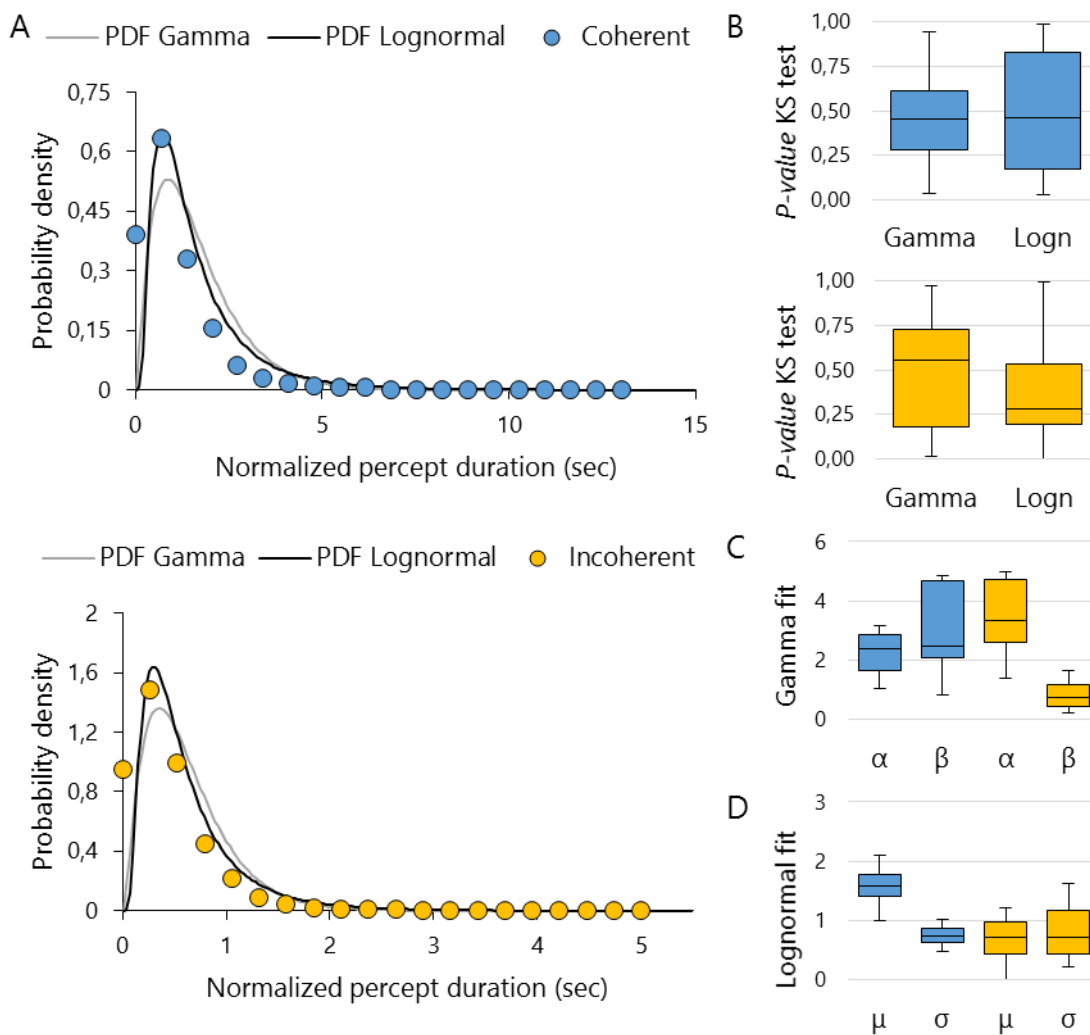


Figure 4-6. Distribution of percept durations during ambiguous bistable stimulation. (A) The group average coherent or incoherent percept durations (30 participants) are well described by a gamma (grey line) or lognormal distribution (black line). The dots are histograms of each percept normalized duration, obtained by first normalizing percept durations per observer by dividing by the mean, and then pooling data over observers. The durations are therefore dimensionless, in this case. (B) Individually, the distribution of durations are adequately fit into a gamma or lognormal distribution for 28 out of 30 participants. The quality of the fit was assessed by Kolmogorov-Smirnov test and rejected for P -value < 0.05 . The distributions of individual P -values of the fits are shown as box plots for coherent (top) and incoherent (bottom) percepts. Distribution of individual fit parameters of gamma (C) and lognormal (D) distributions are shown as boxplots for coherent and incoherent percepts, displaying median, 25% and 75% quartile, and extreme values.

On the other hand, the unambiguous stimulus clearly produced unequivocal either coherent or incoherent percepts which were readily reported as such by participants and concurred with the direction of motion followed by the dotted texture, i.e. coherent configuration when dots moved downward and incoherent configuration when dots moved inward. Moreover, the perceptual properties of perceiving a coherent or incoherent percept (e.g. lines in or out of phase, disparity in depth perception) were reported by subjects to be similar to the ones elicited by the ambiguous stimulus.

Single-subject analysis in MT+

Pattern and component global percepts (first GLM approach)

The probability map of location of MT+ across participants is shown in Figure 4-7A. Figure 4-7B and Figure 4-7C show the activity elicited in MT+ by coherent pattern and incoherent component motion during ambiguous stimulation across participants. One can clearly see a gradient of activity levels depending on whether participants integrate information from both hemispheres and perceive one coherent surface (pattern motion) or do instead perceive two incoherent surfaces (component motion). The GLM beta values that explain signal changes are in accordance with the anticipation of higher signal changes in response to component than pattern motion, both in ambiguous and unambiguous experiments. Average group data (Figure 4-8 and Table 4-1) confirmed that pattern motion provoked, on average, significantly lower activity than component motion, which demonstrates the effect does not come from a single participant, as further demonstrated by random effects analysis. Notably, activity elicited by the unambiguous motion stimulus was higher than activity in response to the ambiguous bistable stimulus in MT+.

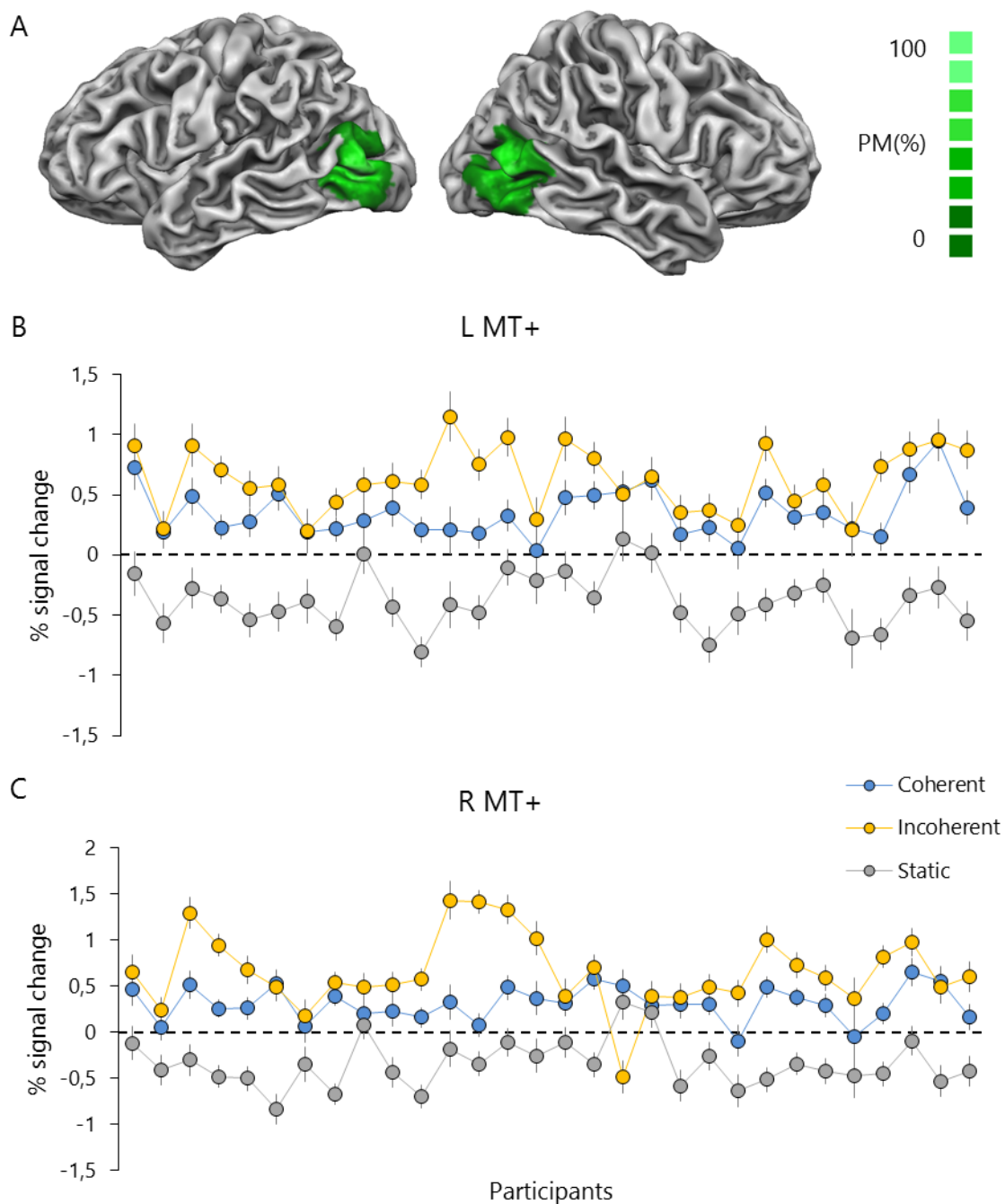


Figure 4-7. (A) Probability map of individual MT+ regions individually defined in all thirty participants. The map is superimposed on a template reconstruction of the cortex in Talairach space. (B, C) Group analysis of the ambiguous experiment individually defined left (B) and right (C) complex MT+ across participants (each dot depicts data for one participant). Activity within MT+ during ambiguous stimulation is modulated by the perception of one coherently moving surface (coherent), two incoherently moving surfaces (incoherent) or no moving surface (static). Average activity is higher when two moving surfaces are perceived. Whisker represent \pm SEM.

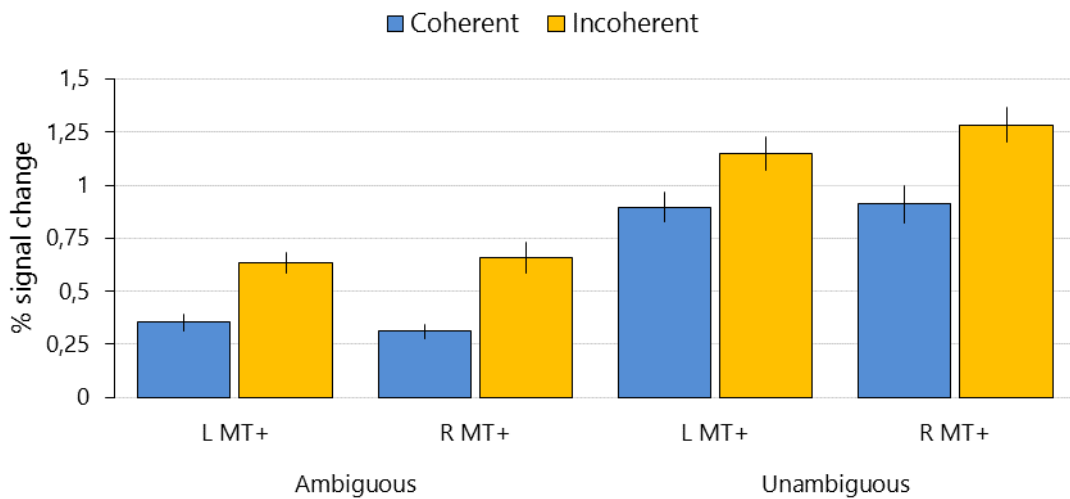


Figure 4-8. Average group activity in MT+ during the ambiguous bistable motion experiment and in the control experiment with unambiguous motion. Note that for each MT+, there was not a significant interaction of type of experiment (ambiguous or unambiguous) with the percept (coherent or incoherent) but the response to component motion (incoherent) was significantly higher than the response to pattern motion (coherent), in both ambiguous and unambiguous experiments, in which participants do not have to explicitly decide on the perceived condition (see Table 1 with two-way repeated measures ANOVA and post hoc tests, *P-value* < 0.001 in all comparisons corrected with Bonferroni).

Table 4-1. Two-way repeated measures ANOVA of BOLD response to ambiguous bistable and unambiguous percepts within left and right MT+

		L MT+	R MT+
	df (error)	1 (29)	1 (29)
Main effect of <i>Type</i> of experiment Ambiguous vs Unambiguous	F	42.789	37.436
	P-value	< 0.001	< 0.001
	η^2	0.596	0.563
	df (error)	1 (29)	1 (29)
Main effect of motion <i>Percept</i> Incoherent vs Coherent motion	F	72.690	58.377
	P-value	< 0.001	< 0.001
	η^2	0.715	0.668

	df (error)	1 (29)	1 (29)
Interaction <i>Type x Percept</i>	F	0.279	0.129
	P-value	0.602	0.722
	ηp^2	0.010	0.004

ηp^2 = partial eta squared, a measure of the estimated effect size; df = degrees of freedom. Pairwise comparisons were corrected with Bonferroni correction for multiple comparisons. When sphericity was not verified we used a Greenhouse-Geisser correction.

When we look at the event-related time courses of response to pattern/coherent and component/incoherent responses in the control unambiguous experiment, in which every motion period is preceded by a static stimulus and the baseline is common to both percepts, we clearly observe a higher response to component/incoherent motion, as corroborated by the statistical test to the group GLM beta values presented. In the ambiguous stimulation, due to random and variable percept durations, only the phase of condition-specific time-courses can be reliably considered. The apparent difference in peak latency between percepts in ambiguous experiment seems to be misleading as it is not present in the common static baseline situation of unambiguous experiment. The individual event-related analysis of both ambiguous and unambiguous motion is presented in Appendix.

Perceptual switches and perceptual phases (second GLM approach)

To investigate activation associated with perceptual transitions we built a GLM that included the static stimulus, spontaneous perceptual changes (to coherent and to incoherent motion) and stable perceptual phases (of coherent and incoherent motion) as regressors. The results of the standard GLM analysis of

transient signal changes in response to perceptual switches within individually defined MT+ complex in both hemispheres is presented in Figure 4-9.

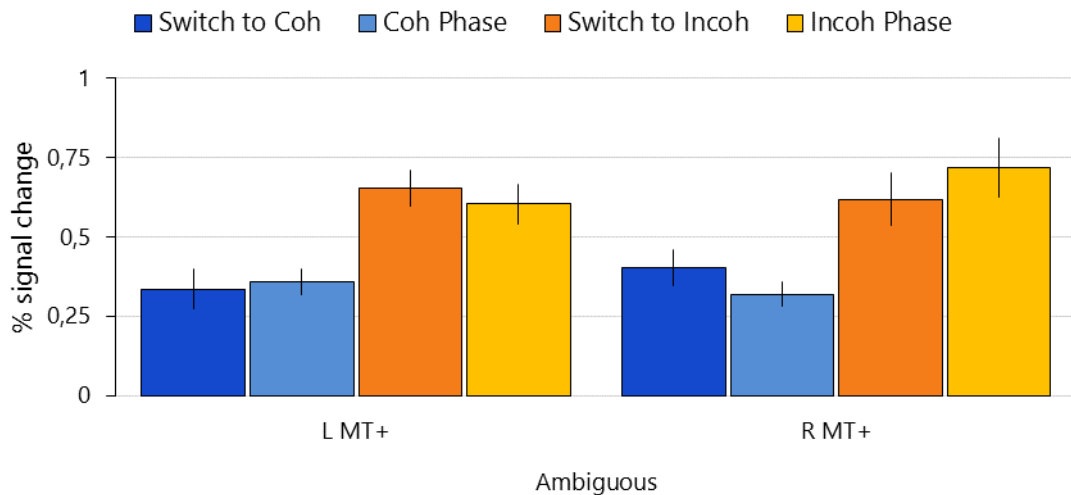


Figure 4-9. Average group activity in MT+ during the ambiguous bistable motion experiment in response to perceptual switches and perceptual phases. There was not a significant difference in response to perceptual switches compared to the response to the perceptual phase of the same percept (see Table 2).

This analysis revealed that the difference in response to coherent or incoherent perceptual phases is similar to the response to global pattern or component percepts in MT+ when considering the whole period between transitions, as computed in the first approach (Figure 4-8). The specific response to perceptual switches is not significantly different from the response to corresponding perceptual phases within MT+. A repeated measures ANOVA with a Greenhouse-Geisser correction, presented in Table 4-2, determined that mean BOLD response to perceptual switches and phases differed statistically significantly between pattern and component motion percepts in both left and right MT+ complex. However, no statistically significant difference was observed between the responses to perceptual switches or perceptual phases of the same percept (coherent/pattern or incoherent/component motion).

Table 4-2. One-way repeated measures ANOVA of BOLD activity within left and right MT+ in response to perceptual switches and perceptual phases during bistable motion

		L MT+	R MT+
	df (error)	1.966 (87)	2.230 (87)
Main effect of perceptual <i>Switches and Phases</i>	F	12.571	8.245
	P-value	< 0.001	< 0.001
	ηp^2	0.302	0.221
Switch to Coherent vs Coherent Phase		1.000	0.692
Switch to Coherent vs Switch to Incoherent		0.008	0.292
Switch to Coherent vs Incoherent Phase		0.009	0.002
Coherent Phase vs Switch to Incoherent	P-values	< 0.001	0.016
Coherent Phase vs Incoherent Phase		< 0.001	0.002
Switch to Incoherent vs Incoherent Phase		1.000	1.000

ηp^2 = partial eta squared, a measure of the estimated effect size; df = degrees of freedom. Pairwise comparisons were corrected with Bonferroni correction for multiple comparisons. When sphericity was not verified we used a Greenhouse-Geisser correction.

As the standard event-related analysis suffers from limitations related to the fact that it does not take into account the variable perceptual durations, we employed a deconvolution analysis to investigate the time course of responses. The average time course of response to perceptual switches as determined by deconvolution is presented in Figure 4-10. As to exclude the significant influence of a particular participant, we looked at individual deconvolution analysis results, presented in

the Appendix. Interestingly, we could observe a higher response to perceptual switches to component/incoherent motion than to pattern/coherent motion, suggesting that MT+ might be involved more in the transitions (incoherent) that do not require higher level integration. This effect do not seem to come from a single participant, as many present a similar response profile, both in left and right MT+, although also several participants seem to show no differential response to both types of perceptual switches. The response to the perceptual switch to pattern/coherent motion however seems to be thoroughly low across participants, further suggesting the involvement of other regions in this type of switch. At the group level, we observed that signal change in response to the switch to component/incoherent motion was statistically significantly higher than the response to the switch to pattern/coherent motion both in left (P-value = 0.0014, paired t-test) and right MT+ (P-value = 0.0486, paired t-test) but there were no significant differences between perceptual switches and perceptual phases of the same percept (see Figure 4-9 and Table 4-2).

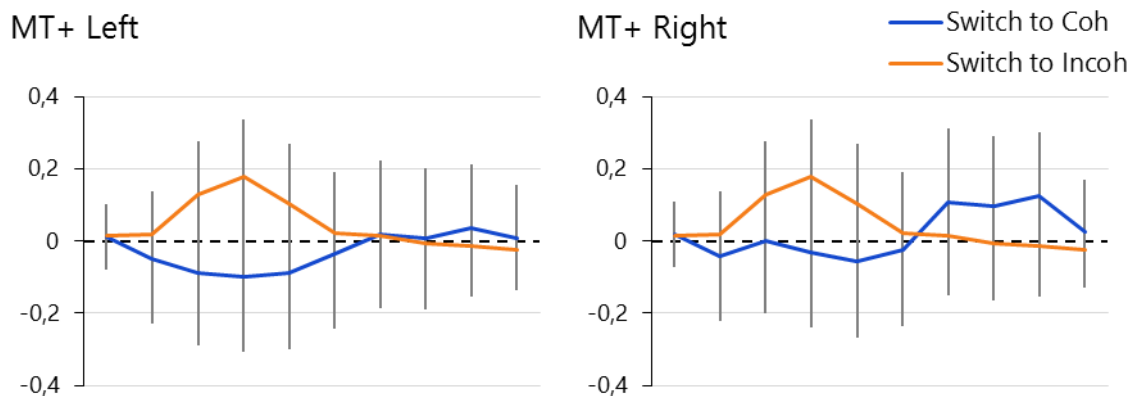


Figure 4-10. Average time course of response to perceptual switches in MT+ during the ambiguous bistable motion experiment as empirically extracted by deconvolution analysis.

Group analysis

Bistable perception of motion (first GLM approach)

The whole brain RFX-GLM group analysis of contrast differences between ambiguous bistable percepts of motion, either coherent or incoherent, and the static stimulus revealed regions with significant changes in motion selective regions, as well as parietal and frontal decision areas. Figure 4-11 shows the clusters with highest contrast superimposed on a template inflated reconstruction of the cortical sheet in Talairach space, at significant P -value < 0.001 corrected for FDR and cluster size corrected. The coordinates of each cluster's peak voxel in Talairach space are presented in Table 4-3. The ROI-GLM analysis within these clusters revealed that most regions show higher signal change during the percept of component/incoherent motion than pattern/coherent motion, as shown in Figure 4-12. On the other hand, the analysis of signal change within the same regions during the unambiguous experiment shows that most regions exhibit a similar amplitude of signal change in response to coherent or incoherent motion, as shown in Figure 4-13. This suggests a different role for high level regions during ambiguous vs non ambiguous percepts. In the latter, perceptual decision is almost automatic. Notably, visual regions MT+ and V3/V3A in both hemispheres, as well as superior parietal lobule, show a clear difference in response amplitude between coherent and incoherent percepts in both ambiguous and unambiguous experiments. Although this difference in measures of global signal change in the GLM analysis, the event-related responses show similar profiles between percepts. Note that GLM computation on the other hand assumes the same baseline and corrects for different duration for all conditions in the design matrix, avoiding this limitation of average event-related responses.

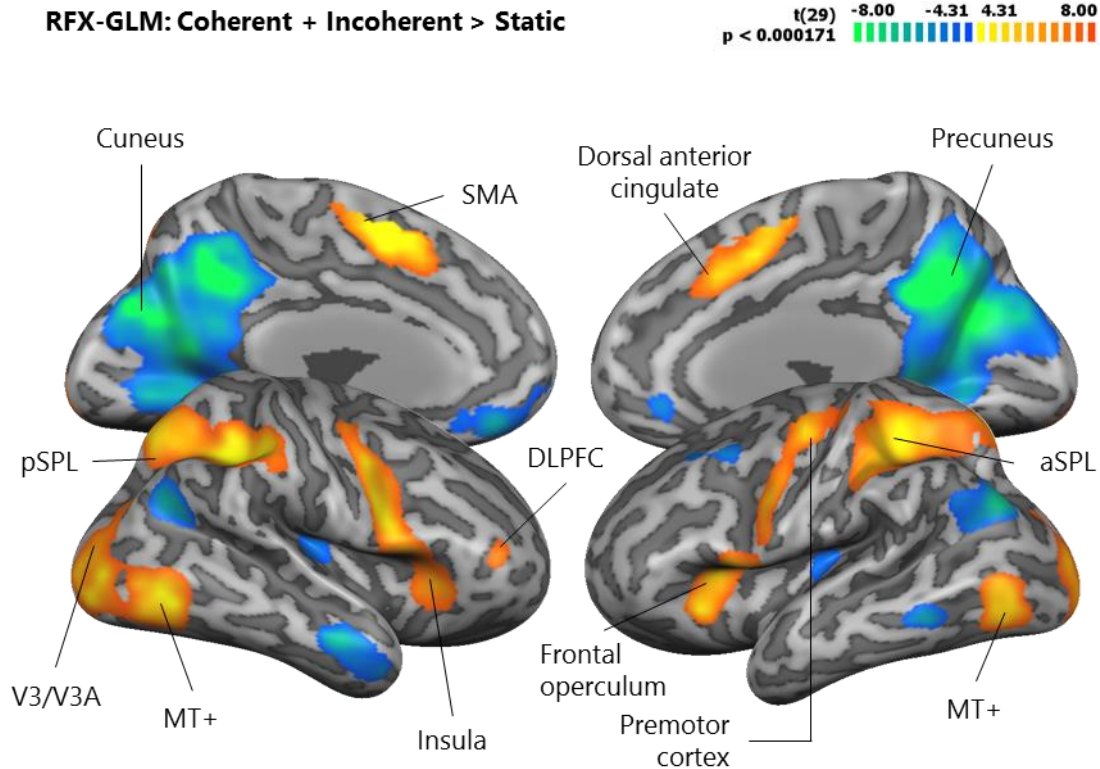


Figure 4-11. Signal changes during ambiguous bistable motion. Group analysis shown in a template inflated brain in Talairach space. RFX-GLM contrast analysis revealed significant clusters (P-value corrected for FDR at 0.001 level) in motion selective regions and decision areas. DLPFC, dorsolateral prefrontal cortex; MT+, middle temporal complex; a/pSPL, anterior/posterior superior parietal lobule; V3A, extrastriate V3 accessory.

Table 4-3. Summary of whole-brain RFX-GLM analysis showing significant clusters with contrast Coherent + Incoherent motion percepts > Static stimulus

Region	Peak coordinates (Talairach)			t(29)	Number of voxels
	X	Y	Z		
Supplementary Motor Area (SMA)	-6	5	43	6.81	1896
Dorsal Anterior Cingulate Gyrus (BA32)	-3	2	50	9.51	2304

L Premotor cortex (BA6)	-54	5	34	5.93	4351
R Premotor cortex (BA6)	42	-1	40	6.43	7235
L Insula/Frontal operculum	-30	20	-2	6.85	6050
R Insula/Frontal operculum	45	8	1	6.16	6291
L anterior Superior Parietal Lobule	-33	-37	49	6.69	10626
R anterior Superior Parietal Lobule	49	-37	49	7.26	9314
L posterior Superior Parietal Lobule	-24	-73	25	4.38	220
R posterior Superior Parietal Lobule	27	-76	31	4.98	835
L MT+	-51	-70	3	5.19	2931
R MT+	48	-61	-2	6.51	5545
L V3/V3A	-27	-85	13	6.00	2110
R V3/V3A	30	-82	13	5.45	3340
L Putamen	-27	-1	4	5.71	986
R Putamen	21	2	-5	5.92	947
R Dorsolateral Prefrontal Cortex	42	45	16	4.11	752
Posterior Cingulate Gyrus (BA30)	3	-43	34	-9.44	8100
L Parahippocampal Gyrus	-18	-46	-2	-7.48	2555
R Parahippocampal Gyrus	21	-40	-5	-5.61	3155
Cuneus	0	-67	22	-8.25	24638
Precuneus	-3	-64	22	-8.06	16590

BA, Brodmann area; R, right; L, left. The number of voxels is based on the resolution of the anatomical dataset 1 x 1 x 1 mm³.

P-value corrected for FDR at 0.001 level and cluster size corrected.

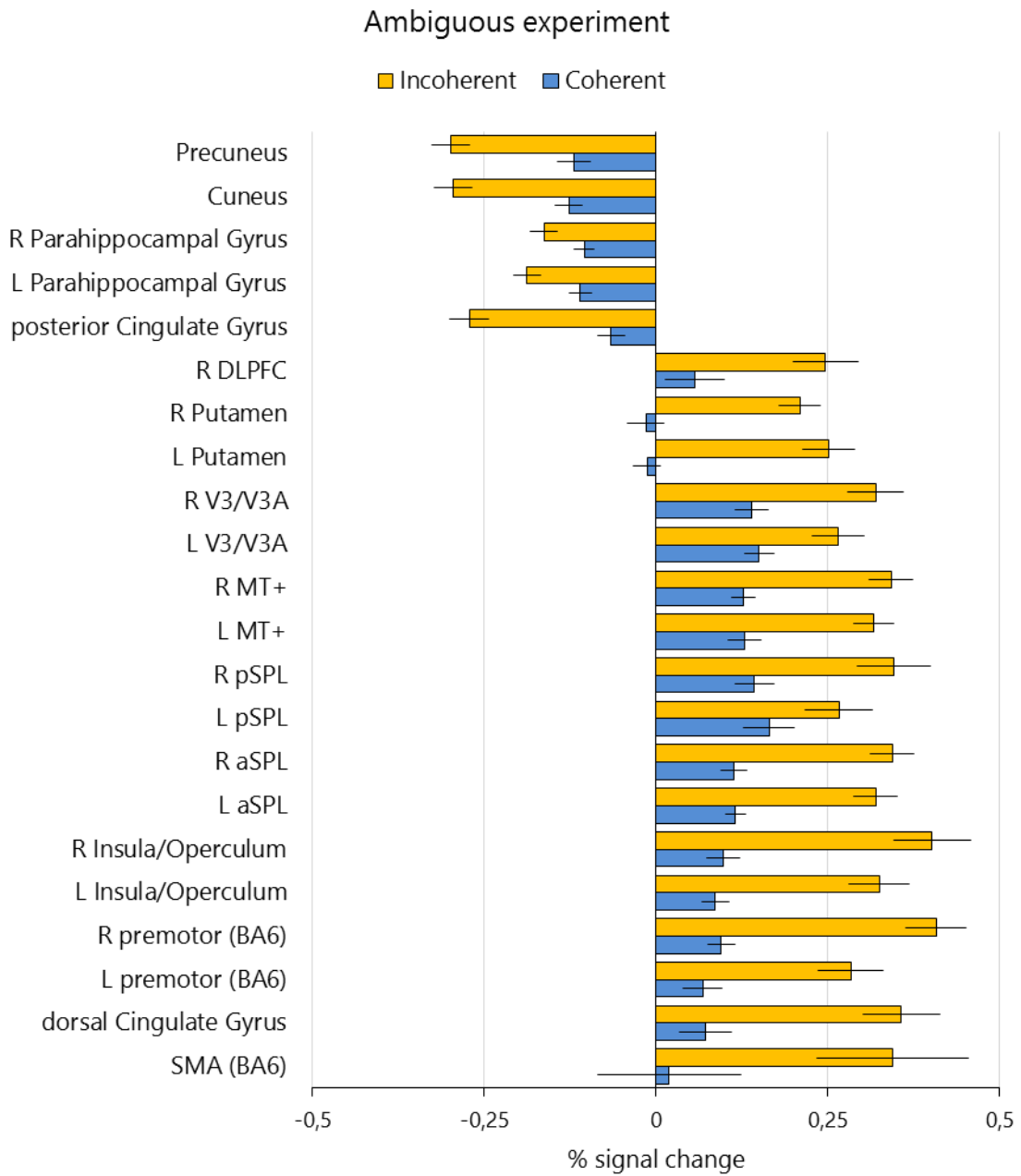


Figure 4-12. Average group activity during ambiguous bistable motion presentation in clusters that showed significant signal change in whole-brain RFX-GLM analysis of the contrast coherent + incoherent > static. Whiskers represent \pm SEM. Note that we observed higher signal change in response to incoherent than coherent motion percept in all identified regions, including motion selective regions, as well as parietal and frontal decision areas.

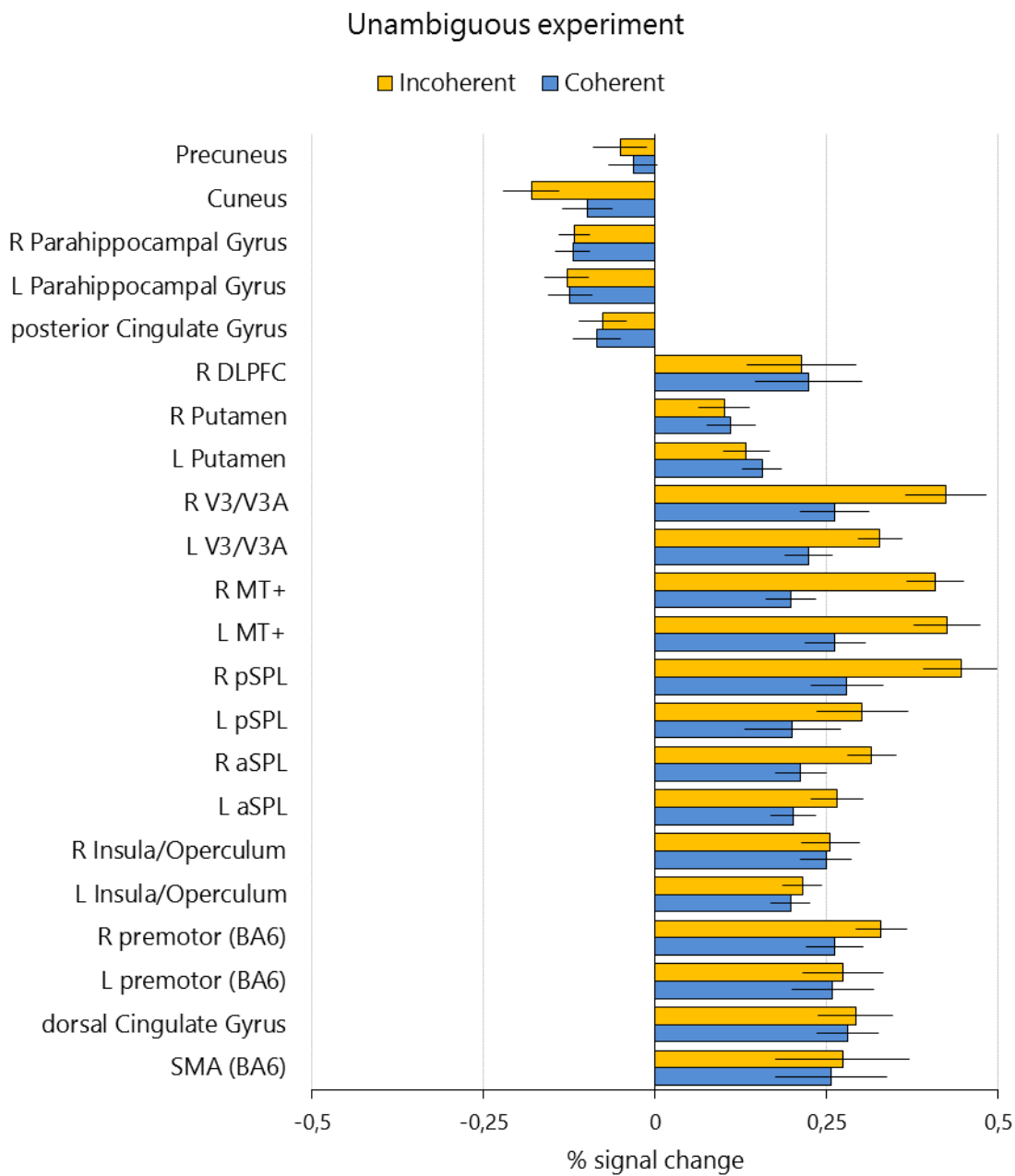


Figure 4-13. Average group activity during unambiguous bistable motion presentation in clusters that showed significant signal change in whole-brain RFX-GLM analysis of the ambiguous experiment with the contrast coherent + incoherent > static. Whiskers represent \pm SEM. Note that most regions exhibit similar responses to both motion percepts, except visual areas.

Whole brain response to perceptual switches (second GLM approach)

The statistical map of the whole brain RFX-GLM analysis of switch-related transient activity is presented in Figure 4-14 showing cortical areas and Figure 4-15 showing cerebellum and sub-cortical regions. In Table 4-4 we show Talairach coordinates, t-value and number of voxels of each cluster showing a significant contrast of perceptual switch-related activity compared to perceptual phase-related activity.

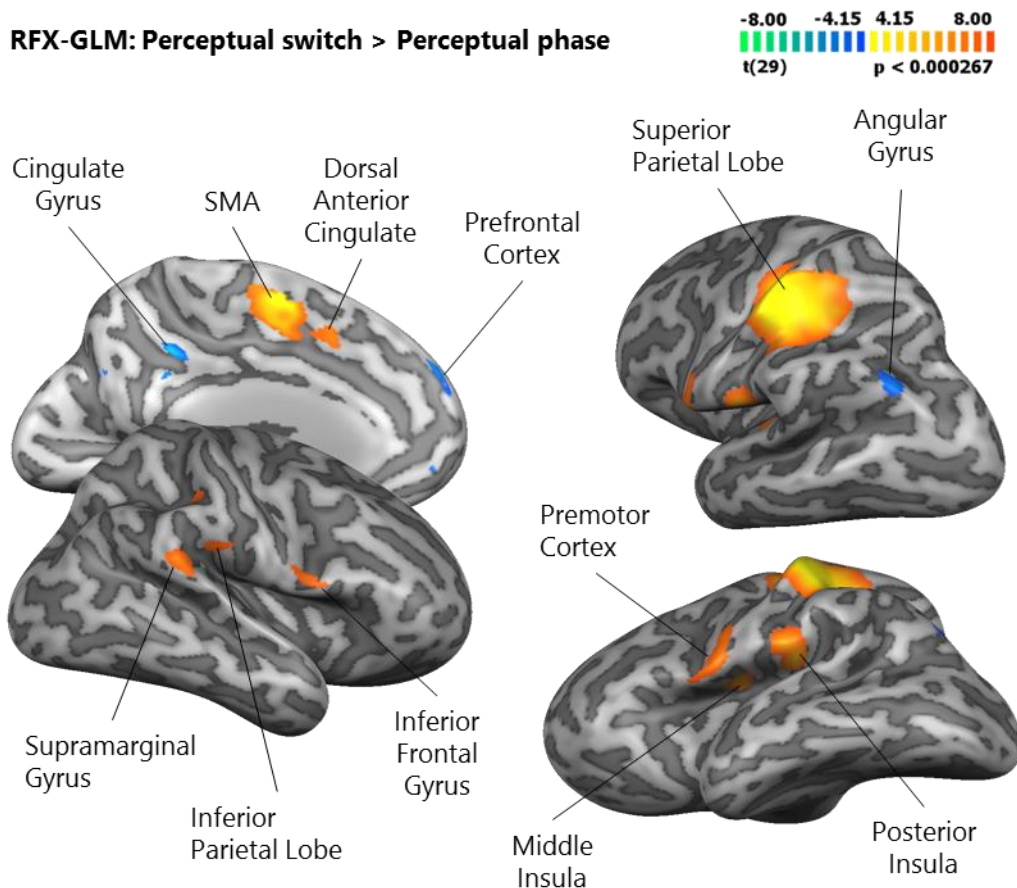


Figure 4-14. Group analysis of switch-related transient signal changes shown in a template inflated cortical sheet in Talairach space. RFX-GLM contrast analysis of switch-related activity revealed significant clusters (P -value corrected for FDR at 0.01 level) in motor, premotor and decision areas but not in motion selective regions. SMA, supplementary motor area.

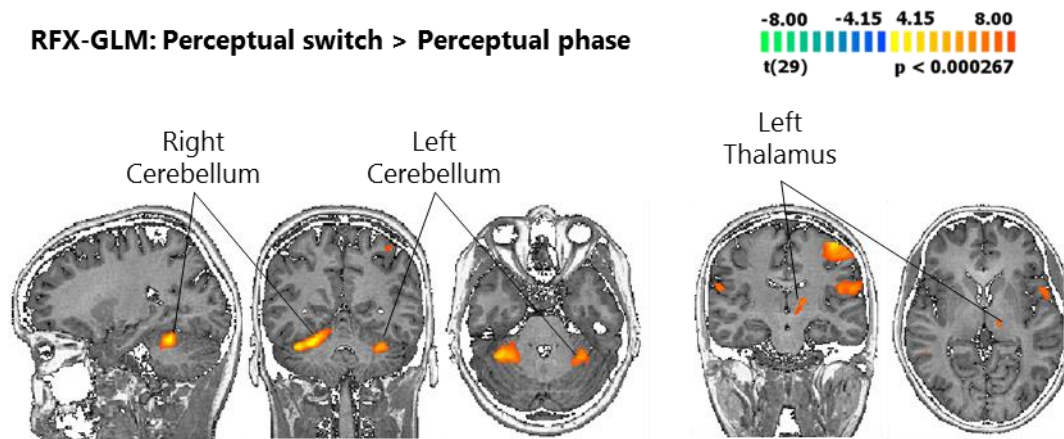


Figure 4-15. Group analysis of switch-related transient signal changes shown in a template brain in Talairach space. RFX-GLM contrast analysis of switch-related activity revealed significant clusters (P -value corrected for FDR at 0.01 level) in the cerebellum and left thalamus.

Table 4-4. Summary of RFX-GLM results revealing clusters with significant (P -value corrected for FDR at 0.01 level) perceptual switch-related transient responses

Region	Peak coordinates (Talairach)			t(29)	Number of voxels
	X	Y	Z		
L Superior Parietal Lobule (SPL)	-45	-28	52	10.06	10510
R Cerebellum	27	-46	-23	9.56	3652
Supplementary Motor Area (SMA)	-6	-3	52	8.46	2250
L Cerebellum (Culmen)	-30	-46	-26	7.23	746
L Middle Insula (BA13)	-42	-7	16	7.23	726
L Posterior Insula	-48	-22	16	7.15	1986
L Thalamus	-15	-19	10	6.41	263
R Superior Parietal Lobule (SPL)	51	-25	28	6.04	544
L Premotor Cortex (BA 6)	-57	2	13	5.84	1313

Dorsal Anterior Cingulate (BA32)	-6	11	37	5.82	498
R Supramarginal Gyrus	54	-34	22	5.79	831
R Inferior Frontal Gyrus (IFG)	54	2	19	5.17	332
R Inferior Parietal Lobule (IPL)	48	-34	46	4.78	392
Cingulate Gyrus (BA 31)	-6	-37	34	-7.23	658
L Prefrontal Cortex (BA9/10)	-3	47	31	-6.02	813
L Precuneus/Angular Gyrus (BA39)	-39	-67	37	-5.84	1290
R Posterior Insula	-9	65	19	-5.74	342

R, right; L, left. The number of voxels is based on the resolution of the anatomical dataset 1 x 1 x 1 mm³.

We found significant signal changes in cortical motor or premotor areas, which can be attributed to the button presses to report perceptual switches. We also found significant responses in cortical decision and executive areas, such as the insula, prefrontal cortex, dorsal anterior cingulate and inferior frontal gyrus. Notably, the cluster with the highest significant signal change was found in the left superior parietal lobule, a somatosensory region known for its involvement in perceptual transitions. Interestingly, we found highly significant signal changes bilaterally in the cerebellum and in left thalamus, in response to perceptual switches as compared to perceptual phases of coherent or incoherent percepts. In Figure 4-16 to Figure 4-20 we present the group results of RFX-GLM as plots of beta values for each condition, which are measures of global % signal change. Additionally, for each significant cluster identified we also show the time courses of response to both perceptual switches and perceptual phases, as extracted from deconvolution analysis.

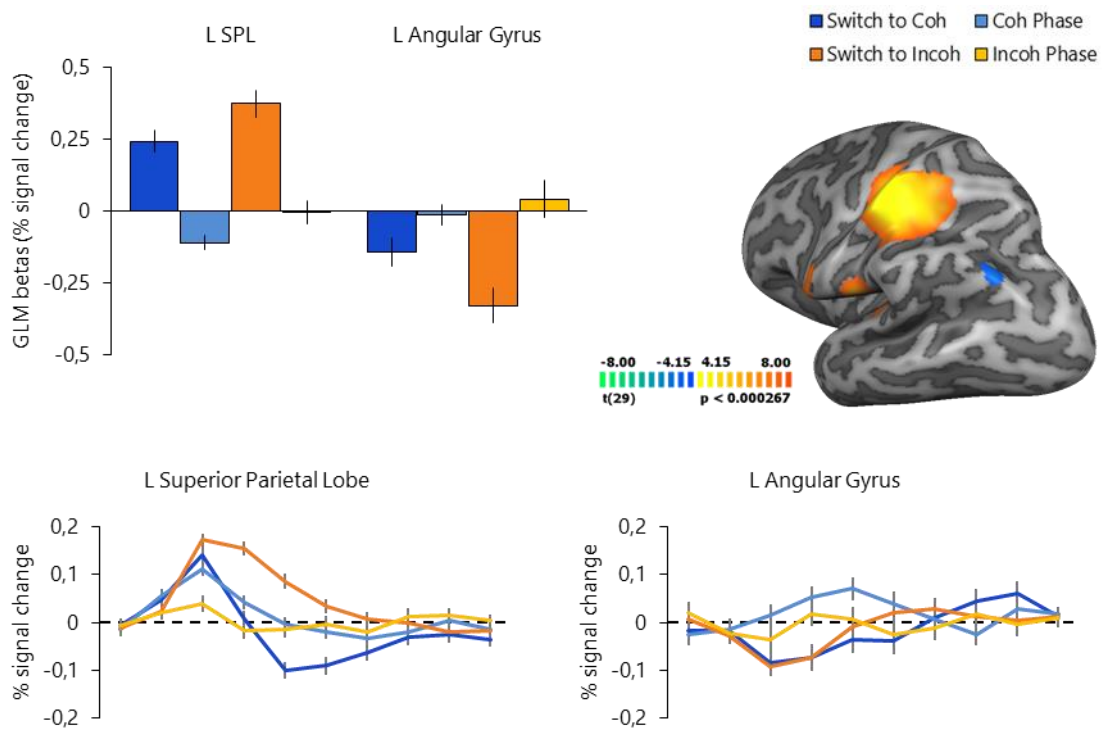


Figure 4-16. RFX-GLM beta values and time courses of responses to perceptual switches and perceptual phases extracted with deconvolution analysis within significant clusters represented in a template Talairach brain. Note that angular gyrus show deactivation in response to perceptual switches, while SPL shows increased activation in response to switches when compared with responses during perceptual phases, particularly in the incoherent condition.

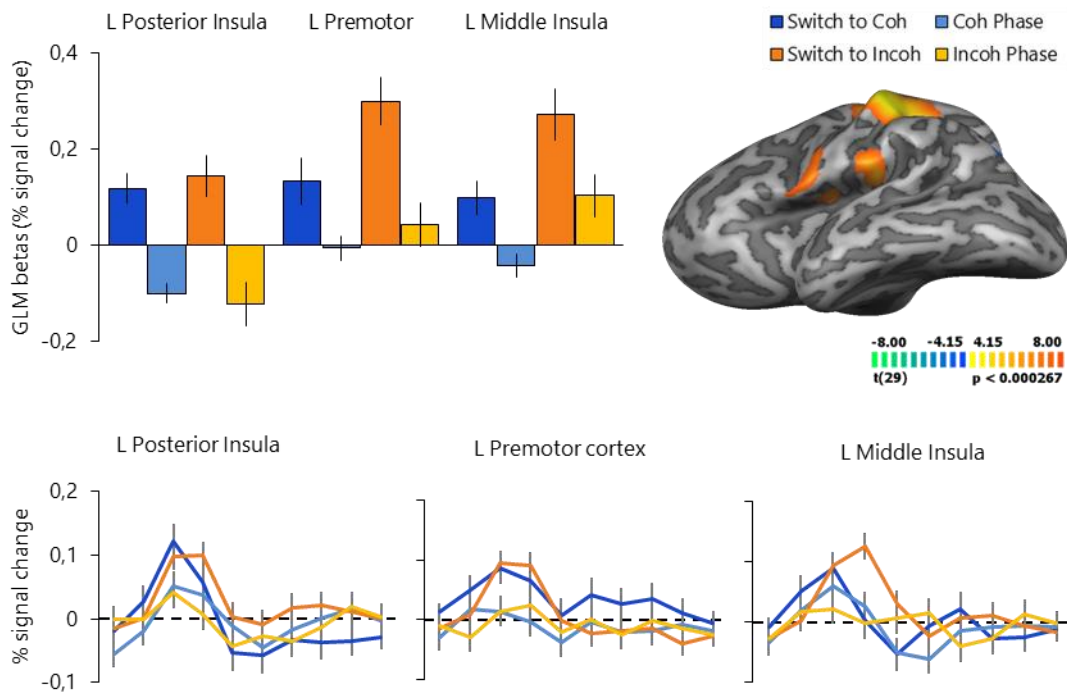


Figure 4-17. RFX-GLM beta values and time courses of responses to perceptual switches and perceptual phases extracted with deconvolution analysis within significant clusters represented in a template Talairach brain. Note that the insula shows increased responses to perceptual switches but also seems to have a role during perceptual phases. Left premotor area however shows increased responses to perceptual switches only.

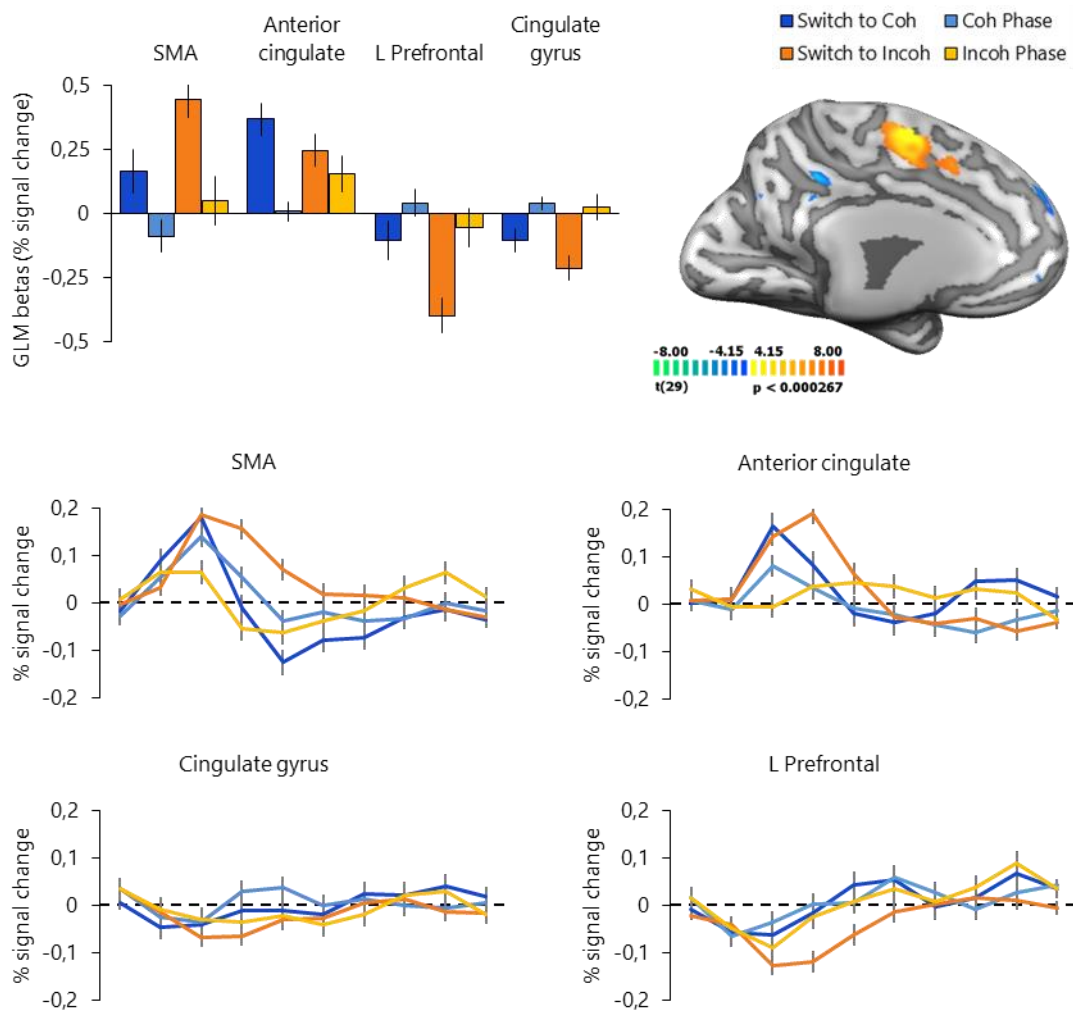


Figure 4-18. RFX-GLM beta values and time courses of responses to perceptual switches and perceptual phases extracted with deconvolution analysis within significant clusters represented in a template Talairach brain.

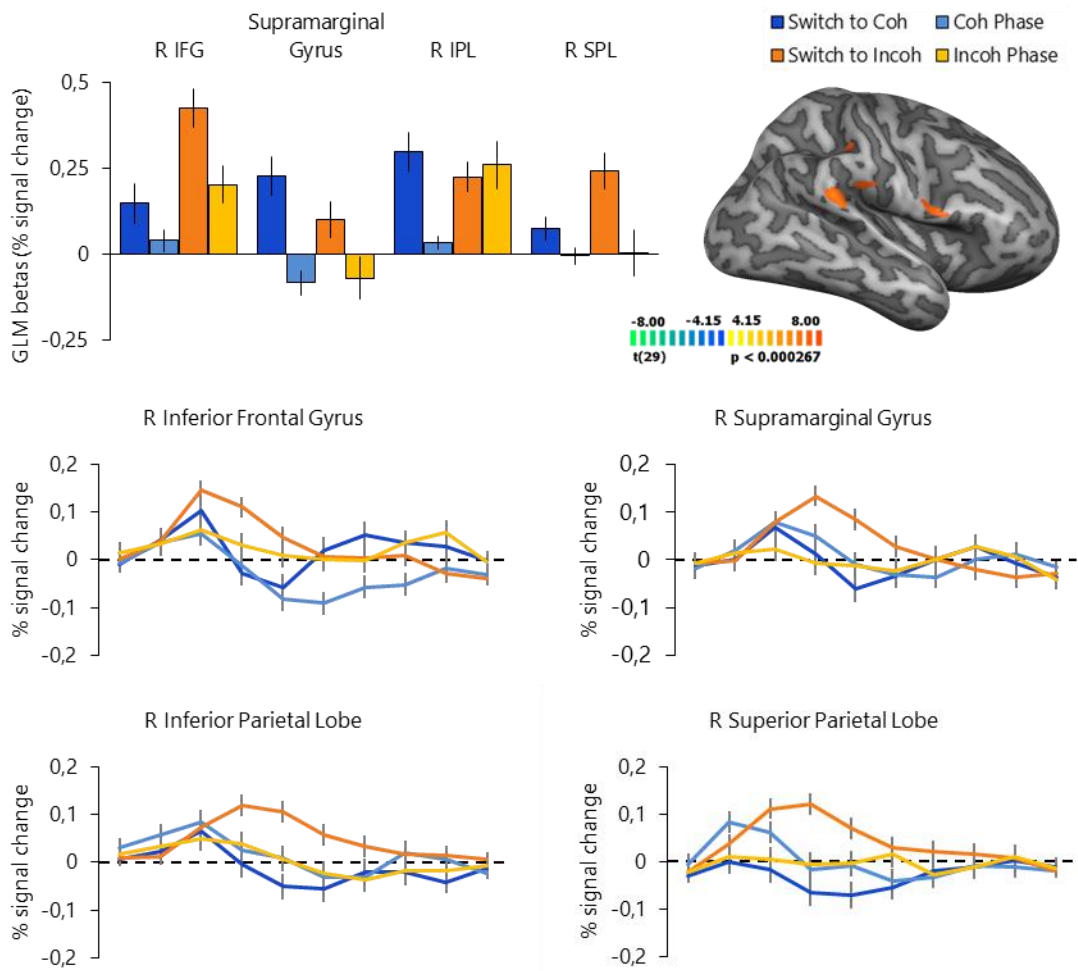


Figure 4-19. RFX-GLM beta values and time courses of responses to perceptual switches and perceptual phases extracted with deconvolution analysis within significant clusters represented in a template Talairach brain. Note that supramarginal gyrus, inferior parietal lobule and superior parietal lobule in the right hemisphere show an increased response particularly to perceptual switches to incoherent/component motion as compared to switches to coherent/pattern motion.

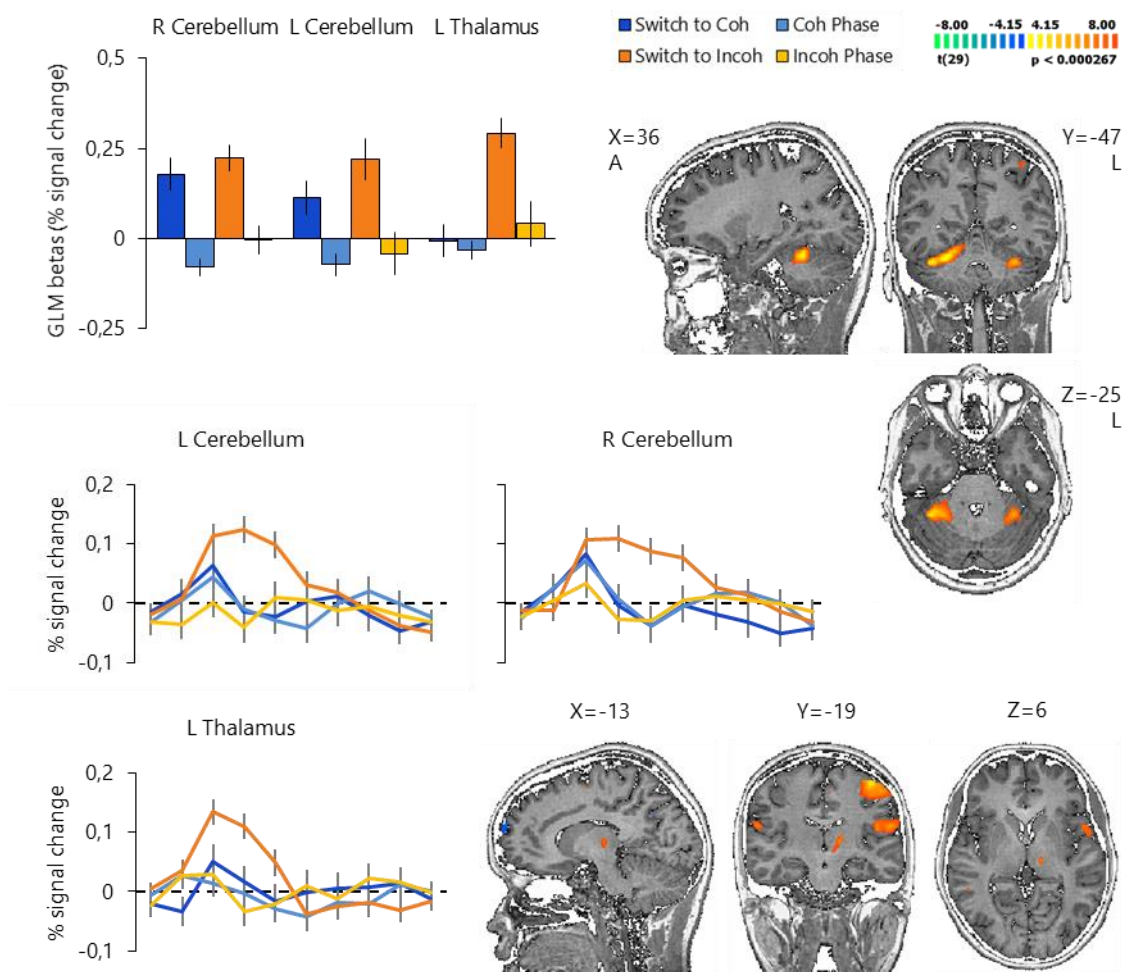


Figure 4-20. RFX-GLM beta values and time courses of responses to perceptual switches and perceptual phases extracted with deconvolution analysis within significant clusters represented in a template Talairach brain. The cerebellum shows a bilateral highly significant increased response to perceptual switches as compared to perceptual phases of both percepts. The left thalamus seems to respond mainly to perceptual switches to incoherent/component motion as compared to any other condition.

Granger causality analysis

We computed whole-brain group RFX-GCM maps showing voxels that are influenced by (positive values in the maps, in blue) or influence (negative values, in green) the activity in left or right MT+, individually defined at the single-subject level. The results are presented in Figure 4-21.

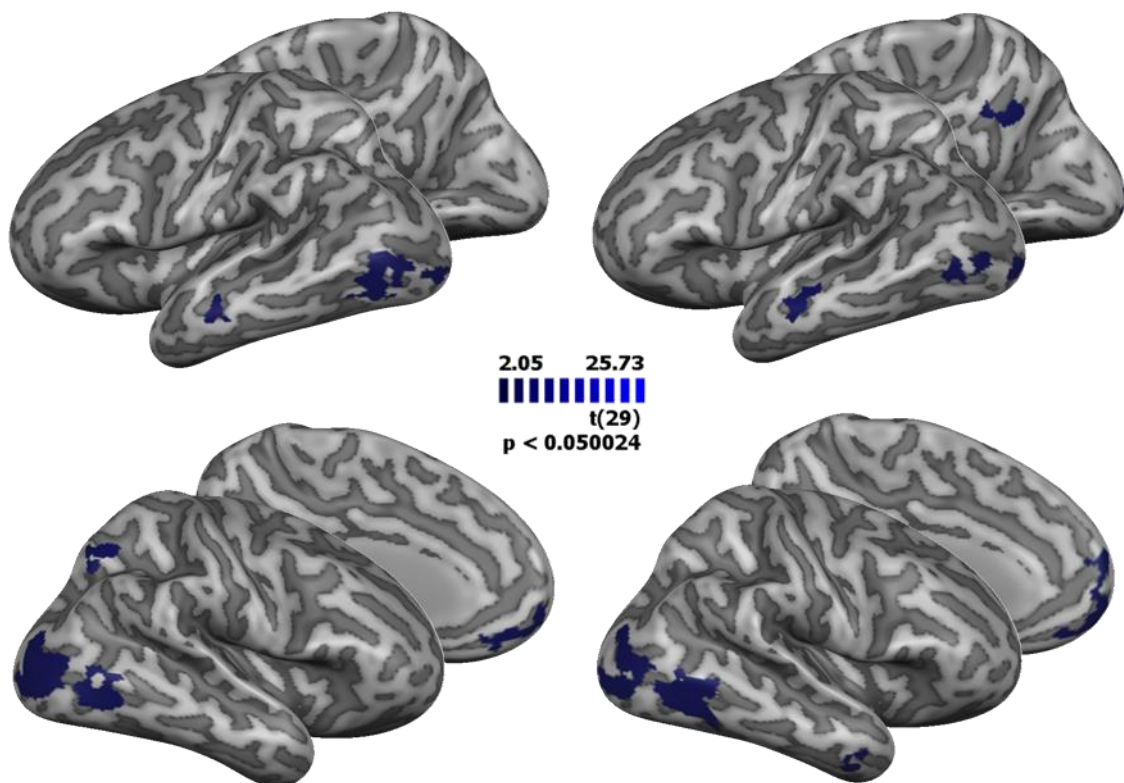


Figure 4-21. RFX Granger causality mapping with the left MT+ (left images) and right MT+ (right images) individually defined in each participant as reference regions. Note that there were no voxels with a significant negative difference between influence from reference region and influence to reference region, which would appear in green. The highlighted regions are those which showed a significant influence from the reference regions, left and right MT+, to every other voxel at the group level (t -test $GCM > 0$). The statistical map is corrected for multiple comparisons at P -value < 0.05 with Bonferroni method.

Granger causality mapping revealed significant directed influences during ambiguous bistable motion from the individually defined left MT+ to left prefrontal cortex (BA10), left middle temporal gyrus (BA21), early visual cortex in the left hemisphere and surrounding areas in MT+ complex including the kinetic occipital (KO) region. There was also significant connectivity from left MT+ to the contralateral hemisphere, namely the right V3/V3A region, right MT+ complex, a more posterior than MT+ region in the right corresponding to KO^{49,50} area and right superior parietal lobule (BA7).

Interestingly, the analysis of connectivity with right MT+ as reference region showed significant influence also to right BA7 in the region of the precuneus, with a role in integration of visual and motor information, and right V3/V3A. Additionally we observed significant connectivity with ipsilateral voxels in middle temporal gyrus (BA21), MT+ complex, KO area and early visual cortex as with the left MT+. These results suggest an important role of right SPL and right V3/V3A in this particular decision task of ambiguous bistable perception of motion with an interhemispheric stimulus. Notably, MT+ in both hemispheres showed significant effective connectivity with each other during bistable motion presentation.

Discussion

Previous studies of interhemispheric perceptual integration and binding in animals have shown that long range synchrony between brain regions correlates with holistic perception in vision⁵¹. This hypothesis cannot be tested using fMRI. Moreover, the binding by synchrony question has been difficult to resolve either in animal models, limited by absent or indirect perceptual reports⁵², or humans as explicit and unequivocal testing for long range synchronization had not been possible due to both recording and paradigm constraints. In this chapter we did

not focus on temporal coding mechanisms, which are not accessible with fMRI, but rather on the neural networks involved in perceptual decision making requiring interhemispheric integration.

In humans visual perception has been often tested with moving ambiguous stimuli, such as plaids¹²⁻¹⁸. Despite being physically constant, this type of stimulus produce a perceptual bistable situation, in which observer's spontaneously switch perception between two independent moving objects (component motion) or one single object moving coherently (pattern motion). There is already evidence that during exposure to ambiguous bistable moving stimuli MT+ underlies integration or segregation of motion components in the visual field and that the spontaneous switches between different perceptions are mediated by the area itself¹⁵. There is also evidence from electrophysiological and functional fMRI data that cortical activity that integrates visual information across hemifields takes place at extrastriate areas during late visual processing and that MT+ and V1 may contribute to bilateral visual integration during early visual processing¹⁹. However, there is still debate about the mechanisms that explain visual motion processing in MT+ and its interactions with lower-level and higher-level regions. One of the models proposed to explain complex motion computation assumes that the global motion direction and velocity of objects is the direction and speed of "blobs" caused by spatial intersection of object components, as appear in a plaid pattern. According to this spatiotemporal energy model, the motion of the plaid as a whole is identical to the motion of the blobs. This low-level monocular mechanism is called the blob tracking model^{12,53,54}. The second and most accepted method for combining 1-D component motion in order to explain 2-D motion is the Intersection of Constraints (IOC) model^{12,54}. In our study, we employed a paradigm of ambiguous multistability where visual motion disambiguation required obligatory interhemispheric integration under conditions of constant and physically identical sensory stimulation with a stimulus

that does not have intersections. Therefore, we could explicitly exclude the blob tracking model as an explanation for computation of 2-D motion of ambiguous bistable stimuli.

A multistable stimulus is characterized by the fact that there are at least two different interpretations or percepts of the stimulus. The ambiguous bistable stimulus we used was based on the work of Hans Wallach^{36,37} and resembles a classic barber pole illusion mirrored at the visual midline so as to cast two distinct images at each visual hemifield. Our study is innovative in the sense it uses an approach with this intersection-free 2-D bistable moving stimulus for the first time to investigate with fMRI the neural correlates of ambiguous motion perception in humans, at least to our knowledge. The ambiguity arises as the image can be perceived as either a single integrated moving pattern – coherent/pattern percept - or as two images segregated across hemifields with opposite motion directions – incoherent/component percept. None of these is absolutely stable, but rather will perception change spontaneously between the two percepts. These perceptual changes are subjective experiences and the timing of their occurrence cannot be exactly predicted. The statistical analysis of the dynamics of perception revealed that, despite a perceptual bias towards a dominant coherent global motion percept⁵⁵ the stimulus behaves as a typical bistable image^{38,40}, with perceptual durations following a gamma distribution^{39,56–59}. The durations of bistable percepts fit the gamma distribution in case of both equiprobable (e.g. Necker cube) and non-equiprobable, as in this study, perceptual interpretations⁵⁸. The gamma fit to durations in our study suggests perceptual rivalling opponent motion systems as an explanation for motion reversal. After adaptation of motion detectors coding for coherent motion, the activity of motion-sensitive neurons coding for incoherent motion may become dominant and drive perception. We also fitted a lognormal distribution to durations of each percept and observed that the lognormal fit was slightly better

than gamma fit to coherent percept durations in some participants. This is in accordance with previous studies showing an improved fit quality of the lognormal compared to the gamma duration distribution in binocular rivalry and bistable motion^{39,40}. The lognormal distribution shape might have implications for mechanisms underlying global coherent motion perception. If we consider perception of coherent global motion to be a large scale integration process composed of n independent sub-processes, and the probability of success in the complex task is the product of the probabilities of all n sub-processes succeeding, then task successes will have a lognormal distribution when n is sufficiently large to apply the central limit theorem³⁹. We consider it beyond the scope of this study to present an exhaustive comparison of fit qualities of the numerous distributions that have over the years been proposed in this context. In any case, the perceptual changes reported under ambiguous conditions are the result of endogenous processes, leading to an alternation of dominance between competing neural assemblies, and were explored to study the neural correlates of perceptual interpretation.

Our psychophysical and imaging data support the existence of two stages in the processing of motion information in the human visual system. In practice, each half-image, which is a 1-D component of the global 2-D pattern, can be seen also as a 1-D pattern itself. The first stage appears to rely on both component and pattern neurons responding to the motion of two 1-D patterns, which are the two halves of the image. The output of this first stage processing leads to the perception of the two patterns moving incoherently inward. The second stage seems to be concerned with establishing the motion of the global 2-D pattern, which is the whole image moving coherently downward, by integration of information relayed from the first stage. While during the incoherent perceptual state both component and pattern neurons are responding to the motion of two

1-D objects, during the coherent percept the pattern neurons in MT are responding to a single 2-D object.

In fact, our analysis of fMRI data is in accordance with this hypothesis, as ambiguous bistable motion stimulation elicited higher signal changes in response to incoherent percept than in response to coherent/pattern percept. This was observed at the single-subject level within MT+ (see Figure 4-7). This result implies MT+ itself in the disambiguation process of motion perception as activity in MT+ correlated with perceptual states, being higher when the perceptual interpretation was compatible with multiple surfaces^{15,60}. These data provide evidence on the putative site of perceptual grouping operations underlying the switches between fusion and segregation of moving stimuli. A possible explanation for the perceptual transitions between states in MT+ is a competitive reconfiguration of cell assemblies in this area, one coding pattern motion and the other coding component motion. The adaptation of pattern neurons produces modulations of fMRI responses in MT+ consistent with the idea that the activity of pattern neurons is reduced when perceptual coherence is lower⁶⁰. Activity in the MT+ complex changes depending on whether subjects integrate all motion signals into the percept of a single surface, or whether they segregate signals and perceive two separate objects. This difference in activity within MT+ was significant as computed from the GLM beta values as measures of % signal change. By analyzing the control unambiguous experiment data with the same stimulus (an unambiguous version) we could clearly observe the higher response to incoherent/component percept also in the event-related average plots (see Figure 4-24 and Figure 4-25 in Appendix), which are matched for duration.

In order to specifically analyze transient signal changes related to perceptual switches, we employed a second GLM approach in which we marked the subjectively defined perceptual switches in the protocol of analysis, after subtracting each participant's reaction time obtained from the unambiguous

experiment. We computed a standard GLM with hemodynamic predictors for perceptual switches to coherent motion and to incoherent motion, and for perceptual phases of coherent motion and incoherent motion. We excluded the first perceptual phase of each bistable motion period to eliminate unspecific stimulus onset effects. We also applied deconvolution analysis to the event-related motion perception task to investigate the neuronal correlates of changes in perception of motion - perceptual switches - within MT+ that were not stimulus driven. We observed with standard GLM analysis that switch-related activity within MT+ was significantly different from baseline but not significantly different from activity related to the following perceptual state (see Figure 4-9). Deconvolution extraction of responses to perceptual switches suggest a mirror-like activation within MT+ in response to perceptual switches, as the response to perceptual transition to incoherent/component motion rises when the response to perceptual transition to coherent/pattern motion seems to be delayed (see Figure 4-10 for group average curves). A possible mechanism explaining these phase differences in response profiles is that switch mechanisms are asymmetric possibly due to differential adaptation. Different cell assemblies of component and pattern neurons might compete with each other (e.g. through reciprocal inhibition) and adaptation of the cell assembly that is more active and supporting the current perception can lead to shifts of dominance between assemblies, causing perceptual switches. This explanation has been previously supported in an fMRI study of perceptual switches and states with apparent motion⁶¹ and plaid stimuli¹⁵. Our results further support this explanation. Nonetheless, the whole-brain RFX-GLM analysis revealed several high-level brain regions that correlated significantly with perceptual switches, suggesting that despite the pivotal role of MT+ in perception of motion there might be other brain regions triggering perceptual switches and causing a redistribution of activity within MT+ by means

of feedback connections. What are these regions and what are the neuronal correlates of perceptual switches in perception of bistable motion?

It is known that bistable perception has both bottom-up and top-down influences²⁴, as for example attentional effects^{48,62–65}. Diverting attention has been shown to slow down perception of perceptual and binocular rivalry, which indicates a high-level, top-down influence of attention⁶⁶. By running the first GLM approach (two perceptual states) in the whole brain we observed activation evoked by ambiguous bistable motion in prefrontal cortex, visual cortex, parietal cortex, premotor areas, cingulate gyrus, insula, opercular cortex and putamen (see Figure 4-11 and Table 4-3), as reported in previous studies of bistable perception and perceptual decision making^{62,65,67–70}. Notably, we found a large and highly significant cluster in superior parietal lobule, which was recently proven to be part of a reciprocal interaction network involving MT+⁷¹. Megumi and colleagues have shown that perceptual switches may be triggered by changes in connectivity between visual areas and parietal cortical regions⁷².

With the second GLM analysis of switch-related transient signal changes we were able to investigate differences in activity elicited by perceptual switches compared to activity elicited by perceptual stable phases. With contrast analysis of [switches > phases] activity we observed significant signal changes in prefrontal cortex, insula, inferior frontal gyrus, angular gyrus, supramarginal gyrus and cingulate gyrus (see Figure 4-14 and Table 4-4). We also observed significant activations in left premotor and motor areas, which can be attributed to the preparation and execution of right-hand motor responses. We replicated the previously described functional association between activity in parietal regions and perceptual switches^{71,73,74}, as we also observed significant activity in superior and inferior parietal lobule. Superior parietal lobule is known for its role in spatial processing, visuo-motor transformation and for receiving widespread connections from visual and premotor areas. Our results seem to agree with a

recent study which revealed that switch-related fronto-parietal BOLD activity is reduced, but not eliminated, when dissociating switches from motor responses, and hypothesized that perceptual switches may arise in the visual system but noticing the change may rely on brain regions involved in behavioural choices ⁷⁵. Interestingly, we found significant activations bilaterally in the cerebellum and left thalamus, in response to perceptual switches. A recent study found increased activity in the cerebellum and thalamus to be time locked to perceptual switching in perceptual multistability with auditory stimuli ⁷⁶. Additionally, recent investigation of perceptual predictions found an important role of cerebellum in the recalibration of sensory prediction capturing the sensory consequences of one's motor behaviour ⁷⁷. Our results suggest that motor-based prediction, produced by neural networks outside the visual system, might as well play essential roles in occurrence of dynamic reconfiguration of cell assemblies allowing both for segregation and integration of disparate motion signals in visual areas, even across visual hemi-fields.

We found directed influences from left and right MT+ to the contralateral MT+ during ambiguous bistable motion, suggesting that these focal motion-responsive regions communicate effectively in order to disambiguate component motion in separate visual hemi-fields from coherent pattern motion across hemi-fields with this bistable stimulus. In other words we found evidence at the fMRI level for interhemispheric directed communication between homologous MT+ regions in this paradigm requiring perceptual decision towards interhemispheric integration vs segregation. Furthermore, we found directed influences from MT+ to kinetic occipital regions, which has been distinguished by its responsiveness to contours defined by differences in velocity ^{22,49} and lower level visual areas V3/V3A, predominantly in the right hemisphere, which agrees with reports that activation in V3A underlies motion coherence ^{78,79}. Activity in V3 has been shown to successfully decode between coherent and incoherent contexts, possibly with

help of higher extrastriate cortex feedback⁸⁰. Notably, we found significant directed connectivity of both left and right MT+ with right superior parietal lobule. Our results are in accordance with recent report of functional causal interactions between right parietal subregions and lower visual areas such as MT+⁷². Surprisingly, we could not reliably identify significant directed influences from other brain regions to MT+ during ambiguous bistable motion with Granger causality mapping. Previous fMRI studies have emphasized the role of top-down processes in perceptual transitions in binocular rivalry^{48,73,81} and for leading attentional resources to brain areas involved in specific tasks, including MT+^{65,82}. Our results seem to suggest that the transition between coherent/pattern and incoherent/component motion percepts of this specific interhemispheric stimulus might mainly require bottom-up activation of MT+ and feedforward connections to other brain regions. However, this does not exclude additional top-down connections with e.g. prefrontal cortex or insula, which shown significant activation found in the RFX-GLM analysis, with specific component vs pattern perception differences in particular for the ambiguous conditions, where decision is less automatic. fMRI difference GCMs have lower sensitivity for reciprocal interactions. Also the temporal sampling rate of 2 seconds is far from ideal for connectivity analysis as it is low for neuronal processing. Thus, interactions at this time scale are likely to reflect modulatory processes related to attention and cognitive control but faster processes leading to perceptual switches might go undetected^{11,27,83}. Ongoing advances in the development of ultra-fast multi-echo fMRI sequences might help substantially increase the temporal resolution of fMRI data. We foresee that with faster sequences and higher MRI field strength it will be possibly to further investigate neuronal correlates of perceptual switches at a finer spatial and temporal scale.

Limitations

The approaches described above are all accompanied by a significant temporal inaccuracy. This is due to the finite reaction time between perceived reversal for the observer and the consecutive button press. It cannot be assumed that the reaction time will be the same for every button press, as it will have a certain variation, even for the same observer. But as there are no direct physiological predictors of perceptual reversals yet, in particular for ambiguous figures, duration measurements still have to rely on self-report. We tried to overcome this issue by computing the individual mean reaction time in unambiguous experiments and accounted for it in the preparation of protocols for analysis of switch-related activity.

Another limitation is the subjectivity of the reports. Some work has been done towards the recognition of perceptual reversals with the use of physiological measures. For several types of bistable stimuli, Einhäuser and colleagues found that pupil dilation preceded perceptual reversals ⁸⁴. Similarly, for discontinuous presentation of the Necker cube, brain activity in the right inferior parietal cortex has been identified as a precursor of perceptual reversals ⁸⁵. In both instances, these changes can only be detected in averages over many trials. Hence, they are not suited as markers for a single perceptual reversal. It will remain a challenge to have more objective predictors of perceptual decision.

Future studies

In future studies we should train a group of observers and also manipulate stimulus parameters in order to optimize the duration of incoherent perceptual phases, which were clearly non-dominant and short in the majority of participants. With longer percept durations we will be able to better investigate if neuronal correlates and effective connectivity between brain regions differ between coherent and incoherent percepts, namely within across hemispheres.

One outstanding question is whether one can relate the switches between the two perceptual representations to the known columnar organization of the mammalian cortex⁸⁶. The perception of two surfaces is probably associated with the formation of two cell assemblies, each of which represents one of the two moving surfaces, whereas the perception of a single coherent pattern likely requires the formation of only one cell assembly representing a single surface moving. Possibly one can relate each assembly with a columnar representation being active¹⁵ which is amenable to experimental testing, now that ultra-high field scanners are becoming available. Their use is already allowing the mapping of columns in human MT⁸⁷ thereby opening the possibility to study perceptual decision at the columnar level.

References

1. Movshon, J. A., Adelson, E. H., Gizzi, M. S. & Newsome, W. T. The analysis of moving visual patterns. *Pattern Recognit. Mech.* 117–151 (1985).
2. Mikami, A., Newsome, W. T. & Wurtz, R. H. Motion selectivity in macaque visual cortex. I. Mechanisms of direction and speed selectivity in extrastriate area MT. *J. Neurophysiol.* **55**, 1308–1327 (1986).
3. Newsome, W. T. & Paré, E. B. A Selective Impairment of Motion Perception Following Lesions of the Middle Temporal Visual Area (MT). *J. Neurosci.* **8**, 2201–2211 (1988).
4. Zeki, S. *et al.* A direct demonstration of functional specialization in human visual cortex. *J. Neurosci.* **11**, 641–649 (1991).
5. Albright, T. D. & Stoner, G. R. Visual motion perception. *Proc. Natl. Acad. Sci. U. S. A.* **92**, 2433–2440 (1995).
6. Tootell, R. B. *et al.* Functional Analysis of Human MT and Related Visual Cortical Areas Using Magnetic Resonance Imaging. *J. Neurosci.* **15**, 3215–3230 (1995).
7. McKeefry, D., Watson, J., Frackowiak, R. S., Fong, K. & Zeki, S. The activity in human areas V1/V2, V3, and V5 during the perception of coherent and incoherent motion. *Neuroimage* **5**, 1–12 (1997).
8. He, S., Cohen, E. R. & Hu, X. Close correlation between activity in brain area MT/V5 and the perception of a visual motion aftereffect. *Curr. Biol.* **8**, 1215–1218 (1998).
9. Kolster, H., Peeters, R. & Orban, G. A. The retinotopic organization of the human middle temporal area MT/V5 and its cortical neighbors. *J. Neurosci.* **30**, 9801–9820 (2010).
10. Huk, A. C., Dougherty, R. F. & Heeger, D. J. Retinotopy and Functional Subdivision of Human Areas MT and MST. *J. Neurosci.* **22**, 7195–7205 (2002).
11. Kaas, A., Weigelt, S., Roebroek, A., Kohler, A. & Muckli, L. Imagery of a moving object: the role of occipital cortex and human MT/V5+. *Neuroimage* **49**, 794–804 (2010).
12. Adelson, E. H. & Movshon, J. A. Phenomenal coherence of moving visual patterns. *Nature* **300**, 523–525 (1982).
13. Burke, D., Alais, D. & Wenderoth, P. A Role for a low level mechanism in determining plaid coherence. *Vision Res.* **34**, 3189–3196 (1994).
14. Wenderoth, P., Alais, D., Burke, D. & van der Zwan, R. The role of the blobs in determining the perception of drifting plaids and their motion aftereffects. *Perception* **23**, 1163–1169 (1994).
15. Castelo-Branco, M. *et al.* Activity patterns in human motion-sensitive areas depend on the

- interpretation of global motion. *Proc. Natl. Acad. Sci.* **99**, 13914–13919 (2002).
16. Castelo-Branco, M., Goebel, R., Neuenschwander, S. & Singer, W. Neural synchrony correlates with surface segregation rules. *Nature* **405**, 685–689 (2000).
 17. Kozak, L. R. & Castelo-Branco, M. Peripheral influences on motion integration in foveal vision are modulated by central local ambiguity and center-surround congruence. *Investig. Ophthalmol. Vis. Sci.* **50**, 980–988 (2009).
 18. Castelo-Branco, M. *et al.* Type of featural attention differentially modulates hMT+ responses to illusory motion aftereffects. *J. Neurophysiol.* **102**, 3016–3025 (2009).
 19. Liu, Z., Zhang, N. & Chen, W. Mapping the bilateral visual integration by EEG and fMRI. *Neuroimage* **46**, 989–997 (2009).
 20. Genç, E., Bergmann, J., Singer, W. & Kohler, A. Interhemispheric connections shape subjective experience of bistable motion. *Curr. Biol.* **21**, 1494–1499 (2011).
 21. Bowns, L. Can spatio-temporal energy models of motion predict feature motion? *Vision Res.* **42**, 1671–1681 (2002).
 22. Blake, R., Sekuler, R. & Grossman, E. in *Primate Vis. Syst.* (eds. Kaas, J. & Collins, C.) 311–344 (CRC Press, 2004).
 23. Derrington, A. M., Allen, H. A. & Delicato, L. S. Visual mechanisms of motion analysis and motion perception. *Annu. Rev. Psychol.* **55**, 181–205 (2004).
 24. Long, G. M. & Toppino, T. C. Enduring Interest in Perceptual Ambiguity: Alternating Views of Reversible Figures. *Psychol. Bull.* **130**, 748–768 (2004).
 25. Kornmeier, J., Hein, C. M. & Bach, M. Multistable perception: When bottom-up and top-down coincide. *Brain Cogn.* **69**, 138–147 (2009).
 26. Wernery, J. *et al.* Temporal processing in bistable perception of the Necker cube. *Perception* **44**, 157–168 (2015).
 27. Roebroek, A., Formisano, E. & Goebel, R. Mapping directed influence over the brain using Granger causality and fMRI. *Neuroimage* **25**, 230–242 (2005).
 28. Friston, K. J., Jezzard, P. & Turner, R. Analysis of functional MRI time-series. *Hum. Brain Mapp.* **1**, (1994).
 29. Stephan, K. E. & Friston, K. J. Analyzing effective connectivity with fMRI. *Wiley Interdiscip. Rev. Cogn. Sci.* **1**, 446–459 (2010).
 30. Friston, K. J. Functional and effective connectivity: a review. *Brain Connect.* **1**, 13–36 (2011).
 31. Goebel, R., Roebroek, A., Kim, D. & Formisano, E. Investigating directed cortical interactions in time-resolved fMRI data using vector autoregressive modeling and Granger causality mapping. *Magn. Reson. Imaging* **21**, 1251–1261 (2003).

32. Seth, A. K., Barrett, A. B. & Barnett, L. Granger Causality Analysis in Neuroscience and Neuroimaging. *J. Neurosci.* **35**, 3293–3297 (2015).
33. Oldfield, R. The assessment and analysis of handedness: the Edinburgh inventory. *Neuropsychologia* **9**, 97–113 (1971).
34. Brainard, D. H. The Psychophysics Toolbox. *Spat. Vis.* **10**, 433–436 (1997).
35. Pelli, D. G. The VideoToolbox software for visual psychophysics: transforming numbers into movies. *Spat. Vis.* **10**, 437–442 (1997).
36. Wallach, H. Über visuell wahrgenommene Bewegungsrichtung. *Psychol. Forsch.* **20**, 325–380 (1935).
37. Wuergler, S., Shapley, R. & Rubin, N. 'On the visually perceived direction of motion' by Hans Wallach: 60 years later. *Perception* **25**, 1317–1367 (1996).
38. Borsellino, A., De Marco, A., Allazetta, A., Rinesi, S. & Bartolini, B. Reversal time distribution in the perception of visual ambiguous stimuli. *Kybernetik* **10**, 139–144 (1972).
39. Zhou, Y., Gao, J., White, K., Merk, I. & Yao, K. Perceptual dominance time distributions in multistable visual perception. *Biol. Cybern.* **90**, 256–263 (2004).
40. Brascamp, J. W., van Ee, R., Pestman, W. R. & van den Berg, A. V. Distributions of alternation rates in various forms of bistable perception. *J. Vis.* **5**, 287–298 (2005).
41. Linden, D. E. *et al.* The functional neuroanatomy of target detection: an fMRI study of visual and auditory oddball tasks. *Cereb. cortex* **9**, 815–823 (1999).
42. Kriegeskorte, N. & Goebel, R. An efficient algorithm for topologically correct segmentation of the cortical sheet in anatomical MR volumes. *Neuroimage* **14**, 329–346 (2001).
43. Friston, K. J., Josephs, O., Rees, G. & Turner, R. Nonlinear event-related responses in fMRI. *Magn. Reson. Med.* **39**, 41–52 (1998).
44. Penny, W., Holmes, A. & Friston, K. J. *Random effects analysis in Human Brain Function.* (Academic Press, 2003).
45. Beckmann, C. F., Jenkinson, M. & Smith, S. M. General multilevel linear modeling for group analysis in FMRI. *Neuroimage* **20**, 1052–1063 (2003).
46. Glover, G. H. Deconvolution of Impulse Response in Event-Related BOLD fMRI. *Neuroimage* **9**, 416–429 (1999).
47. Hupé, J.-M. & Rubin, N. The dynamics of bi-stable alternation in ambiguous motion displays: a fresh look at plaids. *Vis. Res.* **43**, 531–548 (2003).
48. Leopold, D. A. & Logothetis, N. K. Multistable phenomena: Changing views in perception. *Trends Cogn. Sci.* **3**, 254–264 (1999).
49. Van Oostende, S., Sunaert, S., Hecke, P. Van, Marchal, G. & Orban, G. A. The Kinetic Occipital

- (KO) Region in Man: An fMRI Study. *Cereb. cortex* **7**, 690–701 (1997).
50. Dupont, P. *et al.* The kinetic occipital region in human visual cortex. *Cereb. cortex* **7**, 283–292 (1997).
 51. Engel, A. K., König, P., Kreiter, A. K. & Singer, W. Interhemispheric synchronization of oscillatory neuronal responses in cat visual cortex. *Science (80-.)*. **252**, 1177–1179 (1991).
 52. Shadlen, M. N. & Movshon, J. A. Synchrony unbound: A critical evaluation of the temporal binding hypothesis. *Neuron* **24**, 67–77 (1999).
 53. Adelson, E. H. & Bergen, J. R. Spatiotemporal energy models for the perception of motion. *J. Opt. Soc. Am. A* **2**, 284–299 (1985).
 54. Alais, D., Wenderoth, P. & Burke, D. The contribution of one-dimensional motion mechanisms to the perceived direction of drifting plaids and their aftereffects. *Vision Res.* **34**, 1823–1834 (1994).
 55. McDermott, J., Weiss, Y. & Adelson, E. H. Beyond junctions: nonlocal form constraints on motion interpretation. *Perception* **30**, 905–921 (2001).
 56. Leopold, D. A., Wilke, M., Maier, A. & Logothetis, N. K. Stable perception of visually ambiguous patterns. *Nat. Neurosci.* **5**, 605–609 (2002).
 57. Sterzer, P., Russ, M. O., Preibisch, C. & Kleinschmidt, A. Neural correlates of spontaneous direction reversals in ambiguous apparent visual motion. *Neuroimage* **15**, 908–916 (2002).
 58. Kline, K. A., Holcombe, A. O. & Eagleman, D. M. Illusory motion reversal is caused by rivalry, not by perceptual snapshots of the visual field. *Vision Res.* **44**, 2653–2658 (2004).
 59. Kaneoke, Y., Urakawa, T., Hirai, M., Kakigi, R. & Murakami, I. Neural basis of stable perception of an ambiguous apparent motion stimulus. *Neuroscience* **159**, 150–160 (2009).
 60. Huk, A. C. & Heeger, D. J. Pattern-motion responses in human visual cortex. *Nat. Neurosci.* **5**, 72–75 (2002).
 61. Muckli, L. *et al.* Apparent motion: event-related functional magnetic resonance imaging of perceptual switches and states. *J. Neurosci.* **22**, RC219 (2002).
 62. Knapen, T., Brascamp, J., Pearson, J., van Ee, R. & Blake, R. The role of frontal and parietal brain areas in bistable perception. *J. Neurosci.* **31**, 10293–10301 (2011).
 63. Weilhhammer, V. A., Ludwig, K., Hesselmann, G. & Sterzer, P. Frontoparietal cortex mediates perceptual transitions in bistable perception. *J. Neurosci.* **33**, 16009–16015 (2013).
 64. Naghavi, H. R. & Nyberg, L. Common fronto-parietal activity in attention, memory, and consciousness: shared demands on integration? *Conscious. Cogn.* **14**, 390–425 (2005).
 65. Kleinschmidt, A., Büchel, C., Zeki, S. & Frackowiak, R. S. Human brain activity during

- spontaneously reversing perception of ambiguous figures. *Proc. R. Soc. London Part B Biol. Sci.* **265**, 2427–2433 (1998).
66. Wernery, J. Bistable Perception of the Necker Cube in the Context of Cognition & Personality. (2013).
 67. Rebola, J., Castelhana, J., Ferreira, C. & Castelo-Branco, M. Functional parcellation of the operculo-insular cortex in perceptual decision making: an fMRI study. *Neuropsychologia* **50**, 3693–3701 (2012).
 68. Sterzer, P., Eger, E. & Kleinschmidt, A. Responses of extrastriate cortex to switching perception of ambiguous visual motion stimuli. *Neuroreport* **14**, 2337–41 (2003).
 69. Sterzer, P., Kleinschmidt, A. & Rees, G. The neural bases of multistable perception. *Trends Cogn. Sci.* **13**, 310–318 (2009).
 70. Zaretskaya, N., Thielscher, A., Logothetis, N. K. & Bartels, A. Disrupting parietal function prolongs dominance durations in binocular rivalry. *Curr. Biol.* **20**, 2106–2111 (2010).
 71. Kanai, R., Carmel, D., Bahrami, B. & Rees, G. Structural and functional fractionation of right superior parietal cortex in bistable perception. *Curr. Biol.* **21**, R106–R107 (2011).
 72. Megumi, F., Bahrami, B., Kanai, R. & Rees, G. Brain activity dynamics in parietal regions during spontaneous switch in bistable perception. *Neuroimage* **107**, 190–197 (2015).
 73. Lumer, E. D., Friston, K. J. & Rees, G. Neural Correlates of Perceptual Rivalry in the Human Brain. *Science (80-.)*. **280**, 1930–1934 (1998).
 74. Lumer, E. D. & Rees, G. Covariation of activity in visual and prefrontal cortex associated with subjective visual perception. *Proc. Natl. Acad. Sci. U. S. A.* **96**, 1669–1673 (1999).
 75. Brascamp, J., Blake, R. & Knapen, T. Negligible fronto-parietal BOLD activity accompanying unreportable switches in bistable perception. *Nat. Neurosci.* (2015).
 76. Kashino, M. & Kondo, H. M. Functional brain networks underlying perceptual switching: auditory streaming and verbal transformations. *Philos. Trans. R. Soc. B Biol. Sci.* **367**, 977–987 (2012).
 77. Roth, M. J., Synofzik, M. & Lindner, A. The cerebellum optimizes perceptual predictions about external sensory events. *Curr. Biol.* **23**, 930–935 (2013).
 78. Tootell, R. B. *et al.* Functional analysis of V3A and related areas in human visual cortex. *J. Neurosci.* **17**, 7060–7078 (1997).
 79. Aspell, J., Tanskanen, T. & Hurlbert, A. Neuromagnetic correlates of visual motion coherence. *Eur. J. Neurosci.* **22**, 2937–2945 (2005).
 80. Schwarzkopf, D. S., Sterzer, P. & Rees, G. Decoding of coherent but not incoherent motion signals in early dorsal visual cortex. *Neuroimage* **15**, 688–698 (2011).

81. Tong, F., Meng, M. & Blake, R. Neural bases of binocular rivalry. *Trends Cogn. Sci.* **10**, 502–511 (2006).
82. O’Craven, K. M., Rosen, B. R., Kwong, K. K., Treisman, A. & Savoy, R. L. Voluntary attention modulates fMRI activity in human MT-MST. *Neuron* **18**, 591–598 (1997).
83. Roebroeck, A., Formisano, E. & Goebel, R. The identification of interacting networks in the brain using fMRI: Model selection, causality and deconvolution. *Neuroimage* **58**, 296–302 (2011).
84. Einhäuser, W., Stout, J., Koch, C. & Carter, O. Pupil dilation reflects perceptual selection and predicts subsequent stability in perceptual rivalry. *Proc. Natl. Acad. Sci. USA* **105**, 1704–1709 (2008).
85. Britz, J., Landis, T. & Michel, C. M. Right Parietal Brain Activity Precedes Perceptual Alternation of Bistable Stimuli. *Cereb. Cortex* **19**, 55–65 (2009).
86. Albright, T. D., Desimone, R. & Gross, C. G. Columnar organization of directionally selective cells in visual area MT of the macaque. *J. Neurophysiol.* **51**, 16–31 (1984).
87. De Martino, F. *et al.* Evidence towards columnar organization of human area MT with sub-millimetric, 3D, T2 weighted BOLD fMRI at 7 Tesla. in *Proc. Int. Soc. Magn. Reson. Med.* **19**, (2011).

Appendix

Single-subject analysis in MT+

The individual MT+ clusters were subjected to an event-related average time course analysis, in which BOLD signal during each trial of each perceptual phase was averaged. The average response time course is shown for each participant's left and right MT+ in Figure 4-22 and Figure 4-23, respectively. The event-related average time course comprises the two volumes before transition from one percept to the other and the eight volumes after the transition (corresponding to an interval of -4 to 16 seconds). As the percept transitions are subject-specific and are likely to occur within 16 seconds, the subsequent trials of the other percept tend to blur the time course of individual responses. We present coloured bars representing the persistence of each percept along time courses in each participant, in which each coloured rectangle represents a functional volume. The colour indicates the proportion of averaged trials on which the percept endured. Dark colour (intensity 100%) indicates that the respective percept (coherent, blue; incoherent, yellow) was present at that functional volume on every one of the averaged trials. White colour (intensity 0%) indicates that the percept had switched again on all averaged time courses. Note the relatively higher persistence of the coherent percept in all participants, explaining the appearance of a second peak. Note that amplitude values are not corrected (as they are in the GLM) for the probability and duration of the percept, and therefore only the phase of the signals can be interpreted. Note that in Figures 4-24 and 4-25, showing event-related average time-courses during the unambiguous experiment, durations are matched and the larger activity for incoherent motion perception becomes obvious.

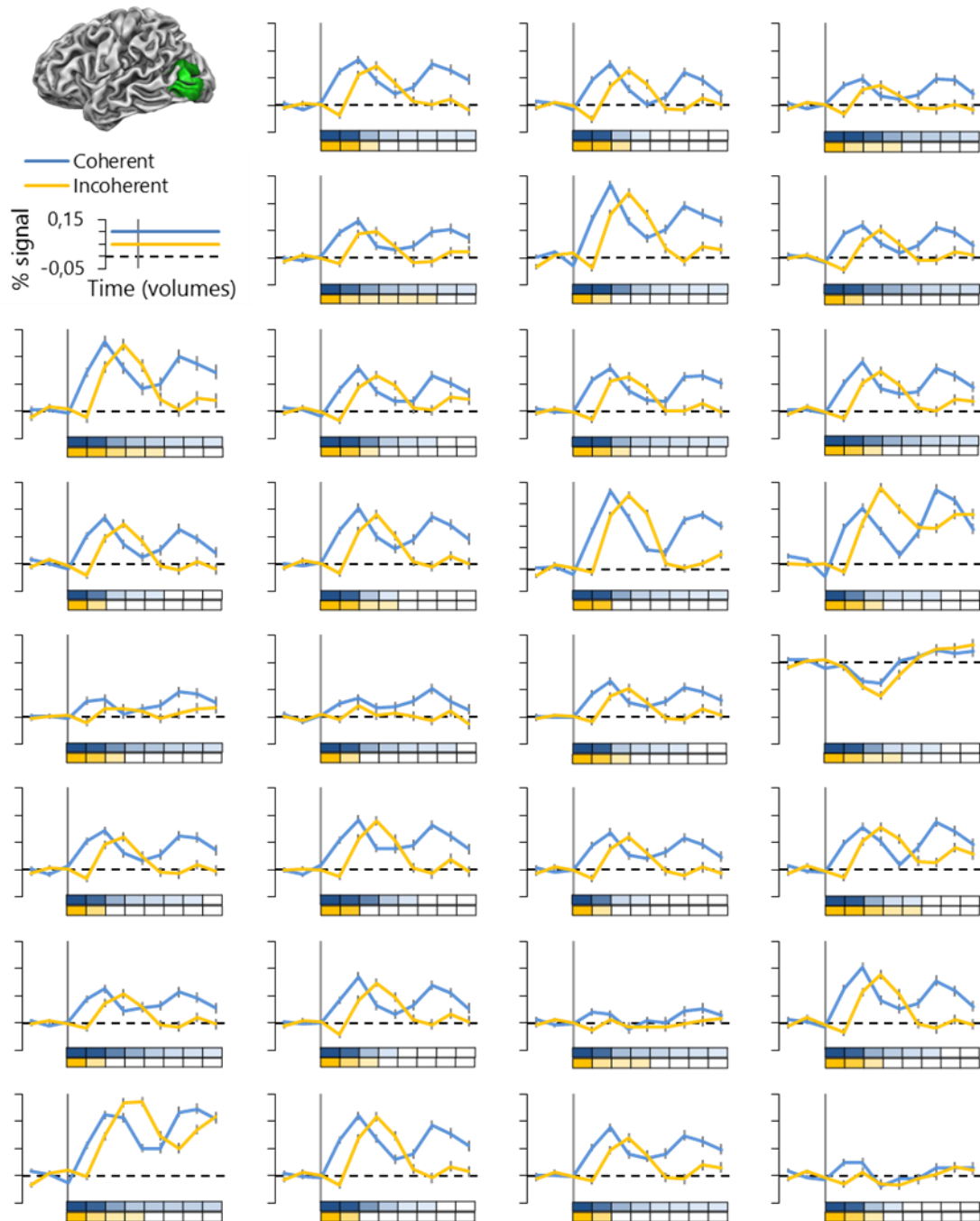


Figure 4-22. Individual event-related analysis of activity within left MT+ (group probability map on top left) during ambiguous bistable motion in 30 participants. Event-related average time courses during coherent and incoherent percepts are shown in blue and orange, respectively. The vertical grey bars indicate percept onset. Whiskers correspond to \pm SEM. The coloured rectangles represent functional volumes (2 sec). Dark colour (intensity, 100%) indicates that the percept was present at that functional volume on every one of the averaged time courses. White colour (intensity, 0%) indicates that the percept had switched again on all averaged time courses.

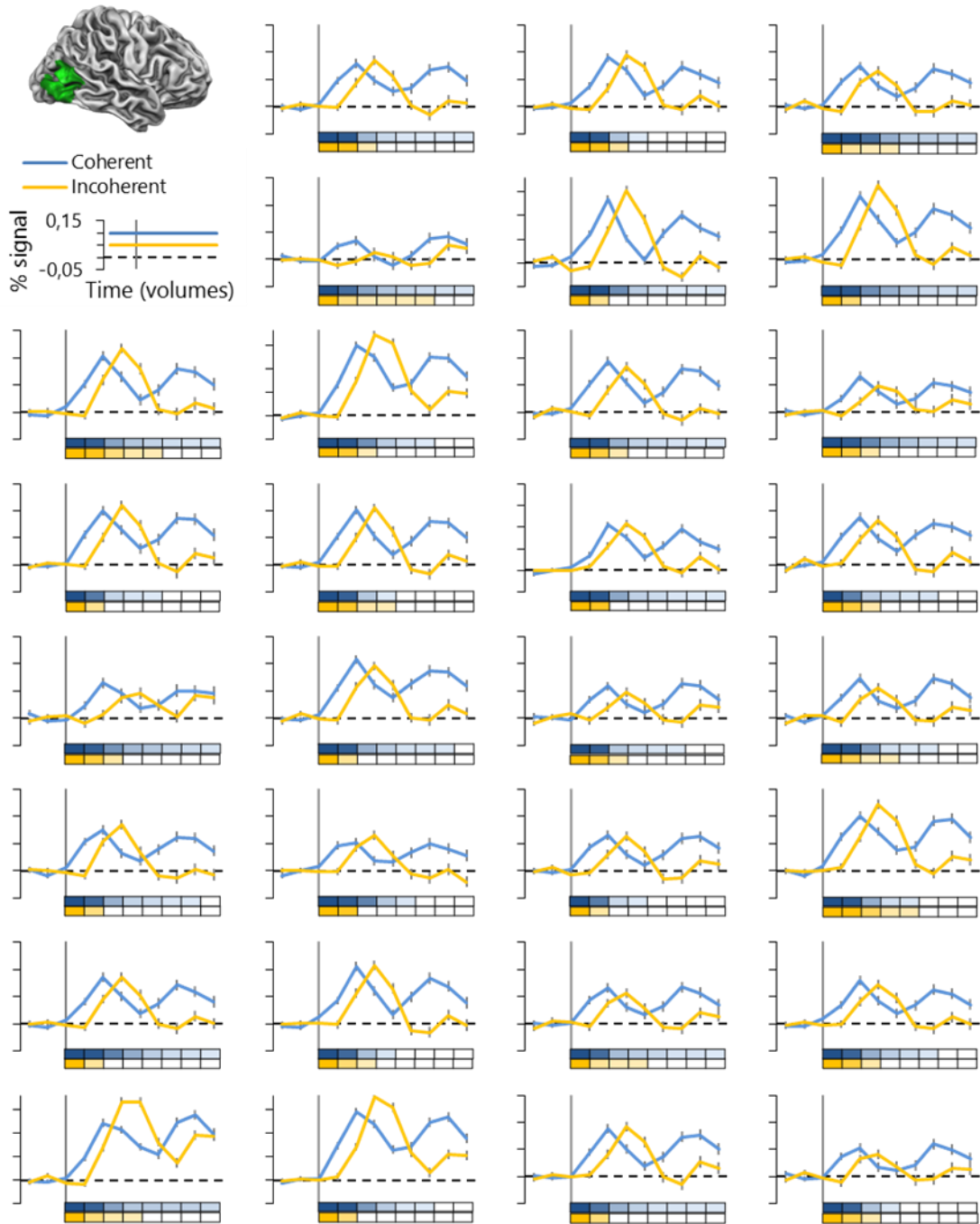


Figure 4-23. Individual event-related analysis of activity within right MT+ (group probability map on top left) during ambiguous bistable motion in 30 participants. Event-related average time courses during coherent and incoherent percepts are shown in blue and orange, respectively. The vertical grey bars indicate percept onset. Whiskers correspond to \pm SEM. The coloured rectangles represent functional volumes (2 sec). Dark colour (intensity, 100%) indicates that the percept was present at that functional volume on every one of the averaged time courses. White colour (intensity, 0%) indicates that the percept had switched again on all averaged time courses.

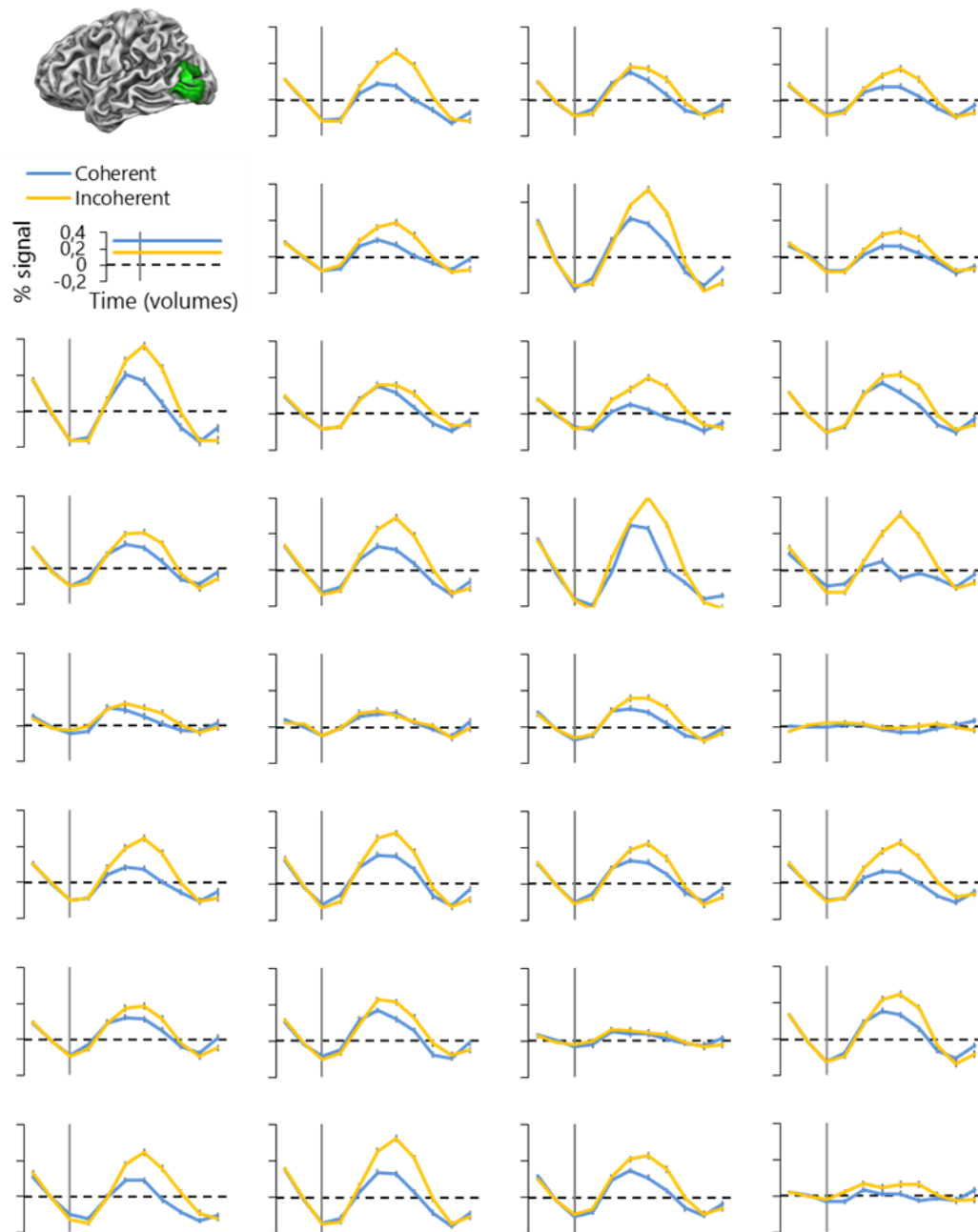


Figure 4-24. Individual event-related analysis of activity within left MT+ (group probability map on top left) during unambiguous motion in 30 participants. Event-related average time courses during pattern and component motion are shown in blue and orange, respectively. The vertical grey bar indicates motion onset. Whiskers correspond to \pm SEM.

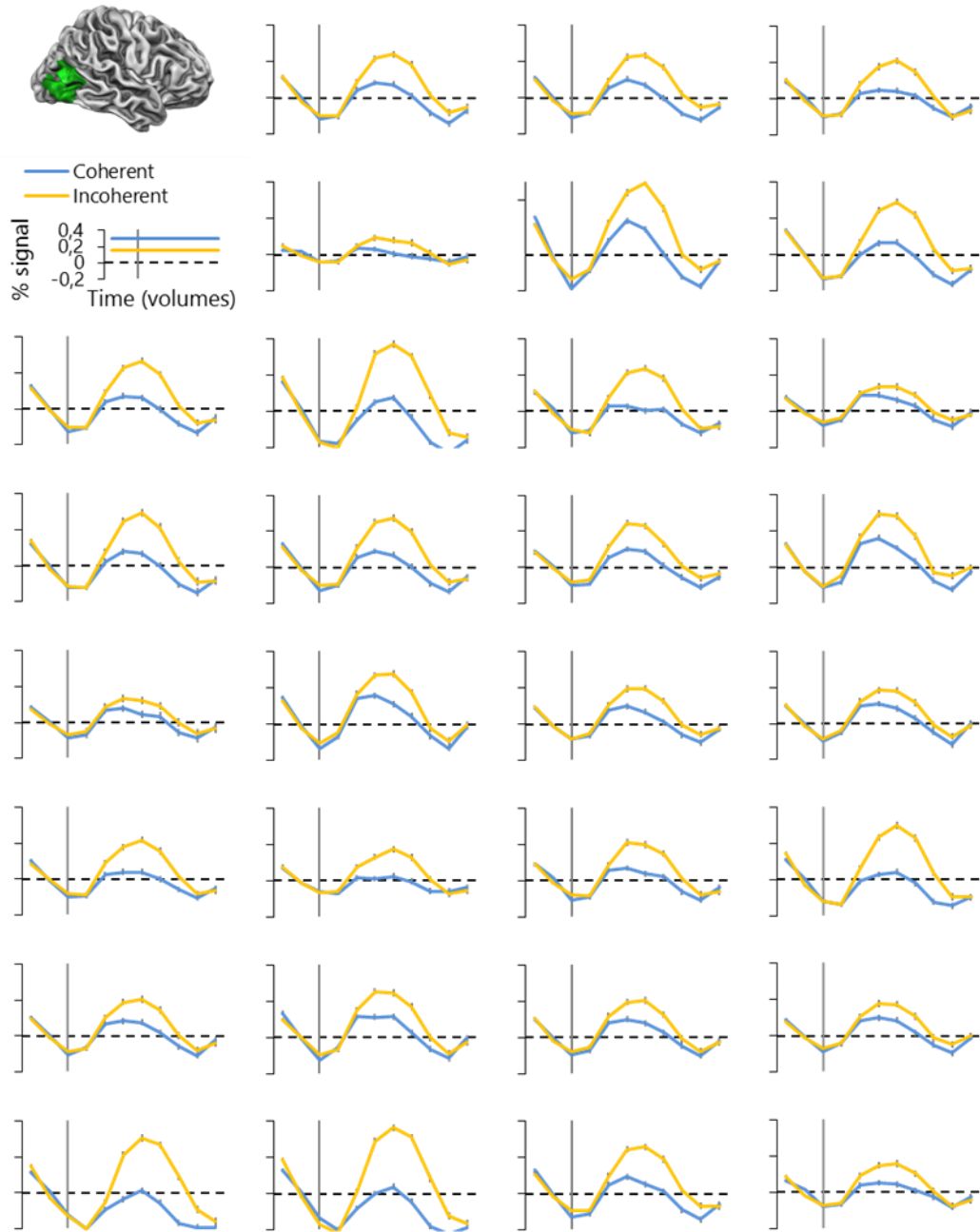


Figure 4-25. Individual event-related analysis of activity within right MT+ (group probability map on top left) during unambiguous motion in 30 participants. Event-related average time courses during pattern and component motion are shown in blue and orange, respectively. The vertical grey bar indicates motion onset. Whiskers correspond to \pm SEM.

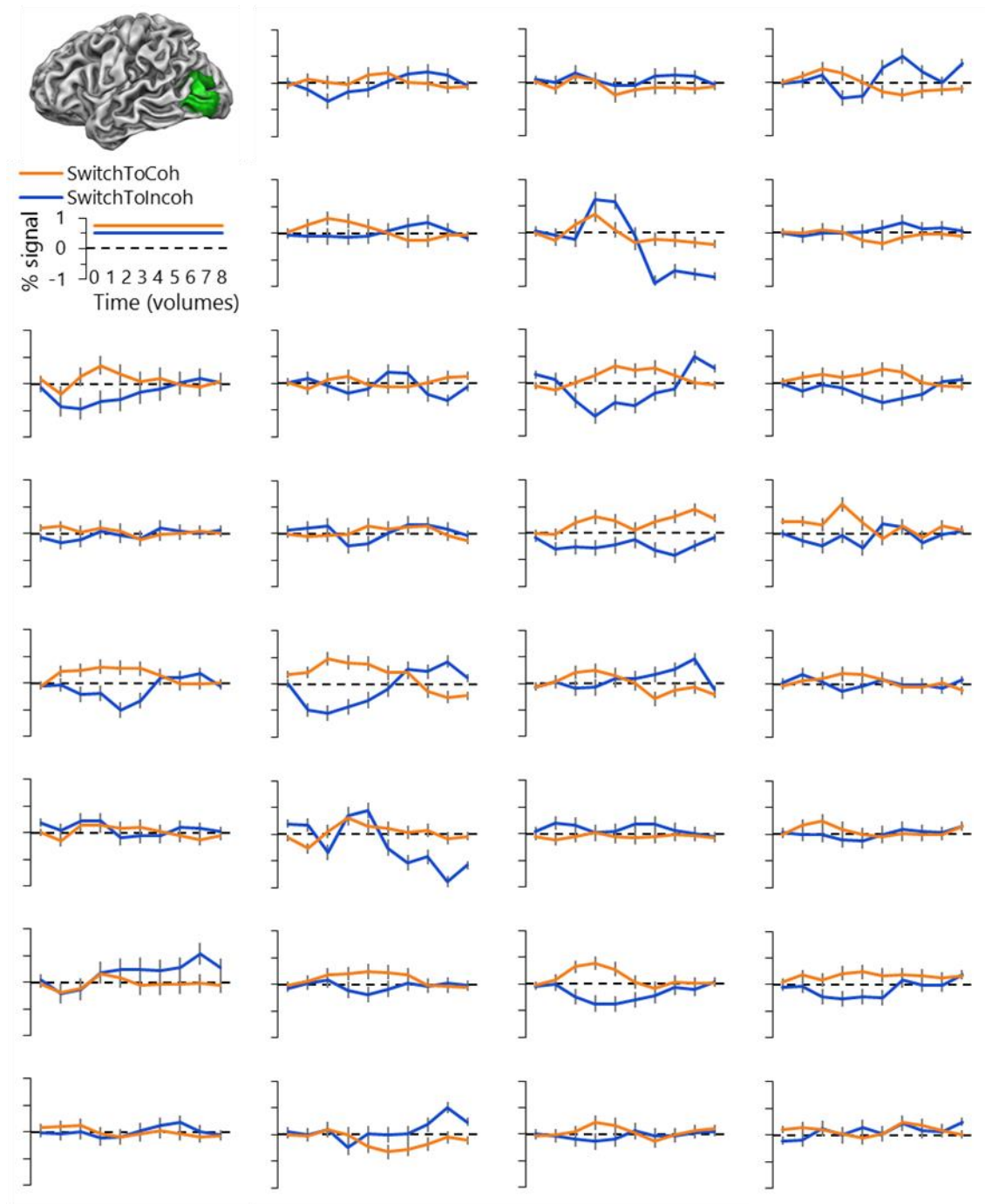


Figure 4-26. Individual deconvolution GLM analysis of switch-related activity within left MT+ during ambiguous bistable motion in thirty participants. The probability map of MT+ location is shown in a reconstruction of the left hemisphere in Talairach space. Signal time courses after perceptual switches from incoherent to coherent percept are shown in blue and after switches from coherent to incoherent in orange. Whiskers correspond to \pm SEM. Note the trend to left MT+ respond slightly more to switches from coherent (pattern motion) to incoherent (component motion) percepts.

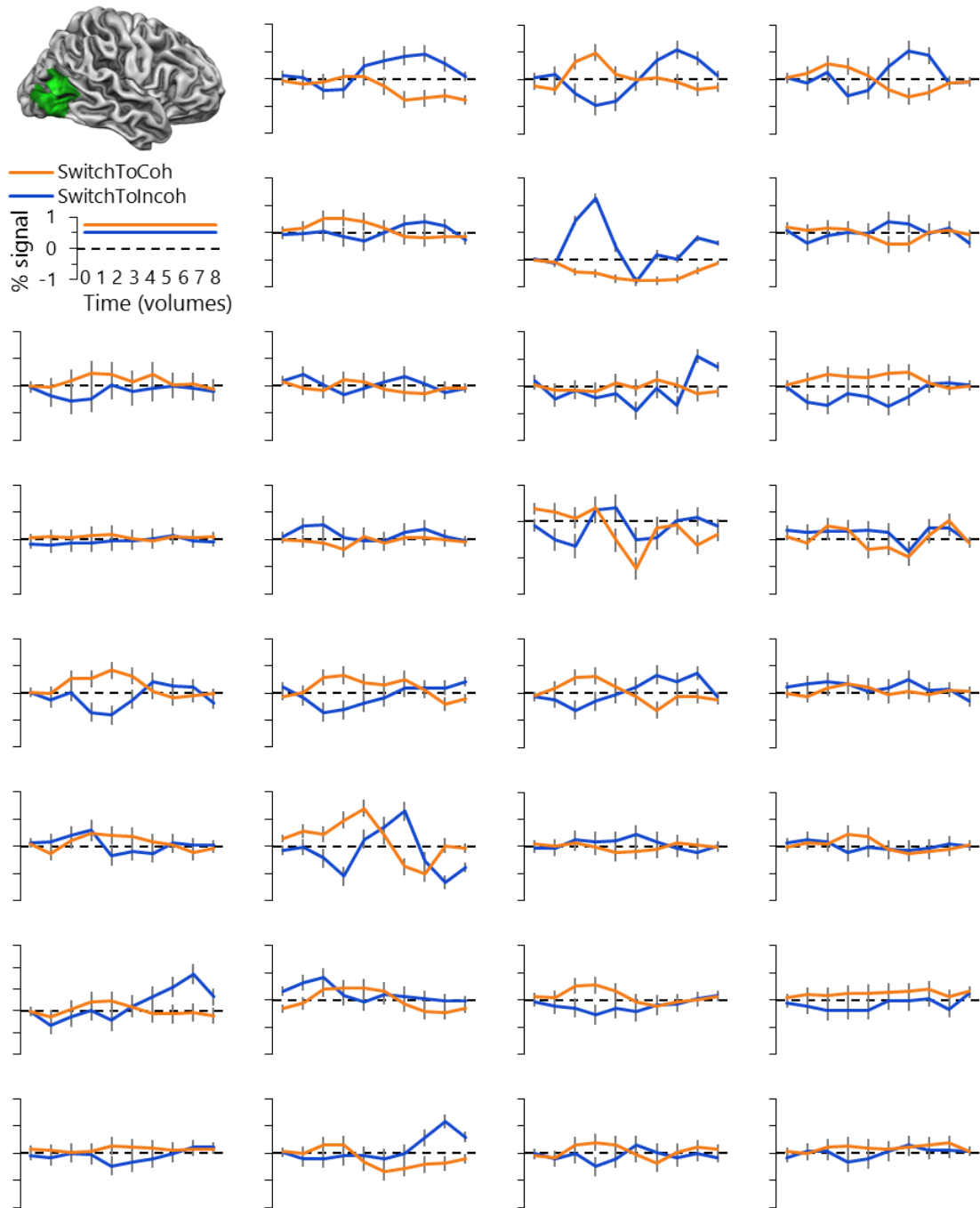


Figure 4-27. Individual deconvolution GLM analysis of switch-related activity within right MT+ during ambiguous bistable motion in thirty participants. The probability map of MT+ location is shown in a reconstruction of the left hemisphere in Talairach space. Signal time courses after perceptual switches from incoherent to coherent percept are shown in blue and after switches from coherent to incoherent in orange. Whiskers correspond to \pm SEM. Note the trend to right MT+ respond slightly more to switches from coherent (pattern motion) to incoherent (component motion) percepts.

Chapter 5

The bistable Necker cube

Competing fronto-parietal neural
resources between perception and
attention

This chapter was based on: **Intaitè M***, **Duarte JV*** & Castelo-Branco M (2016). Working memory load influences perceptual ambiguity by competing for fronto-parietal attentional resources. In revision in *Brain Research*. (* co-first authorship)

Abstract

A visual stimulus is defined as ambiguous when observers perceive it as having at least two distinct and spontaneously alternating interpretations. Neuroimaging studies suggest an involvement of a right fronto-parietal network regulating the balance between stable percepts and the triggering of alternative interpretations. As spontaneous perceptual reversals may occur even in the absence of attention to these stimuli, we investigated neural activity patterns in response to perceptual changes of ambiguous Necker cube under different amounts of working memory load using a dual-task design. We hypothesized that the same regions that process working memory load are involved in perceptual switching and confirmed the prediction that perceptual reversals led to fMRI responses that linearly depended on load. Accordingly, posterior Superior Parietal Lobule, anterior Prefrontal and Dorsolateral Prefrontal cortices exhibited differential BOLD signal changes in response to perceptual reversals under working memory load. Our results also suggest that the posterior Superior Parietal Lobule may be directly involved in the emergence of perceptual reversals, given that it specifically reflects both perceptual *versus* real changes and load levels. The anterior Prefrontal and Dorsolateral Prefrontal cortices, showing a significant interaction between reversal levels and load, might subserve a modulatory role in such reversals, in a mirror symmetric way: in the former activation is suppressed by the highest loads, and in the latter deactivation is reduced by highest loads, suggesting a more direct role of the aPFC in reversal generation.

Introduction

The human visual system seems unfit to tolerate ambiguity. Vision is designed to guide behavior and a behaving organism cannot afford to be halted by indecision.

However, some stimuli may be prone to perceptual changes that occur during visual processing. On such occasions, rather than choosing a single interpretation, perception interchanges between two (or more) valid alternatives. Ambiguous figures are a good example of such stimuli: they are physically constant, yet our brain perceives them as changing. The origin of perceptual reversals is still highly under debate regarding whether low or high level visual mechanisms play a major role in determining perceptual decisions (for a review see ¹). Some studies suggest that bottom-up mechanisms are the most important for the perception of ambiguous figures ²: the neural channels determining one of the available percepts, satiate and thus perceptual interpretation changes to the alternative one. The cognitive theories suggest that perceptual decisions might be induced by feedback from higher to lower levels of processing, for example, by activation of a high-level “exploratory” mechanism that directs selective attention in a way that causes a recurrent “renewal” of the type of representation in low-level perceptual systems ³. A growing number of studies ^{1,4-9} indicate that both perceptual processes play definable roles in the perception of ambiguity.

Selective attention orients the focus of conscious awareness toward relevant stimuli. Working memory (WM) maintains an active and brief representation of just obtained information to be used for subsequent processing or recall, while selective attention filters that information thus controlling what is encoded and maintained in WM. Studies using functional magnetic resonance imaging (fMRI) reveal an overlap between attention and WM networks over visual, parietal and frontal areas ¹⁰⁻¹², supporting the view that these cognitive functions share neural resources and are both governed by the fronto-parietal attention network ^{13,14}.

The brain regions activated during perceptual changes seem as well to overlap with the fronto-parietal attention network ¹⁵⁻¹⁹. Our study was motivated to help unravel the nature of such overlap. Prefrontal and dorsolateral prefrontal cortices (as parts of the fronto-parietal attention network) may control the updating of

ambiguous stimulus representations in the extrastriate visual areas as suggested by transient signal increases in prefrontal cortex during perceptual reversals^{16,17,20}. Sterzer and Rees²¹ reported activations in visual cortex alongside with activity in prefrontal and parietal regions for percept-specific signals in response to binocular rivalry stimuli and discussed comparable BOLD signal changes over visual and fronto-parietal regions in response to voluntary engagement of facial WM²²⁻²⁴. The authors suggested that perceptual durations might be influenced by higher-order mechanisms that share a common anatomical substrate with WM. The Superior Parietal Lobule (SPL) might also be differentially involved in perception of reversals: stimulating the right anterior or right posterior SPL, respectively increases or decreases the number of perceived reversals²⁵. Right SPL seems to be also activated when participants perform WM manipulation of stimulus content²⁶. However, the exact role of fronto-parietal regions in shaping perceptual decisions remains to be clarified. Sterzer and colleagues²⁷ hypothesize that fronto-parietal activations may participate in inferential processes that are helping to achieve perceptual stability and suggest that perceptual ambiguity might result from continuous reciprocations between low-level and high-level brain regions.

The aim of the present study was to investigate WM dependent brain mechanisms that induce perceptual bistability. We set to investigate how neural activity in response to perceptual decisions is modulated by concurrent recruitment of attentional resources in fronto-parietal regions that are hypothesized to subserve a dual role in such processes. More explicitly, the spatial locus of the possible effects related to concurrent processing was examined with fMRI. We chose a WM load (hereafter WML) task as a secondary task since it depletes the available attentional resources^{28,29}. When WML, or a similar secondary task employing attentional resources (e.g., motion-detection, mental arithmetic), is used concurrently with the reversal task, the participants consequently perceive less

reversals of a given ambiguous image^{5,30–35}. In our study, participants were required to detect perceptual reversals of an ambiguous Necker cube while performing a concurrent task with four levels of WML. In order to manipulate the amount of available WM resources, the WML stimuli (letter strings) consisted of either no letters (sham-load), five, six or seven consonants. The concurrent task involved memorization of the letter strings, which were followed by an ambiguous Necker cube presentation. Finally, to control for possible differences in perception of the perceptual *versus* real change of the Necker cube under WML, we used an extra condition in which two unambiguous images, each representing one of the two different percepts of the Necker cube, were presented subsequently while the participants had to report the real changes while completing the WML task with six consonants. We theorized that if WM resources are actively involved in the construction of the available percepts of the ambiguous stimulus, a concurrent WML will decrease the reversal rates and modulate the efficiency of the neural processes involved in reversals. Due to enhanced usage of attentional resources, we hypothesized that BOLD signal changes in response to perceptual decisions under sham-load would be stronger than the signal variation obtained under WML conditions over anterior prefrontal cortex (aPFC), dorsolateral prefrontal cortex (DLPFC) and SPL.

Materials and methods

Participants

We recruited 14 healthy participants (8 male; mean age \pm standard deviation = 26.3 ± 3.1 years) to take part in the study. They had normal vision and were naive as to the specific experimental question. All participants were right-handed, as confirmed by Edinburgh Handedness Inventory³⁶. A written informed consent (in

accordance to the declaration of Helsinki) was obtained from all participants and the institutional ethics committee formally approved the study. The experiments were conducted in compliance with the safety guidelines for MR research on humans.

Stimulus presentation and apparatus

We wrote our experiments in MATLAB, using the Psychophysics Toolbox extensions^{37,38}. The stimuli were shown inside the MR scanner by means of an LCD screen (refresh rate 60 Hz) located ~156 cm away from the participant. The participants viewed the images through a mirror mounted above the participant's eyes. All stimuli were presented at high contrast levels in black on a white background. The participants were responding by pressing buttons on a Cedrus Lumina LP-400, LU400 PAIR MR-compatible response box (Cedrus Corporation, San Pedro, CA 90734, USA). To determine whether participants were able to maintain central fixation during the experimental task, eye tracking data (sample frequency 1000 Hz) were recorded inside the scanner using eye tracker software Eyelink 1000 (SR Research, Ottawa, Ontario, Canada). The eye tracker was individually calibrated with a 9-point calibration routine in the beginning of experiment.

Working memory stimuli

In order to manipulate working memory, a memory set, consisting of the memory prime and the memory probe, was used as depicted in Figure 5-1A. In the sham-load condition the prime consisted of five asterisks (*****; size $0.41^\circ \times 0.41^\circ$). In the ambiguous-5-letter-load (a-5LL), ambiguous-6-letter-load (a-6LL) and ambiguous-7-letter-load (a-7LL) conditions the prime consisted of 5, 6 and 7

consonants (size: $0.61^\circ \times 0.5^\circ$), respectively, except H, K, Q and W (the selection of consonants was based on Portuguese alphabet). An unambiguous-6-letter-load (u-6LL) condition was used as a control to check for possible differences induced by perceptual *versus* real changes of the stimuli both in perception and BOLD signal. The memory probe was presented in the end of each trial and consisted of two arrows (arrow size $0.5^\circ \times 0.5^\circ$) to the left (<<) or the right (>>) in the sham-load condition, or one letter in all other conditions. Multiple randomized sequences of consonants were created for the memory stimuli and the occurrence (as well as the position) of each consonant in each trial was equiprobable.

Ambiguous and unambiguous Necker cube stimuli

The Necker cube, of size $4.15^\circ \times 4.11^\circ$, was used as the main experimental stimulus. In the u-6LL condition two unambiguous cubes (representing 'down' and 'up' orientations of the ambiguous Necker cube) were used and they were interchanged randomly with an aim to mimic perceptual reversals (see Figure 5-1B). The position of the fixation point on the unambiguous cubes was kept to match the centre of the ambiguous Necker cube. The durations of both unambiguous stimuli were based on the mean values of perceptual durations (under a-6LL) from 29 participants: values from 14 participants were obtained from data of ⁵ and data from 15 participants were collected during pilot experimentation outside the scanner. For each ambiguous and unambiguous cube a mirror image version with respect of the left-right orientation was created and shown on half of the trials.

Experimental design

In the beginning of the experiment, a static version of a Necker cube was shown for each participant. If a participant was initially unable to perceive the ambiguity of the figure, the experimenter prompted him/her until the participant was able to perceive the figure in both interpretations. Then each participant performed a short practice block of 15 trials outside the scanner in order to get used to the task. Each trial of all conditions began with the presentation of the memory prime (containing either asterisks or letters) for 3 sec followed by the fixation dot for 1 sec. Participants were asked to memorize the letter stimuli in conditions involving letter primes or just to look at the asterisks in the sham-load condition. In all conditions, except sham-load, the participants were instructed to use mental repetition to complete the WML task. After the fixation dot, an ambiguous Necker cube was presented for 10 sec. The participants were asked to report the perceived reversals by a button press. The cube was followed by the blank screen for 0.5 sec. At the end of each trial the memory probe was presented for 3.5 sec and the participant had to discriminate left-oriented *versus* right-oriented arrows in the sham-load condition, or had to indicate whether the letter presented in the probe matched (positive probe) or did not match (negative probe) any of the letters presented in the prime by pressing the left or the right designated buttons, respectively. The sequence of each experimental trial in u-6LL condition was the same as in other conditions, except during the 10 sec interval two unambiguous cubes, each representing an orientation of the ambiguous Necker cube, were presented interchangeably and the participants were instructed to press a designated button for each orientation change. Trials were later ranked as few (2 real changes) or many (3 real changes) for behavioral and brain imaging analyses (to mimic the data parcellation in ambiguous trials). The probe (Figure 5-1C) was followed by a 2 sec masking grid (made from scrambled Necker cube image) used in order to diminish the afterimages. After each trial a 6 sec inter-trial rest period

was given. The participants were instructed to keep their eyes focused on the fixation dot (or letter strings when presented) throughout the whole experiment. Response hand assignments of the buttons and the order of experimental conditions were counterbalanced across participants. It was emphasized that they should press the 'reversal' button only when they actually saw a perceptual reversal, and they were instructed to pay attention to unambiguous stimuli in order to correctly report the real changes. The experiment included 100 trials (20 trials of each condition) divided in 20 runs (5 trials per run). One block lasted ~2.2 min. In the beginning of each run, the participants fixated on a fixation cross for 4 sec. We presented unambiguous and ambiguous conditions in separate runs.

MRI data acquisition

Data were collected with a Siemens Magnetom TIM Trio 3T research scanner with a phased array 12-channel birdcage head coil (Siemens, Munich, Germany). The experiment consisted of one MR scanning session during which one structural volume and 20 functional runs (67 volumes per run) were acquired. The scanning session began by acquiring a 3-D anatomical T1-weighted MPRAGE (magnetization-prepared rapid gradient echo) sequence (TR = 2530 msec, TI = 1100 msec, TE = 3.42 msec, flip angle = 7°, 176 interleaved slices (no-gap) with voxel size = 1 × 1 × 1 mm, FOV 256 mm). Functional images were acquired axially using T2*-weighted gradient echo EPI sequences covering the whole brain. Each functional run consisted of 67 volumes (TR = 2000 msec, TE = 40 msec, flip angle = 90°, 35 interleaved slices (no-gap) with voxel size 3 × 3 × 3 mm; FOV 256 mm). The head of the participant was stabilized by means of foam pillows placed on both sides of the head.

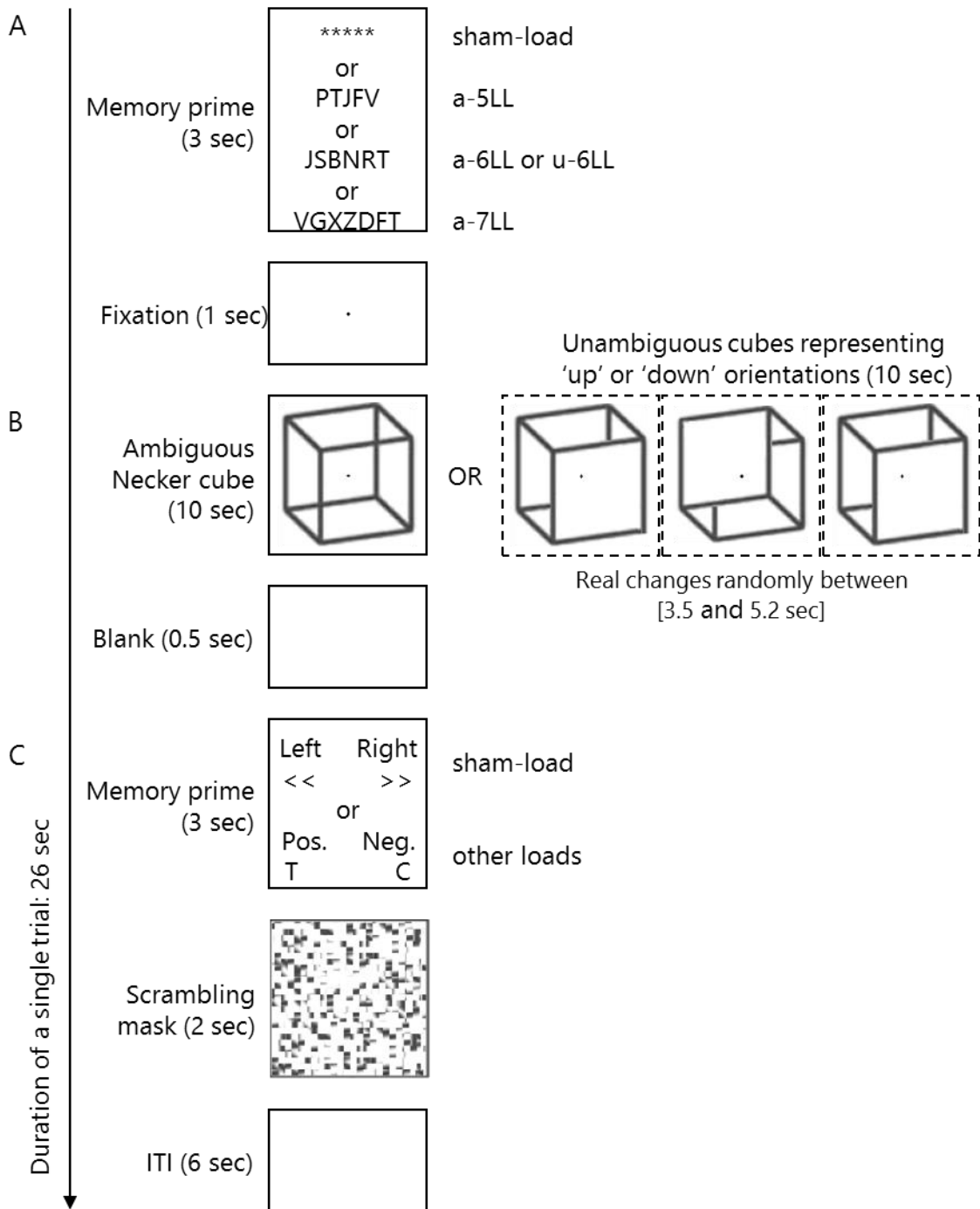


Figure 5-1. Graphical representation of the stimuli and experimental protocol. (A) An illustration of the experimental trials in all conditions: schematic representation of the memory primes in the sham-load, ambiguous-five-letter-load (a-5LL), ambiguous-six-letter-load (a-6LL), unambiguous-six-letter-load (u-6LL), and ambiguous-seven-letter-load (a-7LL) conditions. (B) In each condition with perceptual changes, the memory prime is followed by a standard Necker cube. In the control condition (u-6LL) the prime is followed by a sequence of unambiguous cubes. (C) Schematic representation of the memory probes in all conditions.

Data preprocessing and analysis

In the beginning of each run, the first 2 volumes of functional data were automatically discarded in the scanner to allow the magnetization to reach a steady state. The data were analyzed using BrainVoyagerQX 2.8. (Brain Innovation, Maastricht, The Netherlands). Functional volumes were realigned and corrected for interleaved slice-timing, coregistered with the participants' corresponding anatomical (T1-weighted) volume, spatially normalized into Talairach stereotaxic space, and spatially smoothed with an 8 mm full-width at half-maximum gaussian kernel. Head motion correction was performed by adjusting all the functional runs with the first functional run presented right after the anatomical acquisition. High pass filtering (3 cycles/scan) was performed in order to compensate for a slow fMRI signal drift. The time-series of each voxel was divided by its mean intensity to convert the data units from image intensity to fractional signal change, and to compensate for distance from the surface coil.

Statistical analysis was performed using a random-effects general linear model (RFX-GLM). The data for each subject was concatenated resulting in mean effect estimates per condition (first level effect). Then the first level effects were entered to the second level as the new dependent variable (instead of the raw data) and were analyzed across subjects (second level analysis).

Multi-subject RFX-GLM fitted the data with regressors that represented all experimental conditions. Each period of a trial was included as a regressor (prime, cube and probe presentation) in the model. Different conditions (sham-load, a-5LL, a-6LL and a-7LL) were modelled with separate regressors. The regressors were defined to be "on" exactly between onset and offset of each presentation of the Necker cube. The onsets of the ambiguous/unambiguous cubes (rounded with respect to a multiple of the repetition time) also served as time markers to extract the mean signal time course starting two scans (4 sec) before stimulus onset and ending 15 scans (30 sec) after stimuli presentation.

In order to be sure that the participants paid attention to the WML task, we included only trials followed by the correct responses to memory probes in the GLM (and other analyses as well), based on the reports of the participants. Predictors for real changes were modeled for u-6LL condition based on the actual changes of the stimuli, taking into account the correct reports to real changes of stimuli and to memory probes provided by the participants. To reduce unexplained variance in the data incorrect trials were added as confound predictors. Baseline signal was considered from twenty baseline fixation periods. The hemodynamic BOLD responses were modeled as boxcar functions convolved with a two-gamma canonical hemodynamic response function as implemented in BrainVoyagerQX.

To investigate the reversal specific effects under WML, an analysis taking into account both the WML task and the number of perceived changes was conducted. After exclusion of erroneous working memory load trials, on average (SD) 20 (0) trials in the sham-load condition, 17.2 (2.22) in the a-5LL, 16.6 (2.79) in the a-6LL and 17.6 (2.13) in the a-7LL conditions remained for all analyses. Reversals perceived in each trial of each condition were ranked as either few (0-2 reversals within a trial) or many (3 or more reversals within a trial). Thus, two regressors for each condition were modeled separately for sham-load, a-5LL, a-6LL, a-7LL, and u-6LL conditions (i.e., sham-load few reversals, sham-load many reversals, a-5LL few reversals, a-5LL many reversals etc.). On average 9.9 (SD: 5.6) and 7.9 (SD: 4.9) trials in sham-load, 9.7 (SD: 5.9) and 7.9 (SD: 4.9) in a-5LL, 8.4 (SD: 4.9) and 7.9 (SD: 4.8) in a-6LL, 10.6 (SD: 5.9) and 6.9 (SD: 5.4) in a-7LL, 9.1 (SD: 1.1) and 8.9 (SD: 1.7) in u-6LL were ranked as having few or many reversals, respectively. Four participants were excluded from these analyses because they perceived either only few or only many reversals in one (or more) of the experimental conditions. The effects were assessed using two-way ANOVAs with two within-subjects factors, in a 2 (Reversals: few and many) \times 4 (Load: sham-

load, a-5LL, a-6LL and a-7LL) design. In case of significant Reversals \times Load interaction, additional one-way ANOVAs, with Load as a within-subjects factor, were conducted within BVQX and post-hoc t-tests were conducted with SPSS 19.0 software. As the number of perceived reversals was different for every load condition, we decided to analyze only those ROIs that revealed significant Reversals \times Load interactions and report only the Load effects obtained from subsequent one-way ANOVAs (few or many reversals, respectively). The ROIs were created by manually selecting significant voxels (within template ROIs consisting of Brodmann areas) in the statistical map resulting from the multi-subject ANOVA whole-brain interactions (FDR corrected *P-value* < 0.05). Individual parameter estimates were averaged across all voxels within each ROI, and submitted to second-level analyses. For ROI analyses of unambiguous changes, the ANOVAs had 2 (Reversals: few and many) \times 2 (Type: u-6LL and a-6LL) as within-subject factors.

Behavioral analyses

For all conditions the probe response accuracies ($D(14) \geq 0.20$, *P-value* > 0.05, K-S test) and probe response times ($D(14) \geq 0.13$, $p > 0.05$, K-S test) were normally distributed. For each load condition, we divided the number of reversals by the amount of trials. This transformed reversal rate was calculated for each participant individually and used in the analyses. K-S test revealed that reversal rate did not meet the condition of normality. The distribution of reversal rate values was leptokurtic and positively skewed, thus square root transformations were applied to these data³⁹.

One-way ANOVAs with a within-subject factor of Load (sham-load, a-5LL, a-6LL and a-7LL) were performed on the mean values of the WML task (accuracy, probe response time). Two-way ANOVAs with within-subject factors of Reversals (few

and many) and Load (sham-load, a-5LL, a-6LL and a-7LL) were performed on normalized reversal rate values.

In all ANOVAs, post-hoc t-tests (Fisher's Least Significant Difference, hereafter Fisher's LSD) were used for pairwise comparisons of conditions in the case of a main effect of Load (or Type). The significant linear trends in the data revealed by the within-subjects contrasts were also reported. In the statistical analyses, we reported the original degrees of freedom, but corrected the *P-value* according to Huynh-Feldt correction whenever the degrees of freedom were greater than 1. The degrees of freedom are reported together with effect sizes (partial eta squared: η_p^2).

Results

Working memory task performance

The memory probe response accuracy decreased with higher working memory load task ($F(3,39) = 10.20$, *P-value* < 0.0001, $\eta_p^2 = 0.44$) (Figure 5-2A). The accuracy in the sham-load condition was higher than those acquired in response to all other conditions (all *P-values* < 0.01, Fisher's LSD corrected).

Probe response times increased with working memory load ($F(3,39) = 56.42$, *P-value* < 0.0001, $\eta_p^2 = 0.81$) (Figure 5-2B). The increase was linear with augmentation in working memory load ($F(1,13) = 149.47$, *P-value* < 0.0001, $\eta_p^2 = 0.92$). The probe response times in the sham-load condition were shorter than those obtained in all other conditions (all *P-values* < 0.0001, Fisher's LSD corrected) and the probe response times to a-5LL were shorter than those in response to a-7LL (*P-value* < 0.05, Fisher's LSD corrected).

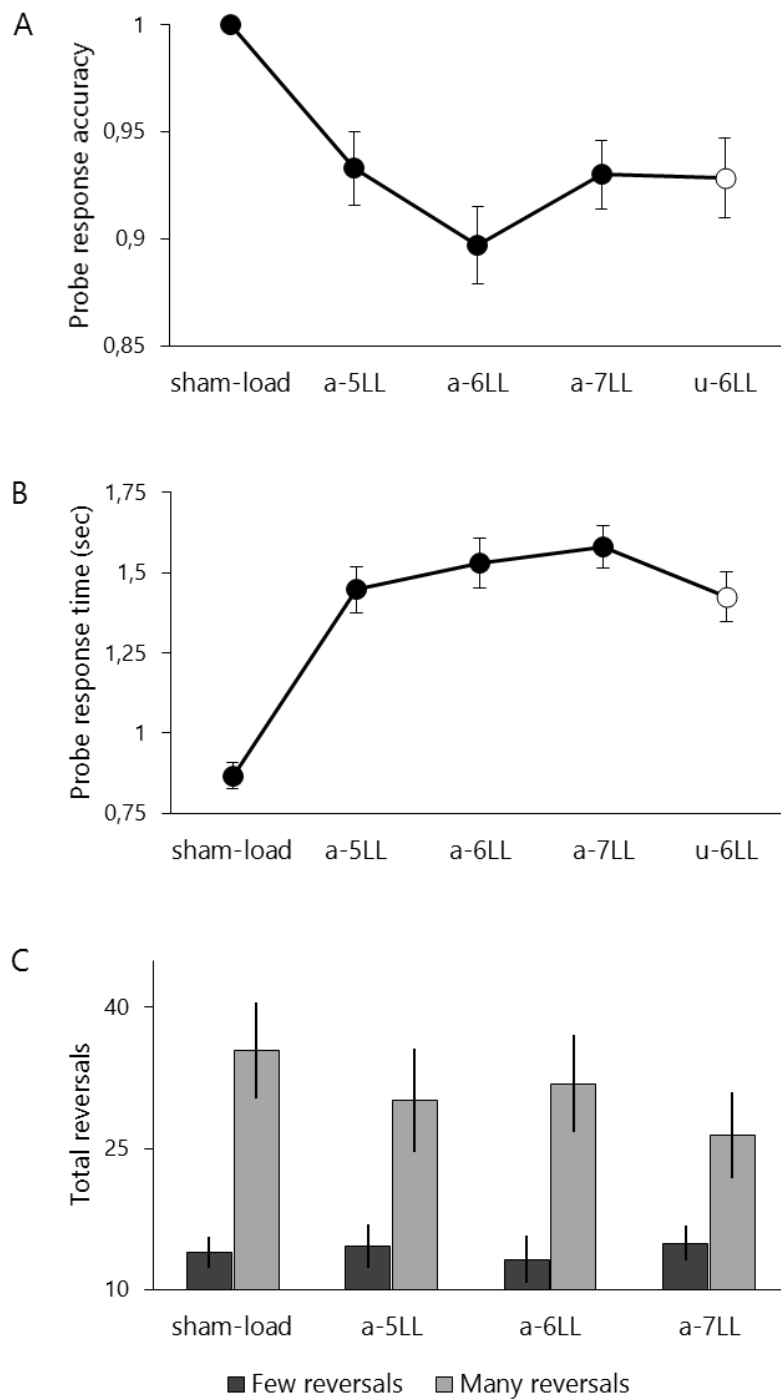


Figure 5-2. Behavioral performance of perceptual reversals and the WML task. (A) The accuracy in responses to the memory probes under sham-load, ambiguous-five-letter-load (a-5LL), ambiguous-six-letter-load (a-6LL), ambiguous-seven-letter-load (a-7LL), and unambiguous-six-letter-load (u-6LL) conditions (N = 14). (B) The response times to the memory probes under sham-load, a-5LL, a-6LL, a-7LL and u-6LL conditions (N = 14). (C) The normalized reversal rate per trial under sham-load, a-5LL, a-6LL and a-7LL conditions (N = 14). Error bars represent \pm SEM.

Reversal task performance

A-WML (presentation of ambiguous Necker cube)

The 2 (Reversals: few and many) \times 4 (Load: sham-load, a-5LL, a-6LL and a-7LL) repeated measures ANOVA revealed significant effect for Load ($F(3,39) = 3.23$, p -value < 0.04 , $\eta^2 = 0.20$) and a significant Reversals \times Load ($F(3,39) = 3.22$, p -value < 0.04 , $\eta^2 = 0.20$) interaction (Figure 5-2C). The decrease was linear with augmentation in working memory load ($F(1,13) = 6.21$, p -value < 0.03 , $\eta^2 = 0.32$). Subsequent one-way ANOVAs showed that the participants perceive less reversals under a-7LL than under sham and a-6LL (all p -values < 0.05 , Fisher's LSD corrected), only when they perceive many reversals ($F(3,39) = 3.97$, p -value < 0.02 , $\eta^2 = 0.23$) in the trial. The decrease was linear with augmentation in working memory load ($F(1,13) = 6.25$, p -value < 0.03 , $\eta^2 = 0.33$).

U-6LL (control presentation of real cube changes)

On average, the participants correctly identified 93% of real changes (SD = 0.07) and took around 600 msec (SD = 0.07) to report them. Memory probe response accuracy (Figure 5-2A), response times (Figure 5-2B) to the memory probe in response to u-6LL were compared with the same responses obtained under a-6LL with one-way ANOVAs with Type (u-6LL and a-6LL) as a within-subject factor. The effects of Type were not statistically significant (all F -values ≤ 2.85). Repeated-measures ANOVA with Reversals (few and many) and Type (u-6LL and a-6LL) as within-subject factors was conducted on the number of reported real and perceptual changes. The effect of Reversals and Reversals \times Type interaction were not statistically significant (all F -values ≤ 3.65).

The distribution of fixations

The analyses of fixations were performed with eight participants; data from six participants were not collected due to eye-tracker malfunction. Fixations were calculated based on the recorded gaze behavior. A fixation duration threshold of 150 msec was used. Fixations that had the same position and were separated by a blink were concatenated. To calculate dwell time, consecutive fixations were concatenated. A rectangular area of interest ($1.46^\circ \times 1.44^\circ$) was defined on the center of the cube. The participants successfully maintained their gaze in the area of interest for $\sim 91\%$ (SD = 0.17) of the ambiguous cube presentation time and 90% (SD = 0.16) of the fixations fell in this region of interest. The participants successfully maintained their gaze $\sim 94\%$ (SD = 0.12) of the unambiguous cubes presentation time and 93% (SD = 0.13) of the fixations fell in the interest area. The average count of fixations falling over the selected interest area ($D(8) \geq 0.23$, $P\text{-value} > 0.05$, K-S test) and the dwell times over the interest area ($D(8) \geq 0.13$, $P\text{-value} > 0.05$, K-S test) were normally distributed. Two separate one-way ANOVAs with within-subject factors of Load (sham-load, a-5LL, a-6LL and a-7LL) and Type (u-6LL and a-6LL) were performed on the average count of fixations and the dwell times, but the effects were not significant (all F-values ≤ 2.73).

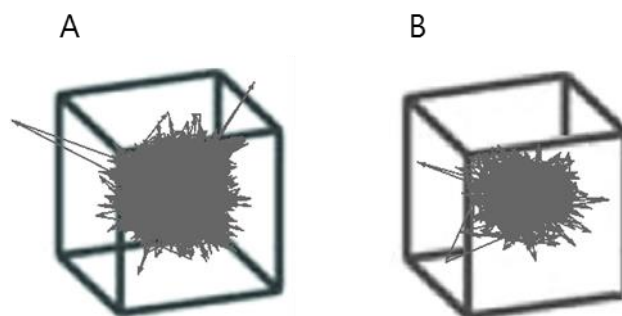


Figure 5-3. Eyes fixation during experimental task. (A) The distributions of the fixations from sham-load, a-5LL, a-6LL and a-7LL conditions (N = 8). (B) The distributions of the fixations from u-6LL condition (N = 8).

ANOVAs of fMRI BOLD signal

The 2 (Reversals: few and many) \times 4 (Load: sham-load, a-5LL, a-6LL and a-7LL) repeated measures ANOVA revealed significant effects for Load over pSPL and visual associative cortex ($F(3, 27) \geq 3.19$, $P\text{-value} < 0.05$, $\eta^2 \geq 0.26$): the BOLD signals in response to sham-load were significantly more positive than those in response to a-6LL and a-7LL over both ROIs and the signal in response to a-5LL (relatively lower load) was more positive than that obtained in response to a-6LL over visual associative cortex. Significant Reversals \times Load interactions ($F(3, 27) \geq 3.25$, $P\text{-value} < 0.05$, $\eta^2 \geq 0.27$) were found over the regions listed in Table 5-1. The statistical maps showing significant ANOVA interactions over left DLPFC, right pSPL and right aPFC are shown in Figure 5-4, Figure 5-5 and Figure 5-6, respectively. For these particular ROIs we also show interaction plots and fMRI response time-courses during trials where participants perceived few perceptual reversals (left DLPFC) or many perceptual reversals (right pSPL and right aPFC). The interaction plots for the other significant ROIs in Table 5-1 are shown in Figure 5-7.

Table 5-1. Interaction effect of Perceptual Reversals x Working Memory Load

Brain region	Talairach			F-score	Nr of voxels
	coordinates				
	X	Y	Z		
Premotor Cortex (BA6)	27	-7	58	8.37	933
left Dorsolateral Prefrontal Cortex	-18	44	40	7.57	384
Associative Visual Cortex	36	-73	16	6.43	556
right anterior Prefrontal Cortex	36	47	22	6.32	410
right posterior Superior Parietal Lobule	15	-76	37	5.68	258
right Angular Gyrus	61	-61	22	5.47	113
right Isthmus of Cingulate Cortex	30	-60	10	5.11	203
dorsal Posterior Cingulate Cortex	-24	-82	22	4.80	121

Regions with significant clusters showing coordinates of peak voxel in Talairach space and statistical F-values obtained from repeated-measures ANOVAs at *P*-value < 0.05 (FDR corrected).

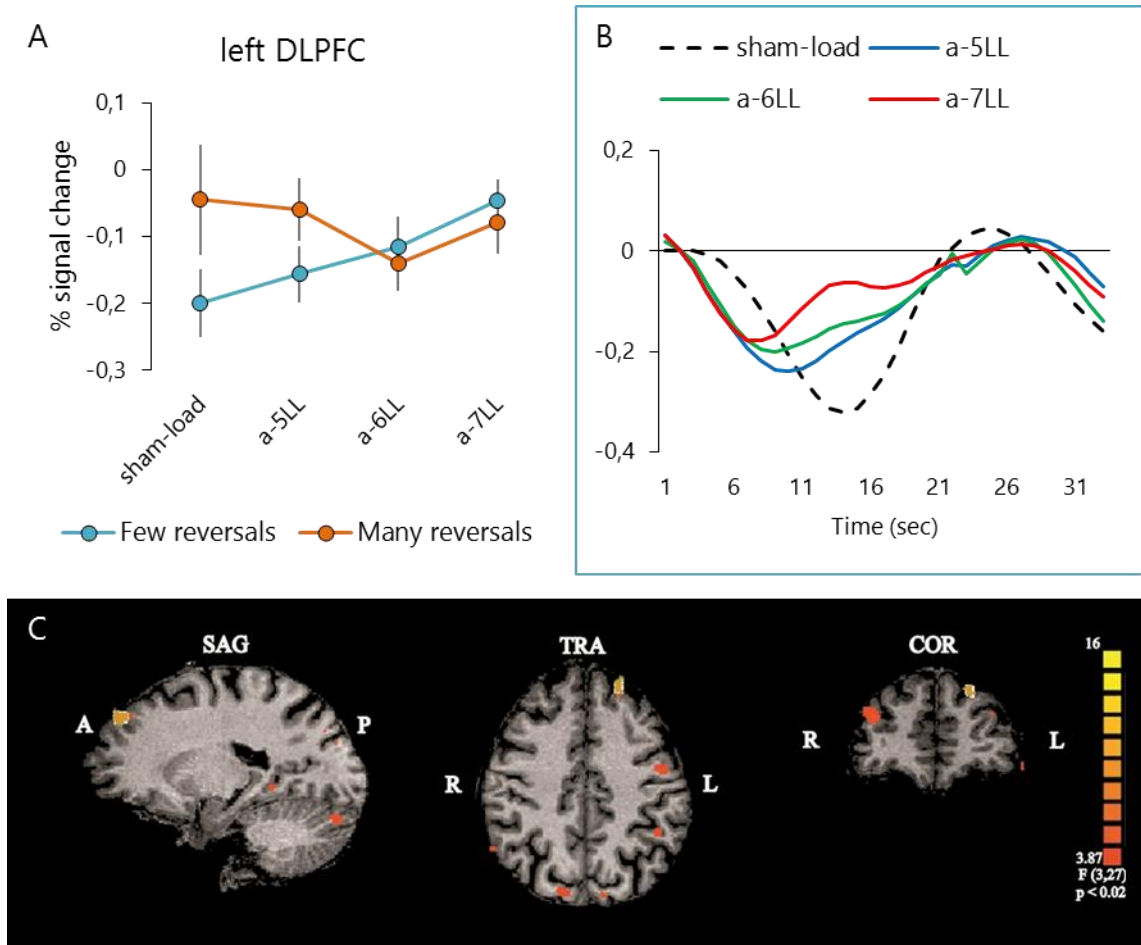


Figure 5-4. BOLD response in left dorsolateral prefrontal cortex (DLPFC) during presentation of the ambiguous Necker cube. (A) An interaction effect between cube reversals and WML was observed with repeated measures 2 (Reversals: few and many) \times 4 (Load: sham-load, a-5LL, a-6LL and a-7LL) ANOVA of signal changes. These interactions show that this brain region competes for attentional resources. (B) Time-course of BOLD response when participants viewed few cube reversals during ambiguous Necker cube presentation under sham, a-5LL, a-6LL and a-7LL working memory load (WML) conditions. (C) Functional map (thresholded at P -value < 0.05 , FDR corrected) generated from ANOVA on fMRI response to perceptual reversals under WML showing significant Reversals \times Load interaction in left DLPFC.

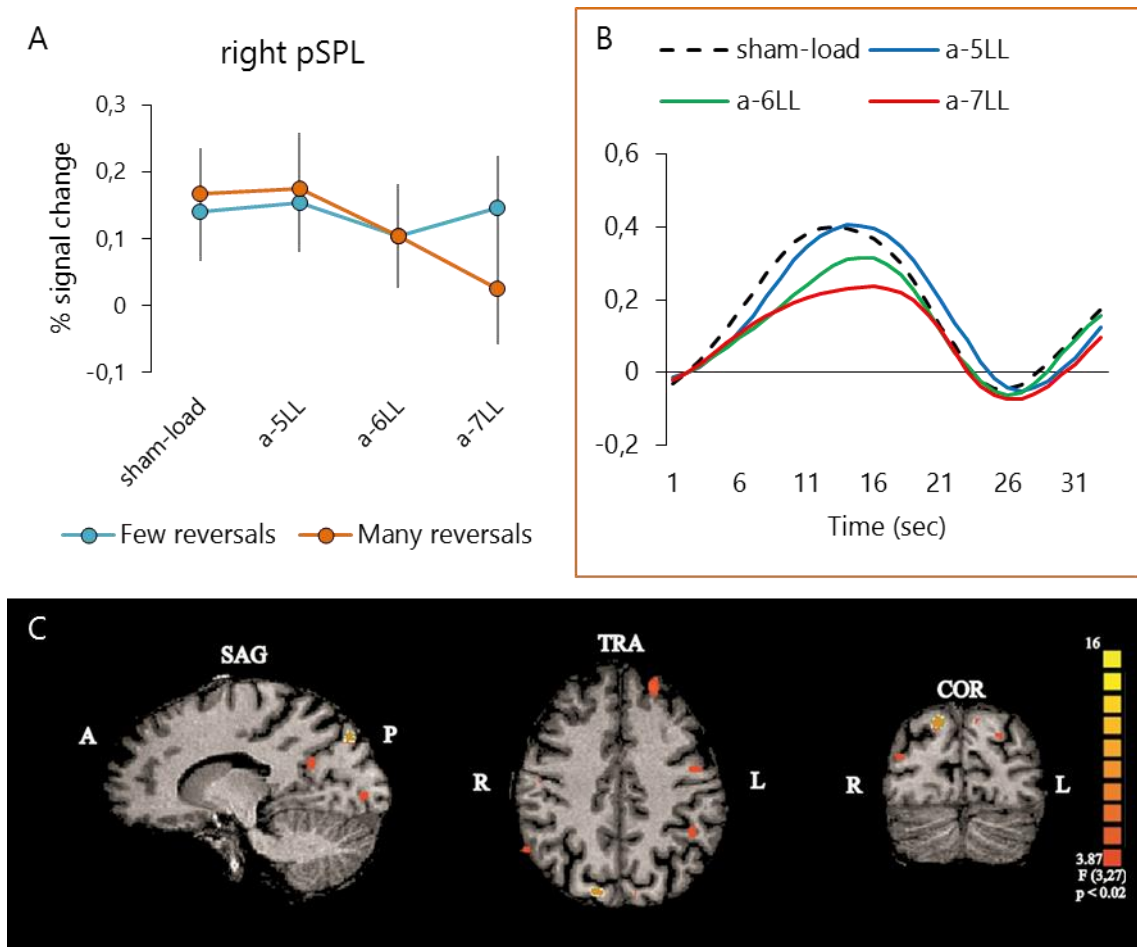


Figure 5-5. BOLD response in right posterior superior parietal lobule (pSPL) during presentation of the ambiguous Necker cube. (A) An interaction effect between cube reversals and WML was observed with repeated measures 2 (Reversals: few and many) \times 4 (Load: sham-load, a-5LL, a-6LL and a-7LL) ANOVA of signal changes. These interactions show that this brain region competes for attentional resources. (B) Time-course of BOLD response when participants viewed many cube reversals during ambiguous Necker cube presentation under sham, a-5LL, a-6LL and a-7LL working memory load (WML) conditions. (C) Functional map (thresholded at P -value < 0.05, FDR corrected) generated from ANOVA on fMRI response to perceptual reversals under WML showing significant Reversals \times Load interaction in right pSPL.

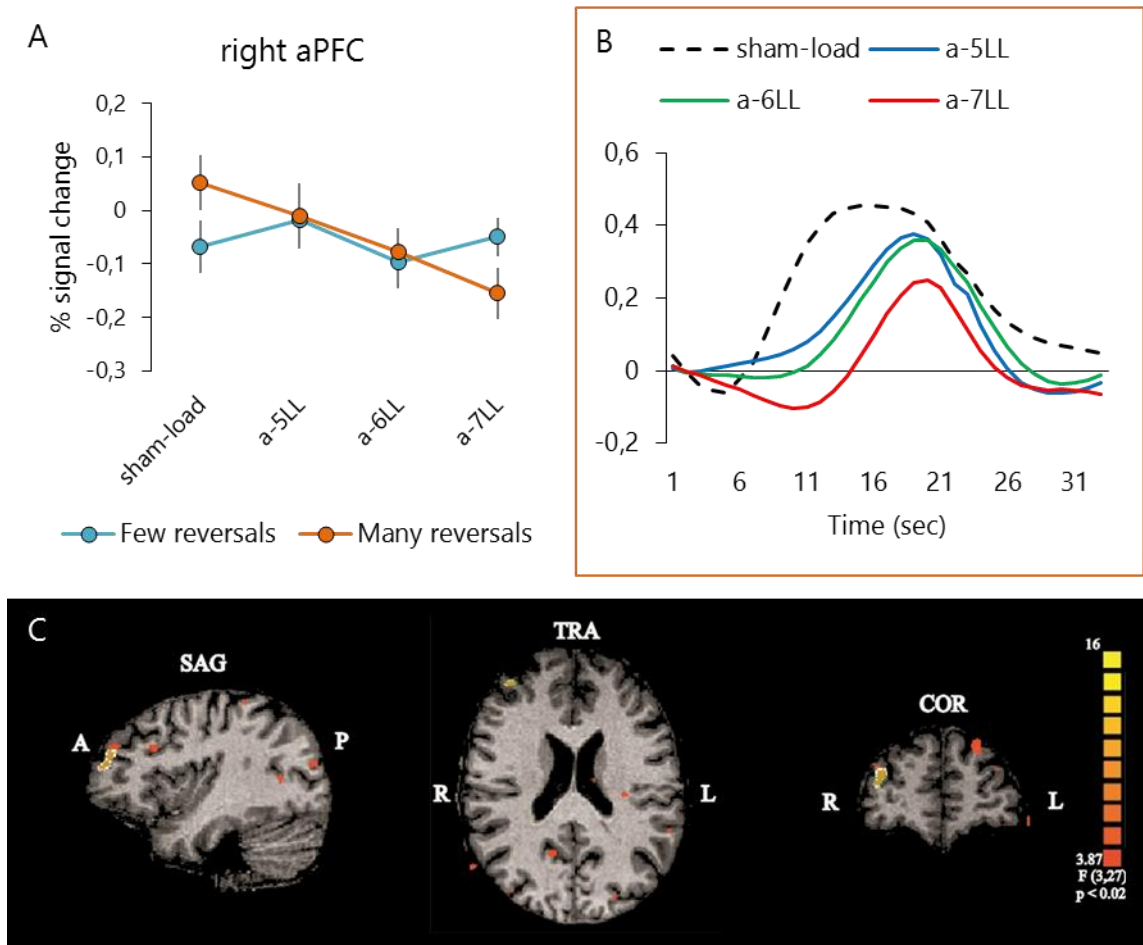


Figure 5-6. BOLD response in right anterior prefrontal cortex (aPFC) during presentation of the ambiguous Necker cube. (A) An interaction effect between cube reversals and WML was observed with repeated measures 2 (Reversals: few and many) \times 4 (Load: sham-load, a-5LL, a-6LL and a-7LL) ANOVA of signal changes. These interactions show that this brain region competes for attentional resources. (B) Time-course of BOLD response when participants viewed many cube reversals during ambiguous Necker cube presentation under sham, a-5LL, a-6LL and a-7LL working memory load (WML) conditions. (C) Functional map (thresholded at P -value < 0.05, FDR corrected) generated from ANOVA on fMRI response to perceptual reversals under WML showing significant Reversals \times Load interaction in right aPFC.

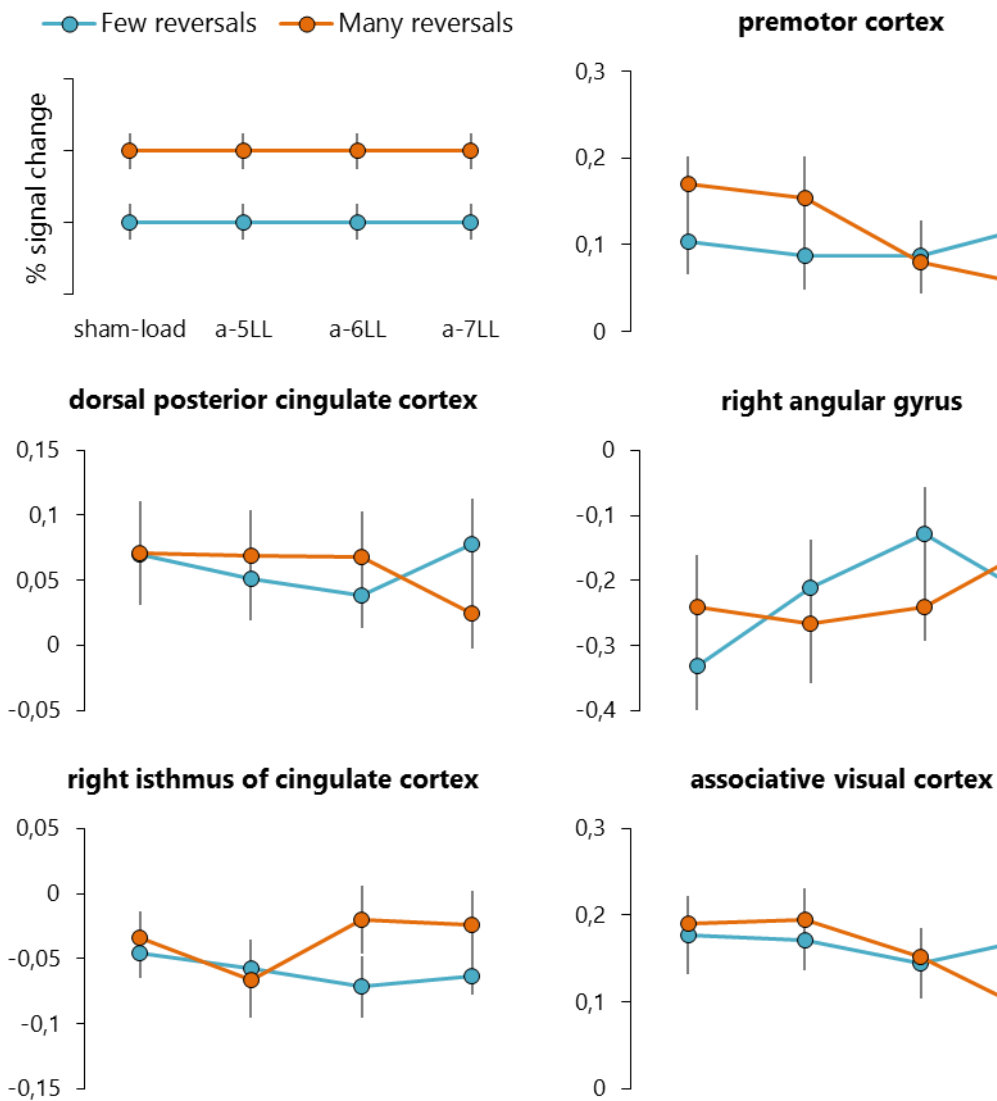


Figure 5-7. Schematic representations of significant Reversal × WML interactions during presentation of the ambiguous Necker cube. Interaction effects were obtained from repeated measures 2 (Reversals: few and many) × 4 (Load: sham-load, a-5LL, a-6LL and a-7LL) ANOVAs of signal changes over associative visual cortex, right angular gyrus, right isthmus of cingulate cortex, dorsal posterior cingulate cortex and premotor cortex. The interactions show that these structures compete for attentional resources. Error bars represent ± SEM.

Subsequent one-way ANOVAs, conducted on each ROI and for each Load level separately, revealed that the BOLD response over right aPFC was significantly more positive in response to many perceptual changes under sham load ($F(1, 9) = 6.67$, $P\text{-value} < 0.04$, $\eta p^2 = 0.43$). The BOLD responses over premotor cortex, left DLPFC and visual association cortex were significantly more positive/less negative in response to many perceptual changes under the low load level a-5LL ($F(1, 9) \geq 5.41$, $P\text{-values} < 0.05$, $\eta p^2 \geq 0.38$). The BOLD responses over right angular gyrus and right isthmus of cingulate cortex were significantly more positive/less negative in response to many perceptual changes under a-6LL ($F(1, 9) \geq 5.85$, $P\text{-value} < 0.04$, $\eta p^2 \geq 0.39$). The BOLD responses over premotor cortex, right pSPL, right aPFC, visual association cortex and dPCC were significantly less positive/more negative in response to many perceptual changes under a-7LL ($F(1, 9) \geq 6.94$, $P\text{-value} < 0.03$, $\eta p^2 \geq 0.44$).

U-6LL versus A-6LL

The 2 (Reversals: few and many) \times 2 (Type: u-6LL and a-6LL) repeated measures ANOVA revealed significant effects for Type over multiple ROIs. The BOLD responses over premotor cortex, pSPL, secondary visual cortex and insular cortex ($F(1, 9) \geq 12.33$, $P\text{-value} < 0.01$, $\eta p^2 \geq 0.58$) were significantly more positive in response to perceptual changes. The BOLD responses over primary visual cortex, isthmus of cingulate gyrus, dPCC, left angular gyrus, left aPFC, and right DLPFC ($F(1, 9) \geq 7.97$, $P\text{-value} < 0.05$, $\eta p^2 \geq 0.47$) were, on the contrary, significantly more negative in response to perceptual changes.

Significant Reversals \times Type interactions ($F(1, 9) \geq 11.02$, $P\text{-value} \leq 0.01$, $\eta p^2 \geq 0.55$) were obtained over several regions, but subsequent one-way ANOVAs revealed significant effect for Type ($F(1, 9) = 7.05$, $P\text{-value} < 0.05$, $\eta p^2 = 0.44$) only for stronger deactivations of right temporopolar area (Talairach coordinates

X=60, Y=8, Z=-14), in response to few perceptual changes than those in response to few real changes.

Discussion

We studied the effects of working memory load (WML) on perceived reversals of ambiguous Necker cube using fMRI. The results revealed that the WML manipulation was effective: the accuracy in response to memory probes decreased and the probe response times linearly increased in response to increasing levels of WML. Furthermore, the WML task modulated, but did not abolish, the dynamics of perceptual reversals. The participants perceived less reversals of the ambiguous Necker cube when they had to perform the concurrent WML task. Moreover, loading WM affects perceptual decisions specifically when the participants perceive more reversals per trial, that is, when their attentional resources are even more depleted. Furthermore, we replicated the previously described functional association between activity in visual, parietal and frontal regions^{18–20,40} and perceptual reversals (see Table 1), thus providing additional evidence that the fronto-parietal network is activated during perceptual changes. Importantly, we found evidence for a pivotal role of right posterior Superior Parietal Lobule (pSPL) in relation to perceptual decisions, as this region specifically reflected both differences in response to perceptual changes under different load levels, and was as well stronger in response to perceptual *versus* real changes. The finding that enhanced BOLD responses in SPL are observed in response to perceptual decisions, has been previously suggested by fMRI^{15–17,19}, studies. Furthermore, TMS^{25,41–43} studies imply a causal SPL role in generating perceptual decisions. Beyond suggesting a general involvement of parietal regions during perceptual switches, our data indicate that the activity in these regions can also be specifically associated with a particular perceptual state. Kanai and colleagues

²⁵ postulated that aSPL generates prediction (i.e., current interpretation) and the pSPL generates "prediction error" (i.e., the mismatch between top-down prediction and bottom-up input) ⁴⁴⁻⁴⁶. We found an interaction between the numbers of perceived reversals under WML: when participants perceived many reversals within a trial while performing a hard WML task, the activation of right pSPL decreases. If pSPL is involved in generating "prediction error", which increases the probability of the perceptual reversals ⁴⁰, interfering with pSPL activity with the WML task should lead to weaker signal activations. Our results confirm this, as right pSPL exhibited stronger activations in response to reversals under sham-load than in response to reversals perceived under higher levels of load (Figure 5-5). Thus, we speculate that WML interferes not with generating predictions per se, but rather with "prediction errors" specifically when the "prediction errors" (i.e., perceptual decisions) are enhanced.

Prefrontal cortex exhibits significant activations in response to reversals of bistable stimuli ^{17,18,20,47}. We found activations of the right aPFC when the participants perceive many reversals under sham-load (Figure 5-6). Left DLPFC was deactivated in response to few perceptual changes under the lowest a-5LL load, suggesting a relatively lower relevance of the region in reversal processes. Thus, the left DLPFC and right aPFC were effectively 'mirror images' of each other, suggesting distinct roles of these regions in the perceptual decision mechanism. Differential activations of aPFC and DLPFC are found in response to various working memory tasks ^{48,49}, thus, it remains unclear whether the pattern of these results was induced by WML task, or if the WML task revealed opposite roles of right aPFC and left DLPFC in response to perceptual decisions. The question, whether fronto-parietal activations associated with perceptual decisions directly contribute to perceptual awareness, is still under debate: fronto-parietal activations might reflect other top-down information processes such as selective attention ²⁷, be caused by the ambiguity of visual information ¹⁵, or reflect

processes occurring in response to introspection and report of perceptual states⁵⁰. Furthermore, a TMS study⁵¹ as well did not find evidence of a causal role of DLPFC in bistable perception. However, the deactivations of left DLPFC in response to few perceived reversals (i.e., longer percept durations) under WML might imply the possible involvement of left DLPFC in maintaining percept stability. Stronger activations of right aPFC under condition without WML are comparable to the results obtained with right SPL, thus they suggest repetition of the “prediction error” in the higher-level areas.

In this study, we replicated the behavioral finding that WML and perceptual reversals partially share attentional resources⁵. However, if only perceptual changes are observed under WML, there is no way to dissect these effects from the fMRI effects that would result from reporting a real change of the stimulus under WML. In order to examine this possibility, we have used an unambiguous control condition (u-6LL). The limitation of the current study was that we were only able to test one level of WML as our control without risking a major increase of the time our participants had to spend in the scanner. The analyses of behavioral data obtained in response to perceived reversals with reported real changes did not reveal any significant differences between conditions. However, stronger signal modulations over several brain areas were obtained in response to perceptual reversals in comparison to real changes. Our data are comparable to those obtained in studies examining the perception of bistable stimuli and unambiguous replay^{16,17,19,20,50}. Additional support for the role of pSPL as the generator of the “prediction error” was provided by stronger pSPL activations in response to perceptual (a-6LL) when compared to real changes (u-6LL). Predictive coding suggests that in case of the unambiguous condition the “predictions” created by higher-order regions are confirmed by sensory input, thus reciprocal interactions between higher and lower regions may be discontinued. However, we agree that a more thorough investigation would be required to test whether

the behavioral performance and fMRI results differ depending on increasing WM loads in unambiguous conditions.

We conclude that pSPL is directly involved in the perceptual decision mechanism and potentially in the reevaluation of a given visual scene (to match the predictions of the brain) thus causing perceptual changes (i.e., prediction errors). Finally, we suggest that aPFC and left DLPFC are involved in top-down modulatory control of the perceptual decisions.

References

1. Long, G. M. & Toppino, T. C. Enduring Interest in Perceptual Ambiguity: Alternating Views of Reversible Figures. *Psychol. Bull.* **130**, 748–768 (2004).
2. Toppino, T. C. & Long, G. M. Selective adaptation with reversible figures: don't change that channel. *Percept. Psychophys.* **42**, 37–48 (1987).
3. Leopold, D. A. & Logothetis, N. K. Multistable phenomena: Changing views in perception. *Trends Cogn. Sci.* **3**, 254–264 (1999).
4. Hochberg, J. & Peterson, M. A. Piecemeal organization and cognitive components in object perception: perceptually coupled responses to moving objects. *J. Exp. Psychol. Gen.* **116**, 370–380 (1987).
5. Intaitė, M., Koivisto, M. & Castelo-Branco, M. The linear impact of concurrent working memory load on dynamics of Necker cube perceptual reversals. *J. Vis.* **14**, 1–9 (2014).
6. Intaitė, M., Noreika, V., Šoliūnas, A. & Falter, C. M. Interaction of bottom-up and top-down processes in the perception of ambiguous figures. *Vision Res.* **89**, 24–31 (2013).
7. Kornmeier, J. & Bach, M. Ambiguous figures - what happens in the brain when perception changes but not the stimulus. *Front. Hum. Neurosci.* **6**, 1–23 (2012).
8. Kornmeier, J., Hein, C. M. & Bach, M. Multistable perception: When bottom-up and top-down coincide. *Brain Cogn.* **69**, 138–147 (2009).
9. Long, G. M., Toppino, T. C. & Kostenbauder, J. F. As the cube turns: evidence for two processes in the perception of a dynamic reversible figure. *Percept. Psychophys.* **34**, 29–38 (1983).
10. Gazzaley, A. & Nobre, A. Top-down modulation: Bridging selective attention and working memory. *Neuroimage* **16**, 129–135 (2012).
11. Gazzaley, A. *et al.* Functional interactions between prefrontal and visual association cortex contribute to top-down modulation of visual processing. *Cereb. Cortex* **17**, 125–135 (2007).
12. Mayer, J. S. *et al.* Common neural substrates for visual working memory and attention. *Neuroimage* **36**, 441–453 (2007).
13. Corbetta, M., Kincade, J. M. & Shulman, G. L. Neural systems for visual orienting and their relationships to spatial working memory. *J. Cogn. Neurosci.* **14**, 508–523 (2002).
14. Zanto, T. P., Rubens, M. T., Thangavel, A. & Gazzaley, A. Causal role of the prefrontal cortex in top-down modulation of visual processing and working memory. *Nat. Neurosci.* **14**, 656–661 (2011).
15. Knapen, T., Brascamp, J., Pearson, J., van Ee, R. & Blake, R. The role of frontal and parietal

- brain areas in bistable perception. *J. Neurosci.* **31**, 10293–10301 (2011).
16. Lumer, E. D., Friston, K. J. & Rees, G. Neural Correlates of Perceptual Rivalry in the Human Brain. *Science (80-.)*. **280**, 1930–1934 (1998).
 17. Lumer, E. D. & Rees, G. Covariation of activity in visual and prefrontal cortex associated with subjective visual perception. *Proc. Natl. Acad. Sci. U. S. A.* **96**, 1669–1673 (1999).
 18. Sterzer, P. & Kleinschmidt, A. A neural basis for inference in perceptual ambiguity. *Proc. Natl. Acad. Sci. U. S. A.* **104**, 323–328 (2007).
 19. Weilhammer, V. A., Ludwig, K., Hesselmann, G. & Sterzer, P. Frontoparietal cortex mediates perceptual transitions in bistable perception. *J. Neurosci.* **33**, 16009–16015 (2013).
 20. Kleinschmidt, A., Büchel, C., Zeki, S. & Frackowiak, R. S. Human brain activity during spontaneously reversing perception of ambiguous figures. *Proc. R. Soc. London Part B Biol. Sci.* **265**, 2427–2433 (1998).
 21. Sterzer, P. & Rees, G. A neural basis for percept stabilization in binocular rivalry. *J. Cogn. Neurosci.* **20**, 389–399 (2008).
 22. Courtney, S. M., Ungerleider, L. G., Keil, K. & Haxby, J. V. Transient and sustained activity in a distributed neural system for human working memory. *Nature* **386**, 608–611 (1997).
 23. Haxby, J. M., Petit, L., Ungerleider, L. G. & S, C. M. Distinguishing the Functional Roles of Multiple Regions in Distributed Neural Systems for Visual Working Memory. **11**, 145–156 (2000).
 24. Sala, J. B., Rämä, P. & Courtney, S. M. Functional topography of a distributed neural system for spatial and nonspatial information maintenance in working memory. **41**, 341–356 (2003).
 25. Kanai, R., Carmel, D., Bahrami, B. & Rees, G. Structural and functional fractionation of right superior parietal cortex in bistable perception. *Curr. Biol.* **21**, R106–R107 (2011).
 26. Champod, A. S. & Petrides, M. Dissociable roles of the posterior parietal and the prefrontal cortex in manipulation and monitoring processes. *Proc. Natl. Acad. Sci. U. S. A.* **104**, 14837–14842 (2007).
 27. Sterzer, P., Kleinschmidt, A. & Rees, G. The neural bases of multistable perception. *Trends Cogn. Sci.* **13**, 310–318 (2009).
 28. Kumar, S., Soto, D. & Humphreys, G. W. Electrophysiological evidence for attentional guidance by the contents of working memory. *Eur. J. Neurosci.* **30**, 307–317 (2009).
 29. Singhal, A. & Fowler, B. The differential effects of Sternberg short- and long-term memory scanning on the late Nd and P300 in a dual-task paradigm. *Cogn. Brain Res.* **21**, 124–132

- (2004).
30. Paffen, C. L. E., Alais, D. & Verstraten, F. A. J. Attention speeds binocular rivalry. *Psychol. Sci.* **17**, 752–756 (2006).
 31. Paffen, C. LE & Alais, D. Attentional modulation of binocular rivalry. *Front. Hum. Neurosci.* **5**, (2011).
 32. Reisberg, D. & O’Shaughnessy, M. Diverting subjects’ concentration slows figural reversals. *Perception* **13**, 461–468 (1984).
 33. Wallace, B. & Priebe, F. Hypnotic susceptibility, interference, and alternation frequency to the Necker cube illusion. *J. Gen. Psychol.* **112**, 271–277 (1985).
 34. Wallace, B. Latency and frequency reports to the Necker cube illusion: Effects of hypnotic susceptibility and mental arithmetic. *J. Gen. Psychol.* **113**, 187–194 (1986).
 35. Zhang, P., Jamison, K., Engel, S., He, B. & He, S. Binocular Rivalry Requires Visual Attention. *Neuron* **71**, 362–369 (2011).
 36. Oldfield, R. The assessment and analysis of handedness: the Edinburgh inventory. *Neuropsychologia* **9**, 97–113 (1971).
 37. Brainard, D. H. The Psychophysics Toolbox. *Spat. Vis.* **10**, 433–436 (1997).
 38. Pelli, D. G. The VideoToolbox software for visual psychophysics: transforming numbers into movies. *Spat. Vis.* **10**, 437–442 (1997).
 39. Howell, D. C. *Statistical methods for psychology*. (Wadsworth Publishing, 2009).
 40. Megumi, F., Bahrami, B., Kanai, R. & Rees, G. Brain activity dynamics in parietal regions during spontaneous switch in bistable perception. *Neuroimage* **107**, 190–197 (2015).
 41. Kanai, R., Bahrami, B. & Rees, G. Human parietal cortex structure predicts individual differences in perceptual rivalry. *Curr. Biol.* **20**, 1626–1630 (2010).
 42. Carmel, D., Walsh, V., Lavie, N. & Rees, G. Right parietal TMS shortens dominance durations in binocular rivalry. *Curr. Biol.* **20**, 799–800 (2010).
 43. Zaretskaya, N., Thielscher, A., Logothetis, N. K. & Bartels, A. Disrupting parietal function prolongs dominance durations in binocular rivalry. *Curr. Biol.* **20**, 2106–2111 (2010).
 44. Bar, M. The proactive brain: using analogies and associations to generate predictions. *Trends Cogn. Sci.* **11**, 280–289 (2007).
 45. Friston, K. A theory of cortical responses. *Philos. Trans. R. Soc. Lond. B. Biol. Sci.* **360**, 815–836 (2005).
 46. Yuille, A. & Kersten, D. Vision as bayesian inference: Analysis by synthesis? *Trends Cogn. Sci.* **10**, 301–308 (2006).
 47. Inui, T. *et al.* Neural substrates for depth perception of the Necker cube; a functional

- magnetic resonance imaging study in human subjects. *Neurosci. Lett.* **282**, 145–148 (2000).
48. De Pisapia, N. & Braver, T. S. Preparation for integration: the role of anterior prefrontal cortex in working memory. *Neuroreport* **19**, 15–19 (2008).
49. Kim, C., Kroger, J. K., Calhoun, V. D. & Clark, V. P. The role of the frontopolar cortex in manipulation of integrated information in working memory. *Neurosci. Lett.* **595**, 25–29 (2015).
50. Frässle, S., Sommer, J., Jansen, A., Naber, M. & Einhauser, W. Binocular Rivalry: Frontal Activity Relates to Introspection and Action But Not to Perception. *J. Neurosci.* **34**, 1738–1747 (2014).
51. de Graaf, T. A., de Jong, M. C., Goebel, R., van Ee, R. & Sack, A. T. On the functional relevance of frontal cortex for passive and voluntarily controlled bistable vision. *Cereb. cortex* **21**, 2322–2331 (2011).

Chapter 6

General discussion and conclusion

General discussion

In this thesis we explored the timely topic of how visual perception is achieved by distributed processing and active analysis of sensory information of the world. As introduced in Chapter 1, visual perception involves the neural integration of visual features processed in parallel in different visual areas¹⁻⁴. Theories of integrative processing explain that distributed parallel processing of different visual features is integrated to form coherent percepts of the visual world. Recent approaches emphasize the constructive nature of perception by assuming that top-down (goal-directed mechanisms such as attention) and bottom-up (stimulus-driven mechanisms) processes cooperate in everyday life to guide brain processing toward behaviourally relevant or particularly salient stimuli^{5,6}. An important question is how visual scenes containing multiple objects are processed in order to achieve successful object segregation. A particular challenge is posed to visual perception in a context when multiple interpretations of a physically constant stimulus are available, leading to rivalrous/conflicting percepts⁷⁻¹⁰. This context is instantiated under multistable conditions, whereby the pattern of sensory stimulation in the retina remains constant and still its perceptual appearance can change dramatically over time leading to perceptual switches that are not stimulus-driven. Multistable stimuli are thus well suited to investigate the origin of perceptual reversals regarding whether low or high level visual mechanisms play a major role¹¹.

In this work we used magnetic resonance imaging (MRI), an important imaging non-invasive modality in human neuroscience. We provided in Chapter 2 an overview of the MRI methods employed throughout this thesis to assess brain structure and function, from physical to physiological principles and data analysis. In this work we used this technique to investigate the influence of bottom-up and top-down mechanisms in the perception of bistable stimuli. We took advantage of a particular type of fMRI data analysis, deconvolution analysis, which allows

estimating any response shape after a short stimulus or event, as a perceptual switch. Despite possibly overlapping responses, employing such a deconvolution procedure recovers the true hemodynamic response function for each stimulation condition from the data ¹²⁻¹⁴. In Chapter 3 we provided an important practical contribution of this thesis in the methodological aspects of fMRI analysis. We explored the use of deconvolution approaches to fMRI data in healthy participants and diabetic patients, a population prone to cerebrovascular disease, in order to probe neurovascular coupling with a visual motion paradigm and empirically extract important features of neuronal response to visual stimuli from hemodynamic variable responses in human brain. The data-driven deconvolution analysis allowed us to estimate transient perceptual switch-related activity in response to a bistable moving stimulus, which we presented in Chapter 4.

We focused on visual perception of motion which poses particular demands because it is not always uniquely solvable by computation from sensory input. In order to segregate multiple objects in a visual scene, the human visual brain needs to solve disambiguation problems, including whether motion signals coming from co-existing contours arise from single or multiple objects. The extrastriate area MT+ is very well known to be involved in the perception of global motion ¹⁵⁻¹⁷. It remains however not completely understood how full integration of multiple globally moving surfaces is achieved within the whole visual hierarchy. These regions are optimal candidates for the investigation of how non-overlapping moving surfaces of a bistable stimulus, restricted to individual visual hemifields, are parsed into different objects or interhemispherically integrated into a single moving pattern.

The analysis of perceptual states, which are inherently subjective and unpredictable, revealed that the coherent global motion percept was dominant, as in other studies of multistability ¹⁸⁻²⁰. The duration of the two alternative percepts followed a gamma or lognormal distribution, suggesting the existence

of perceptual rivalling opponent motion systems²⁰⁻²⁵. Our psychophysical and imaging data support the existence of two stages in the processing of motion information in the human visual system. Each half-image in one side of the visual field can be envisaged as a 1-D component of the global 2-D pattern extending in both visual hemi-fields. We found that incoherent/component perception elicited higher signal changes than coherent/pattern motion percept in MT+. This can be explained as the result of a larger population of responsive neurons, including both component and pattern neurons responding to the motion of two incoherently moving 1-D patterns, which is assumed to be the first stage processing. The second stage seems to be concerned with establishing the motion of the global 2-D pattern, during which a smaller population of pattern neurons in MT+ are responding to a single 2-D object. This would result in smaller fMRI signal change, as we observed at the single-subject level within MT+. Previous studies had presented an explanation for the perceptual transitions between perceptual states in MT+, based in a competitive reconfiguration of cell assemblies in this area, one coding pattern motion and the other coding component motion^{8,26}. However, both used plaid stimuli and were not able to definitely prove the two-stage model and rule out the blob tracking model²⁷. We took advantage of a paradigm of perceptual emergence of coherence using a physically constant bistable stimuli that requires motion integration across interhemispheric regions. Our study is innovative in the sense it uses a new intersection-free 2-D bistable moving stimulus for the first time to investigate with fMRI the neural correlates of ambiguous motion perception in humans, at least to our knowledge. We observed that activity in the MT+ complex changes depending on whether subjects integrate all motion signals into the percept of a single surface, or whether they segregate signals and perceive two separate objects. The control experimental data using an unambiguous version of the same stimulus confirmed higher response to incoherent/component percept.

Is this redistribution of activity in assemblies representing component and pattern motion within MT+ triggered by local mechanisms in MT+ itself, or are there other regions causing switches in neuronal activity competition and perception? In order to specifically analyze transient signal changes related to perceptual switches, we employed a second GLM approach in which we marked the subjectively defined perceptual switches in the protocol of analysis. We also extracted response features of perceptual switches that were not stimulus driven by deconvolution of fMRI data within MT+. Deconvolution extraction of responses to perceptual switches confirmed stronger component responses within MT+ in response to perceptual switches, and lagged pattern responses, suggesting that more time is need for second stage integration. Adaptation effects might also play a role, as previously supported in an fMRI study of perceptual switches and states with apparent motion²⁸ and plaid stimuli⁸.

The whole-brain RFX-GLM analysis revealed several high-level brain regions that correlated significantly with perceptual switches. We observed activation evoked by ambiguous bistable motion in prefrontal cortex, visual cortex, parietal cortex, premotor areas, superior parietal lobule (SPL), cingulate gyrus, insula, opercular cortex and putamen, as reported in previous studies of bistable perception and perceptual decision making^{29–34}. With the specific contrast whole-brain analysis of [switches > phases] activity we observed significant signal changes elicited by perceptual switches rather than perceptual stable phases in prefrontal cortex, insula, inferior frontal gyrus, angular gyrus, supramarginal gyrus and cingulate gyrus. We replicated the previously described functional association between activity in parietal regions and perceptual switches^{35–37}, and we observed in particular significant activity in inferior and superior parietal lobule, which was recently proven to be part of a reciprocal interaction network involving MT+^{37,38}. Our results seem to agree with a recent study which hypothesized that perceptual switches may arise in the visual system but awareness of the change may rely on

brain regions dedicated to behavioural responses such as parietal areas³⁹. Interestingly, we found significant activations bilaterally in the cerebellum and left thalamus in response to perceptual switches, which were previously involved in perceptual multistability with auditory stimuli^{40,41}. Our results suggest that neural networks outside the visual system might as well participate in dynamic reconfiguration of cell assemblies allowing both for segregation and integration of disparate motion signals in visual areas, even across visual hemi-fields.

To improve our understanding of how the brain processes information in the context of interhemispherically bound bistable perception we investigated the interactions of activated brain areas - functional integration⁴². By using Granger causality^{42,43} we found directed influences from left and right MT+ to the contralateral MT+ during ambiguous bistable motion, suggesting that these focal motion-responsive regions communicate effectively in antagonistic decision processes that require disambiguation concerning either component motion in separate visual hemi-fields or coherent pattern motion across hemi-fields with this bistable stimulus. Furthermore, we found directed influences from MT+ to other visual areas such as right V3/V3A, which agrees with reports that activation in V3A underlies motion coherence^{44,45}. Notably, we found significant directed connectivity of both left and right MT+ with right SPL. Our results are in accordance with recent reports of functional causal interactions between right parietal subregions and lower visual areas such as MT+³⁸. Surprisingly, we could not reliably identify significant directed influences from other brain regions to MT+ during ambiguous bistable motion with Granger causality mapping. Our results seem to suggest that the transition between coherent/pattern and incoherent/component motion percepts of this specific interhemispheric stimulus might mainly require bottom-up activation of MT+ and feedforward connections to other brain regions. However, this does not exclude additional top-down connections with e.g. prefrontal cortex or insula, which shown significant

activation found in the RFX-GLM analysis, as this negative finding could be due to low sensitivity of difference GCM mapping for reciprocal interactions and low temporal sampling rate (2 seconds is far from ideal for connectivity analysis of neuronal processing).

Then, what is the role of regions in the parietal and frontal lobule, in particular in which concerns top-down effects? Research on bistable perception has been strongly influenced by the debate about whether it reflects a bottom-up, such as low-level local adaptation, or a top-down phenomenon ^{11,46,47}.

Indeed, previous fMRI studies have emphasized the role of top-down processes in perceptual transitions in binocular rivalry ^{35,48,49} and for leading attentional resources to brain areas involved in specific tasks ^{30,33,49–51}, including MT+ ^{30,52}.

The mechanism by which sensory information is filtered and maintained in working memory (WM) to be used for subsequent processing is known as selective attention, which orients the focus of conscious awareness toward relevant stimuli. Studies fMRI revealed an overlap between attention and WM networks over visual, parietal and frontal areas ^{53–55}, supporting the view that these cognitive functions share neural resources and are both governed by the fronto-parietal attention network ^{56,57}. The brain regions activated during perceptual changes seem as well to overlap with the fronto-parietal attention network as suggested by our results of perception of ambiguous motion and supported by previous studies ^{33,35,36,50,58}. Our study presented in Chapter 5 was motivated to help unravel the nature of such overlap.

We studied using fMRI the effects of working memory load (WML) on perceived reversals of another ambiguous bistable condition, the Necker cube. We tested whether perceptual reversals of the Necker cube orientation induce signal changes of fronto-parietal attention network by comparing reversals under four levels of WML. The results revealed that the WML manipulation was effective: the accuracy in response to memory probes decreased and the probe response times

linearly increased in response to increasing levels of WML. Furthermore, the WML task modulated, but did not abolish, the dynamics of perceptual reversals. The participants perceived less reversals of the ambiguous Necker cube when they had to perform the concurrent WML task. Furthermore, we found that activations of right SPL are reduced in response to perceptual reversals under harder levels of WML. We replicated the previously described functional association between activity in visual, parietal and frontal regions^{30,38,50,58} and perceptual reversals, thus providing additional evidence that the fronto-parietal network is activated during perceptual changes. Importantly, we found evidence for a pivotal role of right posterior superior parietal lobule (pSPL) in relation to perceptual decisions, as this region specifically reflected both differences in response to perceptual changes under different load levels, and was as well stronger in response to perceptual *versus* control real changes. Our results favour the hypothesis that pSPL generates "prediction errors"³⁷, leading to perceptual reversals, as we observed that right pSPL exhibited stronger activations in response to more reversals under sham-load than in response to few reversals perceived under higher levels of load, which increases the probability of the perceptual reversals. Prefrontal cortex exhibits as well significant activations in response to reversals of bistable stimuli^{30,36,58,59}. We found activations of the right anterior prefrontal cortex (aPFC) when the participants perceive many reversals in the condition of no WML. Left dorsolateral prefrontal cortex (DLPFC) was deactivated in response to few perceptual changes under the lowest load condition, suggesting a relatively lower relevance in reversal processes. Thus, the left DLPFC and right aPFC were effectively 'mirror images' of each other, suggesting distinct roles of these regions in the perceptual decision mechanism. Differential activations of aPFC and DLPFC are found in response to various working memory tasks^{60,61}, thus, it remains unclear whether the pattern of these results was induced by WML task, or if the WML task revealed opposite roles of right aPFC and left DLPFC in

response to perceptual decisions. Nonetheless we replicated the behavioural finding that WML and perceptual reversals partially share attentional resources⁶². In order to investigate separate effects of perceptual transitions and WML, we have performed an unambiguous control experiment with unambiguous physical transitions of the Necker cube. We observed stronger signal modulations over several brain areas in response to perceptual reversals in comparison to real changes. Our data are comparable to those obtained in studies examining the perception of bistable stimuli and unambiguous replay^{30,35,36,50,63}. Additional support for the role of pSPL as the generator of the “prediction error” was provided by stronger pSPL activations in response to perceptual when compared to real changes. Predictive coding suggests that in case of the unambiguous condition the “predictions” created by higher-order regions are confirmed by sensory input, thus reciprocal interactions between higher and lower regions may be discontinued. However, we agree that a future research should further test in which regions behavioural performance and fMRI responses would be also be modulated with varying WM loads in unambiguous conditions.

Conclusions

The work presented in this thesis, confirmed a close relation between activity changes in MT+ and perceptual switches involving differential segregation or integration of motion signals separate across visual hemi-fields, leading to perception of incoherent/component or coherent/pattern motion, respectively. The dynamic reconfiguration of cell assemblies within MT+ leading to bistable percepts might be mediated by local competition but also additional sources of influence triggering perceptual transitions, such as attention. We could confirm the involvement of frontal and parietal brain regions in perceptual transitions, suggesting they are pivotal in top-down modulatory control of visual perceptual decisions. In particular we could observe a significant modulation of perceptual reversals of an ambiguous figure with different levels of experimental interference of the fronto-parietal attention network.

We proved that fMRI can address spatial and temporal correlates of decision making processes, namely with deconvolution analysis of fMRI data. Granger causality analyses showed strong cross directional influences between left and right MT+ regions as well as with the superior parietal lobe during ambiguous decision-making. We believe advances in the development of faster fMRI sequences might help substantially increase the temporal resolution of fMRI data, which will help to further investigate neuronal correlates of perceptual transitions at a finer spatial and temporal scale with connectivity analysis.

These findings improve our understanding of the neural mechanisms underlying visual motion integration mechanisms and provide additional knowledge into the functional organization and involvement of high-order executive areas in visual perceptual decision-making.

References

1. Kandel, E. R., Schwartz, J. H., Jessel, T. M., Siegelbaum, S. A. & Hudspeth, A. *Principles of Neural Science*. (McGraw Hill, 2013).
2. Engel, A. K., Roelfsema, P. R., Fries, P., Brecht, M. & Singer, W. Role of the temporal domain for response selection and perceptual binding. *Cereb. cortex* **7**, 571–582 (1997).
3. Gregory, R. L. Knowledge in perception and illusion. *Philos. Trans. R. Soc. Lond. B. Biol. Sci.* **352**, 1121–1127 (1997).
4. Wandell, B. A. Computational Neuroimaging: Color Representations and Processing. *Psychology* 1–26 (1999).
5. Engel, A. K., Fries, P. & Singer, W. Dynamic predictions: oscillations and synchrony in top-down processing. *Nat. Rev. Neurosci.* **2**, 704–716 (2001).
6. McMains, S. & Kastner, S. Interactions of top-down and bottom-up mechanisms in human visual cortex. *J. Neurosci.* **31**, 587–597 (2011).
7. Castelo-Branco, M., Goebel, R., Neuenschwander, S. & Singer, W. Neural synchrony correlates with surface segregation rules. *Nature* **405**, 685–689 (2000).
8. Castelo-Branco, M. *et al.* Activity patterns in human motion-sensitive areas depend on the interpretation of global motion. *Proc. Natl. Acad. Sci.* **99**, 13914–13919 (2002).
9. Castelo-Branco, M. *et al.* Type of featural attention differentially modulates hMT+ responses to illusory motion aftereffects. *J. Neurophysiol.* **102**, 3016–3025 (2009).
10. Kozak, L. R. & Castelo-Branco, M. Peripheral influences on motion integration in foveal vision are modulated by central local ambiguity and center-surround congruence. *Investig. Ophthalmol. Vis. Sci.* **50**, 980–988 (2009).
11. Long, G. M. & Toppino, T. C. Enduring Interest in Perceptual Ambiguity: Alternating Views of Reversible Figures. *Psychol. Bull.* **130**, 748–768 (2004).
12. Dale, A. M. Optimal experimental design for event-related fMRI. *Hum. Brain Mapp.* **8**, 109–114 (1999).
13. Glover, G. H. Deconvolution of Impulse Response in Event-Related BOLD fMRI. *Neuroimage* **9**, 416–429 (1999).
14. Goebel, R. in *Clinical Functional MRI* 9–51 (2007).
15. Huk, A. C., Dougherty, R. F. & Heeger, D. J. Retinotopy and Functional Subdivision of Human Areas MT and MST. *J. Neurosci.* **22**, 7195–7205 (2002).
16. Kaas, A., Weigelt, S., Roebroek, A., Kohler, A. & Muckli, L. Imagery of a moving object: the role of occipital cortex and human MT/V5+. *Neuroimage* **49**, 794–804 (2010).

17. Kolster, H., Peeters, R. & Orban, G. A. The retinotopic organization of the human middle temporal area MT/V5 and its cortical neighbors. *J. Neurosci.* **30**, 9801–9820 (2010).
18. McDermott, J., Weiss, Y. & Adelson, E. H. Beyond junctions: nonlocal form constraints on motion interpretation. *Perception* **30**, 905–921 (2001).
19. Borsellino, A., De Marco, A., Allazetta, A., Rinesi, S. & Bartolini, B. Reversal time distribution in the perception of visual ambiguous stimuli. *Kybernetik* **10**, 139–144 (1972).
20. Brascamp, J. W., van Ee, R., Pestman, W. R. & van den Berg, A. V. Distributions of alternation rates in various forms of bistable perception. *J. Vis.* **5**, 287–298 (2005).
21. Zhou, Y., Gao, J., White, K., Merk, I. & Yao, K. Perceptual dominance time distributions in multistable visual perception. *Biol. Cybern.* **90**, 256–263 (2004).
22. Leopold, D. A., Wilke, M., Maier, A. & Logothetis, N. K. Stable perception of visually ambiguous patterns. *Nat. Neurosci.* **5**, 605–609 (2002).
23. Sterzer, P., Russ, M. O., Preibisch, C. & Kleinschmidt, A. Neural correlates of spontaneous direction reversals in ambiguous apparent visual motion. *Neuroimage* **15**, 908–916 (2002).
24. Kline, K. A., Holcombe, A. O. & Eagleman, D. M. Illusory motion reversal is caused by rivalry, not by perceptual snapshots of the visual field. *Vision Res.* **44**, 2653–2658 (2004).
25. Kaneoke, Y., Urakawa, T., Hirai, M., Kakigi, R. & Murakami, I. Neural basis of stable perception of an ambiguous apparent motion stimulus. *Neuroscience* **159**, 150–160 (2009).
26. Huk, A. C. & Heeger, D. J. Pattern-motion responses in human visual cortex. *Nat. Neurosci.* **5**, 72–75 (2002).
27. Adelson, E. H. & Movshon, J. A. Phenomenal coherence of moving visual patterns. *Nature* **300**, 523–525 (1982).
28. Muckli, L. *et al.* Apparent motion: event-related functional magnetic resonance imaging of perceptual switches and states. *J. Neurosci.* **22**, RC219 (2002).
29. Rebola, J., Castelhana, J., Ferreira, C. & Castelo-Branco, M. Functional parcellation of the operculo-insular cortex in perceptual decision making: an fMRI study. *Neuropsychologia* **50**, 3693–3701 (2012).
30. Kleinschmidt, A., Büchel, C., Zeki, S. & Frackowiak, R. S. Human brain activity during spontaneously reversing perception of ambiguous figures. *Proc. R. Soc. London Part B Biol. Sci.* **265**, 2427–2433 (1998).
31. Sterzer, P., Eger, E. & Kleinschmidt, A. Responses of extrastriate cortex to switching perception of ambiguous visual motion stimuli. *Neuroreport* **14**, 2337–41 (2003).
32. Sterzer, P., Kleinschmidt, A. & Rees, G. The neural bases of multistable perception. *Trends Cogn. Sci.* **13**, 310–318 (2009).

33. Knapen, T., Brascamp, J., Pearson, J., van Ee, R. & Blake, R. The role of frontal and parietal brain areas in bistable perception. *J. Neurosci.* **31**, 10293–10301 (2011).
34. Zaretskaya, N., Thielscher, A., Logothetis, N. K. & Bartels, A. Disrupting parietal function prolongs dominance durations in binocular rivalry. *Curr. Biol.* **20**, 2106–2111 (2010).
35. Lumer, E. D., Friston, K. J. & Rees, G. Neural Correlates of Perceptual Rivalry in the Human Brain. *Science* **280**, 1930–1934 (1998).
36. Lumer, E. D. & Rees, G. Covariation of activity in visual and prefrontal cortex associated with subjective visual perception. *Proc. Natl. Acad. Sci. U. S. A.* **96**, 1669–1673 (1999).
37. Kanai, R., Carmel, D., Bahrami, B. & Rees, G. Structural and functional fractionation of right superior parietal cortex in bistable perception. *Curr. Biol.* **21**, R106–R107 (2011).
38. Megumi, F., Bahrami, B., Kanai, R. & Rees, G. Brain activity dynamics in parietal regions during spontaneous switch in bistable perception. *Neuroimage* **107**, 190–197 (2015).
39. Brascamp, J., Blake, R. & Knapen, T. Negligible fronto-parietal BOLD activity accompanying unreportable switches in bistable perception. *Nat. Neurosci.* (2015).
40. Kashino, M. & Kondo, H. M. Functional brain networks underlying perceptual switching: auditory streaming and verbal transformations. *Philos. Trans. R. Soc. B Biol. Sci.* **367**, 977–987 (2012).
41. Roth, M. J., Synofzik, M. & Lindner, A. The cerebellum optimizes perceptual predictions about external sensory events. *Curr. Biol.* **23**, 930–935 (2013).
42. Roebroeck, A., Formisano, E. & Goebel, R. Mapping directed influence over the brain using Granger causality and fMRI. *Neuroimage* **25**, 230–242 (2005).
43. Goebel, R., Roebroeck, A., Kim, D. & Formisano, E. Investigating directed cortical interactions in time-resolved fMRI data using vector autoregressive modeling and Granger causality mapping. *Magn. Reson. Imaging* **21**, 1251–1261 (2003).
44. Tootell, R. B. *et al.* Functional analysis of V3A and related areas in human visual cortex. *J. Neurosci.* **17**, 7060–7078 (1997).
45. Aspell, J., Tanskanen, T. & Hurlbert, A. Neuromagnetic correlates of visual motion coherence. *Eur. J. Neurosci.* **22**, 2937–2945 (2005).
46. Kornmeier, J., Hein, C. M. & Bach, M. Multistable perception: When bottom-up and top-down coincide. *Brain Cogn.* **69**, 138–147 (2009).
47. Wernery, J. *et al.* Temporal processing in bistable perception of the Necker cube. *Perception* **44**, 157–168 (2015).
48. Tong, F., Meng, M. & Blake, R. Neural bases of binocular rivalry. *Trends Cogn. Sci.* **10**, 502–511 (2006).

49. Leopold, D. A. & Logothetis, N. K. Multistable phenomena: Changing views in perception. *Trends Cogn. Sci.* **3**, 254–264 (1999).
50. Weilhhammer, V. A., Ludwig, K., Hesselmann, G. & Sterzer, P. Frontoparietal cortex mediates perceptual transitions in bistable perception. *J. Neurosci.* **33**, 16009–16015 (2013).
51. Naghavi, H. R. & Nyberg, L. Common fronto-parietal activity in attention, memory, and consciousness: shared demands on integration? *Conscious. Cogn.* **14**, 390–425 (2005).
52. O’Craven, K. M., Rosen, B. R., Kwong, K. K., Treisman, A. & Savoy, R. L. Voluntary attention modulates fMRI activity in human MT-MST. *Neuron* **18**, 591–598 (1997).
53. Gazzaley, A. & Nobre, A. Top-down modulation: Bridging selective attention and working memory. *Neuroimage* **16**, 129–135 (2012).
54. Gazzaley, A. *et al.* Functional interactions between prefrontal and visual association cortex contribute to top-down modulation of visual processing. *Cereb. Cortex* **17**, 125–135 (2007).
55. Mayer, J. S. *et al.* Common neural substrates for visual working memory and attention. *Neuroimage* **36**, 441–453 (2007).
56. Corbetta, M., Kincade, J. M. & Shulman, G. L. Neural systems for visual orienting and their relationships to spatial working memory. *J. Cogn. Neurosci.* **14**, 508–523 (2002).
57. Zanto, T. P., Rubens, M. T., Thangavel, A. & Gazzaley, A. Causal role of the prefrontal cortex in top-down modulation of visual processing and working memory. *Nat. Neurosci.* **14**, 656–661 (2011).
58. Sterzer, P. & Kleinschmidt, A. A neural basis for inference in perceptual ambiguity. *Proc. Natl. Acad. Sci. U. S. A.* **104**, 323–328 (2007).
59. Inui, T. *et al.* Neural substrates for depth perception of the Necker cube; a functional magnetic resonance imaging study in human subjects. *Neurosci. Lett.* **282**, 145–148 (2000).
60. De Pisapia, N. & Braver, T. S. Preparation for integration: the role of anterior prefrontal cortex in working memory. *Neuroreport* **19**, 15–19 (2008).
61. Kim, C., Kroger, J. K., Calhoun, V. D. & Clark, V. P. The role of the frontopolar cortex in manipulation of integrated information in working memory. *Neurosci. Lett.* **595**, 25–29 (2015).
62. Intaitè, M., Koivisto, M. & Castelo-Branco, M. The linear impact of concurrent working memory load on dynamics of Necker cube perceptual reversals. *J. Vis.* **14**, 1–9 (2014).
63. Frässle, S., Sommer, J., Jansen, A., Naber, M. & Einhauser, W. Binocular Rivalry: Frontal Activity Relates to Introspection and Action But Not to Perception. *J. Neurosci.* **34**, 1738–1747 (2014).

List of publications

Intaitè M*, **Duarte JV***, Castelo-Branco M (2016): *Working memory influences perceptual ambiguity by competing for fronto-parietal attentional resources*. Brain research; *In revision*. * Co-first authorship

Duarte JV*, Faustino R*, Lobo M, Cunha G, Nunes C, Ferreira C, Januário C, Castelo-Branco M (2015): *Parametric fMRI of paced motor responses uncovers novel whole brain imaging biomarkers in SCA3*. Human Brain Mapping; *In revision*. * Co-first authorship

Al-Rawi MS, Freitas A, **Duarte JV**, Cunha JP, Castelo-Branco M (2015): *Permutations of fMRI Classification May Not Be Normally Distributed*. Statistical Methods in Medical Research; *In press*.

Duarte JV, Pereira JMS, Quendera B, Raimundo M, Moreno C, Gomes L, Carrilho F, Castelo-Branco M (2015): *Early disrupted neurovascular coupling and changed event level hemodynamic response function in type 2 diabetes: an fMRI study*. Journal of Cerebral Blood Flow and Metabolism, 35(10): p1671 - 1680.

Al-Rawi MS, Freitas A, **Duarte JV**, Castelo-Branco M (2014): *Permutation distributions of fMRI classification do not behave in accord with central limit theorem*. International Workshop on Pattern Recognition in Neuroimaging (PRNI).

Duarte JV, Ribeiro MJ, Violante IR, Cunha G, Silva E, Castelo-Branco M (2014): *Multivariate pattern analysis reveals subtle brain anomalies relevant to the cognitive phenotype in Neurofibromatosis type 1*. Human Brain Mapping; 35(1), p89-106.

Violante IR, Ribeiro MJ, Cunha G, Bernardino I, **Duarte JV**, Ramos F, Saraiva J, Silva E, Castelo-Branco M (2012): *Abnormal brain activation in neurofibromatosis type 1: a link between visual processing and the default mode network*. PLoS One; 7(6):e38785.

Duarte JV, Ribeiro M, Violante I, Cunha G, Al-Rawi M, Cunha JP, Castelo-Branco M (2011): *Multivariate pattern analysis of brain structure: A diagnostic tool for Neurofibromatosis type 1*. Portuguese chapter of IEEE EMBS, Proceedings of the Portuguese Meeting in Bioengineering (ENBENG).

Direito B, **Duarte JV**, Teixeira CA, Le Van Quyen M, Schulze-Bonhage A, Sales F, Dourado A (2011): *Feature selection in high dimensional EEG feature spaces for epileptic seizure prediction*. International Federation of Automatic Control (IFAC) World Congress.

Curriculum Vitae

João Duarte was born on February 18, 1984 in Coimbra. In 2002, he completed his secondary school education at Escola Secundária D. Dinis in Coimbra, after which she studied Biomedical Engineering at the Faculty of Science and Technology of the University of Coimbra. For his Master thesis, entitled "*Machine learning approaches in Genome-Wide Association Studies: SNP2Net, a tool for gene-based predictive modelling*", he did a research internship the Laboratory of Biomedical Informatics at the University of Pavia, Italy. After finishing the Master degree in 2009 he started his PhD research project on the "*The role of long-range synchrony underlying perceptual coherence*" at the Visual Neuroscience Laboratory at IBILI - Faculty of Medicine, University of Coimbra, Portugal, under the supervision of Professor Miguel Castelo-Branco and Professor Maria Ribeiro. He has done parallel work in the application of multivariate computational tools for the analysis of genetic, electroencephalographic and neuroimaging data in the context of health and disease.

